

Copyright
by
Raul Hernan Santa Maria
2001

Committee Certification of Approved Version

**The Dissertation Committee for Raul Hernan Santa Maria Certifies that this
is the approved version of the following dissertation :**

Behavior of Hollow, Rectangular Concrete Piers Subjected to Biaxial Bending

Committee:

Sharon L. Wood, Supervisor

John E. Breen

Eric B. Becker

Richard E. Klingner

Michael E. Kreger

**Behavior of Hollow, Rectangular Concrete Piers Subjected to
Biaxial Bending**

by

Raul Hernan Santa Maria, B.S, M.S.

Dissertation

Presented to the Faculty of the Graduate School of

The University of Texas at Austin

in Partial Fulfillment

of the Requirements

for the Degree of

Doctor of Philosophy

The University of Texas at Austin

December, 2001

Dedication

Nicole, sin tu amor y paciencia nada de lo que sigue habria sido possible.

Behavior of Hollow, Rectangular Concrete Piers Subjected to Biaxial Bending

Publication No. _____

Raul Hernan Santa Maria, Ph.D.
The University of Texas at Austin, 2001

Supervisor: Sharon L. Wood

Hollow, rectangular concrete piers have been used to support cable stay and long-span balanced cantilever bridges for the last forty years. Compared with solid columns, hollow piers offer the advantages of high bending and torsional stiffness, significant reductions in the volume of materials, and large reductions in dead load. Earlier investigations concluded that no reduction in strength should occur for cross sections subjected to combined axial load and uniaxial bending with wall slenderness ratios, defined as the unsupported length of the cross section divided by the wall thickness of the slender walls, less than 15. However, the response of hollow, rectangular piers subjected to simultaneous axial load and biaxial bending has not been studied.

Five rectangular, hollow concrete columns, with wall slenderness ratios between 6 and 14 and designed in accordance to the AASHTO LRFD Bridge

Design Specifications, were tested under quasi-static, monotonic simultaneous axial load and biaxial bending. Neither cyclic loading nor horizontal or transverse loads were considered. A fiber model of the cross section and two material models for confined concrete were used to perform sectional analysis of each specimen. A finite element model was used to calculate the behavior of the test specimens. Also, the current design procedures for hollow, rectangular concrete piers were re-evaluated and found to produce safe estimates of the strength of such piers.

In hollow, rectangular concrete piers the value of the strength ratio, defined as the measured axial strength divided by the axial strength calculated using a rectangular stress block model of concrete, decreases as the wall slenderness ratio increases. The main parameter that controls those variations is the wall slenderness ratio. The current approximate design procedures for hollow, rectangular concrete piers with wall slenderness ratios 15, are valid for piers subjected to axial compression and biaxial bending.

Material models for confined concrete provided accurate estimates of the axial capacity and moment-curvature response of the hollow piers tested in this investigation. Future areas of research are recommended.

Table of Contents

List of Tables.....	xv
List of Figures	xxi
Chapter 1 Introduction	1
1.1 Overview	1
1.2 Objectives.....	3
1.3 Scope of the Investigation	4
Chapter 2 Review of Previous Investigations of the Performance of Hollow Concrete Piers	7
2.1 Behavior of Hollow Concrete Piers	8
2.1.1 Procter	8
2.1.2 Jobse and Moustafa	10
2.1.3 Poston, Gilliam, Yamamoto and Breen.....	11
2.1.4 Taylor, Rowell, and Breen	14
2.1.5 Mander, Priestley and Park	19
2.1.6 Mo, Yeh and Yang	19
2.2 Behavior of Thin Concrete Plates	20
2.2.1 Ernst	20
2.2.2 Swartz, Rosebraugh, and Berman	23
2.2.3 Saheb and Desayi	28
2.3 Summary	31
Chapter 3 Overview of Design Procedures	32
3.1 AASHTO Design Procedures for Compression Members in the early 1990s	32
3.2 Approximate Method for Design of Hollow rectangular Compression Members.....	34
3.2.1 Reinforcing details	35

3.2.2 Design Procedures.....	35
3.3 Evaluation of Design Provisions.....	36
3.3.1 Strength Ratios Calculated Using Analysis Procedures Developed by Taylor.....	37
3.3.2 Strength Ratios Calculated Using Equivalent Rectangular Stress Block.....	40
3.3.3 Strength Ratios Calculated Using Equivalent Rectangular Stress Block and Concrete Design Strength.....	44
3.4 Summary.....	48
Chapter 4 Experimental Program.....	50
4.1 Overview.....	50
4.1.1 Scale of the Models.....	51
4.2 Design of the Specimens.....	53
4.2.1 Governing Provisions of AASHTO Specifications.....	53
4.2.2 Reinforcing details.....	58
4.3 Materials.....	67
4.3.1 Concrete.....	67
4.3.2 Reinforcement.....	67
(a) Longitudinal Reinforcement.....	67
(b) Transverse Reinforcement.....	67
(c) Reinforcement of End Blocks.....	67
4.4 Fabrication of Specimen.....	68
4.4.1 Construction Method.....	68
4.4.2 Placing of Concrete.....	77
4.4.2.1 Consolidation.....	77
4.4.2.2 Curing and Form Removal.....	78
4.4.3 Pier Dimensions and Wall Thicknesses.....	78
4.5 Loading Arrangement.....	81
4.5.1 Loading Method.....	81
4.5.2 Loading Apparatus.....	82

4.5.3 Spherical Bearings.....	84
4.6 Instrumentation.....	86
4.6.1 Load.....	86
4.6.2 Displacements	87
4.6.3 Curvature.....	92
4.6.4 Data Acquisition System.....	94
4.7 Test Procedure.....	95
4.7.1 Transportation of Specimens.....	95
4.7.2 Alignment of Specimens	95
4.7.3 Measurement of Eccentricities	96
4.7.4 Loading of Specimens	96
Chapter 5 Experimental Results.....	98
5.1 Notation and Parameters used to Interpret Response.....	99
5.1.1 Horizontal Deflections	100
5.1.2 Rotations of the End Blocks.....	102
5.1.3 Vertical Deflections.....	103
5.1.4 Curvature	104
5.2 Measured Response of Specimen P6	105
5.2.1 Observed Crack Patterns	106
5.2.2 Behavior of the Reinforcement	107
5.2.3 Longitudinal Profiles.....	111
5.2.4 Profile of East Wall	113
5.2.5 Rotations of the End Blocks.....	115
5.2.6 Vertical Deflections.....	116
5.2.7 Curvature	117
5.3 Measured Response of Specimen P8	119
5.3.1 Observed Crack Patterns	119
5.3.2 Behavior of the Reinforcement	121
5.3.3 Longitudinal Profiles.....	125

5.3.4 Profile of East Wall	127
5.3.5 Rotations of the End Blocks.....	129
5.3.6 Vertical Deflections.....	129
5.3.7 Curvature	131
5.4 Measured Response of Specimen P10	133
5.4.1 Observed Crack Patterns	133
5.4.2 Behavior of the Reinforcement	134
5.4.3 Longitudinal Profiles.....	138
5.4.4 Profile of East Wall	140
5.4.5 Rotations of the End Blocks.....	142
5.4.6 Vertical Deflections.....	142
5.4.7 Curvature	143
5.5 Measured Response of Specimen P12	146
5.5.1 Observed Crack Patterns	146
5.5.2 Behavior of the Reinforcement	147
5.5.3 Longitudinal Profiles.....	152
5.5.4 Profile of East Wall	154
5.5.5 Rotations of the End Blocks.....	156
5.5.6 Vertical Deflections.....	156
5.5.7 Curvature	158
5.6 Measured Response of Specimen P14	159
5.6.1 Observed Crack Patterns	160
5.6.1 Behavior of the Reinforcement	161
5.6.3 Longitudinal Profiles.....	165
5.6.4 Profile of East Wall	167
5.6.5 Rotations of the End Blocks.....	168
5.6.6 Vertical Deflections.....	169
5.6.7 Curvature	170
5.7 Discussion of Experimental Results.....	172

5.7.1 Longitudinal Profiles.....	172
(a) Influence of Possible Lateral Translation of the Top Block.....	176
(b) Influence of Possible Initial Misalignment of the Test Specimens.....	185
(c) Influence of Simultaneous Varying Curvature and Translation of the Top Block	193
(d) Possible Explanation of the Shape of the Measured Longitudinal Profiles.....	197
5.7.2 Profiles of the East Walls.....	200
5.7.3 Rotations of the End Blocks.....	201
5.7.4 Vertical Deflections.....	203
5.7.5 Moment-Curvature Response.....	206
5.7.6 Cracking	210
5.7.7 Location of Failure	212
5.7.8 Confinement of the Concrete	213
5.7.9 Reinforcing details	214
5.7.10 Plane Sections	216
5.8 Summary	219
Chapter 6 Analytical Evaluation of the Capacity of the Test Specimens	221
6.1 Calculation of the Axial Capacity at Nominal Eccentricity of the Tested Specimens Using Approximate Design Procedure.....	221
6.2 Influence of Transverse Reinforcement on the Compressive Strength of the Concrete	225
6.3 Moment-Curvature Response.....	228
6.4 Axial Capacities of the Tested Specimens Calculated at the Measured Eccentricities Using Models for Confined Concrete.....	241
6.4.1 Evaluation of Pier P14.....	243
6.4.2 Stability of Longitudinal Bars	245
6.4.3 Hypothesized Failure Sequence of the Test Specimens.....	253
6.5 Summary	254

Chapter 7 Overall Analytical Model	257
7.1 Finite Element Model.....	257
7.1.1 Materials.....	257
(a) Concrete	258
(b) Steel Reinforcement	266
7.1.2 Element.....	266
7.1.3 Loading Method	267
7.1.4 Local Buckling.....	270
7.2 Calculation of Buckling in Thin Concrete Panels	270
7.2.1 Responses of Thin Concrete Panels Calculated using Finite Element Model	273
7.3 Comparison of the measured and calculated response of hollow piers tested in this investigation	285
7.3.1 Verification of the Finite Element Model Using Test Results from Current Investigation	285
7.3.1.1 Comparison of Measured and Calculated Capacities... ..	288
7.3.1.2 Local Buckling.....	292
7.3.1.3 Comparison of Failure Modes.....	293
7.3.1.4 Comparison of Crack Patterns.....	293
7.3.1.5 Comparison of Vertical Deflections.....	294
7.3.1.6 Comparison of Moment–Curvature Responses.....	298
7.3.1.7 Summary of Observations	304
7.3.2 Comparison of the Measured and Calculated Capacity of Hollow Piers Tested by other Researchers.....	305
7.4 Summary	313
Chapter 8 Design Considerations	315
8.1 Parameters Influencing the Strength of Hollow, Rectangular Concrete Piers	316
8.1.1 Wall Slenderness Ratio	316
8.1.2 Confinement Provided by the Transverse Reinforcement	318

8.1.3 Maximum Compressive Strain in the Concrete	330
8.1.4 Loading Pattern	332
8.1.5 Results from Linear Regression Analyses	336
8.2 Design Procedures.....	338
8.3 Summary	342
Chapter 9 Conclusions	344
9.1 Summary	344
9.1.1 Experimental Program.....	345
9.1.2 Confinement Models	345
9.1.3 Overall Finite Element Model.....	345
9.1.4 Limitations of the Investigation	346
9.2 Conclusions	346
9.3 Design Recommendations.....	347
9.4 Research Recommendations	348
Appendix A Measured Material Properties.....	350
A.1 Concrete.....	350
A.1.1 Measured Concrete Material Properties	350
A.1.2 Calculated Concrete Material Properties.....	353
A.1.2.1 Modulus of Elasticity	353
A.1.2.2 Stress-Strain Curve.....	354
A.1.2.3 Tensile Strength.....	357
A.2 Reinforcement	358
A.2.1 Longitudinal Reinforcement.....	359
A.2.2 Transverse Reinforcement.....	360
A.2.3 Reinforcement in End Blocks.....	361
Appendix B Measured Response of the Test Specimens.....	362
B.1 Horizontal Displacements Measured Along the East and North Walls.....	362

B.2 Vertical Displacements Measured at the Center of the Solid Blocks..	374
B.3 Vertical Displacements Measured at the Edges of the Solid Blocks...	377
B.4 Vertical Displacements used to Calculate Curvature	380
B.5 Horizontal displacements measured at the Top Solid Block.....	386
Appendix C Stress-Strain Models for Confined Concrete	390
C.1 Use of Models for Confined Concrete in Hollow Piers.....	390
C.2 Mander, Priestley and Park.....	391
C.2.1 Analytical Model	392
C.2.2 Application of Model to Hollow Piers	397
C.3 Saatcioglu, M. and Razvi, S.R.....	404
C.3.1 Analytical Model	405
C.3.2 Application of Model to Hollow Piers	408
C.4 Comparison of Models for Stress-Strain Relationships of Confined Concrete	415
References	423
Vita.....	429

List of Tables

Table 2.1	Dimensions and Capacity of Specimens Tested by Procter (1977)	9
Table 2.2	Capacities of Specimens Tested by Jobse and Moustafa (1984)	11
Table 2.3	Dimensions of Specimens Tested by Poston et al. (1983, 1985)	13
Table 2.4	Test Results of Specimens Tested by Poston et al. (1983, 1985)	14
Table 2.5	Dimensions of Specimens Tested by Taylor et al. (1990)	17
Table 2.6	Measured and Calculated Capacities of Specimens Tested by Taylor et al. (1990).....	18
Table 2.7	Dimensions and Strength of Specimens Tested by Ernst (1952)	22
Table 2.8	Dimensions of Specimens Tested by Swartz et al. (1974).....	25
Table 2.9	Measured Buckling Load and Failure Load, and Calculated Buckling Load Using Tangent Modulus (Swartz and Rosebraugh 1974).....	27
Table 2.10	Specimens Tested by Saheb and Desayi (1990).....	30
Table 3.1	Nominal Capacities of Hollow Piers Tested by Other Researchers Calculated Using Cylinder Strength.....	42
Table 3.2	Nominal Capacities of Hollow Piers Tested by Other Researchers Calculated Using Compressive Design Strength of Concrete.....	47
Table 4.1	Geometric Properties of Test Specimens	53
Table 4.2	Summary of Requirements for Reinforcing details in One-Fifth Scale Hollow Piers	57
Table 5.1	Summary of Experimental Tests.....	98

Table 5.2	Calculated Rigid-Body Translations and Rotations of the Top Blocks at the Measured Capacity of the Piers.....	184
Table 5.3	Calculated Values of β at the Measured Capacity	189
Table 5.4	Calculated Translations of the Top Blocks in the East Direction Assuming Linear Variation of the Curvature Along the Length of the Piers at the Measured Capacity	197
Table 5.5	Elastic Bending Stiffness about the East-West Axis.....	209
Table 5.6	Curvatures Measured at Failure	210
Table 5.7	Ratio of Measured Strength to Load of First Observed Crushing in Concrete	214
Table 6.1	Measured and Calculated Capacities of Tested Specimens	224
Table 6.2	Calculated Ratios of Confined to Unconfined Compressive Strength of the Concrete Calculated in Appendix C	228
Table 6.3	Measured Ultimate Curvatures and Curvatures Calculated at the Maximum Load	240
Table 6.4	Capacities of Piers Calculated Using Models for Confined and Unconfined Concrete.....	242
Table 6.5	Capacities and Maximum Curvatures for Specimen P14 Calculated using Material Models M and S assuming the Maximum Compressive Strain in the Unconfined Concrete Equal to 0.003...	244
Table 6.6	Calculated Compressive Strain in the Concrete and in Longitudinal Bars in Northeast Corner at Peak Axial Load	247

Table 6.7	Calculated Compressive Strain in the Concrete and in Longitudinal Bars Along East Wall with Largest Buckled Length at Peak Axial Load.....	247
Table 6.8	Ratios S/d_b of Longitudinal Bars with Largest Buckled Length and Bars Located at the Northeast Corner of the Piers	252
Table 7.1	Capacity of Concrete Panels Tested by Ernst (1952) Calculated Using Various Numbers of Elements.....	272
Table 7.2	Comparison of Measured and Calculated Capacity for Specimens tested by Ernst (1952)	281
Table 7.3	Comparison of Measured and Calculated Capacity for Specimens tested by Swartz et al. (1974).....	282
Table 7.4	Comparison of Measured and Calculated Capacity for Specimens tested by Saheb and Desayi (1990)	283
Table 7.5	Summary of Averages of Ratios of Measured Strengths to Calculated Capacities Calculated Using All the Available Panel Tests, Grouped in Ranges of Wall Slenderness Ratios	284
Table 7.6	Averages of Ratios of Measured to Calculated Capacities of Panels with Wall Slenderness Ratio Between 6 and 12 and Calculated Using an Imperfection Ratio Equal to 0.0.....	284
Table 7.7	Calculated Capacities of Specimen P14 using Models with Different Meshes in the Longer Walls and Imperfection Ratio of 0.24.....	286

Table 7.8	Calculated Capacity Using Finite Elements for the Specimens from the Current Investigation.....	290
Table 7.9	Ratios of Measured to Calculated Capacities.....	291
Table 7.10	Observed Cracking Loads and Computed Cracking Loads	294
Table 7.11	Comparison of Measured Capacity and Calculated Capacity Using Finite Elements for all the Available Test Results (Imperfection Ratio Equal 0.0).....	307
Table 7.12	Comparison of Measured Capacity and Calculated Capacity Using Finite Elements for all the Available Test Results (Imperfection Ratio Equal 0.16).....	308
Table 7.13	Comparison of Measured Capacity and Calculated Capacity Using Finite Elements for all the Available Test Results(Imperfection Ratio Equal 0.24).....	309
Table 7.14	Comparison of Measured Capacity and Calculated Capacity Using Finite Elements for all the Test Results (Imperfection Ratio From Table 7.5)	311
Table 8.1	Values of Various Parameters that Influence Strength Ratios	327
Table 8.2	Number of Tests Conducted Under Each Loading Pattern in Different Ranges of Wall Slenderness Ratio (λ_w).....	335
Table 8.3	Coefficients and Standard Errors Obtained from the Linear Regressions.....	338
Table A.1	Compression Strength of Concrete	352
Table A.2	Average Concrete Parameters Determined from Stress-Strain Data	352

Table A.3 Tensile Strength of Concrete from Split-Cylinder Tests.....	353
Table A.4 Comparison of Measured and Estimated Modulus of Elasticity of the Concrete used in the Hollow Piers	354
Table A.5 Comparison of Measured and Estimated Tensile Strength of Concrete	358
Table A.6 Measured Strength of the Steel Reinforcement.....	359
Table A.7 Measured Hardening Properties of the Steel Reinforcement	359
Table C.1 Dimensions Used to Calculate the Strength of the Confined Concrete in the East Walls	399
Table C.2 Dimensions Used to Calculate the Strength of the Confined Concrete in the North Walls.....	400
Table C.3 Dimensions Used to Calculate the Strength of the Confined Concrete in the Northeast Corners of the Piers	401
Table C.4 Confining Stresses and Ratios of Unconfined to Confined Compressive Strength of Concrete Calculated Using Models Developed by Mander et al. (1988b).....	402
Table C.5 Strains and Coefficients Used to Define the Stress-Strain Relationship of Confined Concrete Using the Model Developed by Mander et al. (1988b).....	403
Table C.6 Limiting Compressive Strain in the Confined Concrete in the Corners of the Test Specimens Calculated Using the Material Model Developed by Mander et al. (1988b)	404

Table C.7	Dimensions Used to Calculate the Strength of the Confined Concrete in the East Walls	410
Table C.8	Dimensions Used to Calculate the Strength of the Confined Concrete in the North Walls.....	410
Table C.9	Dimensions Used to Calculate the Strength of the Confined Concrete in the Northeast Corners of the Piers	411
Table C.10	Confining Stresses and Ratios of Unconfined to Confined Compressive Strength of Concrete Calculated Using Models Developed by Saatcioglu, M. and Razvi, S.R. (1992)	412
Table C.11	Strains used to Define the stress-Strain Relationship of the Confined Concrete along the East and North Walls Using the Model Developed by Saatcioglu, M. and Razvi, S.R. (1992)	413
Table C.12	Strains used to Define the Stress-Strain Relationship of the Confined Concrete in the Northeast Corners Using the Model Developed by Saatcioglu, M. and Razvi, S.R. (1992)	414
Table C.13	Limiting Compressive Strain of Confined Concrete of Specimens Calculated Using the Model Developed by Kaar et al. (1978)	415
Table C.14	Volumetric Ratio of the Transverse Confinement Reinforcement..	417

List of Figures

Figure 1.1 Bridge Puente Amolanas, With Three Hollow, Octagonal Concrete Piers	2
Figure 1.2 Definition of the Wall Slenderness Ratio for a Hollow Rectangular Cross-Section (AASHTO 1998).....	2
Figure 2.1 Details of Hollow Columns Tested by Procter (1977)	9
Figure 2.2 Cross-Section of Hollow Columns Tested by Jobse and Moustafa (1984)	11
Figure 2.3 Typical Exterior Dimensions of Columns Tested by Poston et al. (1983, 1985)	13
Figure 2.4 Cross-Sectional Dimensions of Specimens Tested by Taylor et al. (1990)	15
Figure 2.5 Ratios of Measured Strength to Calculated Capacity Using Analytical Model Developed by Taylor et al. (1990) (P_{meas}/P_{calc}) ...	16
Figure 2.6 Concrete Plate Loaded in In-Plane Compression	21
Figure 3.1 Equivalent Rectangular Stress Block Distribution for a Hollow Rectangular Section Subjected to Combined Biaxial Compression and Bending	34
Figure 3.2 Variation of Strength Ratio with Wall Slenderness Ratio	38
Figure 3.3 Strength Ratios of all the Available Specimens Calculated using the Nominal Capacity of the Cross-Section (P_{meas}/P_n)	43

Figure 3.4 Strength Ratios of all the Available Specimens Calculated using the Nominal Capacity of the Cross-Section (P_{meas}/P_n) and Estimated Concrete Compressive Design Strength.....	48
Figure 4.1 Overall Dimensions of Pier Specimens	51
Figure 4.2 Typical Details for Transverse Reinforcement and Cross-Ties.....	59
Figure 4.3 Cross-Section of Specimen P6.....	60
Figure 4.4 Cross-Section of Specimen P8.....	61
Figure 4.5 Cross-Section of Specimen P10.....	62
Figure 4.6 Cross-Section of Specimen P12.....	63
Figure 4.7 Cross-Section of Specimen P14.....	64
Figure 4.8 Hairpins at Corner.....	65
Figure 4.9 Typical Cross-Tie	66
Figure 4.10 Checkerboard Pattern Distribution of Cross-Ties.....	66
Figure 4.11 Transparent Exterior Forms	69
Figure 4.12 Reinforcing details of the Top and Bottom End Blocks.....	70
Figure 4.13 Reinforcement Cage of Bottom End Block	71
Figure 4.14 Process Used to Build the Curtains of Longitudinal Reinforcement	72
Figure 4.15 Alignment of the Longitudinal Reinforcement.....	72
Figure 4.16 Bracing System Used to Align Vertically the Longitudinal Reinforcement	73
Figure 4.17 Sand and Neoprene Pads Used as Support for the Pier's Formwork.....	74

Figure 4.18 Exterior Forms on a Pier	74
Figure 4.19 Spacer Used to Separate Exterior and Interior Forms	75
Figure 4.20 Top End Block Forms	76
Figure 4.21 Bottom Forms of Top End Block	77
Figure 4.22 Measured Thickness of Walls Subjected to Compression	80
Figure 4.23 Loading Path for all Specimens	82
Figure 4.24 Test Setup	83
Figure 4.25 Loading Apparatus	84
Figure 4.26 Spherical Bearing at Bottom End Block	85
Figure 4.27 Spherical Bearing at Top End Block	86
Figure 4.28 Distribution of Linear Potentiometers used to Measure the Profile of the Walls in Compression	88
Figure 4.29 Linear Potentiometers to Measure Wall Profile Before Test	89
Figure 4.30 Steel Plate Used as Reference to Measure Vertical Displacements of Top End Block	90
Figure 4.31 Plan View of the Top End Block with the Location of the Linear Potentiometers used to Measure Vertical Displacements of Both End Blocks	90
Figure 4.32 Plan View of the Top End Block with the Location of the Instruments used to Measure Horizontal Displacements	91
Figure 4.33 Linear Transducers (Black Instruments) Used to Measure Lateral Displacement of the Top End Block	92
Figure 4.34 Instrumentation Used to Measure Curvature	93

Figure 4.35 Location of the Linear Motion Transducers used to Measure Curvature Along the Walls of the Specimens	94
Figure 4.36 Transportation of a Specimen	96
Figure 5.1 Identification of Walls within each Test Specimen	100
Figure 5.2 Definition of Profile of East Walls	101
Figure 5.3 Definition of Rotations of End Blocks	103
Figure 5.4 Specimen P6: Photo of East Wall at End of Test	107
Figure 5.5 Specimen P6: Photo of North Wall at End of Test	108
Figure 5.6 Specimen P6: Photo of West Wall at End of Test	108
Figure 5.7 Specimen P6: Vertical Cracks along the East Side of the End Blocks	109
Figure 5.8 Specimen P6: Photo of South Wall at End of Test	109
Figure 5.9 Specimen P6: Cracks and Crushed Concrete at South End of East Wall	110
Figure 5.10 Specimen P6: Observed Crack Patterns	110
Figure 5.11 Specimen P6: Buckled Longitudinal Reinforcement near the Top of the East Wall	111
Figure 5.12 Specimen P6: Longitudinal Profile Measured Near the North- East Corner	112
Figure 5.13 Specimen P6: Relative Displacements of the East Wall	114
Figure 5.14 Specimen P6: Rotations of the End Blocks	115

Figure 5.15 Specimen P6: Relative Vertical Deflections Measured at the Center of the End Blocks and at the Point of Application of the Axial Load.....	117
Figure 5.16 Specimen P6: Moment-Curvature Response about the East-West Axis	118
Figure 5.17 Specimen P6: Moment-Curvature Response about the North- South Axis	118
Figure 5.18 Specimen P8: Photo of East Wall at End of Test	121
Figure 5.19 Specimen P8: Photo of Specimen at End of Test	122
Figure 5.20 Specimen P8: Photo of North Wall at End of Test	122
Figure 5.21 Specimen P8: Photo of West Wall at End of Test	123
Figure 5.22 Specimen P8: Vertical Crack at East Side of the Top End Block .	123
Figure 5.23 Specimen P8: Observed Crack Patterns.....	124
Figure 5.24 Specimen P8: Buckled Longitudinal Bars at the Northeast Corner and in the East Wall	124
Figure 5.25 Specimen P8: Longitudinal Profile Measured Near the North- East Corner.....	126
Figure 5.26 Specimen P8: Relative Displacements of the East Wall.....	128
Figure 5.27 Specimen P8: Rotations of End Blocks	129
Figure 5.28 Specimen P8: Relative Vertical Deflections Measured at the Center of the End Blocks and at the Point of Application of the Axial Load.....	130

Figure 5.29 Specimen P8: Moment-Curvature Response about the East-West Axis	131
Figure 5.30 Specimen P8: Moment-Curvature Response about the North- South Axis	132
Figure 5.31 Specimen P10: Photo of East Wall at End of Test	135
Figure 5.32 Specimen P10: Photo of North Wall at End of Test	135
Figure 5.33 Specimen P10: Photo of West Wall at End of Test	136
Figure 5.34 Specimen P10: Photo of at Top of Northwest Corner at End of Test	136
Figure 5.35 Specimen P10: Photo of West and South Walls at End of Test.....	137
Figure 5.36 Specimen P10: Observed Crack Patterns.....	137
Figure 5.37 Specimen P10: Buckled Longitudinal Reinforcement near Top of Northeast Corner	138
Figure 5.38 Specimen P10: Longitudinal Profile Measured Near the North- East Corner	139
Figure 5.39 Specimen P10: Relative Displacements at Mid-height of East Wall	141
Figure 5.40 Specimen P10: Rotations of the End Blocks	142
Figure 5.41 Specimen P10: Relative Vertical Deflections Measured at Center of End Blocks and at the Point of Application of Axial Load	143
Figure 5.42 Specimen P10: Moment-Curvature Response about the East- West Axis	144

Figure 5.43 Specimen P10: Moment-Curvature Response about the North-South Axis	145
Figure 5.44 Specimen P12: Photo of East Wall at End of Test	148
Figure 5.45 Specimen P12: Photo of North Wall at End of Test	148
Figure 5.46 Specimen P12: Photo of West Wall at End of Test	149
Figure 5.47 Specimen P12: Photo of West and South Walls at End of Test.....	149
Figure 5.48 Specimen P12: Photo of South Wall at End of Test	150
Figure 5.49 Specimen P12: Cracks at the End Blocks	150
Figure 5.50 Specimen P12: Observed Crack Patterns.....	151
Figure 5.51 Specimen P12: Buckled Longitudinal Reinforcement along the North Wall and Opened Transverse Reinforcement	151
Figure 5.52 Specimen P12: Buckled Longitudinal Bars along the East Wall...	152
Figure 5.53 Specimen P12: Longitudinal Profile Measured Near the North-East Corner	153
Figure 5.54 Specimen P12: Relative Displacements of East Wall	155
Figure 5.55 Specimen P12: Rotations of End Blocks	156
Figure 5.56 Specimen P12: Relative Vertical Deflections Measured at Center of End Blocks and at the Point of Application of Axial Load	157
Figure 5.57 Specimen P12: Moment-Curvature Response about East-West Axis	158
Figure 5.58 Specimen P12: Moment-Curvature Response about North-South Axis	159
Figure 5.59 Specimen P14: Photo of East Wall at End of Test	161

Figure 5.60 Specimen P14: Photo of North Wall at End of Test	162
Figure 5.61 Specimen P14: Photo of West Wall at End of Test	162
Figure 5.62 Specimen P14: Photo of South Wall at End of Test	163
Figure 5.63 Specimen P14: Vertical Cracks at Top End Block	163
Figure 5.64 Specimen P14: Observed Crack Patterns.....	164
Figure 5.65 Specimen P14: Buckled Longitudinal Reinforcement near Top of East Wall	164
Figure 5.66 Specimen P14: Longitudinal Profile Measured Near North-East Corner.....	166
Figure 5.67 Specimen P14: Relative Displacements of East Wall	167
Figure 5.68 Specimen P14: Rotations of End Blocks	169
Figure 5.69 Specimen P14: Relative Vertical Deflections Measured at the Center of the End Blocks and at the Point of Application of the Axial Load.....	170
Figure 5.70 Specimen P14: Moment-Curvature Response about East-West Axis	171
Figure 5.71 Specimen P14: Moment-Curvature Response about North-South Axis	172
Figure 5.72 Horizontal Deflection Measured at Midheight of the Piers in the North-South Direction.....	174
Figure 5.73 Horizontal Deflection Measured at Midheight of the Piers in the East-West Direction	174

Figure 5.74	Longitudinal Displacement Profile for Pier without and with Horizontal Displacement of the Top Block in the South Direction	178
Figure 5.75	Longitudinal Displacement Profile for Pier without and with Horizontal Displacement of Top Block in the East Direction	180
Figure 5.76	Measured and Calculated Longitudinal Profiles in the North- South Direction at Ultimate Load	182
Figure 5.77	Measured and Calculated Longitudinal Profiles in the East-West Direction at Ultimate Load	183
Figure 5.78	Longitudinal Displacement Profile for Pier without Horizontal Displacement of the Top Block, with Linear Variation of the Curvature Along the Specimen	186
Figure 5.79	Determination of Changes in Moment due to Changes in Curvature	187
Figure 5.80	Variation of β as Function of the Ratio of Top to Bottom End Rotations (r_{θ})	188
Figure 5.81	Measured and Calculated Longitudinal Profiles in the North- South Direction at Ultimate Load	191
Figure 5.82	Measured and Calculated Longitudinal Profiles in the East-West Direction at Ultimate Load	192
Figure 5.83	Longitudinal Displacement Profile for Pier without and with Horizontal Displacement of the Top Block in the East Direction and with Linear Variation of the Curvature Along the Height	194
Figure 5.84	Maximum Relative Horizontal Displacement of East Walls	201

Figure 5.85 Average End-Blocks Rotations about the East-West Axis.....	202
Figure 5.86 Average End-Blocks Rotations about the North-South Axis	202
Figure 5.87 Relative Axial Deflections Measured at the Center of End Blocks	204
Figure 5.88 Relative Axial Deflections Measured on the Line of Application of the Axial Load.....	205
Figure 5.89 Moment-Curvature Relationships about the East-West Axis Calculated Using the Measured Longitudinal Strains along the West Walls	207
Figure 5.90 Moment-Curvature Relationships about the East-West Axis Calculated Using the Average Rotations of the End Blocks.....	208
Figure 5.91 Stress Trajectories and Crack Orientation in End Blocks.....	212
Figure 5.92 Pier P12: Separation of Spliced Transverse Reinforcement along the North Wall.....	216
Figure 5.93 Locations of Four Measurements of Average Strains	217
Figure 5.94 Average Strains Measured at the Top Half and Bottom Half of the Specimens, at 50% and 100% of the Ultimate Load.....	218
Figure 6.1 Calculated Axial Capacity of Test Specimens at Nominal Eccentricity.....	222
Figure 6.2 Ratios of Measured to Calculated Nominal Capacity of Test Specimens.....	225
Figure 6.3 Idealized Distribution of Confined Concrete within the Test Specimens.....	229

Figure 6.4 Typical Distribution of Fibers used to Calculate Moment-Curvature Response of Piers	230
Figure 6.5 Strain and Stress Distributions Over Cross-Section	231
Figure 6.6 Calculation of Curvatures About East-West and North-South Axes in a Cross Section Loaded Under Biaxial Eccentricity	233
Figure 6.7 Specimen P6: Comparison of Moment-Curvature Response from End-Block Rotations and Calculated Moment-Curvature Response.....	235
Figure 6.8 Specimen P8: Comparison of Moment-Curvature Response from End-Block Rotations and Calculated Moment-Curvature Response.....	236
Figure 6.9 Specimen P10: Comparison of Moment-Curvature Response from End-Block Rotations and Calculated Moment-Curvature Response.....	237
Figure 6.10 Specimen P12: Comparison of Moment-Curvature Response from End-Block Rotations and Calculated Moment-Curvature Response.....	238
Figure 6.11 Specimen P14: Comparison of Moment-Curvature Response from End-Block Rotations and Calculated Moment-Curvature Response.....	239
Figure 6.12 Post-Buckling Behavior of Perfectly Plastic Bars (Mau and El-Mabsout 1989).....	251
Figure 7.1 Concrete Failure Surfaces in Plane Stresses (Hibbitt et al. 1994a)...	260

Figure 7.2 Concrete Failure Surfaces in the (p-q) Plane (Hibbitt et al. 1994a)..	260
Figure 7.3 Unconfined Concrete Uniaxial Stress-Strain Relationship.....	261
Figure 7.4 Uniaxial Compression Stress-strain Relationship for Unconfined Concrete Proposed by Hognestad (1951, 1952).....	262
Figure 7.5 Tension-Stiffening Model.....	264
Figure 7.6 Assumed Stress-Strain Behavior of Steel Reinforcement	266
Figure 7.7 Vertical Deflection and Horizontal Load-Deflection Responses of Pier P14 Calculated Using Displacement Controlled and Load Controlled Loading	268
Figure 7.8 Load Paths Followed in Different Testing Programs	269
Figure 7.9 Finite Element Mesh used for Panels	273
Figure 7.10 Calculated Response of Panel $\frac{1}{2} \times 40 \times 40$ Tested by Ernst (1952)	275
Figure 7.11 Calculated Response of Panel 15 Tested by Swartz et al. (1974)...	275
Figure 7.12 Calculated Response of Panel 10 Tested by Saheb and Desayi (1990).....	276
Figure 7.13 Calculated Lateral Deflections for Panels Shown in Figures 7.10 through 7.12	277
Figure 7.14 Ratios of Measured to Calculated Capacities of all the Plate Results Available for Three Values of Imperfection Ratio	279
Figure 7.15 Finite Element Mesh of a Pier	287
Figure 7.16 Definition of Infinitely Rigid Plane and Reference Nodes.....	288
Figure 7.17 Compressive Strains on Both Surfaces of East Walls of Test Specimens.....	292

Figure 7.18 Specimen P6: Relative Vertical Deflections Measured at Centroid of the Cross-Section and at Point of Application of the Load.....	295
Figure 7.19 Specimen P8: Relative Vertical Deflections Measured at Centroid of the Cross-Section and at Point of Application of the Load	296
Figure 7.20 Specimen P10: Relative Vertical Deflections Measured at Centroid of the Cross-Section and at Point of Application of the Load.....	296
Figure 7.21 Specimen P12: Relative Vertical Deflections Measured at Centroid of the Cross-Section and at Point of Application of the Load.....	297
Figure 7.22 Specimen P14: Relative Vertical Deflections Measured at Centroid of the Cross-Section and at Point of Application of the Load.....	297
Figure 7.23 Pier P6: Moment-Curvature Responses about the East-West Axis	299
Figure 7.24 Pier P6: Moment-Curvature Responses about the North-South Axis	299
Figure 7.25 Pier P8: Moment-Curvature Responses about the East-West Axis	300
Figure 7.26 Pier P8: Moment-Curvature Responses about the North-South Axis	300
Figure 7.27 Pier P10: Moment-Curvature Responses about the East-West Axis	301

Figure 7.28 Pier P10: Moment-Curvature Responses about the North-South Axis	301
Figure 7.29 Pier P12: Moment-Curvature Responses about the East-West Axis	302
Figure 7.30 Pier P12: Moment-Curvature Responses about the North-South Axis	302
Figure 7.31 Pier P14: Moment-Curvature Responses about the East-West Axis	303
Figure 7.32 Pier P14: Moment-Curvature Responses about the North-South Axis	303
Figure 7.33 Compressive Strains on both Surfaces of the Wall in Compression of Specimen 11ML34, Calculated at the Point of Maximum Lateral Deflection	312
Figure 8.1 Influence of the Wall Slenderness Ratio on the Strength Ratio	317
Figure 8.2 Effectively Confined Core for Rectangular Hoop Reinforcement ...	319
Figure 8.3 Geometry of the Slender Wall Subjected to Compression	320
Figure 8.4 Effectively Confined Core for Rectangular Hoop Reinforcement (Mander et al. 1988b).....	322
Figure 8.5 Definition of Thickness of the Confined Concrete Core	324
Figure 8.6 Relationship Between Measured Strength Ratios of Various Parameters	326
Figure 8.7 Relationship Between Wall Slenderness Ratio and Strength Ratio for Test Specimens with Coefficient k_c between 0.15 and 0.16	330

Figure 8.8 Strength Ratios Calculated using the Nominal Capacity of the Cross-Section (P_{meas}/P_n or M_{meas}/M_n)	340
Figure A.1 Stress-Strain Curves for Concrete of Hollow Specimen P6	355
Figure A.2 Stress-Strain Curves for Concrete of Hollow Specimen P8	355
Figure A.3 Stress-Strain Curves for Concrete of Hollow Specimen P10	356
Figure A.4 Stress-Strain Curves for Concrete of Hollow Specimen P12	356
Figure A.5 Stress-Strain Curves for Concrete of Hollow Specimen P14	357
Figure A.6 Stress-Strain Curve for Longitudinal Reinforcement	360
Figure A.7 Stress-Strain Curve for Transverse Reinforcement	360
Figure A.8 Stress-Strain Curve for Deformed Reinforcement in End Blocks ...	361
Figure B.1 Distribution of Linear Potentiometers used to Measure Horizontal Displacements of the Walls in Compression.....	363
Figure B.2 Horizontal Deflections of East Wall, Specimen P6	364
Figure B.3 Horizontal Deflections of North Wall, Specimen P6.....	365
Figure B.4 Horizontal Deflections of East Wall, Specimen P8	366
Figure B.5 Horizontal Deflections of North Wall, Specimen P8.....	367
Figure B.6 Horizontal Deflections of East Wall, Specimen P10	368
Figure B.7 Horizontal Deflections of North Wall, Specimen P10.....	369
Figure B.8 Horizontal Deflections of East Wall, Specimen P12	370
Figure B.9 Horizontal Deflections of North Wall, Specimen P12.....	371
Figure B.10 Horizontal Deflections of East Wall, Specimen P14	372
Figure B.11 Horizontal Deflections of North Wall, Specimen P14.....	373
Figure B.12 Vertical Displacements Measured at Center of End Blocks	374

Figure B.13 Vertical Displacements measured at the middle of the West and South Edges of the End Blocks	377
Figure B.14 Vertical Displacements Along the West Wall Used to Calculate Curvature in the North-South Direction.....	381
Figure B.15 Vertical Displacements at South Wall Used to Calculate Curvature in the East-West Direction	384
Figure B.16 Horizontal Displacements Measured at the Top End Block of Specimen P6.....	387
Figure B.17 Horizontal Displacements Measured at the Top End Block of Specimen P8.....	387
Figure B.18 Horizontal Displacements Measured at the Top End Block of Specimen P10.....	388
Figure B.19 Horizontal Displacements Measured at the Top End Block of Specimen P12.....	388
Figure B.20 Horizontal Displacements Measured at the Top End Block of Specimen P14.....	389
Figure C.1 Typical Location of the Neutral Axis of a Hollow Pier Tested in this Investigation	391
Figure C.2 Stress-Strain Model Proposed for Monotonic Loading of Confined and Unconfined Concrete (1988b).....	392
Figure C.3 Effectively Confined Core for Rectangular Hoop Reinforcement (1988b).....	394

Figure C.4 Effectively Confined Core for Rectangular Reinforcement and Checkerboard Distribution of Cross-Ties	398
Figure C.5 Definition of Core Dimensions and X and Y Directions for East and North Walls	399
Figure C.6 Stress-Strain Model Proposed for Monotonic Loading of Confined and Unconfined Concrete (Saatcioglu, M. and Razvi, S. R. 1992)	406
Figure C.7 Effectively Confined Core for Rectangular Hoop Reinforcement(Saatcioglu, M. and Razvi, S. R. 1992)	407
Figure C.8 Definition of Core Dimensions and X and Y Directions for East and North Walls	409
Figure C.9 Specimen P6: Stress-Strain Relationships for Unconfined and Confined Concrete at (a) East and North Walls and (b) Northeast Corner.....	418
Figure C.10 Specimen P8: Stress-Strain Relationships for Unconfined and Confined Concrete at (a) East and North Walls and (b) Northeast Corner.....	419
Figure C.11 Specimen P10: Stress-Strain Relationships for Unconfined and Confined Concrete at (a) East and North Walls and (b) Northeast Corner.....	420
Figure C.12 Specimen P12: Stress-Strain Relationships for Unconfined and Confined Concrete at (a) East and North Walls and (b) Northeast Corner.....	421

Figure C.13 Specimen P14: Stress-Strain Relationships for Unconfined and
Confined Concrete at (a) East and North Walls and (b) Northeast
Corner..... 422

Chapter 1 Introduction

1.1 OVERVIEW

Hollow concrete piers have been used to support cable-stay and long-span balanced cantilever bridges for the last forty years. Compared with solid columns, hollow piers offer the advantages of high bending and torsional stiffness, significant reductions in the volume of materials, and large reductions in dead load, which reduces the design loads for the foundations.

Taylor et al. (1990) surveyed the cross-sectional properties of hollow concrete piers used in twenty bridges from around the world that were constructed between 1963 and 1990. The results indicate that hollow rectangular cross-sections are the most common. The cross-sectional dimensions were expressed in terms of the wall slenderness ratio, λ_w , defined as the unsupported length of the cross-section divided by the wall thickness. Wall slenderness ratios varied from 6 to 27 for the bridges surveyed.

Figure 1.1 shows a photograph of the Puente Amolanas bridge, which is under construction 400 km north of Santiago, Chile. The bridge is supported by three hollow, concrete piers, with octagonal cross-sections and with wall slenderness ratios approximately equal to 5. The tallest pier is 100 m (328 ft) long.

The wall slenderness ratio is shown in Fig. 1.2 using the definition from the commentary of the AASHTO LRFD Bridge Design Specifications (1998) Section 5.7.4.7.1. The wall slenderness ratio is calculated as:

$$\lambda_w = \frac{X_u}{t} \tag{1.1}$$

where X_u is the unsupported length of the pier wall and t is the wall thickness.



Figure 1.1 Bridge Puente Amolanas, With Three Hollow, Octagonal Concrete Piers

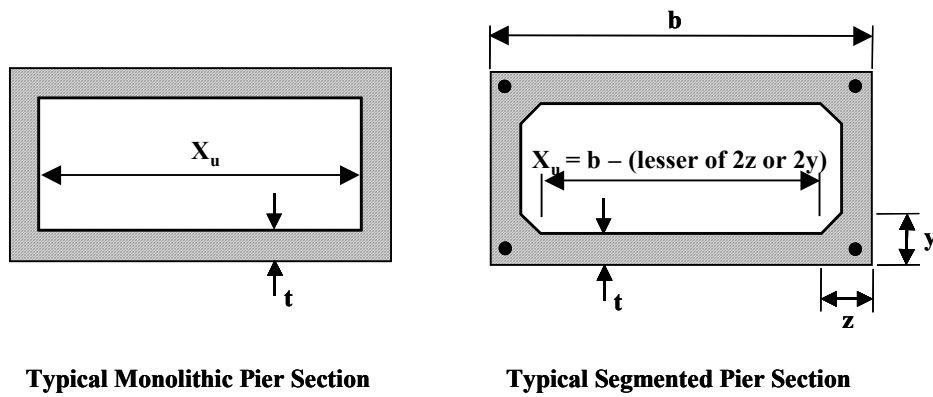


Figure 1.2 Definition of the Wall Slenderness Ratio for a Hollow Rectangular Cross-Section (AASHTO 1998)

1.2 OBJECTIVES

The behavior of hollow box sections has been assessed in several experimental investigations (Procter (1977), Poston et al. (1983), Jobse and Moustafa (1984), and Taylor et al. (1990, 1995)). In those tests, the hollow piers were subjected to pure compression, axial load and uniaxial moment, or axial load and biaxial moment. Taylor and Breen (1994) evaluated available data and developed relationships between the wall slenderness ratio and the strength ratio, which is defined as the ratio of the maximum axial load supported by the test specimen to the calculated nominal capacity of the pier using the actual eccentricity of the axial load (P_{TEST}/P_n). The results indicated that standard design procedures could be used for cross-sections with wall slenderness ratios less than 15. However, the strength of the specimen was limited by local buckling of the walls when the wall slenderness ratio exceeded 15. Design procedures were developed for hollow piers (Taylor et al. (1990), Taylor and Breen 1994), and were later included in the AASHTO Specifications (1998).

Variations in the loading sequences used in the different investigations influenced the strength ratios that served as the basis for the design procedures developed by Taylor et al. (1990) In most cases, the researchers increased the axial load from zero to the capacity of the specimen while maintaining a constant eccentricity. In these tests P_{TEST}/P_n was an appropriate parameter for evaluating the importance of the wall slenderness ratio.

However, Poston et al. (1983) applied a known level of axial load to the test specimens, and then maintained the level of axial load as the eccentricities in

the two principal directions of the cross-section were increased. By default, the strength ratio for these specimens is 1.0 using the definition based on the axial capacity. If the strength ratio is calculated using the ratio of applied moment to nominal capacity, M_{TEST}/M_n , then strength reductions on the order of 5% were observed for hollow piers with slenderness ratios as low as 7.5. With this change in the definition of the strength ratio, the biaxial loading condition appears to be critical for hollow piers.

The design of tall piers and pylons is frequently governed by biaxial bending with strong axis to weak axis moment ratios of 2 to 3. This condition of biaxial bending should be checked analytically and experimentally to determine where the reduction in capacity occurs.

The objectives of this project were to investigate experimentally and analytically the behavior of thin-walled concrete compression members subjected to biaxial bending and determine if a reduction in capacity occurs due to local instability.

To accomplish these objectives, five specimens with wall slenderness ratios between 5 and 15 were tested under compressive load and biaxial bending. The measured response was compared with the current design provisions in the AASHTO Specifications (1998).

1.3 SCOPE OF THE INVESTIGATION

The scope of this research was limited to monolithic hollow rectangular concrete sections subjected to simultaneous compressive load and biaxial

bending. No consideration was given to overall column buckling, lateral or cyclic loading, or post-tensioned segmental construction.

The experimental program comprised tests to failure of five, one-fifth-scale, thin-walled, rectangular, concrete hollow pier specimens with wall slenderness ratios varying from 6 to 14. The specimens were loaded eccentrically under simultaneous axial compression and biaxial bending.

Fiber models and the general-purpose finite element program ABAQUS (Hibbitt, Karlson and Sorensen 1994a, 1994b) were used to estimate the behavior of hollow concrete piers under compressive loading and biaxial bending. The test results were used to evaluate the analytical models.

This dissertation is divided into nine chapters. Chapter 2 presents a review of previous experimental studies of rectangular hollow concrete piers. The experimental programs are described and the analytical models used to interpret the results. Chapter 3 gives an overview of the design procedures available for hollow concrete piers.

The design of the test specimens and loading scheme is discussed in Chapter 4 and the measured response of the piers is discussed in Chapter 5. The influence of the wall slenderness ratio and the confinement provided by the transverse reinforcement on the strength of the piers is studied in Chapter 6. Two material models were used to estimate the influence of confinement on the capacity of the specimens using a fiber model with sectional analysis.

The finite element model used to study the response of the test specimens is discussed in Chapter 7. The current design procedures for hollow rectangular

concrete piers are evaluated in Chapter 8 using the experimental data obtained in this investigation. The conclusions and future research recommendations are presented in Chapter 9.

Chapter 2 Review of Previous Investigations of the Performance of Hollow Concrete Piers

The results of previous investigations have demonstrated that the capacity of a hollow concrete pier is likely to be less than the nominal capacity calculated using typical design procedures. This reduction in strength is expected to increase as the wall panels that form the piers become more slender, due to local buckling of the wall panels.

New provisions have been included in the AASHTO LRFD Bridge Design Specifications (1998) to consider this observed phenomenon. These provisions are described in Chapter 3. The experimental research results that form the basis of these provisions are discussed in this chapter.

Six experimental studies were identified that investigated the behavior of rectangular, hollow concrete sections. The local stability of the thin pier walls was studied in four of these investigations, while the seismic performance was studied in the other two investigations. Brief summaries of each investigation are presented in Section 2.1.

In addition, three experimental studies of the stability of concrete panels subjected to uniaxial compression are summarized in Section 2.2. These studies are relevant to the current investigation because the capacity of hollow piers with slender walls is limited by the stability of the individual walls.

2.1 BEHAVIOR OF HOLLOW CONCRETE PIERS

2.1.1 Procter

Procter (1977) tested six hollow, rectangular columns under concentric loading. The columns had a height of 250 mm (9.8 in.) and the cross-sectional dimensions shown in Fig. 2.1. The wall slenderness ratios varied from 2.4 to 7.5 (Table 2.1). The columns were cast horizontally on steel forms, and the interior cavity was formed using blocks of expanded polystyrene. The longitudinal reinforcement consisted of four twisted, 7.62-mm (0.3-in.) square, high-tensile strength steel rods with a yield stress equal to 524 MPa (76 ksi). The transverse reinforcement consisted of mild steel wire hoops spaced vertically at 100 mm (3.9 in.). The longitudinal reinforcement ratio varied between 0.011 for the specimen with thickest walls to 0.019 for the specimen with thinnest walls. The concrete compressive strength, determined from cube specimens, was 50.3 MPa (7300 psi) for all the columns.

Procter (1977) did not develop a special analysis procedure to calculate the strength of these specimens. The axial capacity was calculated as the sum of the total resistance of the concrete ($\frac{2}{3}$ x cube strength x concrete area) and the resistance of the steel (steel area x yield stress) (Table 2.1).

Two specimens, R8 and R13, failed at a load smaller than the calculated capacity. The measured strength of R13 was slightly less than the calculated capacity, while the measured capacity of R8 was 13% less than the calculated capacity. The failure of specimen R8 was caused by spalling of the concrete cover along nearly half the length of the test specimen.

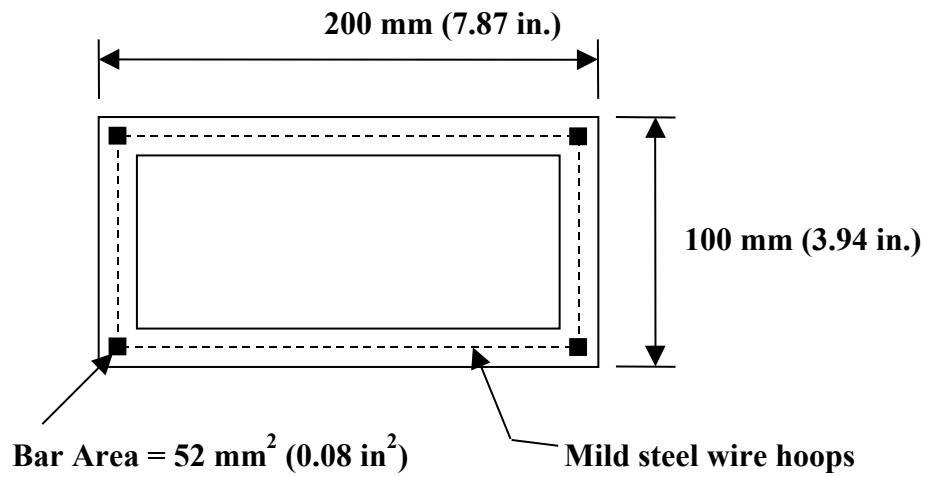


Figure 2.1 Details of Hollow Columns Tested by Procter (1977)

Table 2.1 Dimensions and Capacity of Specimens Tested by Procter (1977)

Spec. ID	Wall Slenderness Ratio λ_w	Wall Thickness mm (in.)	Concrete Area mm ² (in. ²)	Steel Area mm ² (in. ²)	Maximum Capacity kN (kips)	Calculated* Capacity kN (kips)	Ratio of Measured to Calculated Capacity
R8	7.5	21 (0.83)	10,630 (16.53)	208 (0.32)	405 (91)	464 (104)	0.87
R9	5.7	26 (1.02)	12,700 (19.61)	208 (0.32)	555 (125)	534 (120)	1.04
R10	4.3	31.5 (1.24)	14,700 (22.82)	208 (0.32)	620 (139)	604 (136)	1.03
R11	3.5	36 (1.42)	16,200 (25.15)	208 (0.32)	722 (162)	649 (146)	1.11
R12	2.8	41.5 (1.63)	17,500 (27.55)	208 (0.32)	725 (163)	689 (155)	1.05
R13	2.4	45.5 (1.79)	18,800 (29.14)	208 (0.32)	740 (166)	744 (167)	0.99

* Capacity calculated by Procter by adding the axial capacities of the concrete and steel.

2.1.2 Jobse and Moustafa

Jobse and Moustafa (1984) tested two square, thin-walled, hollow column specimens with wall slenderness ratios of 32.0 under simultaneous compression and uniaxial bending. The axial load was applied at a constant eccentricity. The specimens were built from three precast cubic segments, that were epoxied and post-tensioned together to form a specimen with a total height of 4.57 m (180 in). One 1¼-in. diameter Dywidag bar was placed in each corner of the specimens. The cross-sectional details are shown in Fig. 2.2 and the test results are summarized in Table 2.2.

Jobse and Moustafa (1984) developed an analytical model that included the effect of buckling of the compression flange. Classic, elastic buckling theory for thin plates was used to find the critical buckling stress in this model, but the modulus of elasticity was replaced by the instantaneous tangent modulus of the concrete. A parabolic stress-strain relationship was used for the concrete, with the peak stress equal to the measured cylinders strength. Interaction diagrams that included the influence of local buckling for hollow piers were computed using the model. As indicated in Table 2.2, capacities calculated with this model overestimated the measured strengths by 15 to 25%.

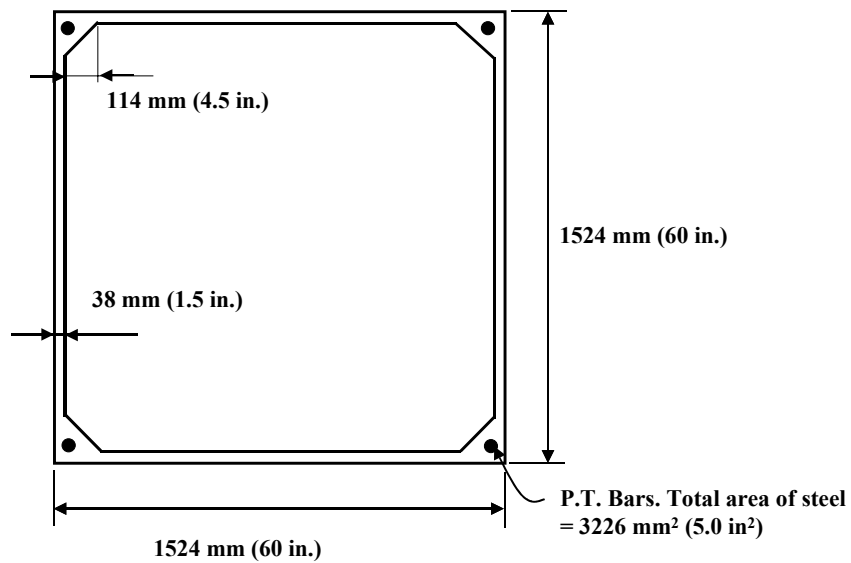


Figure 2.2 Cross-Section of Hollow Columns Tested by Jobse and Moustafa (1984)

Table 2.2 Capacities of Specimens Tested by Jobse and Moustafa (1984)

Spec. ID	Wall Slenderness Ratio λ_w	Concrete Strength MPa (psi)	Axial Stress due to Post-tensioning MPa (psi)	Eccentricity of Applied Load mm (in.)	Measured Capacity kN (kips)	Calculated Capacity kN (kips)	Ratio of Measured to Calculated Capacity
1	32.0	59.8 (8680)	8.4 (1218)	124 (4.9)	7175 (1613)	9800 (2200)	0.73
2A	32.0	68.1 (9880)	8.4 (1218)	513 (20.2)	5987 (1346)	7100 (1600)	0.84

2.1.3 Poston, Gilliam, Yamamoto and Breen

Poston, Gilliam, Yamamoto and Breen (1983, 1985) tested three hollow, rectangular, concrete columns under biaxial bending. All specimens had the same overall dimensions and wall thicknesses, and the wall slenderness ratio was varied

by adding internal stiffeners. One specimen had a single cell, one had two cells, and one had three cells (Fig. 2.3). The values of the wall slenderness ratio were low, varying between 1.9 and 7.6 (Table 2.3). The specimens were 1.83 m (72 in.) high, with a wall thickness of 63.5 mm (2.5 in.).

The longitudinal reinforcement consisted of 6-mm deformed bars with a yield stress of 420 MPa (61.1 ksi). The transversal reinforcement consisted of No. 13 gage wires, with an average area equal to 4.1 mm^2 (0.0064 in^2), spaced vertically every 51 mm (2 in.). The average yield stress was 252 MPa (36.6 ksi). The longitudinal reinforcement ratio varied between 0.015 and 0.018.

The specimens were tested using three hydraulic rams: one was located at the geometric centroid of the cross-section, and the other two were located along the strong and weak axes respectively. The specimen was first subjected to a concentric axial load of $0.4 P_o$ using the first hydraulic ram, where P_o is the calculated capacity of the specimen subjected to uniaxial compression. As testing progressed, the axial force in the two eccentric rams increased while the axial force in the concentric ram decreased. Using this technique, the total axial load was maintained at $0.4 P_o$, while the specimens were subjected to increasing moments about the longitudinal and transverse axes. The ratio of the eccentricity in the direction of the strong axis to the eccentricity in the direction of the weak axis was 3.0 in all tests.

The behavior of the test specimens was calculated using a finite strip approximation where local wall buckling was not considered. Good agreement was found between the measured and calculated capacities. Table 2.3 summarizes

the cross-sectional dimensions and the material properties, and Table 2.4 summarizes the measured strength and calculated capacity for each specimen.

The measured capacity of the specimen with largest wall slenderness ratio was approximately 15% less than the calculated capacity.

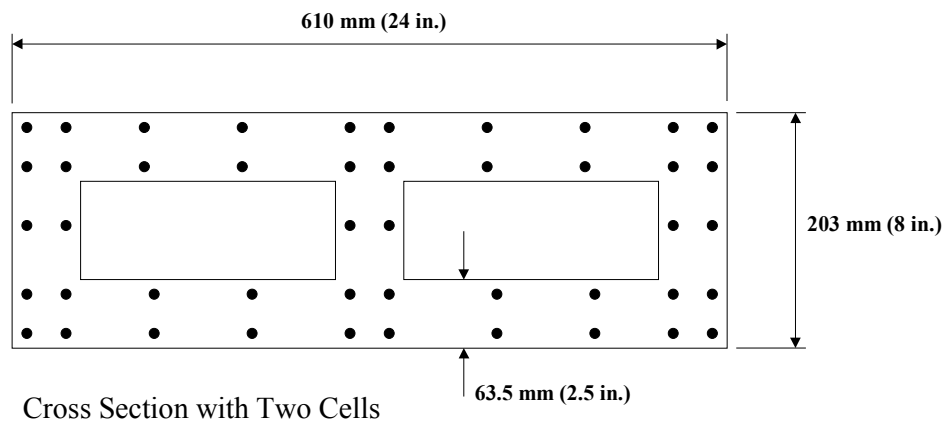


Figure 2.3 Typical Exterior Dimensions of Columns Tested by Poston et al. (1983, 1985)

Table 2.3 Dimensions of Specimens Tested by Poston et al. (1983, 1985)

Spec. ID	λ_w	Concrete Strength MPa (psi)	Concrete Area mm ² (in. ²)	Reinf. Ratio
1 Cell	7.6	287 (4160)	87100 (135.0)	0.0148
2 Cells	3.3	296 (4300)	91950 (142.5)	0.0161
3 Cells	1.9	345 (5000)	96800 (150)	0.0173

Table 2.4 Test Results of Specimens Tested by Poston et al. (1983, 1985)

Spec. ID	Wall Slender. Ratio λ_w	Measured Strength			Calculated Capacity			Ratio of Measured to Calculated Moment
		Axial Load kN (kip)	Moment Weak kN-m (kip-in.)	Moment Strong kN-m (kip-in.)	Axial Load kN (kip)	Moment Weak kN-m (kip-in.)	Moment Strong kN-m (kip-in.)	
1 Cell	7.6	1210 (272)	54.0 (480)	163 (1440)	1210 (272)	63.0 (560)	190 (1685)	0.86
2 Cells	3.3	1290 (290)	67.0 (590)	200 (1770)	1290 (290)	64.0 (565)	192 (1695)	1.04
3 Cells	1.9	1510 (340)	79.0 (695)	236 (2085)	1510 (340)	72.0 (640)	217 (1920)	1.09

2.1.4 Taylor, Rowell, and Breen

Taylor, Rowell, and Breen (1990,1995) tested twelve, 1/5-scale, hollow rectangular piers under combined axial load and uniaxial bending. Five piers had post-tensioned reinforcement. The wall slenderness ratios for the specimens varied between 8.8 and 33.6. All the specimens were 1.83 m high (72 in.), with cross-sectional dimensions as summarized in Table 2.5.

Two curtains of vertical and horizontal steel were distributed throughout the cross-section. The longitudinal reinforcement consisted of 6-mm deformed bars with yield stress equal to 518 MPa (75.1 ksi). The transverse reinforcement was made of No. 10 gage smooth wire (3.4-mm (0.135-in.) diameter). High strength Dywidag threaded rods 16 and 25-mm (5/8 and 1-in.) diameters were

used for the tendons in the post-tensioned specimens. The longitudinal reinforcement ratio varied between 0.015 and 0.026. Figure 2.4 shows the range of cross-sectional dimensions for the test specimens.

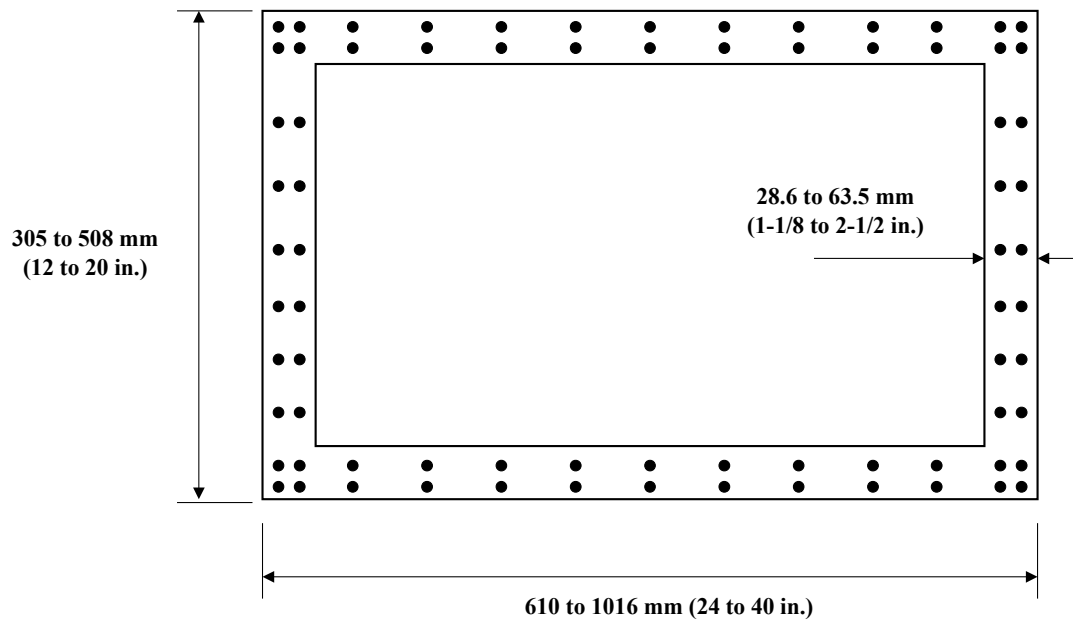


Figure 2.4 Cross-Sectional Dimensions of Specimens Tested by Taylor et al. (1990)

Taylor et al. (1990) developed an analytical model similar to that used by Jobse and Moustafa (1984) to calculate the axial capacity of the test specimens. The model also considered the influence of the transverse walls in restraining the compression wall. Analyses followed a two-step procedure. First the plate buckling stress was calculated for the most slender wall of each specimen. Bending stiffness of the short walls was considered along the unloaded edges of the plates. Then the capacity of the cross-section was calculated using the

calculated critical buckling stress as the limiting stress in the concrete. The expression developed by Hognestad (1951,1952) was used to model the stress-strain curve of the concrete, using as peak stress 85% of the compressive strength measured using cylinders. This approach was used to calculate the capacity of specimens subjected to concentric axial load or combined axial load and uniaxial bending.

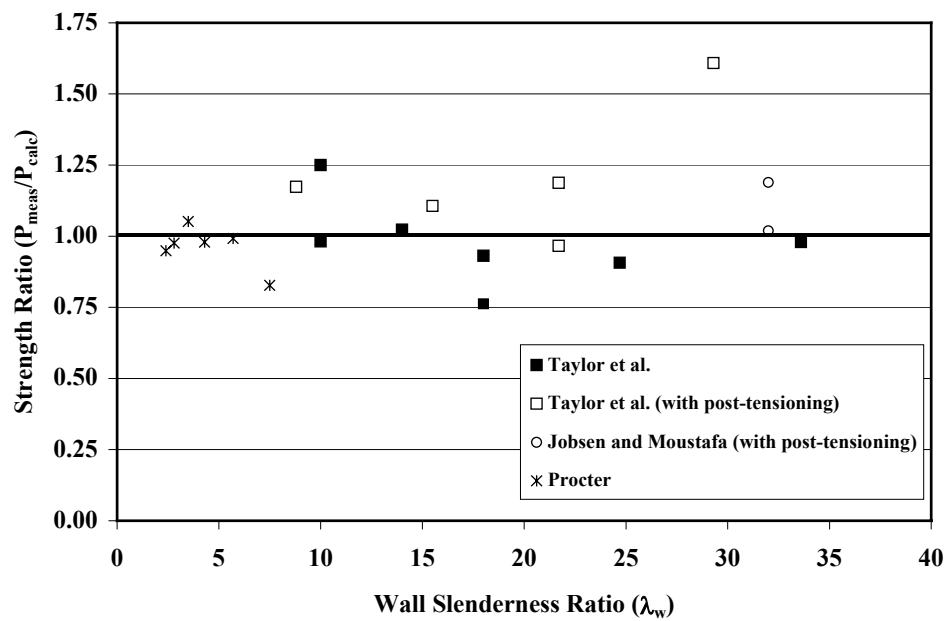


Figure 2.5 Ratios of Measured Strength to Calculated Capacity Using Analytical Model Developed by Taylor et al. (1990) (P_{meas}/P_{calc})

Taylor et al. (1990) also used this analytical model to calculate the capacity of the specimens tested by Procter (1977) and Joseb and Moustafa (1984). The ratios of the measured axial strength (P_{meas}) to the calculated capacity (P_{calc}) are plotted in Fig. 2.5). With the exception of one specimen, the calculated capacities were within $\pm 25\%$ of the measured loads at failure. Comparisons

between measured and calculated capacities of the specimens tested by Taylor et al. (1990) are summarized in Table 2.6.

Table 2.5 Dimensions of Specimens Tested by Taylor et al. (1990)

Spec. ID	Wall Thickness mm (in.)	Section Depth mm (in.)	Section Width mm (in.)	Wall Slenderness Ratio λ_w	Concrete Compressive Strength MPa (psi)	Steel Area mm ² (in. ²)	Reinf. Ratio	P.T. Steel Area mm ² (in. ²)
1M10	63.5 (2.50)	381 (15)	762 (30)	10.0	54 (7860)	2820 (4.37)	0.022	-
2M10	50.8 (2.00)	305 (12)	610 (24)	10.0	22 (3170)	1350 (2.09)	0.016	-
3M14	63.5 (2.50)	508 (20)	1016 (40)	14.0	24 (3540)	2820 (4.37)	0.016	-
4M18	50.8 (2.00)	508 (20)	1016 (40)	18.0	53 (7700)	2210 (3.42)	0.015	-
5S9	63.5 (2.5)	381 (15)	762 (30)	8.8	47 (6830)	2820 (4.37)	0.022	723 (1.12)
6S16	50.8 (2.0)	508 (20)	1016 (40)	15.5	33 (4840)	2210 (3.42)	0.015	2194 (3.40)
7S22	38.1 (1.5)	508 (20)	1016 (40)	21.7	48 (6920)	2210 (3.42)	0.019	723 (1.12)
8ML25	38.1 (1.50)	508 (20)	1016 (40)	24.7	44 (6310)	2210 (3.42)	0.020	-
9MLP22	38.1 (1.5)	508 (20)	1016 (40)	21.7	45 (6460)	2210 (3.42)	0.019	723 (1.12)
10ML18	50.8 (2.0)	508 (20)	1016 (40)	18.0	46 (6680)	2210 (3.42)	0.015	-
11ML34	28.6 (1.125)	508 (20)	1016 (40)	33.6	36 (5260)	2210 (3.42)	0.026	-
12S29	28.6 (1.125)	508 (20)	1016 (40)	29.3	32 (4680)	2210 (3.42)	0.025	723 (1.12)

* Determined from tests of concrete cylinders

Table 2.6 Measured and Calculated Capacities of Specimens Tested by Taylor et al. (1990)

Specimen ID	Measured Capacity		Calculated Capacity		Ratio of Measured to Calculated Capacity
	Axial Load kN (kips)	Moment kN-m (kip-in.)	Axial Load KN (kips)	Moment kN-m (kip-in.)	
1M10	2344 (527)	519.0 (4590)	2389 (537)	526.0 (4653)	0.98
2M10	2091 (470)	37.4 (331)	1673 (376)	30.1 (266)	1.25
3M14	4172 (938)	110.0 (975)	4079 (917)	107.0 (945)	1.02
4M18	4172 (938)	294.0 (2600)	5476 (1231)	384.0 (3397)	0.76
5S9	5062 (1138)	104.0 (922)	5480 (1232)	112.0 (994)	0.92
6S16	4217 (948)	109.0 (967)	4604 (1035)	118.0 (1047)	0.92
7S22	4444 (999)	115.0 (1020)	4653 (1046)	120.0 (1061)	0.96
8ML25	4021 (904)	104.0 (922)	4435 (997)	114.0 (1010)	0.91
9MLP22	4275 (961)	111.0 (980)	4426 (995)	114.0 (1005)	0.96
10ML18	4506 (1013)	317.0 (2810)	4840 (1088)	339.0 (3000)	0.93
11ML34	2771 (623)	71.7 (635)	2829 (636)	73.0 (646)	0.98
12S29	3034 (682)	77.1 (682)	2576 (579)	65.0 (575)	1.18

Based in these results, Taylor et al. (1990) concluded that use of the same design procedures for hollow concrete piers as those for members with solid cross-sections, would be unconservative for piers with wall slenderness ratios

exceeding 15. An approximate design procedure was proposed to account for the reduction in capacity due to wall slenderness. This approach formed the basis for the design procedures for hollow piers that were introduced in the AASHTO Specifications (1998).

2.1.5 Mander, Priestley and Park

Mander, Priestley and Park (1983) tested four hollow reinforced concrete bridge piers. The specimens were 3.2 m (126 in.) high, 750 mm (29.5 in.) square with 120-mm (4 ¾-in.) thick walls, corresponding to a wall slenderness ratio of 4.25. The objective of the research was to study the seismic performance of the hollow piers using different levels of axial load and different arrangements of confining steel in the plastic hinge zone. Cyclic lateral loads were applied while maintaining a constant axial load. While these tests are not directly relevant to this investigation, some of its observations are of importance for this study. The ratios of the measured flexural strength to the capacity calculated using an interaction diagram (that considered the measured concrete strength, measured steel yield stress, and ultimate concrete compressive strain of 0.003) varied between 1.11 and 1.33. It was shown that the largest increase in strength was due to the increase in concrete strength produced by the confinement provided by the lateral reinforcement.

2.1.6 Mo, Yeh and Yang

Mo, Yeh and Yang¹ tested two full scale and twelve models of square hollow concrete piers subjected to lateral loading. The objectives of the

¹ Presented at the March 2000 ACI Convention, San Diego, CA.

investigation were to study the seismic performance of hollow bridge columns used in a high-speed rail project and to develop an analytical model to predict the behavior of those columns. The specimens had wall slenderness ratios between 2.2 and 3.0.

The modified Kent and Park (1971) model for confined concrete gave results closest to the responses of the tests.

2.2 BEHAVIOR OF THIN CONCRETE PLATES

2.2.1 Ernst

Ernst (1952) tested ten concrete plates. All specimens were simply supported along all four edges and loaded in compression on two sides (Fig. 2.6). Five specimens were 1016 mm (40 in.) wide (the loaded side) and 1054 mm (41.5 in.) tall, and five were 1016 mm (40 in.) wide and 584 mm (23 in.) tall. The reinforcement consisted of a 25x25-mm (1x1-in.) welded wire mesh, with 15-gage wires, placed at mid-depth of the concrete plates. The compressive strength of the concrete was 31.5 MPa (4570 psi) for all specimens. Table 2.7 summarizes the dimensions and strength of each specimen. A stress-strain curve was measured from 51x102 mm (2x4 in.) cylinders and was used to represent the composite action of the steel and concrete in the panels.

Ernst reported that the specimens with slenderness ratios larger than 40 exhibited rapid out of plane deflection of the center of the panels prior to failure. This suggests that plate buckling was the failure mode of those test specimens.

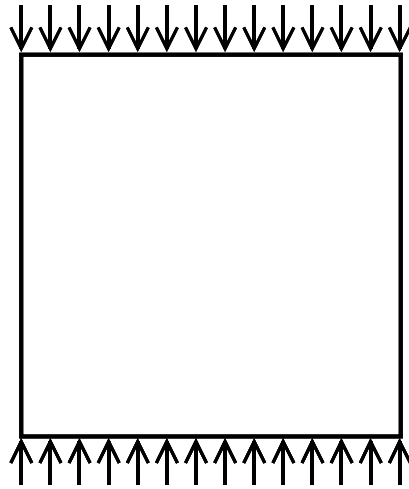


Figure 2.6 Concrete Plate Loaded in In-Plane Compression

Ernst (1952) used the tangent modulus concept to analyze the results of the tests. Classic elastic buckling theory for thin plates was used to find the critical buckling stress given the aspect ratio of the plate and the boundary conditions. The instantaneous tangent modulus of the concrete was used as the modulus of elasticity to account for material nonlinearities.

Table 2.7 Dimensions and Strength of Specimens Tested by Ernst (1952)

Spec. ID	Panel Thickness mm (in.)	Panel Height mm (in.)	Panel Slenderness Ratio λ_w	Ratio of Measured Eccentricity to Wall Thickness	Maximum Measured Load kN (kips)	Maximum Measured Stress MPa (psi)
½x40x40	14 (0.55)	1054 (41.5)	72.7	0.04	126 (28.3)	14.0 (2040)
¾x40x40	20 (0.77)	1054 (41.5)	51.9	0.15	196 (44.0)	23.0 (3340)
1x40x40	26.5 (1.04)	1054 (41.5)	38.5	0.10	300 (68.0)	21.9 (3180)
1¼x40x40	32.5 (1.28)	1054 (41.5)	31.3	0.03	580 (130.0)	31 (4500)
1½x40x40	38.5 (1.52)	1054 (41.5)	26.3	0.01	1050 (236.0)	28.0 (4060)
½x40x20	14 (0.56)	584 (23.0)	71.4	0.23	73 (16.5)	17.0 (2460)
¾x40x20	20.5 (0.81)	584 (23.0)	49.4	0.23	170 (38.5)	21.8 (3160)
1x40x20	27.5 (1.08)	584 (23.0)	37.0	0.04	580 (130.1)	28.5 (4140)
1¼x40x20	32 (1.25)	584 (23.0)	32.0	0.07	490 (111.0)	30.3 (4390)
1½x40x20	38.5 (1.52)	584 (23.0)	26.3	0.07	900 (202.5)	31.5 (4570)

The steel was neglected in the calculation of the buckling stress and accidental eccentricities were considered by measuring the strains across the thickness of the plates at low load levels. The results from the analysis were reported as a standardized curve of buckling stress and provided good results in estimating the maximum stress measured in the concrete before failure.

2.2.2 Swartz, Rosebraugh, and Berman

Swartz, Rosebraugh, and Berman (1974) tested 24 rectangular concrete plates that were simply supported along all edges and subjected to uniaxial compression along two edges (Fig. 2.6). The concrete plates were 1219 mm (48 in.) wide by 2438 mm (96 in.) tall, had one or two layers of reinforcement, and had wall slenderness ratios between 38 and 64. The steel reinforcement was No. 12 gage wire, 2.7 mm in diameter (0.1055 in.), with yield stress of 530 MPa (76.8 ksi). Table 2.8 summarizes the dimensions of the test specimens.

Swartz and Rosebraugh (1974) used the analytical approach developed by Sherbourne Liaw and March (1971) for orthotropic plates subjected to uniaxial compression. This approach allows the analyst to specify different amounts of reinforcement and different values of stiffness for the concrete in the two orthogonal directions and estimate the buckling strain of the plate. Swartz considered both orthotropic and isotropic idealizations of the plates and used tangent and double-modulus buckling theories. The stress strain relationship of the concrete was modeled using the expression proposed by Hognestad (1951, 1952).

Swartz and Rosebraugh (1974) found that the four analytical approaches provided reasonable estimates of the buckling load. However, the model based on an isotropic plate and the tangent modulus approach gave, for the most part, conservative estimates of the buckling load for all specimens. In addition, this was the only approach that could be represented using a closed-form solution. Equation 2.1 gives the value of the buckling strain:

$$\begin{aligned} \varepsilon_{cr}^2 - \left\{ 2 + CD_{y1} \left[\left(\frac{mb}{a} \right) + \left(\frac{a}{mb} \right) \right]^2 + D_{s1} \right\} \varepsilon_{cr} \\ + C(D_{y1} + D_s) \left[\left(\frac{mb}{a} \right)^2 + \left(\frac{a}{mb} \right)^2 \right] + 2CD_{y1} = 0 \end{aligned} \quad (\text{Eq. 2.1})$$

In Eq. 2.1 ε_{cr} , a , b , and m are the strain at buckling; the length of the unloaded edges of the panels; the length of the loaded edges of the panels; and the buckling mode integer, respectively. The other terms are material-geometry constants defined as:

$$C = \frac{\pi^2}{0.85f'_c h b^2 (1 - \rho)} \quad (\text{Eq. 2.2})$$

$$D_{y1} = \frac{1.7f'_c h^3}{12(1 - \nu^2)\varepsilon_0} \quad (\text{Eq. 2.3})$$

$$D_s = E_s h \sum \rho_i Z_i^2 \quad (\text{Eq. 2.4})$$

$$D_{s1} = \frac{E_s \varepsilon_0 \rho}{0.85f'_c (1 - \rho)} \quad (\text{Eq. 2.5})$$

where h is the panel thickness; f'_c and ε_0 are the peak stress and the strain at peak stress of the concrete; ν is poisson's ratio of the concrete; ρ and ρ_l are the total steel ratio and the steel ratio for the i th layer of reinforcement, respectively; and Z_i is the distance from the i th reinforcement layer to the middle surface of the plate.

Table 2.8 Dimensions of Specimens Tested by Swartz et al. (1974)

Spec. ID	Panel Thickness mm (in.)	Panel Slenderness Ratio λ_w	Number of Layers of steel	Nominal Total Steel Ratio (Percent)	Concrete Compressive Strength MPa (psi)
1	25.5 (1.00)	48.0	1	0.20	26.9 (3896)
2	25.5 (1.00)	48.0	1	0.20	26.2 (3802)
3	25.5 (1.01)	47.5	2	0.50	21.8 (3156)
4	25.5 (1.00)	48.0	2	0.50	23.6 (3430)
5	25.5 (1.00)	48.0	2	0.75	22.7 (3298)
6	26.5 (1.04)	46.2	2	0.75	24.4 (3546)
7	25.0 (0.99)	48.5	2	1.00	25.4 (3688)
8	24.5 (0.97)	49.5	2	1.00	22.1 (3201)
9	32.0 (1.25)	38.4	1	0.20	17.7 (2564)
10	32.0 (1.25)	38.4	1	0.20	18.3 (2653)
11	32.0 (1.26)	38.1	2	0.50	16.6 (2414)
12	31.5 (1.24)	38.7	2	0.50	17.9 (2600)
13	32.0 (1.25)	38.4	2	0.75	17.6 (2546)
14	32.0 (1.27)	37.8	2	0.75	19.8 (2873)
15	32.5 (1.28)	37.5	2	1.00	19.9 (2882)
16	31.5 (1.24)	38.7	2	1.00	17.9 (2590)
17	19.0 (0.757)	63.4	1	0.20	22.6 (3272)

Table 2.8 (cont.) Dimensions of Specimens Tested by Swartz et al. (1974)

Spec. ID	Panel Thickness mm (in.)	Panel Slenderness Ratio λ_w	Number of Layers of steel	Nominal Total Steel Ratio (Percent)	Concrete Compressive Strength MPa (psi)
18	19.0 (0.763)	62.9	1	0.20	23.3 (3386)
19	19.0 (0.757)	63.4	2	0.50	23.8 (3448)
20	19.0 (0.747)	64.3	2	0.50	24.4 (3546)
21	19.0 (0.760)	63.2	2	0.75	25.0 (3626)
22	19.0 (0.758)	63.3	2	0.75	24.8 (3590)
23	19.0 (0.763)	62.9	2	1.00	23.4 (3396)
24	20.0 (0.782)	61.4	2	1.00	27.0 (3917)

Swartz and Rosebraugh (1974) also found that the contribution of the steel reinforcement in the calculation of the buckling strain was negligible. But the steel plays an important role when calculating the ductility and capacity of the plate. Table 2.9 summarizes the measured strengths and the buckling load calculated using the recommended approach (assuming an isotropic plate and using the tangent modulus).

Table 2.9 Measured Buckling Load and Failure Load, and Calculated Buckling Load Using Tangent Modulus (Swartz and Rosebraugh 1974)

Spec. ID	Experimental Buckling Load kN (kips)	Failure Load kN (kips)	Tangent Modulus Buckling Load kN (kips)	Ratio of Measured to Calculated Buckling Load
1	556 (125.1)	490 (110.2)	490 (116.0)	1.08
2	447 (100.4)	507 (113.9)	507 (119.0)	0.84
3	403 (90.6)	444 (99.9)	444 (105.0)	0.86
4	559 (125.7)	534 (120.1)	534 (118.0)	1.07
5	579 (130.2)	624 (140.2)	624 (113.0)	1.15
6	593 (133.4)	692 (155.5)	692 (119.0)	1.12
7	578 (130.0)	640 (143.9)	640 (124.0)	1.05
8	448 (100.8)	455 (102.3)	455 (106.0)	0.95
9	516 (116.0)	626 (140.7)	626 (116.0)	1.00
10	632 (140.0)	696 (156.5)	696 (123.0)	1.14
11	535 (120.4)	637 (143.1)	637 (120.0)	1.00
12	535 (120.2)	640 (143.8)	640 (119.0)	1.01
13	446 (100.2)	512 (115.1)	512 (128.0)	0.78
14	578 (129.9)	716 (161.0)	716 (148.0)	0.88
15	668 (150.1)	766 (172.3)	766 (155.0)	0.97
16	580 (130.6)	722 (162.3)	722 (134.0)	0.97
17	360 (80.4)	429 (96.5)	429 (59.0)	1.36
18	355 (80.1)	396 (89.1)	396 (65.5)	1.22
19	310 (70.1)	378 (84.9)	378 (63.1)	1.11

Table 2.9 (cont.) Measured Buckling Load and Failure Load, and Calculated Buckling Load Using Tangent Modulus Modulus (Swartz and Rosebraugh 1974)

Spec. ID	Experimental Buckling Load kN (kips)	Failure Load kN (kips)	Tangent Modulus Buckling Load kN (kips)	Ratio of Measured to Calculated Buckling Load
20	335 (75.3)	373 (83.8)	373 (61.0)	1.23
21	335 (75.6)	368 (82.8)	368 (63.2)	1.20
22	310 (70.0)	355 (80.0)	355 (64.4)	1.09
23	310 (70.0)	347 (78.0)	347 (68.9)	1.02
24	355 (80.0)	400 (90.0)	400 (78.3)	1.02

2.2.3 Saheb and Desayi

Saheb and Desayi (1990) tested 24 rectangular, reinforced concrete panels. All panels were simply supported along all four edges and were subjected to eccentric compression along two edges. The aspect ratios of the panels varied between 0.67 and 2, and the slenderness ratios varied between 6 and 18. The panels were 50 mm (2.0 in.) thick, with two layers of steel reinforcement. The dimensions of the panels, material properties, and measured strengths are presented in Table 2.10 (failure loads were reported for 21 of the 24 panels).

The load was applied with an eccentricity of one-sixth of the panel thickness. The strength of the panels decreased as the slenderness ratio increased. Vertical reinforcement increased the strength of the panels, while horizontal reinforcement had negligible influence on their capacity. Two equations were

developed to estimate the strength of the panels. The first (Eq. 2.6) was an empirical equation that provided a conservative estimate of the maximum load.

$$P_u = 0.67\phi Lt \left[1 - \left(\frac{L}{120t} \right)^2 \right] \left[1 + 0.12 \left(\frac{h}{L} \right) \right] \quad (\text{Eq. 2.6})$$

where P_u is the ultimate capacity; ϕ is the capacity reduction factor; f'_c is the cylinder strength of the concrete; h is the length of the unloaded edges; L is the length of the loaded edges; and t is the panel thickness.

The second equation (Eq. 2.7) was based on the buckling strength of simply-supported, thin, rectangular, metal plates, but adjusted to fit the data from their experiments and from plates tested by Swartz et al. (1974). To fit the data, the strength provided by the reinforcement was included in the calculations, but the expression proposed includes only the strength of the concrete, and neglects the reinforcement. Thus, the equation gives conservative estimates of the strength for most of the test data included not because of buckling considerations, but because the steel is not considered to estimate the strength of the plates.

$$P_u = \phi \left[0.8352 \left(\frac{L}{t} \right) - 0.0052 \left(\frac{L}{t} \right)^2 \right] \left[\frac{L t f'_c + A_{sv} f_{yv} \left(1 + \frac{A_{sh} f_{yh}}{A_{sv} f_{yv}} \right)}{\frac{L}{t}} \right] \quad (\text{Eq. 2.7})$$

where A_{sh} and A_{sv} are total areas of horizontal and vertical reinforcement and f_{yh} and f_{yv} are the corresponding yield strengths.

Table 2.10 Specimens Tested by Saheb and Desayi (1990)

Spec. ID	Panel Height mm (in.)	Panel Width mm (in.)	Panel Slenderness Ratio λ_w	Steel Yield Stress MPa (ksi)	Nominal Vertical Steel Ratio (Percent)	Concrete* Compressive Strength MPa (psi)	Measured Strength kN (kips)
1	600 (23.6)	900 (35.4)	18.0	297 (43.0)	0.173	22.33 (3240)	556 (125)
2	600 (23.6)	600 (23.6)	12.0	297 (43.0)	0.173	22.33 (3240)	413 (93)
3	600 (23.6)	400 (15.7)	8.0	297 (43.0)	0.173	22.33 (3240)	285 (64)
4	600 (23.6)	300 (11.8)	6.0	297 (43.0)	0.173	22.33 (3240)	235 (53)
5	450 (17.7)	300 (11.8)	6.0	297 (43.0)	0.165	21.67 (3140)	284 (64)
6	600 (23.6)	400 (15.7)	8.0	297 (43.0)	0.165	21.67 (3140)	347 (78)
7	900 (35.4)	600 (23.6)	12.0	297 (43.0)	0.165	21.67 (3140)	463 (104)
8	1350 (53.1)	900 (35.4)	18.0	297 (43.0)	0.165	21.67 (3140)	534 (120)
10	600 (23.6)	900 (35.4)	18.0	286 (41.5)	0.331	25.17 (3650)	598 (134)
11	600 (23.6)	900 (35.4)	18.0	581 (84.3)	0.528	25.17 (3650)	709 (159)
12	600 (23.6)	900 (35.4)	18.0	570 (82.7)	0.845	25.17 (3650)	823 (185)
13	1200 (47.2)	800 (31.5)	16.0	297 (43.0)	0.177	22.83 (3310)	498 (112)
14	1200 (47.2)	800 (31.5)	16.0	286 (41.5)	0.335	22.83 (3310)	613 (138)
15	1200 (47.2)	800 (31.5)	16.0	581 (84.3)	0.528	22.83 (3310)	717 (161)
16	1200 (47.2)	800 (31.5)	16.0	570 (82.7)	0.856	22.83 (3310)	790 (178)
18	600 (23.6)	900 (35.4)	18.0	297 (43.0)	0.173	24.5 (3550)	712 (160)
19	600 (23.6)	900 (35.4)	18.0	297 (43.0)	0.173	24.5 (3550)	712 (160)
20	600 (23.6)	900 (35.4)	18.0	297 (43.0)	0.173	24.5 (3550)	683 (154)
22	1200 (47.2)	800 (31.5)	16.0	297 (43.0)	0.176	20.17 (2925)	598 (134)
23	1200 (47.2)	800 (31.5)	16.0	297 (43.0)	0.176	20.17 (2925)	648 (146)
24	1200 (47.2)	800 (31.5)	16.0	297 (43.0)	0.176	20.17 (2925)	633 (142)

* Determined from tests of concrete cubes

The capacities calculated using the proposed equations were not reported. Averages of ratios of calculated to experimental strength equal to 0.943 and 0.865, with COV of 0.132 and 0.175, were reported for the first and second proposed equations, respectively.

2.3 SUMMARY

The results from six previous experimental investigations of the behavior of rectangular hollow concrete piers are presented in this chapter. The wall slenderness ratios ranged from 1.9 to 33.6. In four studies the specimens were subjected to high axial compressive stresses combined with simultaneous uniaxial or biaxial bending. It was found that the capacity of piers with wall slenderness ratios greater than 15 was less than the nominal strength calculated using standard design methods for solid piers. New design methods were proposed by Taylor et al. (1990) and Taylor and Breen (1994) and formed the basis for the provisions in the AASHTO Specifications (1998).

The results from three previous experimental investigations of the behavior of thin concrete panels are presented in this chapter. All the panels had four edges simply supported and were subjected to in-plane compression in one direction. The slenderness ratios varied between 6 and 73, and the failure load decreased as the slenderness increased. The tangent modulus model gave for most of the tested specimens safe predictions of the strength of the panels.

Chapter 3 Overview of Design Procedures

As indicated in Chapter 2, new design provisions for hollow concrete piers were introduced in the AASHTO Specifications (1998). These provisions consider the reduction in capacity due to local buckling of thin pier walls (Taylor et al. 1990, Taylor and Breen 1994).

The design provisions used before 1998 are summarized in Section 3.1 and the provisions introduced in 1998 are discussed in Section 3.2. The new design provisions were developed using the experimental data described in Section 2.1. These design provisions are re-evaluated in Section 3.3.

3.1 AASHTO DESIGN PROCEDURES FOR COMPRESSION MEMBERS IN THE EARLY 1990S

Before the current Specifications (AASHTO 1998) were issued by AASHTO, all structural concrete compression members were designed using the same provisions. No distinction was made between hollow piers and solid cross-sections.

The design of concrete compression members from the AASHTO Standard Specifications for Highway Bridges (1996) (Sections 8.15.4 and 8.16.4) was based on typical assumptions of strain compatibility and an assumed maximum strain of 0.003 at the extreme concrete compression fiber. Any appropriate relationship between stress and strain may be used for concrete in compression, but the Whitney (1937) rectangular stress block (Section 8.16.2.7 AASHTO (1996)) was considered to be satisfactory.

When using the design procedures in the AASHTO Specifications (1996) the following assumptions are made: (1) planes within the cross-section remain plane after deformation, and (2) there is perfect bond between the concrete and the steel reinforcement.

In addition, the following assumptions are made about the material stress-strain relationships: (1) the equivalent rectangular block has a stress of $0.85 f'_c$; (2) the stress block is bounded by the edges of the section and a straight line parallel to the neutral axis, located at a distance $\beta_1 c$ from the extreme compression fiber, where c is the distance from the extreme concrete compression fiber to the neutral axis and β_1 decreases linearly from 0.85 to 0.65 as f'_c increases from 28 to 55 MPa (4 to 8 ksi); (3) the strain at the extreme concrete compression fiber is 0.003; (4) the tensile strength of the concrete is neglected; and (5) the steel is assumed to have a linear, elastic perfectly plastic stress-strain curve. Figure 3.1 shows the rectangular stress distribution described above for a hollow rectangular section subjected to compression and biaxial bending.

Design of biaxially loaded sections was based on strain compatibility or an approximate expression such as the load contour method (Bresler 1960).

The slenderness effects on the overall stability of compression members were considered using a magnified moment. No special design considerations were given for compression members with hollow cross sections. The only reference to hollow concrete piers made in the AASHTO Specifications (1996) was in Section 7.4. This section states that tubular piers may be constructed of steel, reinforced concrete or prestressed concrete, and that the piers must have

sufficient wall thickness to sustain forces and moments for all appropriate loading situations. However, the specifications did not include any special design provisions for the walls of the hollow piers.

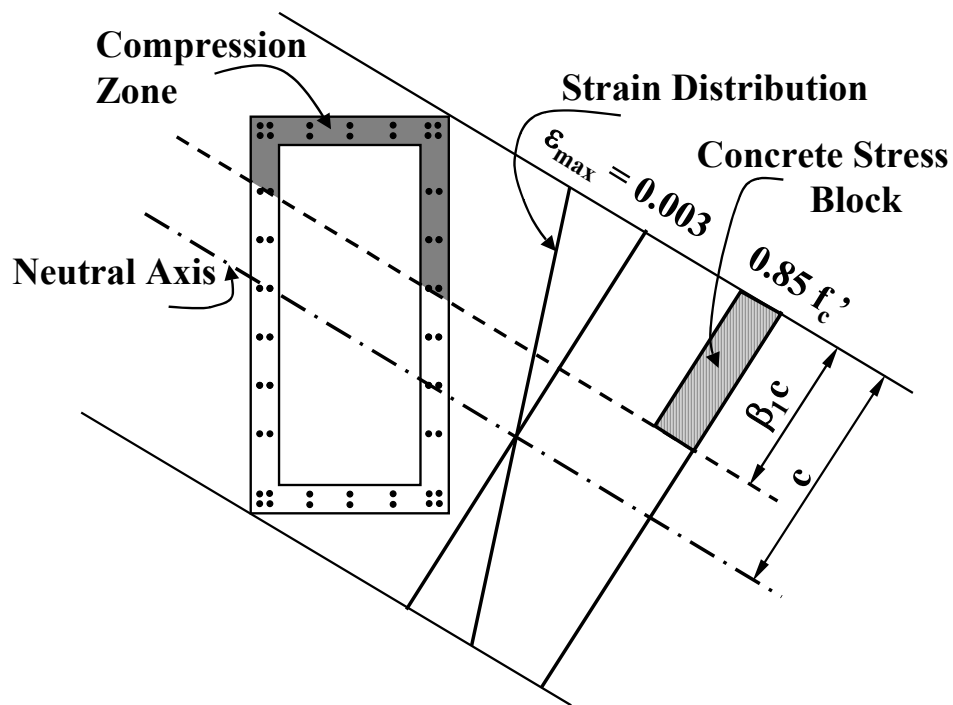


Figure 3.1 *Equivalent Rectangular Stress Block Distribution for a Hollow Rectangular Section Subjected to Combined Biaxial Compression and Bending*

The AASHTO Specifications (1994) used the same specifications for the design of compression members as the AASHTO Specifications (1996).

3.2 APPROXIMATE METHOD FOR DESIGN OF HOLLOW RECTANGULAR COMPRESSION MEMBERS

Provisions for the design and reinforcing of hollow, rectangular concrete compression members were introduced in the AASHTO Specifications (1998).

Two sections were added: Section 5.10.12 specifies reinforcing details for hollow compression members, and Section 5.7.4.7 governs the design of hollow rectangular compression members.

3.2.1 Reinforcing details

The specifications for reinforcing details in rectangular, hollow compression members were based on recommendations given by Taylor et al. (1990).

The key requirements are summarized below:

- Longitudinal reinforcement must be distributed in two layers throughout the cross-section and the amount of longitudinal reinforcement must not be less than 1% of the gross area of the concrete cross-section.
- Cross-ties must be provided and the hooks of the ties must enclose both lateral and longitudinal bars.

3.2.2 Design Procedures

The design procedures for compression members have not changed from those in previous specifications, but Section 5.7.4.7 (AASHTO 1998) was added to take into account the effects of wall slenderness on the response of hollow, rectangular compression members.

The current provisions are the same for hollow piers with wall slenderness ratios less than 15 and for solid piers. For hollow piers with wall slenderness ratio exceeding 15, two design methods are defined.

The first method, in Section 5.7.4.7.2b, is more complicated, and requires the designer to calculate the local buckling strain in the most slender wall in the cross-section. The only recommendations given to calculate the local buckling strain of the wall are: (1) simply supported boundary conditions on all four edges of the wall can be used; and (2) tangent moduli have to be used to model the nonlinear behavior of the materials. Stress-strain curves for the concrete and the principles of Article 5.7.3 (AASHTO 1998) for flexural members must be used to calculate the flexural strength of the pier using the lesser value of the buckling strain and 0.003 as the limiting strain in the concrete.

The second method is approximate, and is intended to alert designers of possible instability in hollow piers with wall slenderness ratios less than 35. The nominal capacity, calculated using standard design procedures, is multiplied by a reduction factor ϕ_w . The factor is defined as:

$$\begin{aligned} \phi_w &= 1.0 && \text{if } \lambda_w \leq 15 \\ \phi_w &= 1 - 0.025(\lambda_w - 15) && \text{if } 15 < \lambda_w \leq 25 \\ \phi_w &= 0.75 && \text{if } 25 < \lambda_w \leq 35 \end{aligned} \quad (3.1)$$

This approximate method cannot be used for hollow piers with wall slenderness ratios larger than 35. Wall buckling must be considered explicitly in those cases. In addition, discontinuous reinforcement used in segmental construction must not be included when calculating the capacity of a hollow pier.

3.3 EVALUATION OF DESIGN PROVISIONS

The design provisions for hollow piers described in Section 3.2 were developed using the results of the analytical and experimental studies by Taylor et

al. (1990), who found that hollow piers with wall slenderness ratios larger than 15 failed at a capacity less than the nominal capacity of the cross-section. Therefore, a reduction factor was introduced to account for differences between the measured and the nominal capacities. This approach was validated using the measured response of hollow piers subjected to concentric axial load, combined axial load and uniaxial bending, and combined axial load and biaxial bending (Section 2.1).

The procedures used by many designers to calculate the nominal capacity of a cross-section, however, are not the same as those used by Taylor et al. (1990). Therefore, the typical design procedures should be compared with the available test data to determine if the reduction factors provide an adequate estimate of the measured capacity of hollow piers.

Background information from Taylor et al. (1990) is summarized in Section 3.3.1 and the current design provisions are evaluated with respect to the experimental data in Section 3.3.2.

3.3.1 Strength Ratios Calculated Using Analysis Procedures Developed by Taylor

The design provisions described in Section 3.2.2 were based on results from the study of the behavior of hollow concrete piers by Taylor et al. (1990, 1995). Figure 3.2 shows the strength ratios reported by Taylor and the curve used in the approximate design method included in Section 5.7.4.7.2.c of the AASHTO Specifications (1998).

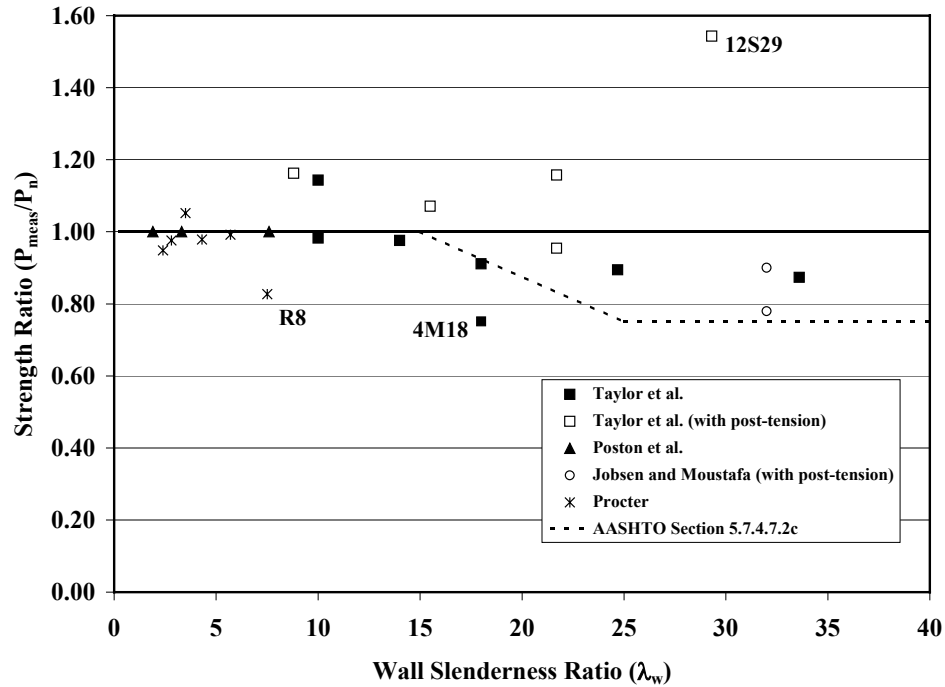


Figure 3.2 Variation of Strength Ratio with Wall Slenderness Ratio

Taylor et al. (1990) used the ratio of the measured axial capacity of a hollow pier to the nominal axial strength of the cross-section to demonstrate that local buckling influences the capacity of hollow piers with wall slenderness ratios exceeding 15. Available data for hollow piers subjected to uniaxial compression (Procter 1977), combined axial load and uniaxial bending (Jobse and Moistafa 1984, Taylor et al. 1990) and combined axial load and biaxial bending (Poston at al. 1983, 1985) were used for these comparisons.

For specimens subjected to uniaxial compression the nominal axial capacity was calculated as:

$$P_n = 0.85 f_{cmax} (A_g - A_{st}) + A_{st} f_y \quad (3.2)$$

where A_g is the gross area of the concrete cross-section, A_{st} is the area of longitudinal steel, f_{cmax} is the compressive strength of the concrete, and f_y is the yield stress of the longitudinal reinforcement.

Procter (1977) tested cubes to determine the compressive strength of the concrete; the reported cube strengths were multiplied by 5/6 to convert to the compressive strength of an equivalent cylinder.

The nominal capacity of specimens subjected to combined axial loading and uniaxial bending was calculated by assuming a linear variation of strain over the depth of the cross-section and a limiting compressive strain of 0.003 in the concrete. The stress-strain relationship for steel was assumed to be bilinear, and the stress-strain curve for concrete was assumed to follow the parabolic relationship proposed by Hognestad (1951, 1952). The maximum strength of the concrete in the test specimen was assumed to be 85% of the compressive strength determined from standard cylinder tests. The strength reduction factor, ϕ , was taken to be 1.0 for all specimens.

Taylor et al. (1990) defined a strength ratio as the measured axial strength divided by the nominal axial capacity regardless of the method of loading. The strength ratios are plotted as a function of the wall slenderness ratios in Fig. 3.2. The reduction factor defined in Section 5.7.4.7.2c of the AASHTO Specifications (1998) are also shown in that figure.

In general, the strength ratio tended to decrease as the wall slenderness ratio increased. However, two specimens, R8, tested by Procter, and 4M18, tested

by Taylor, exhibited measured strengths that were less than expected, and one specimen, 12S29, tested by Taylor, exhibited a measured capacity that was considerably more than expected.

Procter (1977) gave no explanation for the relatively low strength of specimen R8, but the construction method and observed mode of failure suggest low-quality concrete. All the specimens tested by Procter were cast horizontally and Specimen R8 had the thinnest walls. It is likely that the concrete was not consolidated properly in this specimen. This hypothesis is supported by the fact that R8 was the only specimen in this series of tests that failed by spalling of the outer layer of concrete. Spalling was observed over half the length of the specimen along all four sides.

Taylor et al. (1990) reported that the relatively low strength of Specimen 4M18 was due to low quality of the concrete. Taylor observed an excessive amount of bleed water about one hour after casting Specimen 4M18. Also, failure occurred very near the top of the specimen, supporting that the concrete strength was lower there due to higher water-cementitious ratio.

Ignoring those two specimens where the quality of the concrete has been questioned, the reduction factor in the AASHTO Specification (1998) appears to represent the trends in the measured data.

3.3.2 Strength Ratios Calculated Using Equivalent Rectangular Stress Block

During design, most engineers use an equivalent rectangular stress block to calculate the compressive force in the concrete. When proportioning rectangular members, the choice of stress-strain model has little influence in the

calculated capacity. The differences may be larger, however, for hollow piers because the shape of the compression zone is irregular.

The strength ratios described in the previous section are calculated again in this section using the equivalent rectangular stress block to calculate the compressive force on the concrete. The strength reduction factor ϕ is taken equal to 1.0; the strength of the concrete is taken as the measured cylinder strength; and all other assumptions are the same as in the previous section unless indicated.

The strength ratios for the three piers tested by Poston et al. (1983) are reevaluated. Because a constant level of axial load was maintained as the biaxial moments were increased during the tests, the calculated axial capacity provides no insight into the behavior of the specimens, it is simply the applied load. Therefore, the nominal flexural capacity for bending about the strong axis was compared with the maximum measured moment about the same axis.

The revised strength ratios are plotted in Fig. 3.3 and summarized in Table 3.1. The reduction factor given in Section 7.4.7.2c of the AASHTO Specification (1998) is also plotted in Fig. 3.3.

Table 3.1 Nominal Capacities of Hollow Piers Tested by Other Researchers Calculated Using Cylinder Strength

Specimen ID	Wall Slenderness Ratio λ_w	Measured Capacity kN (kip)	Nominal Capacity kN (kip)	Ratio of Measured to Nominal Capacity
Procter R8	7.5	405 (91)	490 (110)	0.83
Procter R9	5.7	556 (125)	560 (126)	0.99
Procter R10	4.3	618 (139)	630 (142)	0.98
Procter R11	3.5	721 (162)	685 (154)	1.05
Procter R12	2.8	725 (163)	740 (167)	0.98
Procter R13	2.4	738 (166)	780 (175)	0.95
Jobse 1	32.0	7175 (1613)	9760 (2195)	0.74
Jobse 2A	32.0	5987 (1346)	7550 (1698)	0.79
Poston 1 Cell *	7.6	163 (1440)	169 (1491)	0.97
Poston 2 Cells *	3.3	200 (1770)	175 (1543)	1.15
Poston 3 Cells *	1.9	236 (2085)	199 (1757)	1.19
Taylor 1M10	10.0	2344 (527)	2490 (559)	0.94
Taylor 2M10	10.0	2091 (470)	1920 (431)	1.09
Taylor 3M14	14.0	4172 (938)	4510 (1013)	0.93
Taylor 4M18	18.0	4172 (938)	5810 (1305)	0.72
Taylor 5S9	8.8	5062 (1138)	4500 (976)	1.17
Taylor 6S16	15.5	4217 (948)	4160 (935)	1.01
Taylor 7S22	21.7	4444 (999)	3950 (887)	1.13
Taylor 8ML25	24.7	4021 (904)	4600 (1034)	0.87
Taylor 9MLP22	21.7	4275 (961)	4580 (1029)	0.93
Taylor 10ML18	18.0	4506 (1013)	5140 (1155)	0.88
Taylor 11ML34	33.6	2771 (623)	3255 (732)	0.85
Taylor 12S29	29.3	3034 (682)	2070 (466)	1.46

* Nominal capacity corresponds to calculated flexural capacity for bending about the strong axis, kN-m (kip-in.).

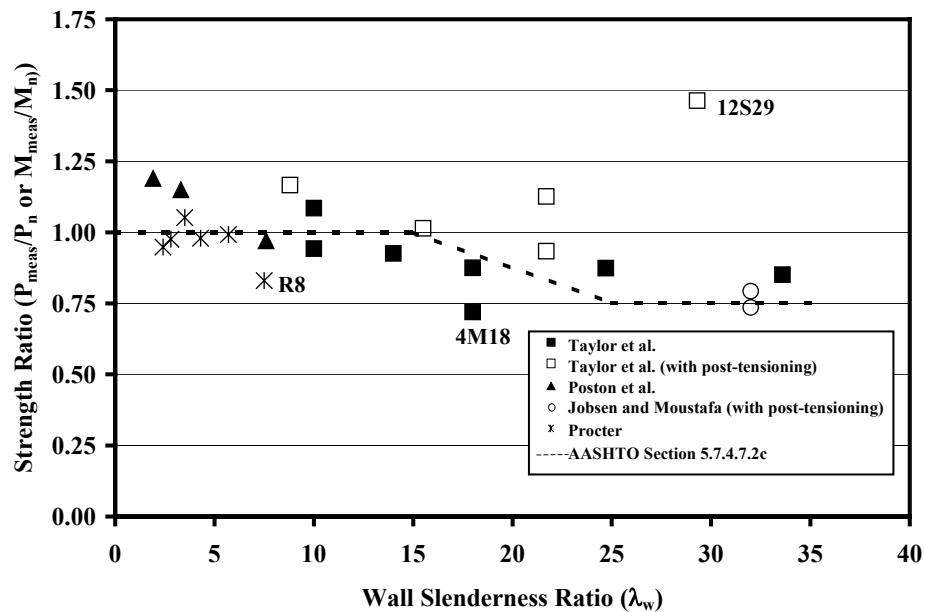


Figure 3.3 Strength Ratios of all the Available Specimens Calculated using the Nominal Capacity of the Cross-Section (P_{meas}/P_n)

Several points in Fig. 3.2 shifted downward in Fig. 3.3 due to the differences in the methods used to calculate the nominal capacity of the specimens. In the range of wall slenderness ratios between 5 and 15, the strength ratios for three specimens that were above 1.0 in Fig. 3.2 are closer to 0.9 in Fig. 3.3. Two of the strength ratios of the specimens tested by Poston et al. (1983), which were reported to be 1.0 (Fig. 3.2), shifted upward. But the calculated strength ratio of the specimen with largest wall slenderness ratio is smaller than 1. This indicates that the approximate design procedure given in the AASHTO Specifications (1998) may not be conservative for walls with wall slenderness ratios less than 20.

In the calculations presented in this chapter, the strength ratios for Specimens R8 and 4M18 are extremely low. Hypotheses of low concrete strength have been proposed, and the strength ratios were recalculated using an assumed concrete strength that was 25% lower than the reported values. This reduction was considered to be a reasonable approximation to the actual concrete strength in the test specimens.

The axial nominal capacities calculated for Specimens R8 and 4M18 using reduced concrete strength were 390 and 4540 kN (88 and 1020 kips), which gave strength ratios of 1.03 and 0.92 respectively. These values are consistent with the other strength ratios plotted in Fig. 3.3 and strengthen the hypothesis of low-strength in these two specimens.

3.3.3 Strength Ratios Calculated Using Equivalent Rectangular Stress Block and Concrete Design Strength

In the previous section strength ratios were calculated using an equivalent rectangular stress block and the concrete strength equal to the measured cylinder strength. However, the compressive design strength of the concrete, f'_c , used in typical concrete design procedures, is smaller than the average measured cylinder strength. Strength ratios are calculated in this section using estimates of the corresponding value of f'_c for each specimen. In the following discussion compressive concrete design strengths are calculated.

Equations 3.2 and 3.3 indicate the average strength, f'_{cr} , required for concrete cylinders in Section 5.3.2 of the ACI-318 (1999). The term s is the standard deviation of the production of concrete.

$$f'_{cr} = f'_c + 1.34s \quad (3.2)$$

$$f'_{cr} = f'_c + 2.33s - 3.45MPa \quad (3.3a)$$

$$f'_{cr} = f'_c + 2.33s - 500psi \quad (3.3b)$$

These equations can be rewritten as follows:

$$f'_c = f'_{cr} - 1.34s \quad (3.4)$$

$$f'_c = f'_{cr} - 2.33s + 3.45MPa \quad (3.5a)$$

$$f'_c = f'_{cr} - 2.33s + 500psi \quad (3.5b)$$

Equations 3.4 and 3.5 can be used to estimate compressive design strengths, f'_c , associated with each value of measured cylinder strengths. To estimate f'_c it can be assumed that the standard deviation s is equal to 15% of the average strength, f'_{cr} (assuming a coefficient of variation of 0.10). The measured cylinder strengths of the available tests range from 21 to 62 MPa (3000 to 9000 psi), approximately. For the purpose of evaluating the design method choosing smaller values of the standard deviation is more a conservative approach. Therefore, the standard deviation is 3.1 MPa (450 psi) and Equations 3.4 and 3.5 become:

$$f'_c = f'_{cr} - 4.15MPa \quad (3.6a)$$

$$f'_c = f'_{cr} - 600psi \quad (3.6b)$$

$$f'_c = f'_{cr} - 3.77MPa \quad (3.7a)$$

$$f'_c = f'_{cr} - 550psi \quad (3.7b)$$

From Equations 3.6 and 3.7 a conservative estimate of the design strength of the available specimens that can be used to evaluate the design method is:

$$f'_c = f'_{cr} - 3.77MPa \quad (3.8a)$$

$$f'_c = f'_{cr} - 500psi \quad (3.8b)$$

The strength ratios described in the previous section are calculated again in this section using the equivalent rectangular stress block. The compressive design strength of the concrete, f'_c , is estimated using Eq. 3.8 and the measured cylinder strength, f'_{cr} .

The revised strength ratios are summarized in Table 3.2 and plotted in Fig. 3.4. The reduction factor given in Section 7.4.7.2c of the AASHTO Specification (1998) is also plotted in Fig. 3.4.

As was expected, compared with Fig. 3.3 all points shifted upward. Not considering the specimens that have low-quality concrete, the design curve produces safe estimates of the strength in almost all cases. One point is unsafe by only 1%,

In summary, it is judged that the current design provisions (AASHTO 1998) reasonable safe designs of hollow rectangular piers with wall slenderness ratios less than 35.

Table 3.2 Nominal Capacities of Hollow Piers Tested by Other Researchers Calculated Using Compressive Design Strength of Concrete

Specimen ID	Wall Slenderness Ratio λ_w	Measured Capacity kN (kip)	Nominal Capacity kN (kip)	Ratio of Measured to Nominal Capacity
Procter R8	7.5	405 (91)	456 (103)	0.89
Procter R9	5.7	556 (125)	521 (117)	1.07
Procter R10	4.3	618 (139)	589 (132)	1.05
Procter R11	3.5	721 (162)	638 (143)	1.13
Procter R12	2.8	725 (163)	688 (155)	1.05
Procter R13	2.4	738 (166)	722 (162)	1.02
Jobse 1	32.0	7175 (1613)	8923 (2006)	0.80
Jobse 2A	32.0	5987 (1346)	6943 (1561)	0.86
Poston 1 Cell *	7.6	163 (1440)	146 (1290)	1.12
Poston 2 Cells *	3.3	200 (1770)	157 (1383)	1.28
Poston 3 Cells *	1.9	236 (2085)	185 (1638)	1.27
Taylor 1M10	10.0	2344 (527)	2380 (535)	0.99
Taylor 2M10	10.0	2091 (470)	1704 (383)	1.23
Taylor 3M14	14.0	4172 (938)	4061 (913)	1.03
Taylor 4M18	18.0	4172 (938)	5475 (1231)	0.76
Taylor 5S9	8.8	5062 (1138)	4114 (925)	1.23
Taylor 6S16	15.5	4217 (948)	3300 (742)	1.28
Taylor 7S22	21.7	4444 (999)	3274 (736)	1.36
Taylor 8ML25	24.7	4021 (904)	4310 (969)	0.93
Taylor 9MLP22	21.7	4275 (961)	3648 (820)	1.17
Taylor 10ML18	18.0	4506 (1013)	4817 (1083)	0.94
Taylor 11ML34	33.6	2771 (623)	3043 (684)	0.91
Taylor 12S29	29.3	3034 (682)	1855 (417)	1.64

* Nominal capacity corresponds to calculated flexural capacity for bending about the strong axis, kN-m (kip-in.).

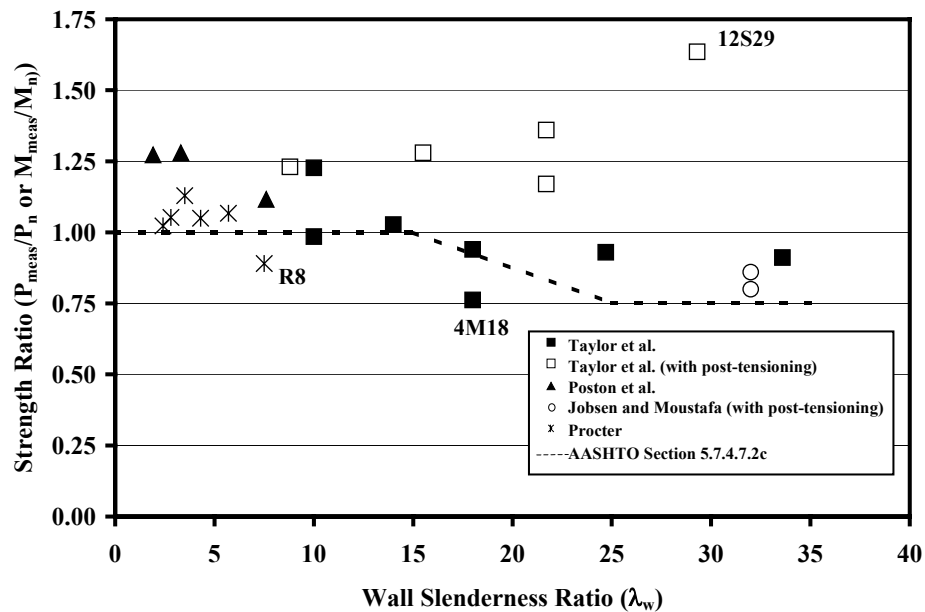


Figure 3.4 Strength Ratios of all the Available Specimens Calculated using the Nominal Capacity of the Cross-Section (P_{meas}/P_n) and Estimated Concrete Compressive Design Strength

3.4 SUMMARY

Before the 1998 AASHTO LRFD Bridge Design Specifications were adopted, no distinction was made between the behavior of hollow piers and solid cross-sections in design. Therefore, the influence of wall slenderness on the strength of hollow piers was ignored.

Two design procedures for rectangular, hollow concrete members subjected to compression and bending were included in the AASHTO Specifications (1998).

The approximate design procedure includes a reduction factor to take into account the influence of local stability in piers with wall slenderness ratios between 15 and 35. As shown in Fig. 3.4, this approach can lead to safe estimates of the nominal capacity of a hollow pier if an equivalent rectangular stress block is used for the concrete.

Chapter 4 Experimental Program

4.1 OVERVIEW

The experimental program of this research consisted of compression tests to failure of five, one-fifth-scale, thin-walled, rectangular, concrete hollow pier specimens. The specimens were loaded eccentrically to induce simultaneous axial compression and biaxial bending.

The height of the specimens, 1.78 m (70 in.), was chosen to avoid overall or Euler buckling of the columns, while permit local buckling of the thin walls. Solid, reinforced concrete blocks, cast at both ends of the specimens, were used to distribute the load from the loading frame to the specimens, and from the specimens to the reaction floor. Figure 4.1 shows the overall dimensions of the test specimens.

The nominal outside dimensions of all piers were 406 by 813 mm (16 by 32 in.). The interior dimensions depended on the thickness of the walls. The nominal wall slenderness ratios under study were 6, 8, 10, 12 and 14. The thicknesses of the walls varied from 51 mm (2 in.) (for a slenderness ratio equal to 14) to 102 mm (4 in.) (for a slenderness ratio equal to 6). Table 4.1 summarizes the geometric properties of the five hollow piers.

The alphanumeric code used to identify the specimens indicates the nominal slenderness ratio of the longer wall. For example, the ratio of the clear length of the longer wall to the wall thickness for Specimen P12 is approximately equal to 12.

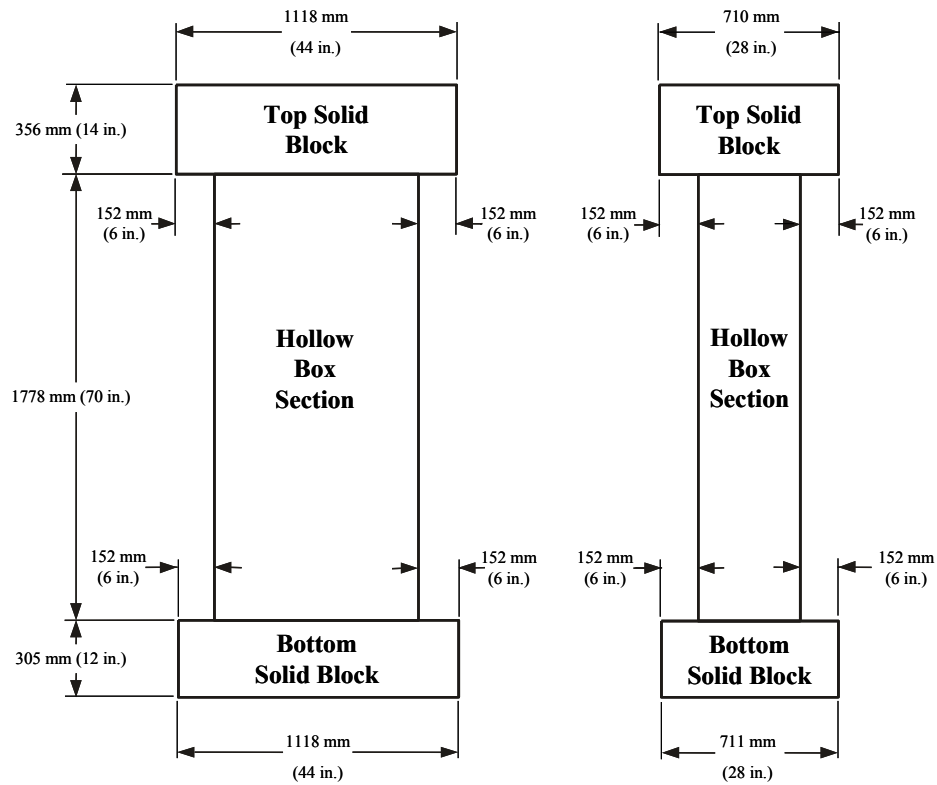


Figure 4.1 Overall Dimensions of Pier Specimens

4.1.1 Scale of the Models

A structural model is a physical representation of a structure or of part of a structure that has been constructed at a smaller size than the prototype structure.

Harris, H.G., White, R. N. and Sabnis, G. M. (1999) define structural models as elastic, indirect, direct, and strength models, depending of the intended use of the models. Other models are used to study wind effects or dynamic loading. These are of no interest in this investigation.

Elastic models have geometric similitude with the prototype, but are made of an elastic material that may not be the same material used in the prototype.

Therefore, these models can be only used to predict the elastic behavior of the prototype. Indirect models are defined as a special case of elastic models used to estimate reactions and internal forces. These models need only to represent the properties of the prototype that controls its behavior.

A direct model has geometric similitude with the prototype, while measured strains, deformations and stresses correspond to the respective scaled down quantities of the prototype.

The strength model is used to predict the inelastic behavior of the prototype and the ultimate strength. It is a direct model made of materials that are similar to the materials used in the prototype. All material properties of the model and prototype are the same, but the geometric dimensions of the model are scaled down. The mass density should be different between the model and the prototype.

A strength model must be used to study the post-cracking behavior of the piers, their ultimate strength, and the possibility of inelastic buckling of the thin walls. Since the tests are not dynamic and the effect of the self-weight of the specimens in their response can be neglected the difference in the mass density is not important.

Fialho, J. F. L. (1970) notes that direct models of reinforced concrete structures are built at one-fifth to one-tenth scale and that the spacing and width of the cracks have geometric similitude with the cracks of the prototype for models built at one-fourth or larger. Taking into consideration the above, the capacity of the loading apparatus, the wall slenderness range under study, and the constructibility of the walls, the specimens were built at a one-fifth scale.

Table 4.1 Geometric Properties of Test Specimens

Spec. ID	Wall Slenderness Ratio λ_w	Nominal Dimensions			Gross Area mm ² (in. ²)	Area of Long. Reinf. mm ² (in. ²)	Number of Long. Bars	Reinf. Ratio
		Section Depth mm (in.)	Section Width mm (in.)	Wall Thickness mm (in.)				
P6	6.00	813 (32)	406 (16)	102 (4.00)	206000 (320)	2190 (3.40)	68	0.011
P8	7.85	813 (32)	406 (16)	83 (3.25)	175000 (270)	1940 (3.00)	60	0.011
P10	9.64	813 (32)	406 (16)	70 (2.75)	151000 (234)	1810 (2.80)	56	0.012
P12	12.22	813 (32)	406 (16)	57 (2.25)	126000 (196)	1940 (3.00)	60	0.015
P14	14.00	813 (32)	406 (16)	51 (2.00)	114000 (176)	2190 (3.40)	68	0.019

4.2 DESIGN OF THE SPECIMENS

4.2.1 Governing Provisions of AASHTO Specifications

The primary objective when selecting the reinforcing details used in the specimens was to comply with the specifications for members in compression given in the AASHTO Standard Specifications for Highway Bridges (1996) and for hollow compression members in Section 5.7.4, AASHTO Specifications (1998). These requirements are summarized below. Most of the requirements were satisfied and any deviations are discussed.

- Minimum longitudinal reinforcement: $0.01 A_g$ (Section 8.18.1.2 (AASHTO 1996) and Section 5.10.12.1 (AASHTO 1998)). The longitudinal reinforcement used for the specimens varied from $0.011 A_g$ to $0.019 A_g$. The larger steel ratios were necessary because only one size of longitudinal bars was used and longitudinal reinforcement was spaced closer in the thinner walls because maximum bar spacing is linked to the wall thickness.
- Minimum size of longitudinal reinforcement: 16-mm diameter bars (#5 bars) (Section 8.18.1.2 (AASHTO 1996)). The smallest deformed bars available for use in this project have a diameter of 6 mm, equivalent to 30 mm bars (#9 bars) at full scale.
- Minimum size of lateral ties: 10 mm (#3) bars for longitudinal bars 32 mm in diameter (#10 bars) or smaller, and 12 mm (#4) bars for larger longitudinal bars (Section 8.18.2.3.1 (AASHTO 1996)). Deformed wire or welded wire fabric may be used for ties (Section 8.18.2.3.1 (AASHTO 1996)). Number 10-gage smooth wire, with a diameter of 3.4 mm (0.135 in.), was used as lateral ties in all specimens. At full scale, the wire is equivalent to 16 mm (#5) bars. The wire exceeded the minimum size and was selected because of availability and ease of fabricating the reinforcing cages.
- Two layers of reinforcement are required in each wall of the cross-section (Section 5.10.12.1 (AASHTO 1998)). Two equal layers of reinforcement were provided.

- The longitudinal reinforcing bars must be spaced not farther apart than 1.5 times the wall thickness or 450 mm (18 in.) (Section 5.10.12.2 (AASHTO 1998)). The controlling requirements in the one-fifth scale specimens were 1.5 times the wall thickness for the specimens with slenderness ratios of 12 and 14, and 91 mm (3.6 in.) for the other specimens. The maximum center-to-center spacing of the longitudinal bars was 89 mm (3.5 in.), which satisfies the requirements.
- Spacing of transverse reinforcing bars must be less than 1.25 times the thickness of the wall and less than 300 mm (12 in.) (Section 5.10.12.2 (AASHTO 1998)). In one-fifth scale, the second requirement corresponds to 60 mm (2.4 in.), so 64 mm (2.5 in.) was used as maximum longitudinal spacing of the transverse reinforcement for all the specimens except pier P14. The spacing of the transverse reinforcement of P14 was 50 mm (2 in.).
- Cross-ties must be provided between layers of reinforcement in each wall. The cross-ties must have a standard 135-degree hook at one end and a standard 90-degree hook at the other end (Section 5.10.12.3 (AASHTO 1998)). No longitudinal bar can be more than 600 mm (2 ft), measured horizontally, from a restrained bar on either side (Section 8.18.2.3.4 (AASHTO 1996)). Cross-ties were used to tie every other longitudinal bar, in a checker-board pattern. The maximum spacing in the specimens varied between 64 and 89 mm (2.5 and 3.5 in.) At full scale those spacing correspond to 320 and 445 mm (12.5 and 17.5 in.) respectively. The 135-

degree hook was replaced by a 90-degree hook in the specimens to have sufficient space between layers of reinforcement to permit placing the concrete.

- Straight lap splices of transverse reinforcing bars are permitted only if overlapping bars are enclosed over the length of the splice by the hooks of at least four cross-ties (Section 5.10.12.4 (AASHTO 1998)). Because of the small dimensions of the specimens only three cross-ties were used along the splice length.
- If closed loops cannot be provided at a corner, then pairs of “U” shaped bars with legs at least twice as long as the wall thickness, and orientated 90 degrees to one another, may be used (Section 5.10.12.5 (AASHTO 1998)). This detail was used in every layer of horizontal reinforcement at each corner in the specimens.
- For cast-in-place concrete, the clear distance between longitudinal bars in a layer must not be less than the smallest of 1.5 bar diameters, 1.5 times the maximum size of coarse aggregate, and 38 mm (1.5 in.) (Section 8.21.1 (AASHTO 1996)). The most restrictive requirement for the specimens was 1.5 times the maximum size of the coarse aggregate, which was 10 mm (3/8 in.), restricting the minimum clear spacing to 15 mm (9/16 in.). It was not possible to satisfy this requirement in the specimens with slenderness ratios of 12 and 14. Longitudinal bars in these specimens had a clear spacing of 13 mm (1/2 in.) between the two layers of reinforcement, only 2 mm (1/16 in.) less than required.

- Concrete cover for structural elements exposed to weather must be at least 50 mm (2 in.) for the primary reinforcement, and 38 mm (1.5 in.) for ties (Section 8.22.1 (AASHTO 1996)). In the one-fifth scale specimens the reduced requirements were 10 mm (0.4 in.) of cover for the primary reinforcement and 8 mm (0.3 in.) of cover for the ties. For ease of construction, 16 mm and 10 mm (5/8 in. and 3/8 in.) were used as the cover for the primary reinforcement and the ties, respectively.

Table 4.2 compares the required and provided reinforcing bar spacings for the five test specimens.

Table 4.2 Summary of Requirements for Reinforcing details in One-Fifth Scale Hollow Piers

Spec. ID	Max. Horizontal Spacing of Long. Reinforcement		Min. Horizontal Spacing of Long. Reinforcement		Maximum Vertical Spacing of Ties	
	Required mm (in.)	Provided Mm (in.)	Required mm (in.)	Provided mm (in.)	Required mm (in.)	Provided mm (in.)
P6	91 (3.60)	64 (2.50)	15 (0.5625)	57 (2.25)	61 (2.40)	64 (2.50)
P8	91 (3.60)	76 (3.00)	15 (0.5625)	38 (1.50)	61 (2.40)	64 (2.50)
P10	91 (3.60)	89 (3.50)	15 (0.5625)	25 (1.00)	61 (2.40)	64 (2.50)
P12	86 (3.38)	83 (3.25)	15 (0.5625)	13 (0.50)	61 (2.40)	64 (2.50)
P14	76 (3.00)	76 (3.00)	15 (0.5625)	13 (0.50)	51 (2.00)	51 (2.00)

4.2.2 Reinforcing details

The reinforcing details used in the test specimens were designed to facilitate the construction process. Cross sections and reinforcing details for the five specimens are shown in Fig. 4.2 to 4.7.

In Specimens P12 and P14 the maximum horizontal spacing of the longitudinal bars, as defined in Section 4.2.1, dictated the amount of steel used in the cross-sections. Only 6 mm diameter (#2 bars) deformed bars were used as longitudinal reinforcement. Two curtains of reinforcement were used in the wall piers.

The transverse reinforcement presented a problem from a construction standpoint. The corners of the walls had to be confined by a closed loop, but the pier had to be easy to be constructed. As a compromise between these two requirements, two “U” shaped hairpin bars were used to confine the corner longitudinal reinforcement. Figure 4.2 shows the two hairpins that were placed in each corner at each layer of horizontal reinforcement. Figure 4.8 shows a photo of the hairpin bars and how they were tied to the longitudinal bars in a corner. The tests later showed that this detail was sufficient to confine the concrete and limit the buckling length of the longitudinal bars to the longitudinal spacing of the transverse reinforcement.

For the horizontal reinforcement, large U-shaped bars were used. Each layer was spliced at the middle of the shorter walls. Taylor et al. (1990) criticized this detail, but constructibility concerns dictated its use. The results from these experiments did not show that the detail influenced the behavior of the test

specimens. The horizontal layers of lateral reinforcement were spaced vertically at 51 mm or 64 mm (2 in. and 2.5 in.) on center, depending of the wall (Table 4.2).

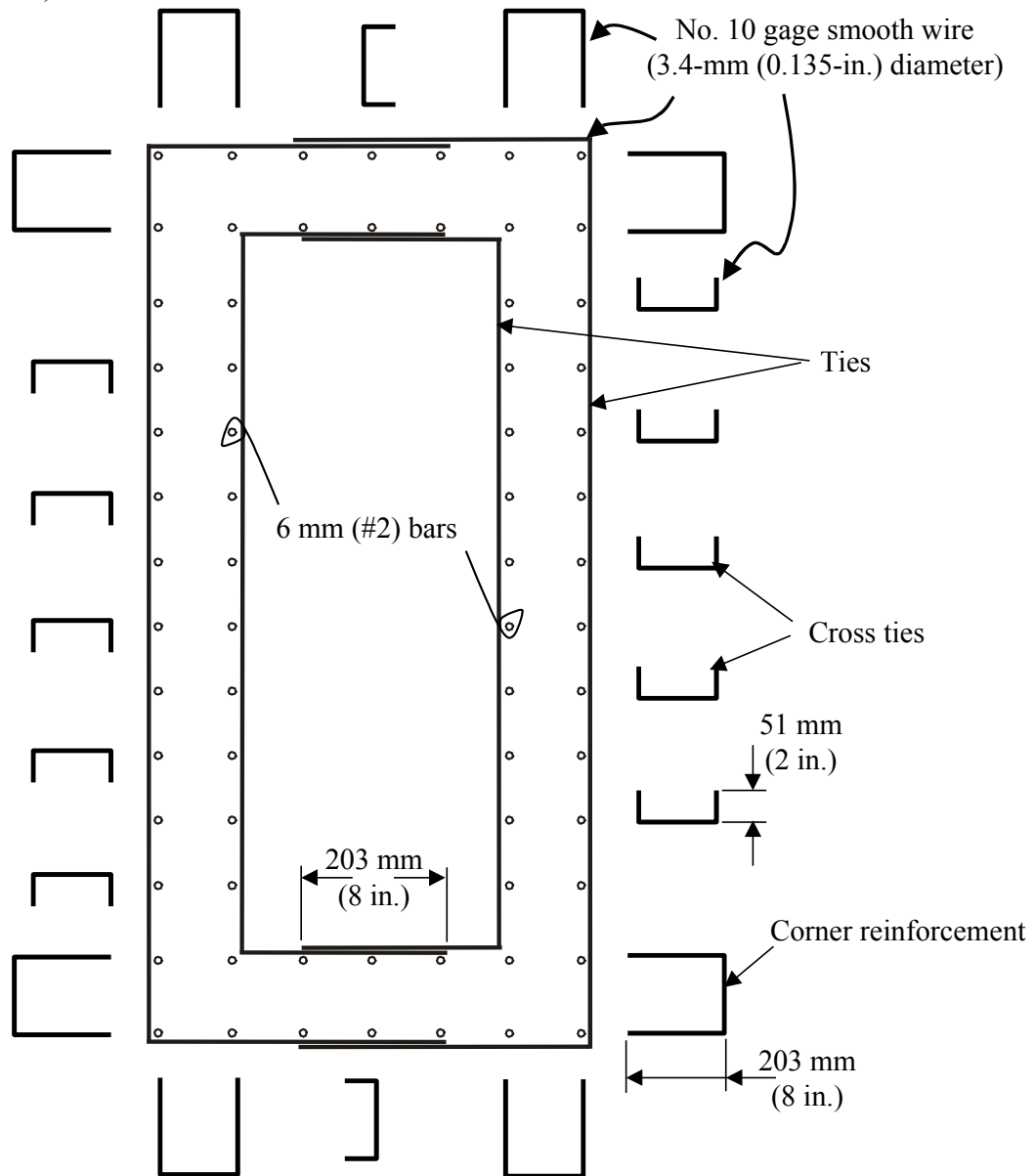


Figure 4.2 Typical Details for Transverse Reinforcement and Cross-Ties

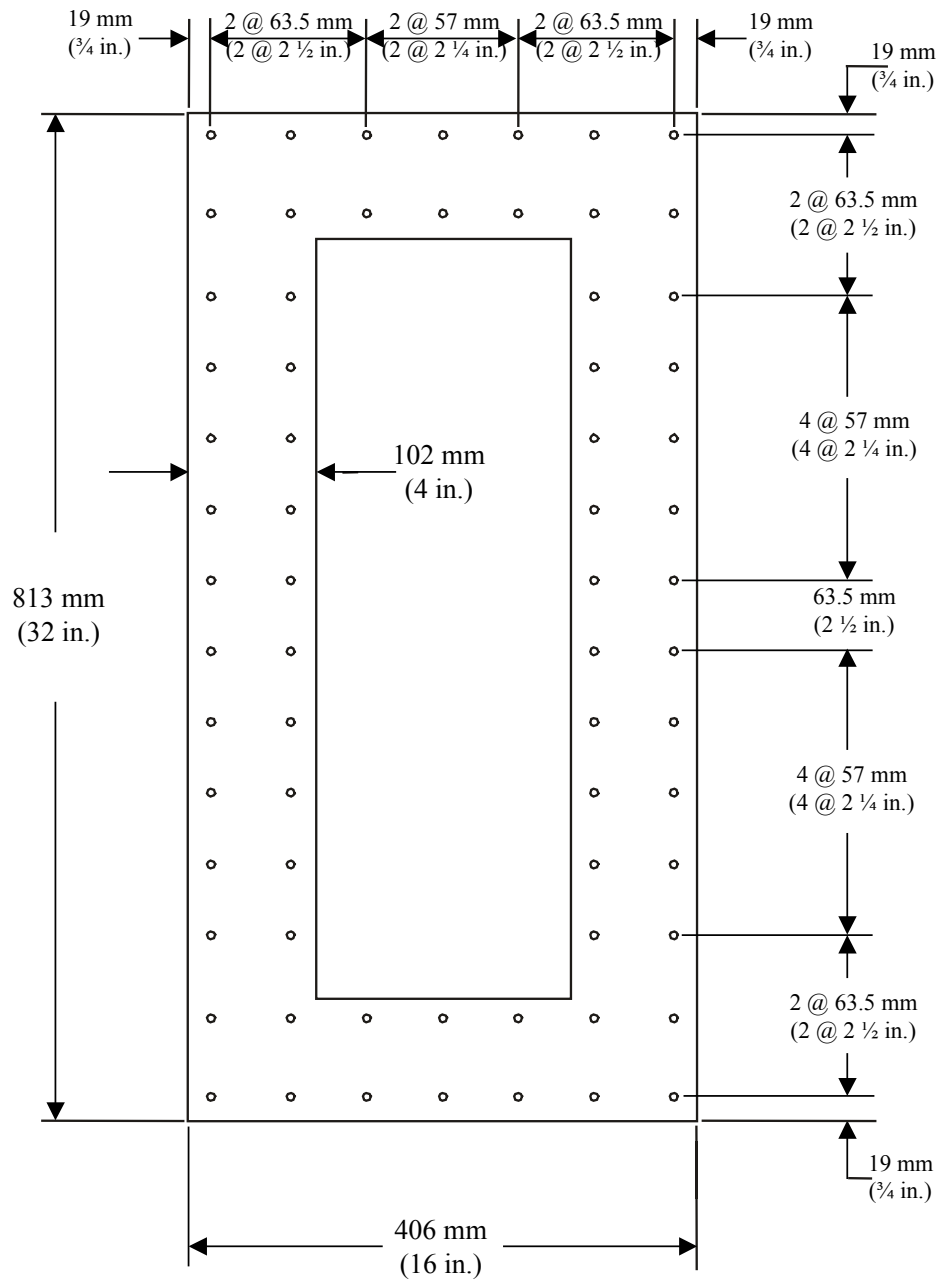


Figure 4.3 Cross-Section of Specimen P6

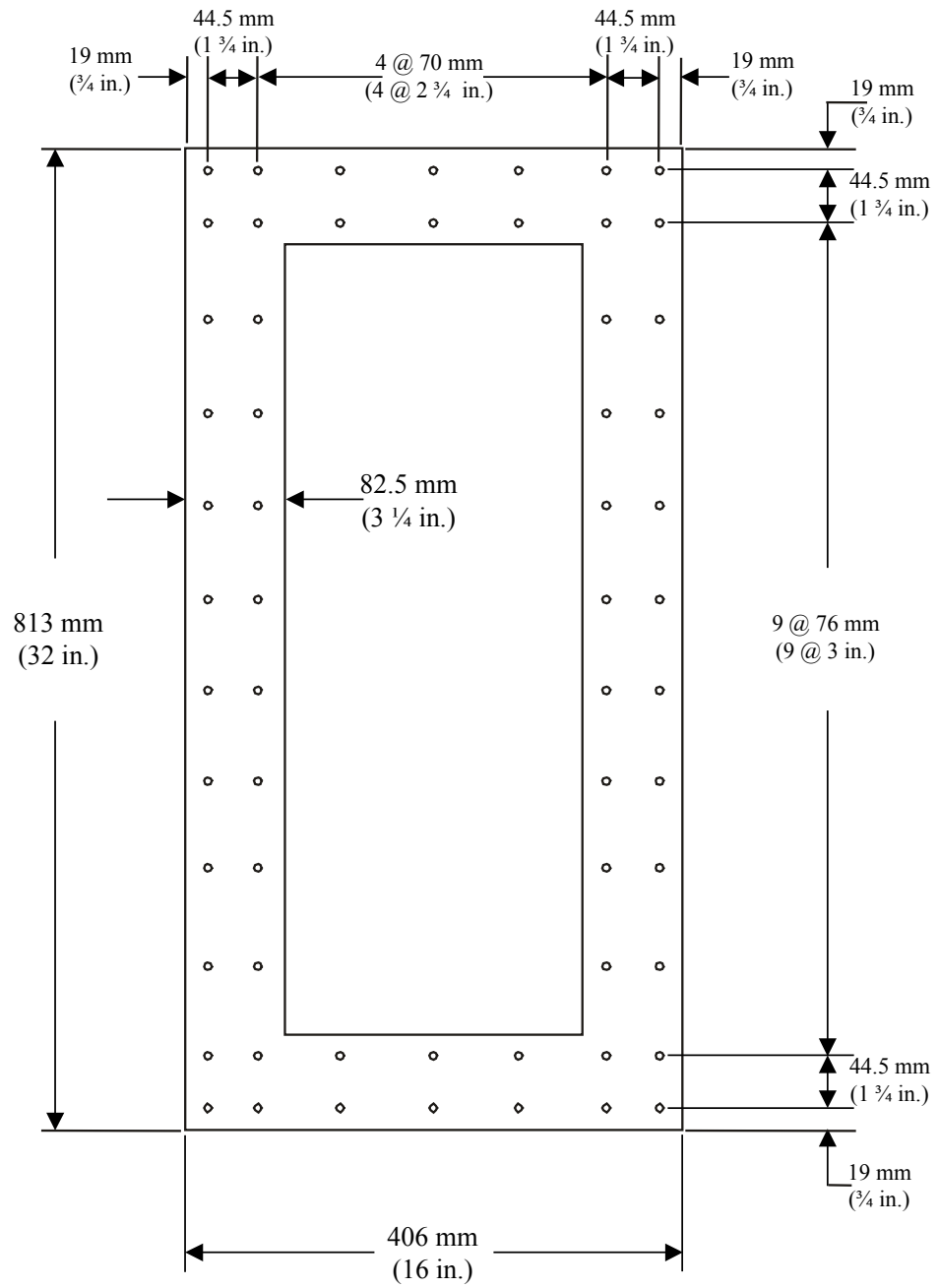


Figure 4.4 Cross-Section of Specimen P8

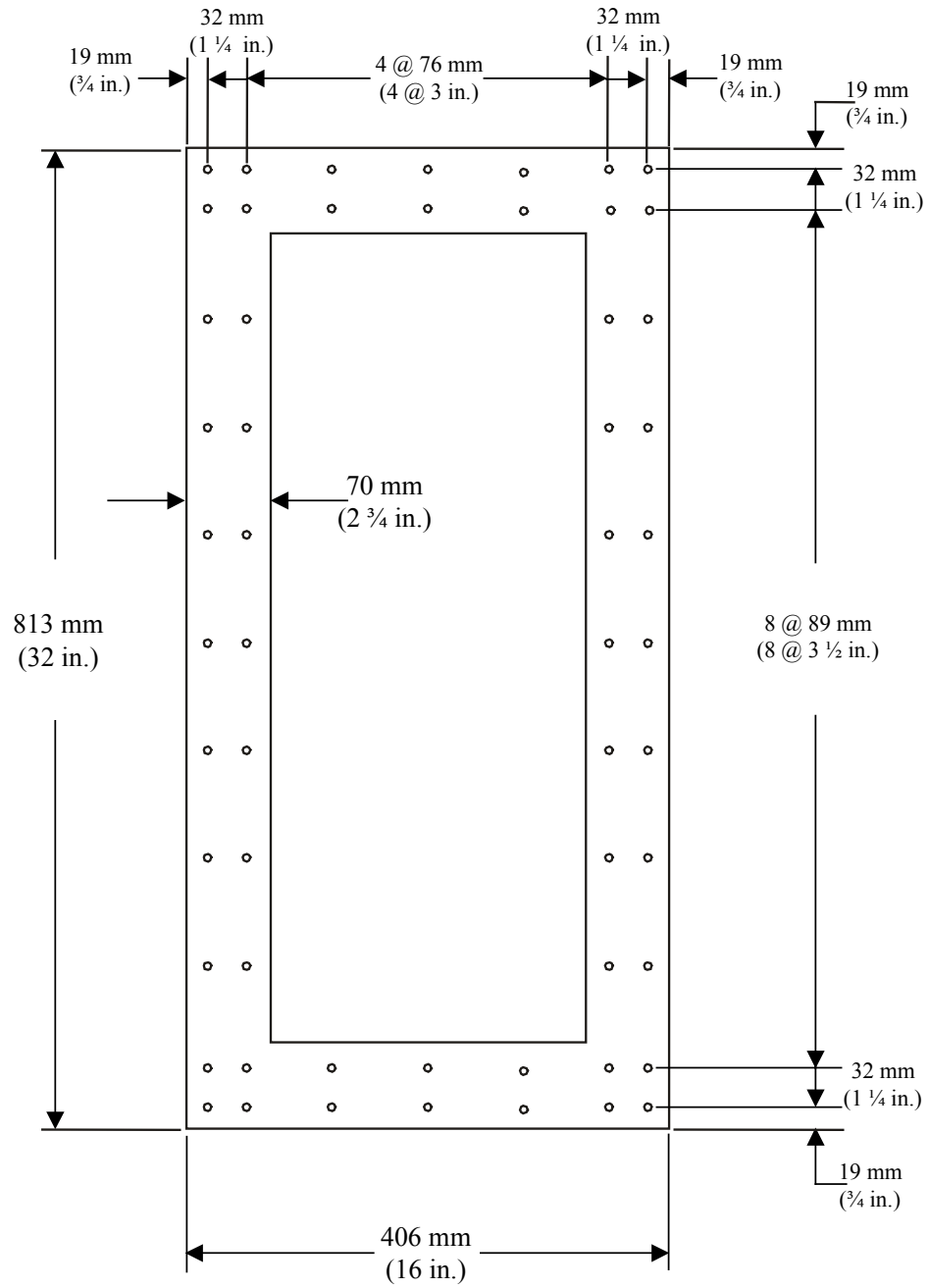


Figure 4.5 Cross-Section of Specimen P10

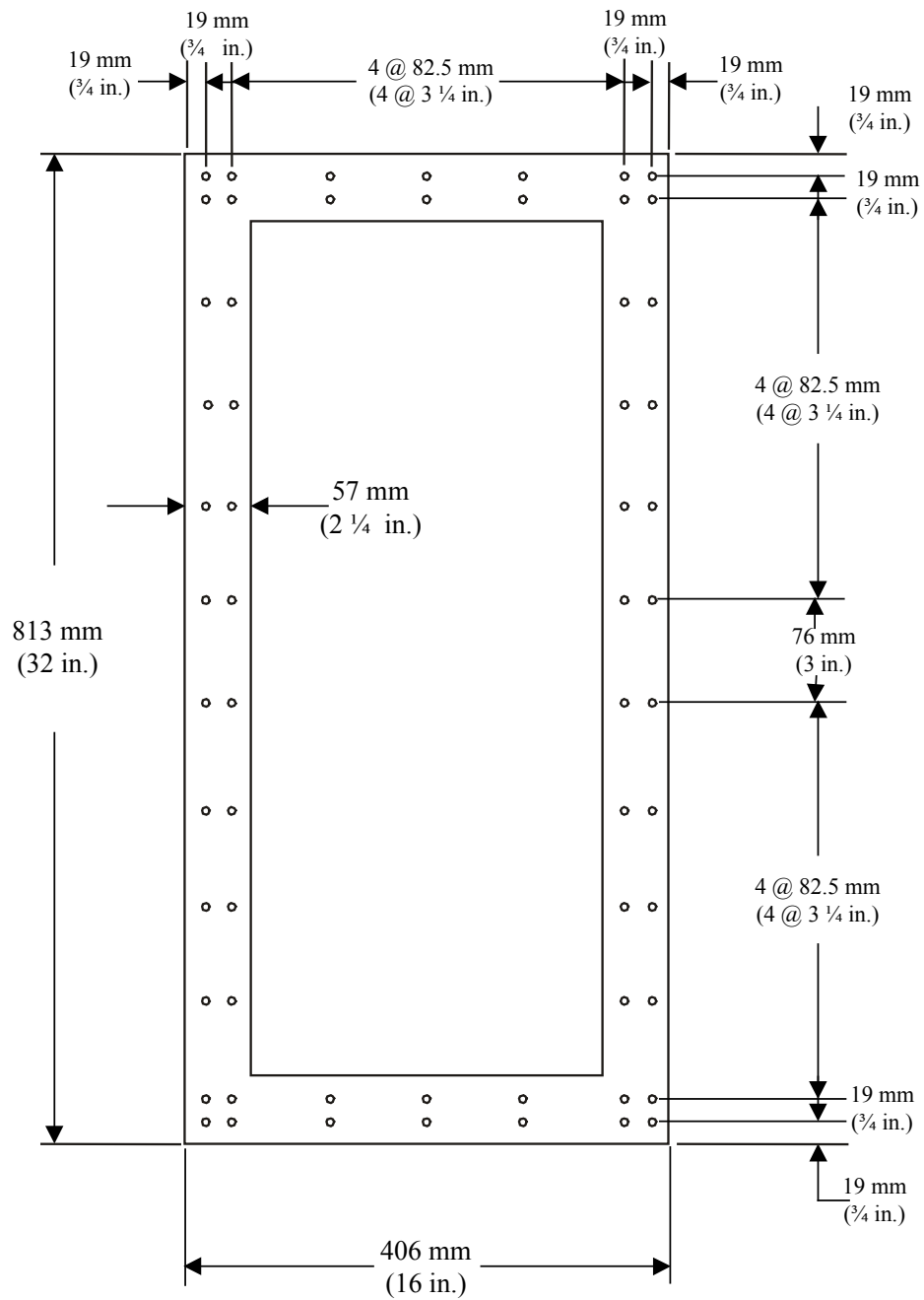


Figure 4.6 Cross-Section of Specimen P12

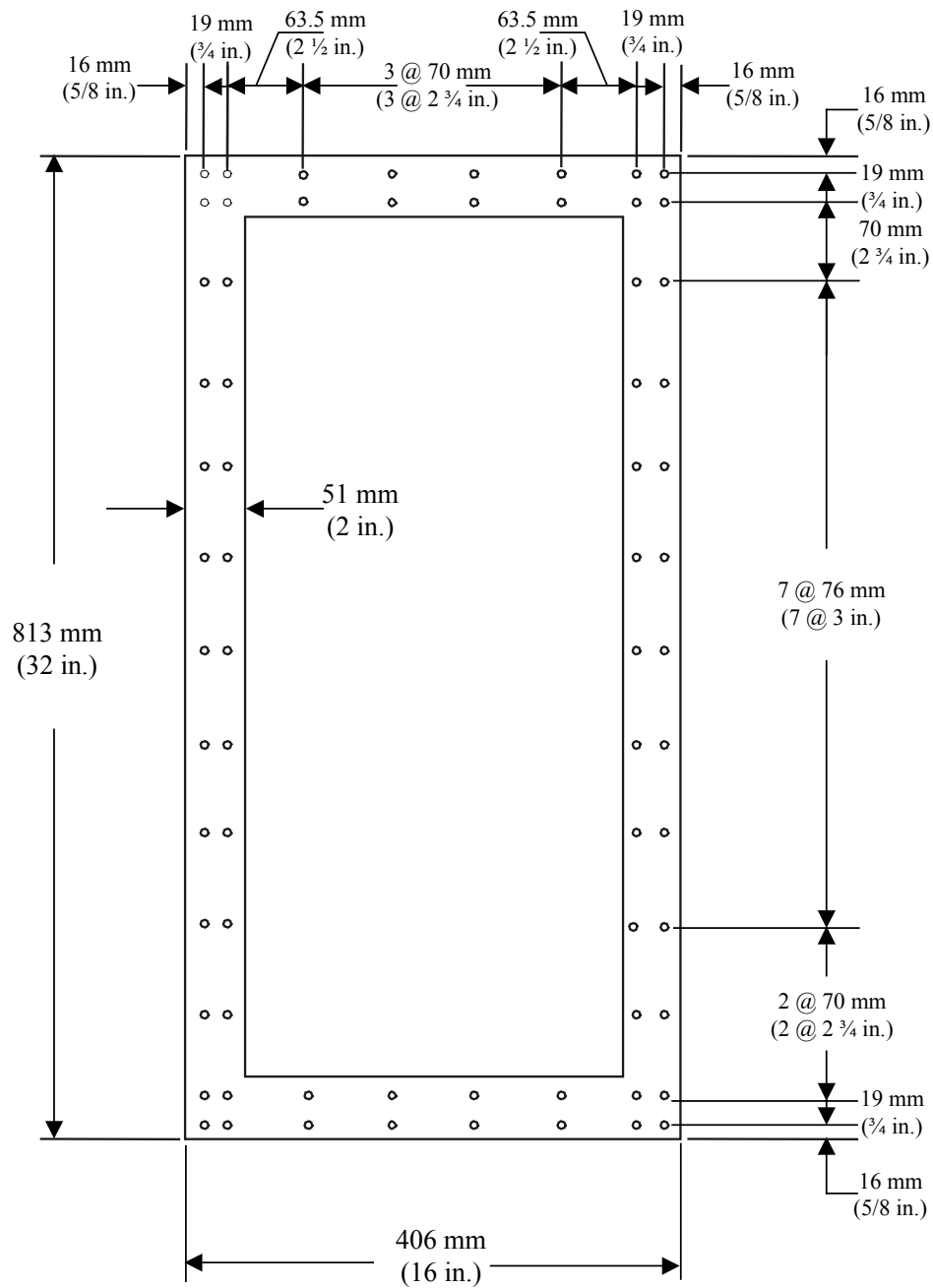


Figure 4.7 Cross-Section of Specimen P14



Figure 4.8 Hairpins at Corner

Cross-ties through the thickness of the walls were provided in a checkerboard pattern. Instead of using cross-ties with a 90 degree hook at one end and a 135-degree hook at the other, U-shaped cross-ties were used to ensure that the space between the two curtains of reinforcement was free of obstructions when casting the concrete. As discussed in Chapters 5 and 6, the U-shaped cross-ties confine the concrete enclosed by the transverse reinforcement, and provided lateral support for the longitudinal reinforcement. White nylon cable ties were used to tie the transverse reinforcement to the longitudinal bars.

A typical cross-tie and a nylon cable tie used to tie the horizontal reinforcement to the longitudinal bars are shown in Fig. 4.9. The checkerboard pattern for placing the cross-ties is shown in Fig. 4.10.



Figure 4.9 Typical Cross-Tie



Figure 4.10 Checkerboard Pattern Distribution of Cross-Ties

4.3 MATERIALS

The measured properties of concrete and reinforcing steel, and procedures for measuring these properties are reported in Appendix A.

4.3.1 Concrete

Concrete was purchased from a local ready-mix plant. The compressive strength of the concrete used to construct the hollow piers varied from 27 to 43 MPa (3900 to 6200 psi), with an average of approximately 34 MPa (5000 psi). The compressive strength of the concrete of the top and bottom end blocks varied from 30 to 50 MPa (4300 to 7200 psi), with an average of approximately 37 MPa (5300 psi).

4.3.2 Reinforcement

(a) Longitudinal Reinforcement

Six-mm deformed bars (equivalent to #2 bars), imported from Sweden, were used as the longitudinal reinforcement in all the five specimens. The average yield stress was 510 MPa (74 ksi).

(b) Transverse Reinforcement

Transverse reinforcement was fabricated using No. 10 gage, smooth wire, with 3.4 mm (0.135 in.) diameter. The average yield stress was 600 MPa (87 ksi).

(c) Reinforcement of End Blocks

Twelve-mm deformed bars (#4 bars) were used as reinforcement in the top and bottom end blocks. The average yield stress was 490 MPa (71 ksi).

4.4 FABRICATION OF SPECIMEN

4.4.1 Construction Method

The five specimens were fabricated using the same type of formwork. Exterior formwork consisted of 13-mm ($\frac{1}{2}$ -in.) Plexiglas sheets reinforced with 2 x 4 in. lumber spaced at 300 mm (12 in.) on center. The same set of exterior forms (Fig. 4.11), was used to build the specimens. Interior formwork consisted of a block of Styrofoam cut to the dimensions needed to obtain the desired thickness of the walls of the hollow specimen. The bottom end block was cast within a box form. The top end block was cast within a box supported by a wooden frame.

The first stage of the construction of a specimen was building the bottom end block. The reinforcing cage for the bottom end block was fabricated using 12-mm (#4), Grade 60 steel bars. Figure 4.12 shows the reinforcing details for the bottom and top end blocks, and Fig. 4.13 shows the reinforcing cage for the bottom end block placed within the forms. Coil loop inserts were placed in the sides of the bottom end block to be used to lift the specimen for transportation. Also, coil inserts were placed on the bottom of the bottom end block. A spherical bearing was attached to the specimens using these inserts prior to testing.



Figure 4.11 Transparent Exterior Forms

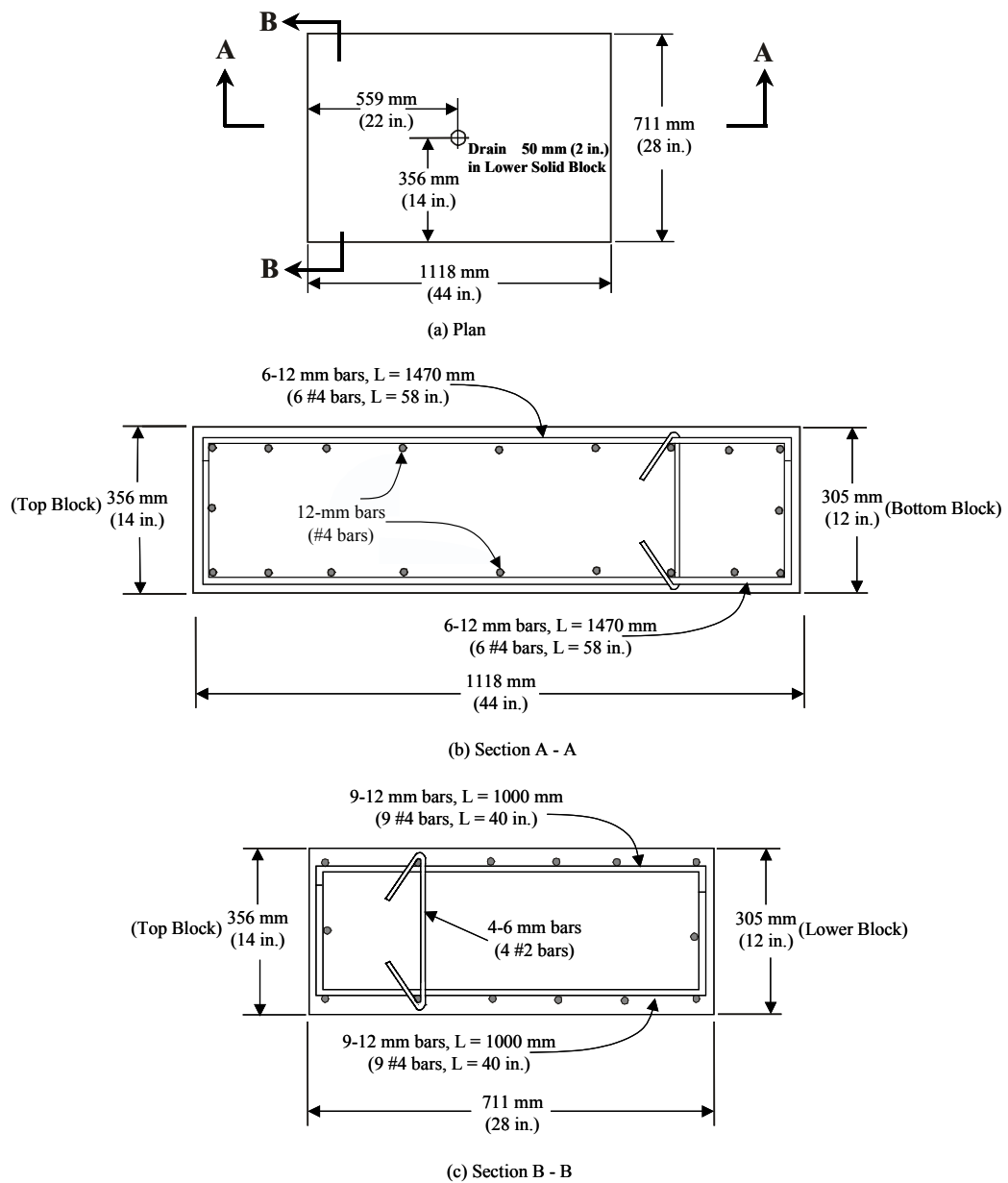


Figure 4.12 Reinforcing details of the Top and Bottom End Blocks



Figure 4.13 Reinforcement Cage of Bottom End Block

The reinforcing cage for the hollow piers was anchored in the bottom block; therefore, the cage had to be assembled before the concrete in the bottom block was cast.

The reinforcing cages were built in four separate layers using guides to ensure the correct spacing of the longitudinal bars. Nylon cable ties were used to tie the horizontal reinforcement to the longitudinal bars. Figure 4.14 shows a layer of longitudinal bars being assembled for Specimen P8. Later, each layer was placed within the bottom block forms and tied to the reinforcing cage. Figure 4.15 shows the 6-mm (#2) bars used as guides to align the layers of steel within the bottom steel cage. The longitudinal reinforcement was embedded at least 285 mm (11.25 in.) in the end blocks.

Using wooden braces of adjustable length, as shown in Fig. 4.16, the reinforcement for the hollow pier specimens was straightened into a vertical position. Then the concrete in the bottom end block was cast.



Figure 4.14 Process Used to Build the Curtains of Longitudinal Reinforcement



Figure 4.15 Alignment of the Longitudinal Reinforcement



Figure 4.16 Bracing System Used to Align Vertically the Longitudinal Reinforcement

Next, the pier formwork was assembled. The interior Styrofoam form, coated in a layer of black PVC plastic, was inserted from the top of the longitudinal reinforcing cage. To give the Styrofoam a stable base, sand was placed on top of the bottom end block. Silicone sealant was used to seal the gap under the Styrofoam so the sand could not absorb the water from the concrete. The exterior forms were placed on top of neoprene pads. Figures 4.17 and 4.18 show the steps described above.



Figure 4.17 Sand and Neoprene Pads Used as Support for the Pier's Formwork



Figure 4.18 Exterior Forms on a Pier

Wooden spacers (Fig. 4.19) were tied to the steel cage to maintain the spacing between the formwork and the steel reinforcement and between the interior and exterior layers of steel. Two spacers were placed for every 0.5 m² (5 ft²) of wall area. The concrete was placed from the top, between the two layers of steel, as described in Section 4.5.2.2. Only one specimen was cast at a time.



Figure 4.19 Spacer Used to Separate Exterior and Interior Forms

After three days, the exterior forms were removed and the interior form was dissolved using gasoline. The melted Styrofoam drained out of the specimen through a 50-mm (2-in.) PVC tube cast in the bottom end block.

The top end block was built during the last stage of construction. A wooden frame (Fig. 4.20) was built around the hollow pier, with the box framework sitting on top of it. Figure 4.21 shows the flat bottom of the forms of the top end block. From that photograph the longitudinal reinforcement of the

hollow pier projected into the top end block, so no lap splices were required along the height of the specimens. Coil loop inserts were placed in the top end block to lift the specimen and to attach a top bearing plate.



Figure 4.20 Top End Block Forms

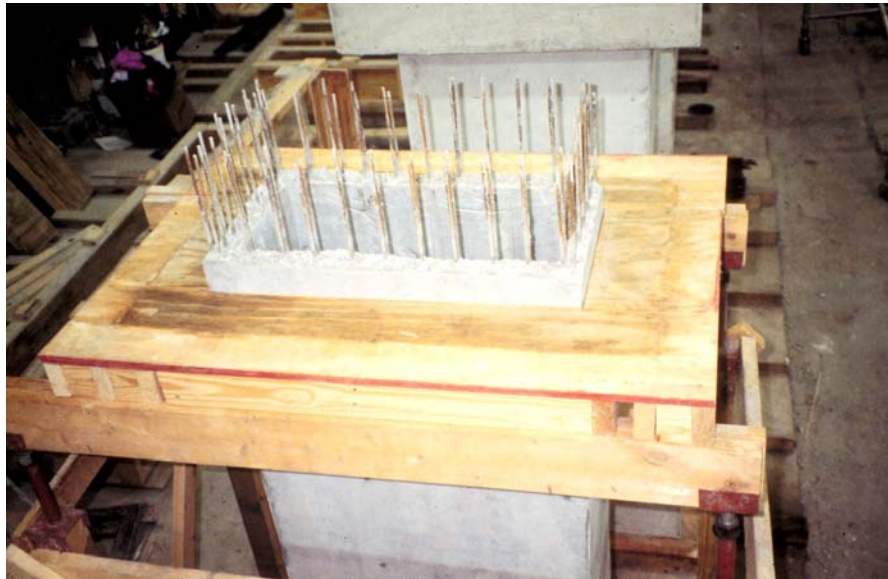


Figure 4.21 Bottom Forms of Top End Block

4.4.2 Placing of Concrete

4.4.2.1 Consolidation

The consolidation of concrete in tall, thin walls was carefully considered at the beginning of the test program, and sample walls were constructed to test various consolidation methods. The best consolidation was obtained by combining several procedures. First, concrete mixes with high slumps of 150 to 250 mm (6 to 10 in.), were used. Second, obstructions between the two layers of longitudinal reinforcement in the walls were minimized. The cross-ties did not have a 135-degree hook at the end so the concrete could fall freely between the layers of longitudinal reinforcement and the vibrator could reach all parts of the walls. Third, the walls were cast using four lifts of, 450 mm (18 in.). Fourth, a vibrator with a 1.8-m (6-ft) long flexible shaft (diameter of 19 mm ($\frac{3}{4}$ in.)) was

used, allowing the vibrator to reach the bottom of the walls (the minimum clear distance between layers of longitudinal reinforcement was 25 mm (1 in.)). Fifth, the transparent exterior forms permitted visual monitoring of the consolidation process and helped to fill the walls uniformly. Finally, the concrete was cast slowly to prevent the freshly cast concrete from plugging the gaps between the layers of reinforcement.

4.4.2.2 Curing and Form Removal

The same curing methods were used for all specimens. The end blocks were cured at least three days with wet burlap. The hollow piers were cured by leaving the Plexiglas forms in place for three or four days. In all cases the concrete cylinders were removed from their molds on the same day that the burlap was removed from the fresh concrete.

4.4.3 Pier Dimensions and Wall Thicknesses

The exterior dimensions of the hollow piers were measured before the tests. Except for Specimen P6, the maximum error in the length of the longer walls was 3 mm (1/8 in.) or approximately 0.5% of the nominal length, and the maximum error for the shorter walls was 2 mm (1/16 in.) or approximately 0.5% of the nominal length.

While casting the concrete for Specimen P6, the forms along the shorter sides of the specimen distorted, leading to bulging of the short walls. The maximum measured dimension of the long wall for Specimen P6 was 838 mm (33 in.) near the bottom of the pier. This dimension decreased nearly linearly to 813 mm (32 in.) at the top of the specimen.

To measure the actual thickness of the walls and the actual cover of the longitudinal reinforcement, 100-mm diameter (4-in.) cores were drilled in the hollow piers after the tests. At least three cores were drilled through each wall subjected to compression, and at least 2 cores were drilled through the longer wall subjected to tension. Figure 4.22 shows average wall thicknesses and the nominal thickness $\pm 10\%$ of the compression walls. The thicknesses of all but two of the walls subjected to compression are within expected values, with maximum variation of 5% of the nominal thickness (approximately 3 mm (1/8 in.)). The actual thickness of the shorter wall subjected to compression in Pier P6 was 13 to 25 mm (1/2 to 1 in.) larger than the nominal thickness of the wall. The actual thickness of the shorter wall subjected to compression wall of Specimen P14 was 5 mm (0.2 in.) larger than the nominal thickness of 51 mm (2 in.), a 10% increase.

The construction tolerances recommended in ACI 117 (1990) are +12 mm (+1/2 in.) and -10 mm (-3/8 in.) for walls 300 mm (12 in.) thick or more, and +10 mm (+3/8 in.) and -6mm (1/4 in.) for walls less than 300 mm (12 in.) thick. Scaled down, only the wall thicknesses of Specimens P8, P10 and P12 were within recommended tolerances.

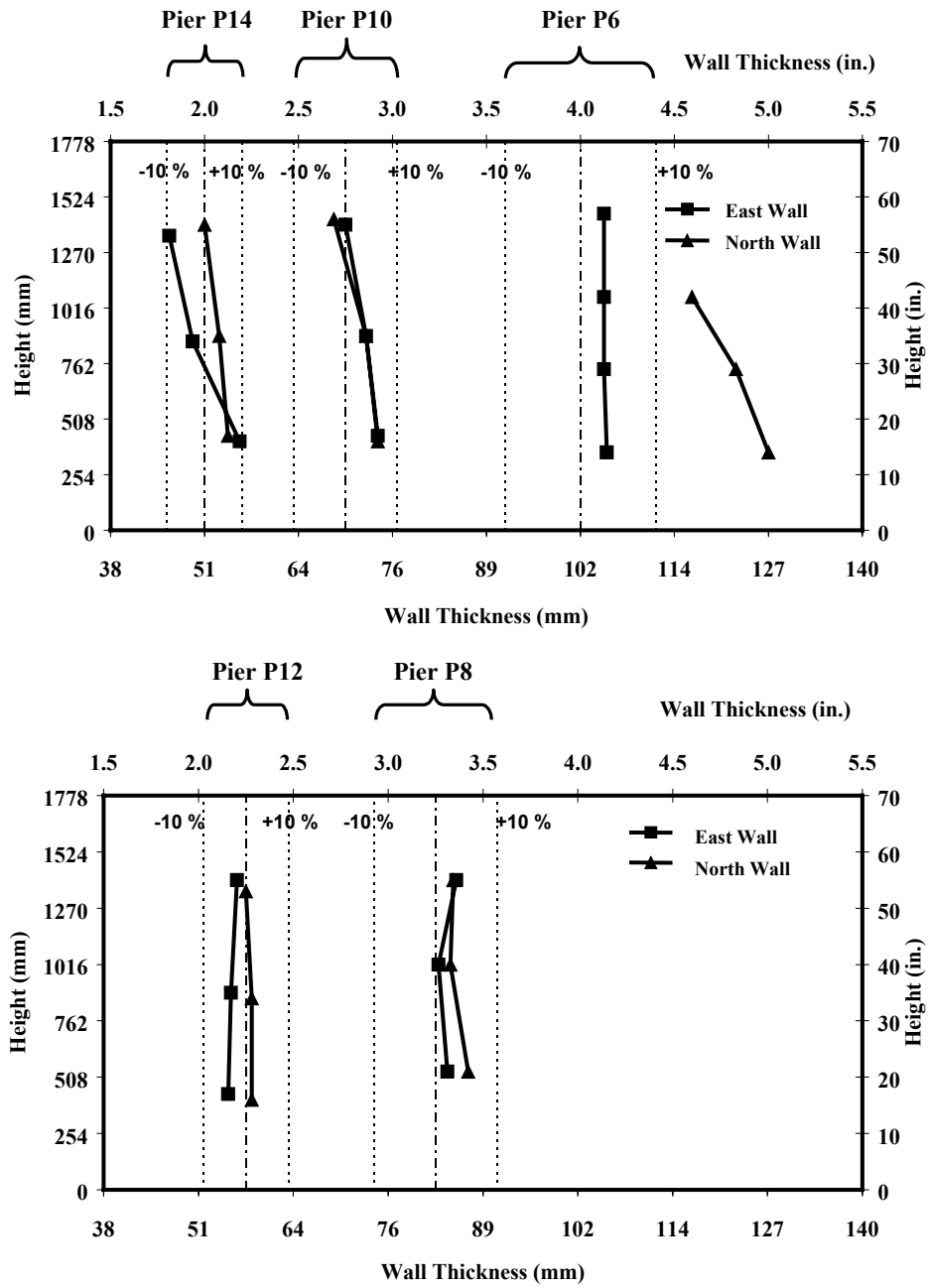


Figure 4.22 Measured Thickness of Walls Subjected to Compression

The cores were also used to measure the concrete cover to the reinforcement and the separation between the longitudinal curtains of steel. The measured separation of the two curtains of reinforcement was 2 to 3 mm (1/16 to 1/8 in.) smaller than the design separation (5% to 8% of the design separation), which was considered acceptable.

The measured cover varied depending on the actual thickness of the walls and positioning of the reinforcing cage. In most cases the actual cover did not exceed the design cover by more than 2 mm (1/16 in.). Specimen P6 had larger exterior cover along the shorter walls due to the observed bulging of those walls. In Specimens P10 and P12, the exterior cover was 6 mm (1/4 in.) more than planned along the longer tension side due to a combination of slightly increased wall thickness and offset of the reinforcing cage with respect to the center of the wall.

4.5 LOADING ARRANGEMENT

4.5.1 Loading Method

The specimens were subjected to axial compression applied at the following nominal eccentricities: 102 mm (4 in.) about the weak axis (25% of the short cross-sectional dimension) and 305 mm (12 in.) about the strong axis direction (38% of the long cross-sectional dimension). The specimens were loaded with a fixed eccentricity, following the loading path shown in Fig. 4.23.

To produce a uniform moment distribution along the length of the piers, both ends were free to rotate about the strong and the weak axis simultaneously.

Spherical plate bearings were used at the top and bottom of the test specimens to allow this rotation.

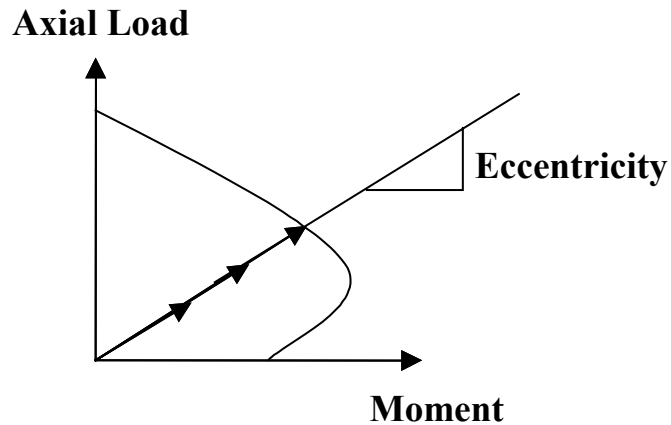


Figure 4.23 Loading Path for all Specimens

4.5.2 Loading Apparatus

The loading apparatus consisted of a steel reaction frame anchored to the laboratory strong floor with four sets of four bolts each. Each bolt had a tensile capacity of 220 kN (50 kips), giving the reaction frame a capacity of 3,500 kN (800 kips). The specimens were aligned vertically under the frame, and the vertical load was applied using a 9,000 kN (2,000-kip) Prescon ram.

The loading apparatus is shown in Fig. 4.24 and 4.25. Figure 4.24 shows that to obtain the desired eccentricity the specimens were placed eccentric with respect to the ram. The north and east walls of the specimens were in compression.

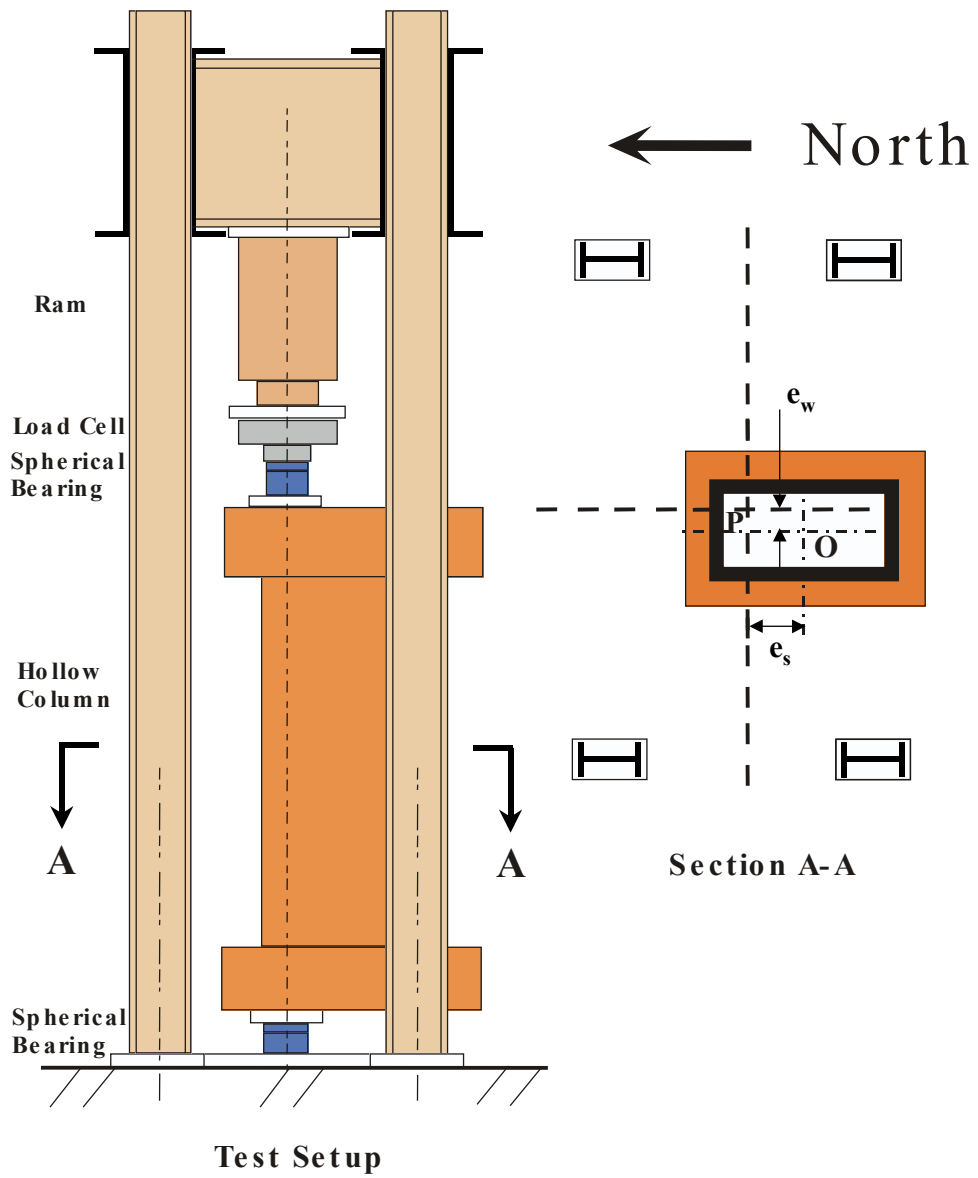


Figure 4.24 Test Setup



Figure 4.25 Loading Apparatus

4.5.3 Spherical Bearings

To provide pinned conditions at the ends of the specimens, steel spherical bearings were used at the point of application of the load and at the reaction point on the floor. In this way, the application of additional bending moments at the ends of the specimen was avoided and a uniform distribution of moment was obtained along the height of the specimen.

To better distribute the load, a 50-mm (2-in.) thick steel plate was placed between the spherical plate and each end concrete block. A thin layer of hydrostone was placed under the steel plate on the top end block to level the steel plate. Graphite was used to ensure free movement of the spherical bearings.

The bottom part of the spherical bearing used to support the piers at the bottom end blocks (Fig. 4.26) was concentric with the ram. The bearing was then fixed in position by welding it to a steel plate that was previously bolted to the reaction floor. In this way the ram and the bottom spherical bearing could later be used as references to align the piers and to measure the actual eccentricities of the load applied to them.

Figures 4.26 and 4.27 show the spherical bearings and the 50-mm (2-in.) steel plates bolted to the top and bottom end blocks to transfer the loads from the steel bearings to the blocks.



Figure 4.26 Spherical Bearing at Bottom End Block



Figure 4.27 Spherical Bearing at Top End Block

4.6 INSTRUMENTATION

Measured responses from the instrumentation are presented in Appendix B in the form of load-displacement curves.

4.6.1 Load

The load was applied vertically to the top of the specimen by a 9,000-kN (2,000-kip) hydraulic ram reacting against the loading frame. The load was measured using a Strainsense load cell, with a capacity of 4,500-kN (1,000-kip), connected to the data acquisition system. The load cell was calibrated 10 months before the tests began. The hydraulic pressure was monitored visually using a dial pressure gage at the pump.

4.6.2 Displacements

Displacements were measured using linear displacement potentiometers with a range of 50 mm (2.0 in.) and linear transducers with a stroke of 12.7 mm (0.5 in.). Three types of displacements were measured: horizontal displacements to measure the profile of the walls in compression; vertical displacements to determine the rotations of the end blocks and the axial shortening of the specimens; and horizontal displacements to monitor lateral displacements of the top end block.

The profile of the walls in compression was measured using three rows of linear potentiometers (Fig. 4.28). The rows were located 380 mm (15 in.) above the bottom end block, at the middle height of the pier and 380 mm (15 in.) below the top end block. Five instruments in each row were used along the east walls and three instruments per row in the north walls, giving a total of 24 linear potentiometers to measure the profile of the compression walls (east and north walls). The linear potentiometers were mounted on a frame that was independent of the specimen, so that the absolute displacements of the walls could be measured. The notation used to identify the linear potentiometers is also shown in Fig. 4.28. Figure 4.29 shows the linear potentiometers used to monitor the east compression wall before testing.

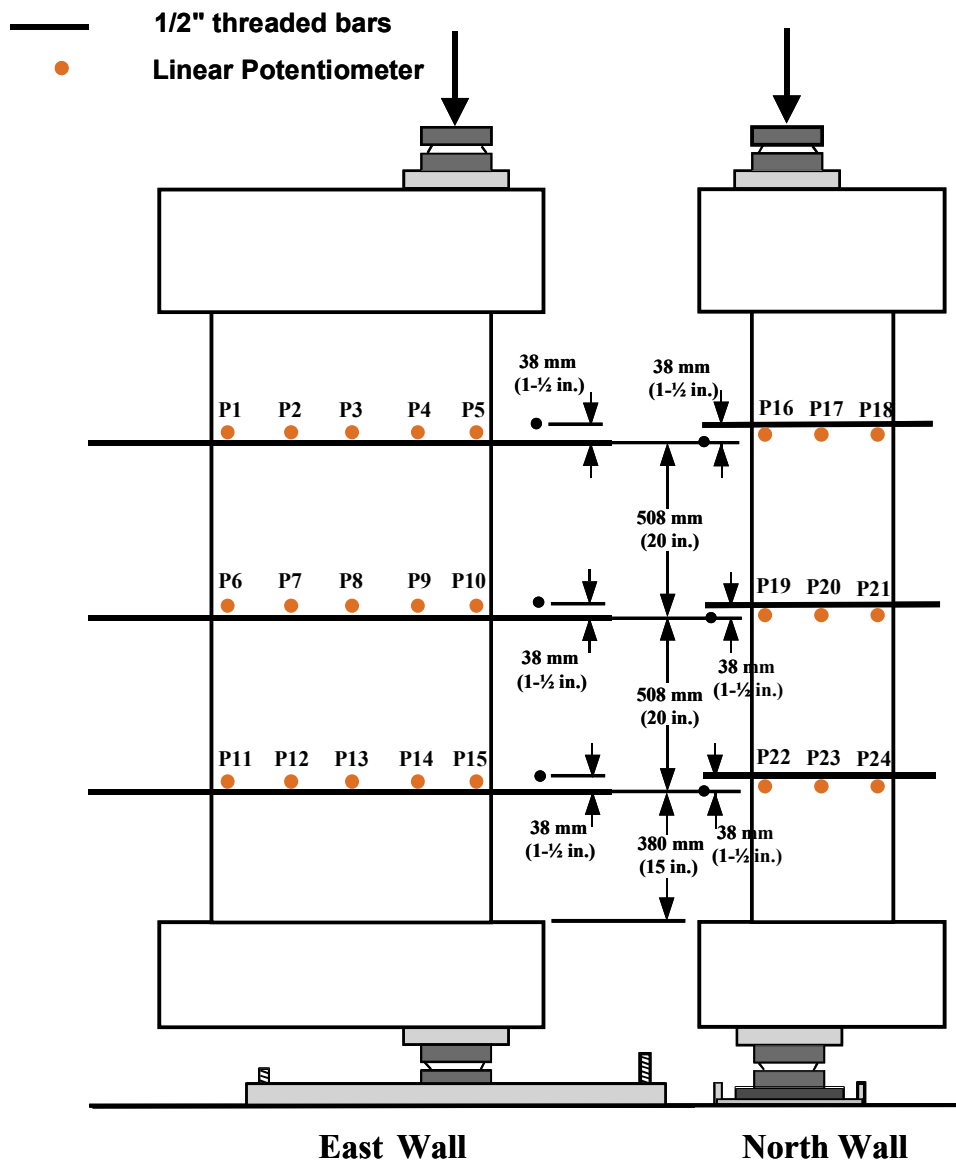


Figure 4.28 *Distribution of Linear Potentiometers used to Measure the Profile of the Walls in Compression*

The rotation of the bottom end block was determined using data from linear displacement potentiometers that measured the vertical displacement of three points of the bottom of the end block with respect to the floor. The rotation

of the top end block was determined by measuring the vertical displacement of three points on the top with respect to a steel plate that was supported independently from the test frame as shown in Fig. 4.30. Figure 4.31 shows a plan view of the top end block and the position of the linear potentiometers used to measure the vertical displacements of the end block.

The code used to identify the linear potentiometers is also shown in Fig. 4.31. TS, TW and TC correspond to the linear potentiometers used in the top end block and located at the south side, at the west side and at the center of the end block respectively. The corresponding linear potentiometers used to measure the bottom end block are identified as BS, BW and BC.



Figure 4.29 Linear Potentiometers to Measure Wall Profile Before Test

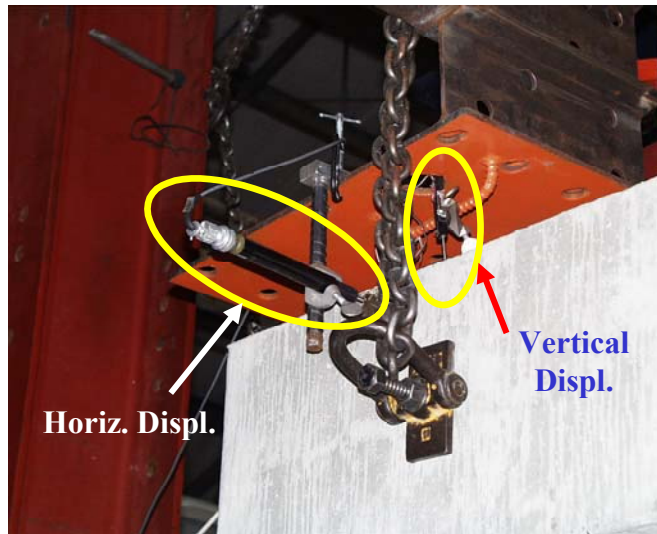
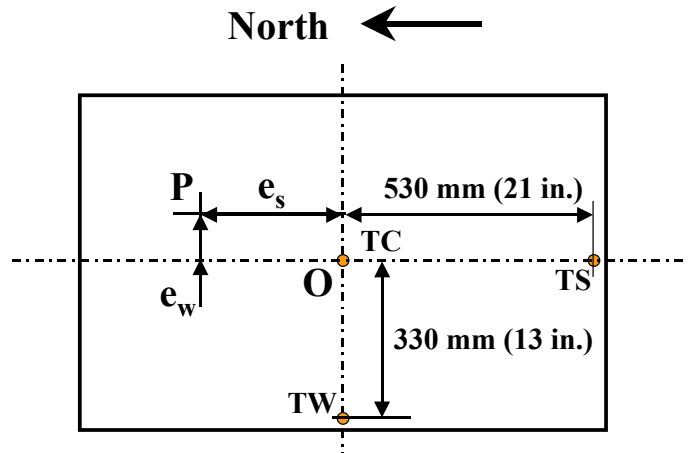


Figure 4.30 Steel Plate Used as Reference to Measure Vertical Displacements of Top End Block



- P = point of application of the compression load
- O = geometric center of the hollow pier
- e_s = eccentricity in north-south direction
- e_w = eccentricity in east-west direction
- = linear potentiometers (TC, TS, TW)

Figure 4.31 Plan View of the Top End Block with the Location of the Linear Potentiometers used to Measure Vertical Displacements of Both End Blocks

The lateral displacements of the top end block were measured in two orthogonal directions using two Trans-Tek linear displacement transducers with a range of 12.7 mm (0.5 in.), last calibrated in September 1998: one located near the center of the west side of the end block and the other near the center of the south side of the end block. Figures 4.32 and 4.33 show the location of both linear transducers and the code used to identify the instrument readings.

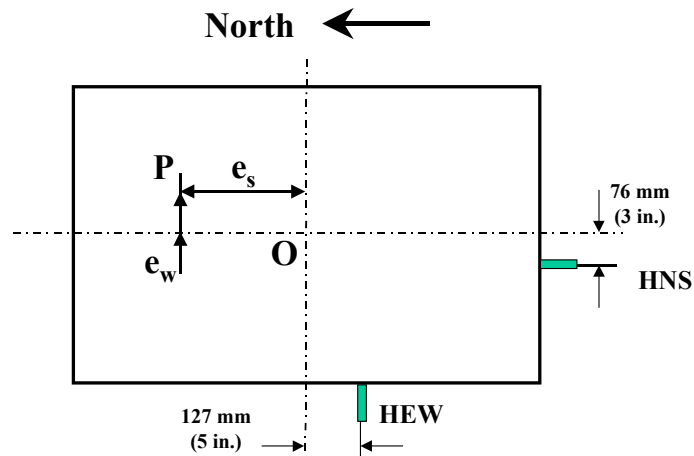


Figure 4.32 Plan View of the Top End Block with the Location of the Instruments used to Measure Horizontal Displacements



Figure 4.33 Linear Transducers (Black Instruments) Used to Measure Lateral Displacement of the Top End Block

4.6.3 Curvature

Curvature was measured in two perpendicular directions along the walls in tension (west and south walls): in the north-south and in the east-west directions. Three aluminum plates were bolted to each wall as shown in Fig. 4.34 and Fig.4.35. Patriot linear motion transducers with a range of 50 mm (2.0 in.) were attached to the ends of the top and bottom aluminum plates and a steel leader was tied from each linear transducer and to the center aluminum plate. Two measurements of curvature were obtained for each direction of bending. For Specimens P6 and P8 it was not possible to take curvature measurement at the top

of the south wall because two transducers were not working at the time of the tests. Figure 4.35 also shows the code used to identify the readings from the instrumentation.



Figure 4.34 Instrumentation Used to Measure Curvature

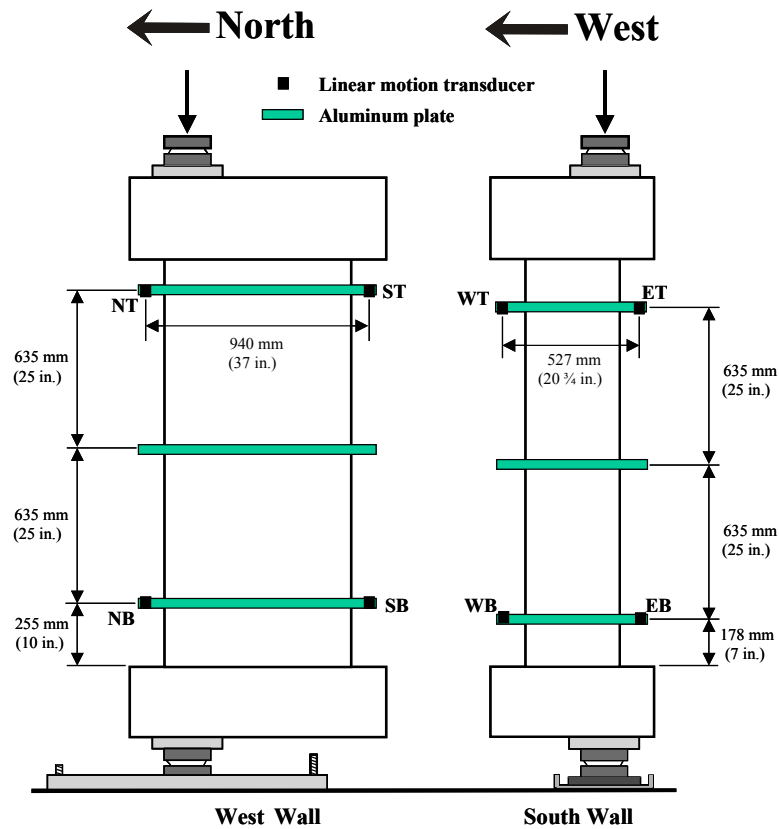


Figure 4.35 Location of the Linear Motion Transducers used to Measure Curvature Along the Walls of the Specimens

4.6.4 Data Acquisition System

A Hewlett Packard HP 75000 Series 8 system was used to acquire the data from the load cell, linear potentiometers, and linear transducers. The data acquisition system was programmed to collect data every 3 to 4 seconds; therefore even if failure occurred as the load was being applied, the maximum load was captured. However, it was not possible to record the post-peak response.

4.7 TEST PROCEDURE

4.7.1 Transportation of Specimens

The specimens were cast and stored at the north end of the laboratory, while the tests were conducted at the south end. The specimens were transported using a forklift. Steel angles were bolted to the sides of the bottom end block and provided a platform for the forklift (Fig. 4.36).

4.7.2 Alignment of Specimens

The specimens were placed within the loading frame using the same forklift used for their transportation. The piers were then supported by the bottom spherical bearing and by two screw jacks. One of the screw jacks can be seen in Fig. 4.26. To align the pier vertically (plumb), the screw jacks were used to rotate the pier about the spherical bearing until the walls were vertical. Center lines drawn on the walls of the piers were used to ensure the alignment of the specimens. When the four centerlines were vertical, the piers were judged to be plumb.



Figure 4.36 Transportation of a Specimen

4.7.3 Measurement of Eccentricities

The actual eccentricities were measured after the piers were aligned. The eccentricities at the top were measured between a point marked at the center of the top end block and the center of the ram (the point of application of the load). The eccentricities at the bottom were measured between a point marked at the center of the bottom end block and the center of the bottom spherical bearing (the point where the pier was going to be supported).

4.7.4 Loading of Specimens

Each specimen was loaded to failure according to the following procedure. First, the instruments were initialized. Then the specimens were loaded to 67 kN (15 kips) and the screw jacks were removed. The actual load was scanned and

then the instruments were again initialized. (The last step was skipped during testing of Specimen P6.) The specimens were first loaded to 180 kN (40 kips), and then they were loaded in 180-kN (40-kip) increments. The instruments were scanned every 3 to 4 seconds. After each load increment, the load was held and the specimens were checked for cracks or crushing. While holding the load, the instruments were scanned every 1 to 2 minutes.

The total time need to test the specimens varied from 3 hours to 4 hours and 40 minutes. The rate of loading varied between 20 and 90 kN/min (5 and 20 kip/min), with an average of 45 kN/min (10 kip/min). Between 5 and 15 minutes were needed to take pictures and mark cracks between each loading increment.

Four specimens failed while being loaded. Specimen P14 failed seconds after the valve from the pump was closed at the end of a loading increment.

Chapter 5 Experimental Results

The results of the five experiments are presented and discussed in this chapter. The measured responses of each of the specimens are described first, and then the responses of the five specimens are compared.

The geometric and material properties of the five specimens are summarized elsewhere (Tables 3.1, A.1, A.2 and A.3). Table 5.1 contains important information about the physical tests of the five hollow pier tests. The failure load varied between 1960 and 2670 kN (440 and 600 kips). In general, the failure load decreased as the wall thickness decreased. However, Specimen P8 failed at an applied axial load that was less than the failure loads for Specimens P10 and P12, because the concrete used to construct Specimen P8 was lower in strength.

Table 5.1 Summary of Experimental Tests

Spec. ID	Actual Slenderness Ratio λ_w	Date of Test	Duration of test	Concrete Compressive Strength MPa (psi)	Strong-axis Eccentricity mm (in)	Weak-axis Eccentricity mm (in)	Observed Failure Load kN (kips)
P6	5.70	05-07-1999	4 hrs 35 min	26.9 (3900)	298 (11 3/4)	95 (3 3/4)	2670 (600)
P8	7.85	05-24-1999	3 hrs 45 min	27.4 (3970)	305 (12)	106 (4 3/16)	2050 (461)
P10	9.64	06-03-1999	4 hrs 40 min	35.1 (5090)	306 (12 1/16)	98 (3 7/8)	2370 (532)
P12	12.22	06-14-1999	3 hrs 20 min	42.3 (6130)	306 (12 1/16)	95 (3 3/4)	2280 (513)
P14	14.00	06-22-1999	3 hrs	42.7 (6200)	302 (11 7/8)	102 (4)	1960 (440)

The actual eccentricities were measured after the specimens were set in place, as described in Section 4.7.3, and before any load was applied. All specimens were positioned so that the actual eccentricities were within 6 mm (1/4 in.) of the nominal values and the ratios of weak-axis to strong-axis eccentricity varied between 0.31 and 0.35.

5.1 NOTATION AND PARAMETERS USED TO INTERPRET RESPONSE

Four parameters were used to interpret the response of the test specimens: (a) horizontal displacements of the hollow piers; (b) rotations of the end blocks; (c) axial displacements of the entire specimen; and (d) curvatures of the hollow piers. Procedures used to calculate each of these quantities and the sign conventions used to plot the results are discussed in this section. The raw data are presented in Appendix B.

As shown in Fig. 5.1, the axial load was applied near the northeast corner of the specimens. Therefore, the north and east walls were subjected to compressive stresses while the south and west walls were subjected to tensile stresses.

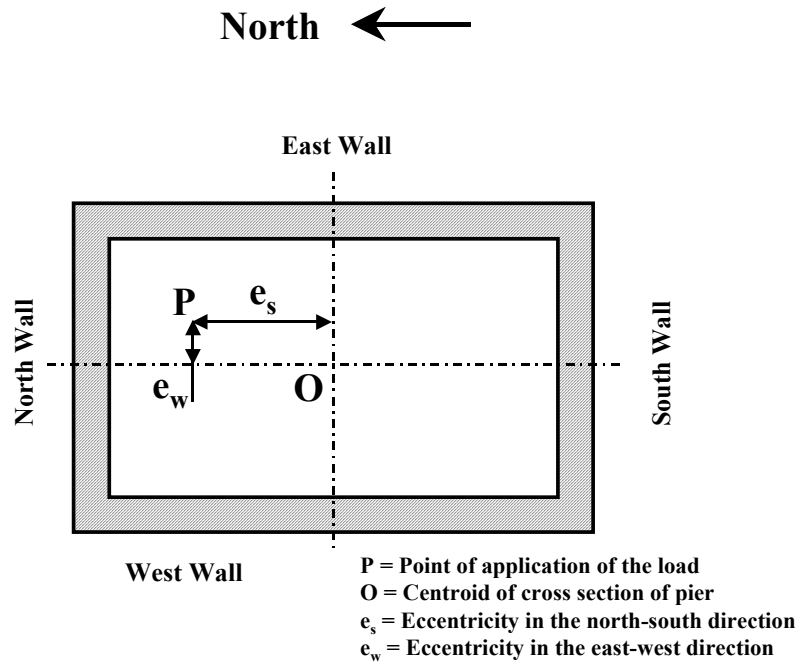


Figure 5.1 Identification of Walls within each Test Specimen

5.1.1 Horizontal Deflections

Horizontal deflections were measured at various locations along the north and east walls as described in Section 4.6.2. The raw data are presented in Section B.1. Four plots are used to characterize these data for each pier. The first two provide information about the longitudinal profiles of the piers in the north-south and in the east-west directions, respectively.

Data from instruments closest to the point of application of the load were used. Instruments P4, P9, and P14 were used to plot the profiles in the north-south direction and Instruments P16, P19, and P22 were used to plot the profiles in the east-west direction (Fig. 4.28). These profiles are presented at several load levels,

including immediately before failure. Positive deflections correspond to outward movement of the walls.

The third plot presents information about the relative movement of the east wall at mid-height of the pier. Readings from Instruments P6, P7, P8, P9, and P10 were used to generate these plots. As shown in Fig. 5.2, a line was drawn between the measured displacements at the north and south ends of the east wall. The horizontal displacements relative to this baseline are plotted. A positive sign indicates outward bowing of the wall.

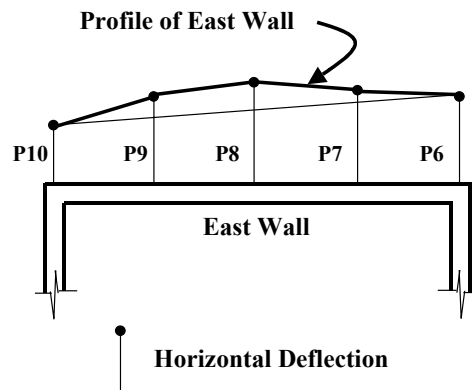


Figure 5.2 Definition of Profile of East Walls

The fourth plot presents information about the relative movement of the east wall measured along a vertical line located at the center of the east wall. Profiles like the one shown in Fig. 5.13(b) were generated using Instruments P1, P2, P3, P4, P5, P11, P12, P13, P14, and P15. The relative horizontal displacements calculated from Instruments P3, P8, and P13 are plotted. A positive sign indicates outward bowing of the wall.

5.1.2 Rotations of the End Blocks

The rotations of the end blocks were calculated using the vertical displacements measured at the center of the blocks (Section B.2) and at the edges of the blocks (Section B.3). If u_{TC} , u_{TW} , and u_{TS} are used to represent the vertical displacements measured by Instruments TC, TW, and TS at the top block (Fig. 5.3), then the rotations about the north-south and east-west axes are given by

$$\theta_{N-S} = \frac{u_{TC} - u_{TW}}{a} \quad (5.1)$$

$$\theta_{E-W} = \frac{u_{TC} - u_{TS}}{b} \quad (5.2)$$

where a and b are the horizontal distances between Instrument TC and Instruments TW and TS, respectively.

Similarly, the rotations of the bottom block about the north-south and the east-west axes were calculated as

$$\theta_{N-S} = \frac{u_{BW} - u_{BC}}{a} \quad (5.3)$$

$$\theta_{E-W} = \frac{u_{BS} - u_{BC}}{b} \quad (5.4)$$

The rotations were considered positive if the blocks rotated in the same direction as the moment applied to the piers. Figure 5.13 shows the direction of the positive rotation about the east-west axis and the direction of the positive rotation about the north-south axis of the end blocks.

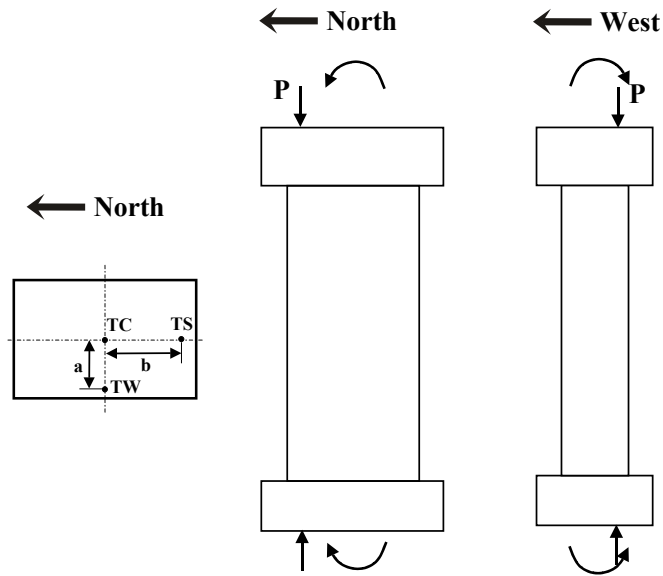


Figure 5.3 Definition of Rotations of End Blocks

5.1.3 Vertical Deflections

The vertical deflections of the specimens were measured at the centroid of the cross-section, as described in Section 4.6.2. The locations of the instruments are shown in Fig. 4.31. The data measured during the tests is presented in Section B.2.

The shortening along the centroidal axis of the piers, δ_{cent} , was calculated as the difference between the vertical displacement measured at the centroid of the top block, Δ_{top} , and the vertical displacement measured at the centroid of the bottom block, Δ_{bot} . A positive sign corresponds to shortening of the centroidal axis.

$$\delta_{cent} = \Delta_{top} - \Delta_{bot} \quad (5.5)$$

Because the neutral axis of the cross-sections shifts toward the northeast corner as each specimen is loaded, the length of the centroidal axis will also elongate due to the end rotations. Therefore, the relative deflections of the ends of the vertical axis along the line of action of the applied load, δ_{load} , was considered to be a better representation of the axial response of the specimens. The axial displacement, δ_{load} , was calculated from the displacement measured along the centroidal axis and the rotations of the end blocks as follows:

$$\delta_{load} = (\Delta_{top} + e_N \theta_{E-W}^{top} + e_E \theta_{N-S}^{top}) - (\Delta_{bot} + e_N \theta_{E-W}^{bot} + e_E \theta_{N-S}^{bot}) \quad (5.6)$$

where e_N and e_E are the eccentricities in the north and east directions, and θ_{E-W}^{top} , θ_{N-S}^{top} , θ_{E-W}^{bot} , and θ_{N-S}^{bot} are the rotations about the east-west and north-south axes, measured at the top and bottom ends of the specimens. A positive sign corresponds to shortening of the axis along the line of action of the applied load.

5.1.4 Curvature

Two methods were used to calculate the curvature from the measured data. In the first method, the curvature was calculated from the average longitudinal strains in the south and west walls.

The relative vertical displacements of the south and west walls were measured at four points (Fig. 4.35). Using the notation defined in Section 4.6.3, u_{NT} and u_{ST} are the relative vertical displacements measured over the top half of the east wall at the north and south ends, respectively. The horizontal separation between the instruments was d , and the vertical gage length was l . The average curvature in the top half of the pier, about the east-west axis, would be

$$\phi_{E-W}^{Top} = \frac{u_{NT} - u_{ST}}{ld} \quad (5.7)$$

Similar calculations were made for the bottom half of the east wall, and both halves of the south wall. The reported curvatures represent the average of the values from the top and bottom sections.

The second method used the measured rotations of the end blocks to calculate the curvature along the pier. Assuming that the curvature along the specimen was uniform, the end rotations should be of equal magnitude. Therefore, the end rotation can be related to the curvature by

$$\theta_{E-W} = \phi_{E-W} \frac{H}{2} \quad (5.8)$$

where ϕ_{E-W} is the curvature about the east-west axis and H is the free height of the pier measured between end blocks (1780 mm (70 in.)).

Therefore, the curvature can be calculated as:

$$\phi_{E-W} = \frac{2\theta_{E-W}}{H} \quad (5.9)$$

where θ_{E-W} is the average measured rotation of the end blocks. The use of average curvatures will be discussed in Section 5.7.1.

5.2 MEASURED RESPONSE OF SPECIMEN P6

Specimen P6 failed explosively at an applied load of 2670 kN (600 kips), during a loading step. A 125-mm (5-in.) zone of concrete, centered 90 mm (3.5 in.) below the top block (Fig. 5.4 and 5.5), crushed and the longitudinal reinforcement buckled between adjacent horizontal bars. The zone of crushed concrete extended along the entire length of the north wall and 610 mm (24 in.) along the east wall.

5.2.1 Observed Crack Patterns

The first two tension cracks were observed along the south and west walls at an applied load of 890 kN (200 kips). The cracks extended from the southwest corner and were located at approximately one-half and three-quarters the height of the hollow section. Figures 5.6, 5.8 and 5.9 show that the tension cracks extended along 75% of the length of the west wall, along the entire length of the south wall, and into the east wall by the end of the test. In general, the cracks were located at the elevations of the horizontal transverse reinforcement.

After the test, it was observed that the cracks extended through the entire thickness of the walls. Figure 5.9 shows the tension cracks converging towards the zone of spalled concrete. These cracks developed near the end of the test and were marked after the specimen failed.

Cracks were also observed in the end blocks. The first crack in the bottom block was observed at an applied load of 1600 kN (360 kips). The first crack in the top block was observed along the east side of the specimen at an applied load of 1780 kN (400 kips), while the second crack was observed along the north side at an applied load of 2580 (580 kips). After the test, the top block exhibited four vertical cracks on the east side, close to the point of application of the load. Two cracks were observed on both the north and west sides of the top block. The bottom block exhibited only two short cracks. Figure 5.7 shows photographs of the cracks on the east side of the end blocks, while the crack patterns on all sides of the end blocks are shown in Fig. 5.10.

Crushing and cracking of concrete in the hollow pier were first observed at the northeast corner of the specimen at an applied load of 2310 kN (520 kips). Vertical cracks extended downward along both north and east walls (Fig. 5.10).

5.2.2 Behavior of the Reinforcement

Spalling of concrete exposed two layers of horizontal transverse reinforcement. The reinforcing details performed well, limiting the effective unbraced length of the longitudinal bars to the vertical spacing of the horizontal reinforcement. Figure 5.11 shows the longitudinal reinforcement buckled outward between horizontal bars.

Only the outer curtain of reinforcement could be seen from the exterior. It was observed later, however, that the longitudinal bars that formed the interior curtain buckled inward.



Figure 5.4 Specimen P6: Photo of East Wall at End of Test



Figure 5.5 Specimen P6: Photo of North Wall at End of Test



Figure 5.6 Specimen P6: Photo of West Wall at End of Test

(a) Top End Block



(b) Bottom End Block



Figure 5.7 Specimen P6: Vertical Cracks along the East Side of the End Blocks

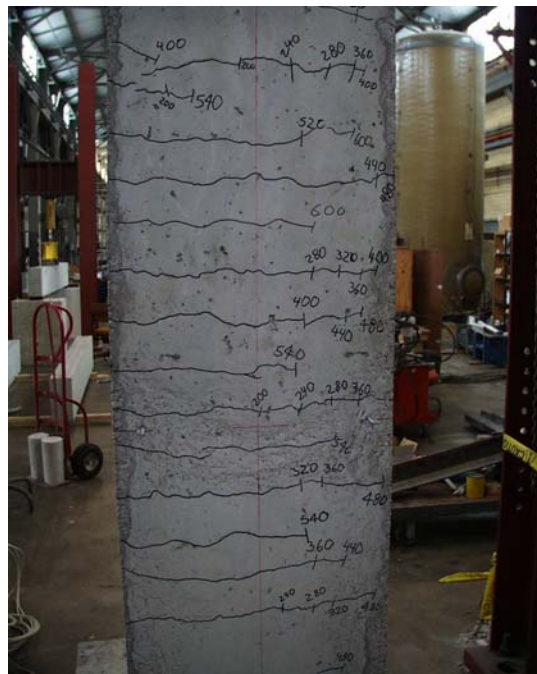


Figure 5.8 Specimen P6: Photo of South Wall at End of Test



Figure 5.9 Specimen P6: Cracks and Crushed Concrete at South End of East Wall

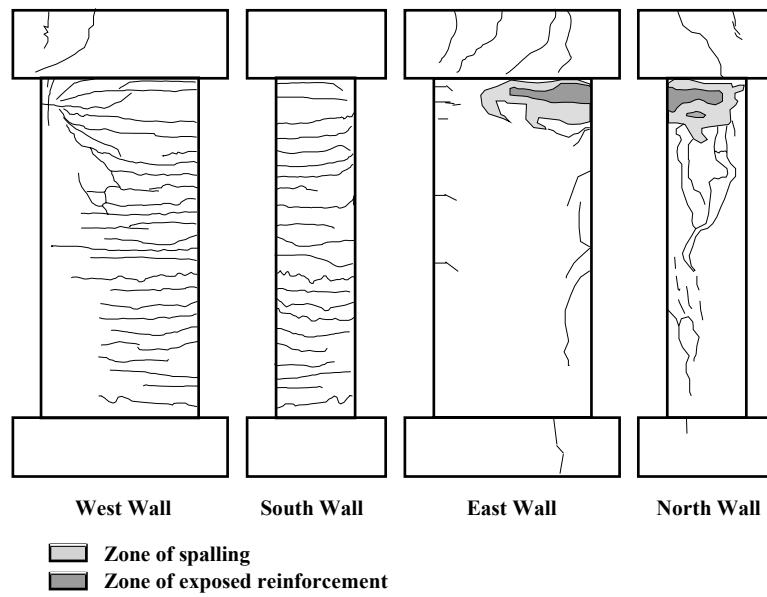


Figure 5.10 Specimen P6: Observed Crack Patterns



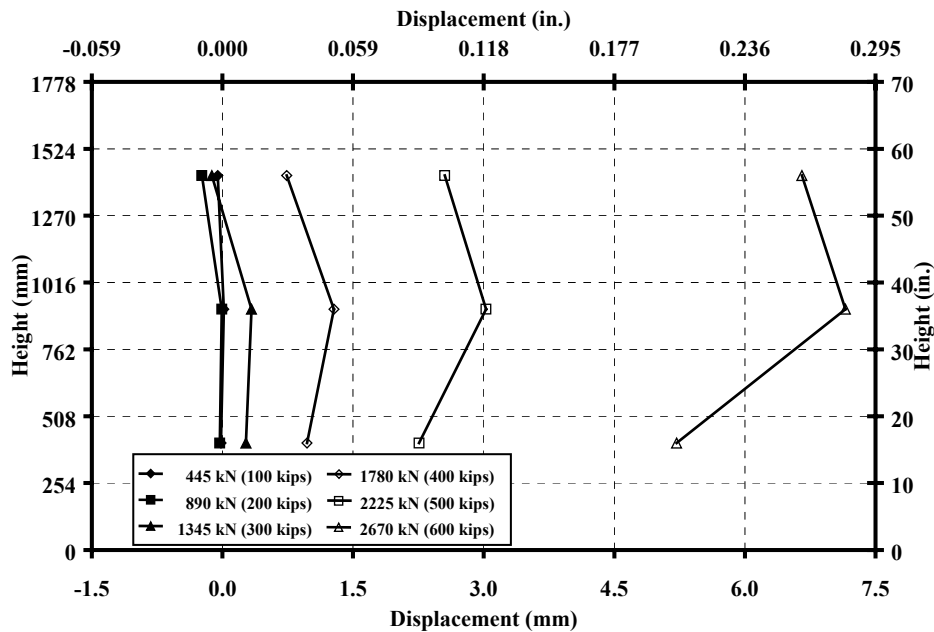
Figure 5.11 Specimen P6: Buckled Longitudinal Reinforcement near the Top of the East Wall

5.2.3 Longitudinal Profiles

The longitudinal profile of the specimen in the north-south direction is shown in Fig. 5.12(a). The deflected shape is similar to that expected for an element subjected to uniform moment along its length. The maximum horizontal deflection in the north-south direction occurred at mid-height and was equal to 7 mm (0.28 in.). At loads smaller than half the failure load, the deflections in the north-south direction were very small, less than 0.5 mm (0.02 in.) at mid-height.

At an applied load of 2225 kN (500 kip), the horizontal deflection at mid-height in the north-south direction, was approximately 40% of the maximum deflection at failure.

(a) Profile in North-South Direction



(b) Profile in East-West Direction

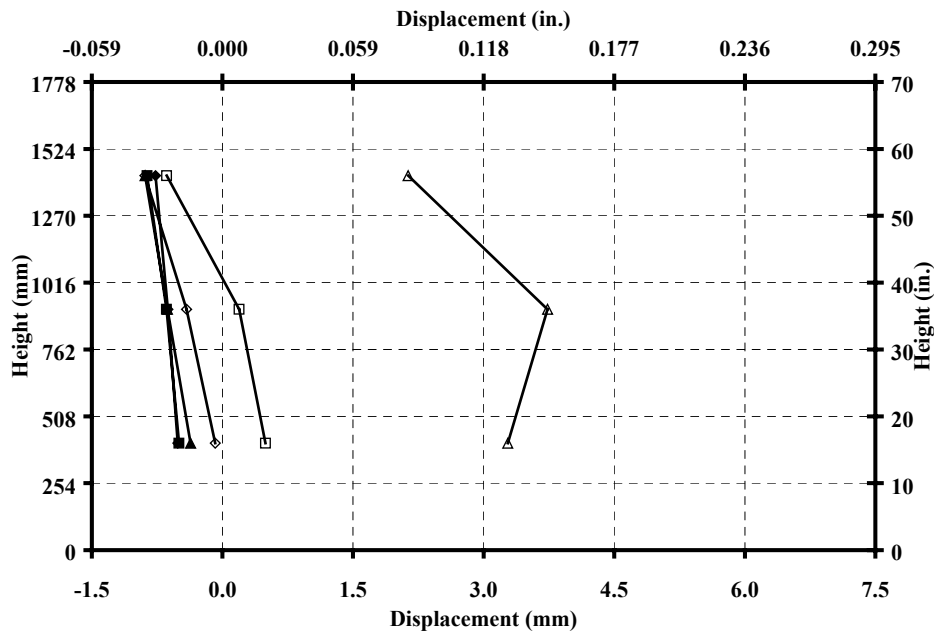


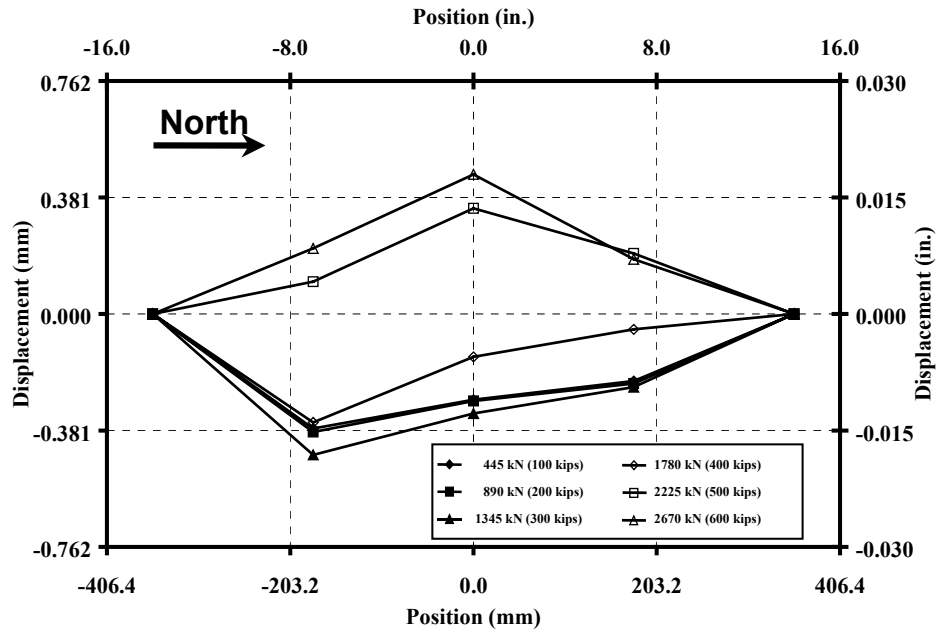
Figure 5.12 Specimen P6: Longitudinal Profile Measured Near the North-East Corner

The maximum deflection in the east-west direction (Fig. 5.12(b)) also occurred at mid-height and was equal to 3.8 mm (0.15 in.). At loads less than 2225 kN (500 kip), the horizontal deflections were negative and the longitudinal profiles of the pier did not exhibit the shape expected for an element subjected to uniform moment. At larger loads, the deflections increased rapidly and the deflected shape also changed. Although the amplitudes of the deflections at mid-height of the east wall were less than those of the north wall, the shapes were similar at failure. The unexpected deflections observed during the tests are discussed later in Section 5.7.1.

5.2.4 Profile of East Wall

Figure 5.13 shows the horizontal and vertical profiles of the east wall. At applied loads less than 50% of the capacity, the center of the wall panel had moved inward relative to the ends. Immediately prior to failure, the direction of the relative movement of the panel had reversed and the center moved outward. The maximum relative movement occurred at three-quarters of the height of the pier and was equal to 0.90 mm (0.36 in.) The maximum relative displacement at the center of the wall was equal to 0.45 mm (0.018 in.).

(a) Horizontal Profile of East Wall



(b) Vertical Profile of East Wall

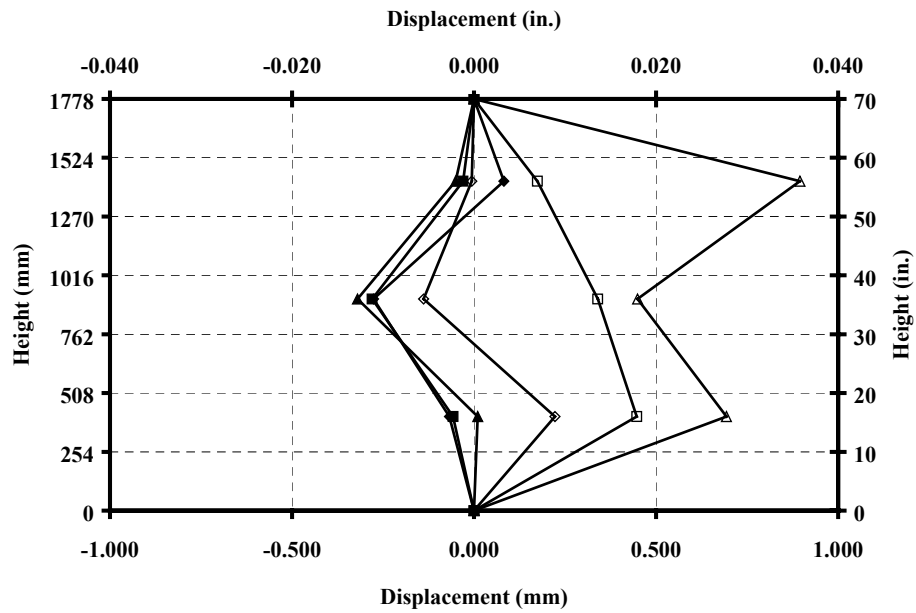


Figure 5.13 Specimen P6: Relative Displacements of the East Wall

5.2.5 Rotations of the End Blocks

The rotations of the end blocks are shown in Fig. 5.14. All the measured rotations occurred in directions consistent with the eccentricities of applied axial load. The rotations measured at the bottom about the east-west axis were twice as large as the rotations measured at the top. In contrast, the rotations about the north-south axis at the bottom were only slightly larger than the rotations at the top. Explanations for the difference between the rotations measured at the bottom and the rotations measured at the top about the east-west axis are discussed later in Section 5.7.1.

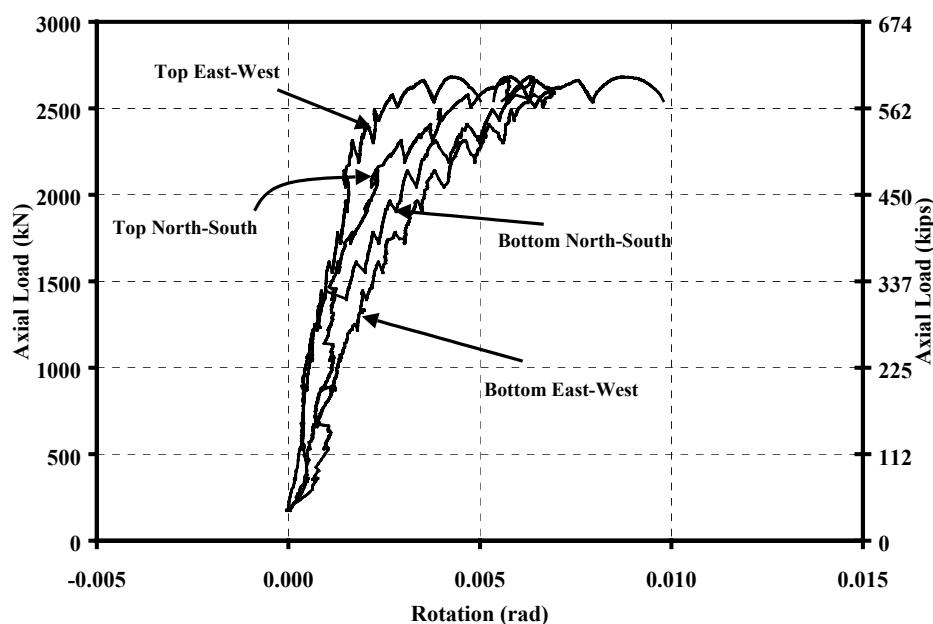


Figure 5.14 Specimen P6: Rotations of the End Blocks

5.2.6 Vertical Deflections

The relative axial deflections within *Specimen* P6 are shown in Fig. 5.15. The response measured along the centroidal axis of the cross-section was linear up to an applied axial load of approximately 445 kN (100 kips), approximately half the load at which the first cracks were observed. The specimen continued to shorten, although at a very low rate, up to an applied load of approximately 2000 kN (450 kips), 15% less than the load at which first crushing was observed. At higher loads, the axial response became erratic, decreasing as the load increased to 2500 kN (560 kips) and then increasing up to failure. The maximum measured relative axial deflection along the centroidal axis was 0.56 mm (0.023 in.).

The longitudinal shortening measured at the point of application of the load was nearly linear up to an applied axial load of approximately 445 kN (100 kips), approximately half the load at which the first cracks were observed. The specimen continued to shorten, although at a reduced rate, up to an applied load of approximately 900 kN (200 kips), the load at which first cracks were observed. The change in stiffness was not observed in the other specimens because during those tests instruments were zeroed again, which was not done with Specimen P6. At higher loads, the axial response softened, and the curve approached a horizontal slope before failure. The maximum measured relative axial deflection was 5.2 mm (0.20 in.).

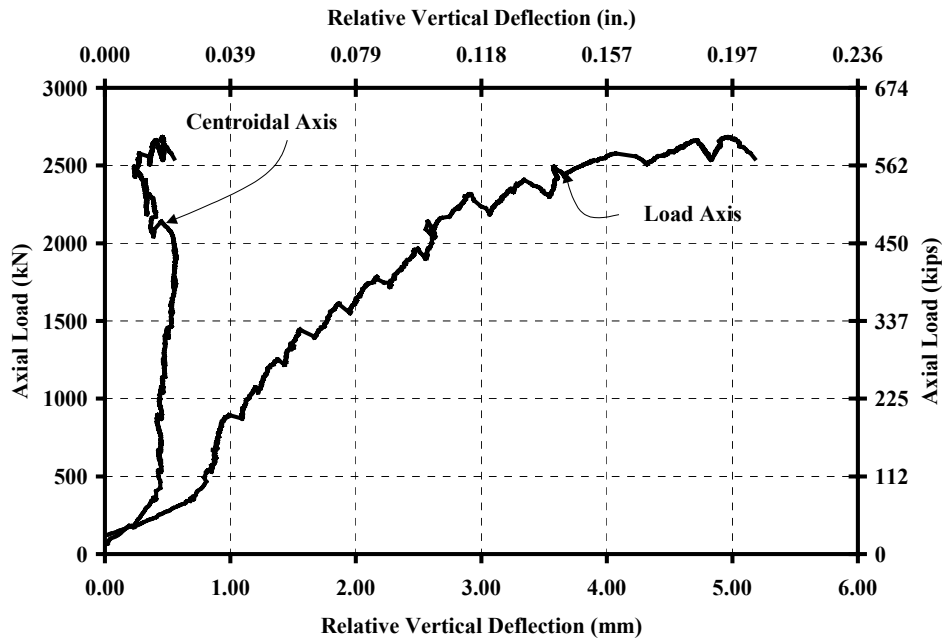


Figure 5.15 Specimen P6: Relative Vertical Deflections Measured at the Center of the End Blocks and at the Point of Application of the Axial Load

5.2.7 Curvature

Curvature was calculated using the two methods described in Section 5.1.4. Measured relationships between moment and curvature are plotted in Fig. 5.16 and 5.17. Instrument EB (Fig. B.15a) did not function properly; therefore, it was not possible to calculate the moment-curvature response about the north-south axis from the measured strains.

About the east-west axis (Fig. 5.16), the curve calculated using strains was initially very stiff and approached a horizontal slope before failure. The other curve had a lower initial slope, and for higher levels of applied load the slope became similar to the slope of the curve from strains.

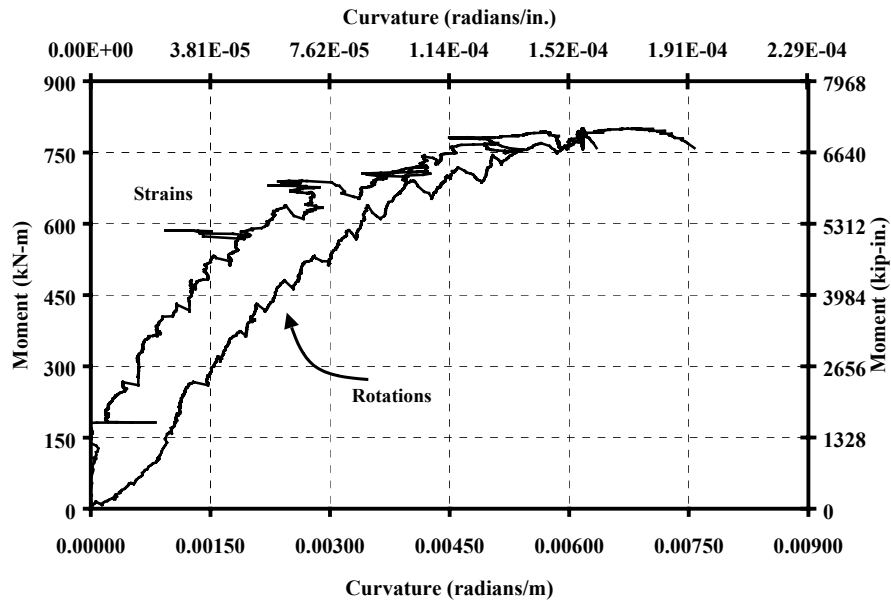


Figure 5.16 Specimen P6: Moment-Curvature Response about the East-West Axis

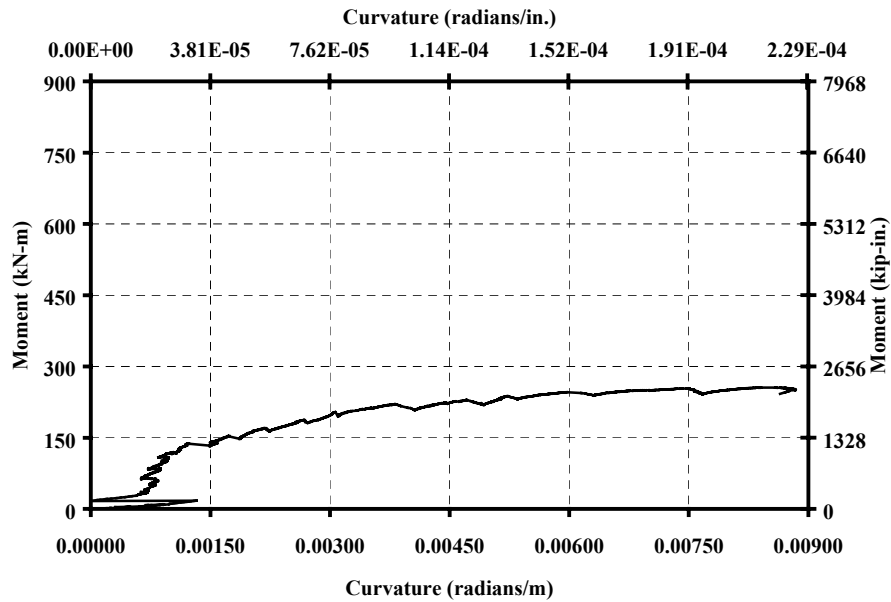


Figure 5.17 Specimen P6: Moment-Curvature Response about the North-South Axis

The maximum curvature about the east-west axis calculated using the longitudinal strains was 0.00629 radians/m (1.60×10^{-4} radians/in.), smaller than the curvature calculated using rotations, that was 0.00752 radians/m (1.91×10^{-4} radians/in.).

The moment-curvature response about the north-south axis (Fig. 5.17) calculated using rotations was initially stiff and approached to a horizontal slope at load levels close to 80% of the failure load. The maximum curvature was equal to 0.00883 radians/m (2.24×10^{-4} radians/in.), larger than the measured curvature about the east-west axis. Table 5.7, presented in Section 5.7.5, summarizes the maximum calculated curvatures of all specimens.

5.3 MEASURED RESPONSE OF SPECIMEN P8

Specimen P8 failed explosively at an applied load of 2050 kN (461 kips), during a loading step. A 150-mm (6-in.) zone of concrete in the north and east walls, centered 775 mm (30 in.) above the bottom block (Fig. 5.18 through 5.20), crushed and the longitudinal reinforcement buckled. The crushed zone of concrete extended 355 mm (14 in.) along the north wall and 735 mm (29 in.) along the east wall.

5.3.1 Observed Crack Patterns

The first two tension cracks were observed along the south and west walls, at an applied load of 530 kN (120 kips). The cracks extended from the southwest corner and were located at approximately one-half and three-quarters the height of the hollow section. Fig. 5.21 shows that the cracks extended along approximately

75% of the length of the west wall. The cracks were located at the elevation of the transverse reinforcement.

After the test, it was observed that the cracks extended through the entire thickness of the walls. Figure 5.21 shows the tension cracks converging to the zone of spalled concrete. These cracks developed near the end of the test and were marked after the specimen failed.

Cracks were also observed in the end blocks. The first crack was observed along the east side of the top block, at an applied load of 1420 kN (320 kips). After the end of the test, the top block showed two vertical cracks along the east side, close to the point of application of the load, and one short crack along the north side. The bottom block exhibited only one short crack, along the north side. Figure 5.22 shows a crack on the east side of the top end block, while Fig. 5.23 shows the crack patterns on all sides of the end blocks.

Crushing and cracking of concrete in the hollow pier were first observed at the northeast corner of the specimen at an applied load of 1730 kN (390 kips). The observed vertical crack was located at mid-height of the pier, and was 635 mm (25 in.) long. Near the end of the test, at an applied load of 2000 kN (450 kips), crushing and spalling of the concrete had extended along most of the length of the north and east walls. Figure 5.23 shows that, after the end of the test, crushing and spalling of concrete extended along more than 75% of the length of those walls.

5.3.2 Behavior of the Reinforcement

Spalling of concrete exposed several layers of transverse reinforcement. The reinforcing details limited the effective unbraced length of the longitudinal bars at the northeast corner to the vertical spacing of the transverse reinforcement. Figure 5.24 shows that the cross-ties on the east wall opened and, therefore, the effective unbraced length of the longitudinal bars was approximately 1.5 to 2 times the vertical spacing of the transverse reinforcement. Only the outer reinforcing curtain could be seen from the exterior, but it was later observed that the bars that formed the interior curtain buckled inward.

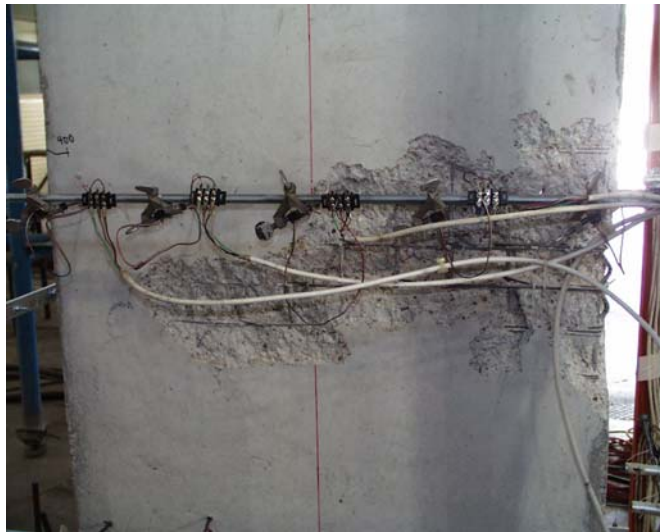


Figure 5.18 Specimen P8: Photo of East Wall at End of Test



Figure 5.19 Specimen P8: Photo of Specimen at End of Test



Figure 5.20 Specimen P8: Photo of North Wall at End of Test

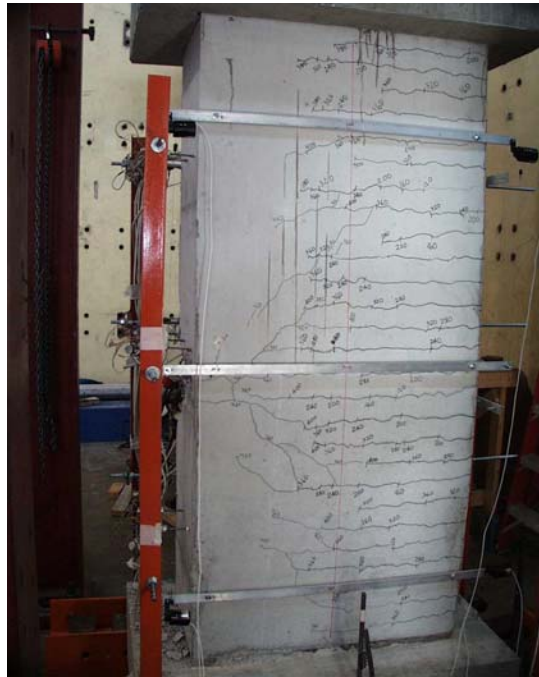


Figure 5.21 Specimen P8: Photo of West Wall at End of Test



Figure 5.22 Specimen P8: Vertical Crack at East Side of the Top End Block

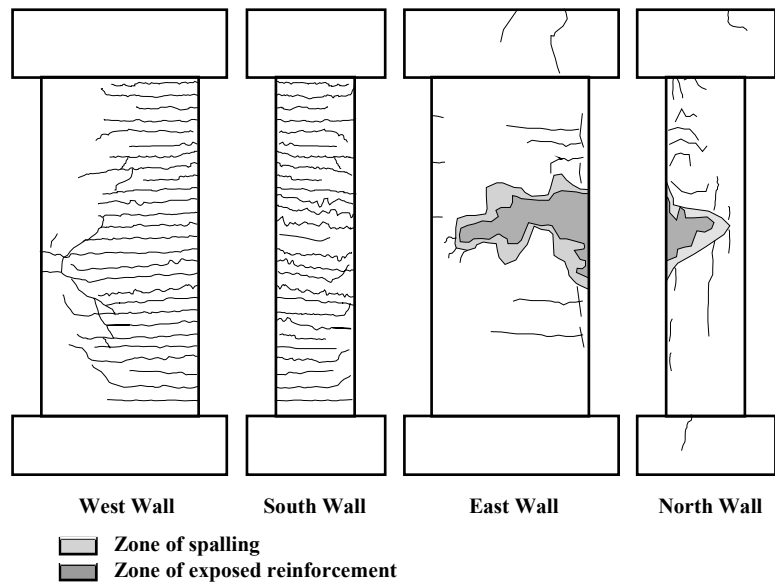


Figure 5.23 Specimen P8: Observed Crack Patterns



Figure 5.24 Specimen P8: Buckled Longitudinal Bars at the Northeast Corner and in the East Wall

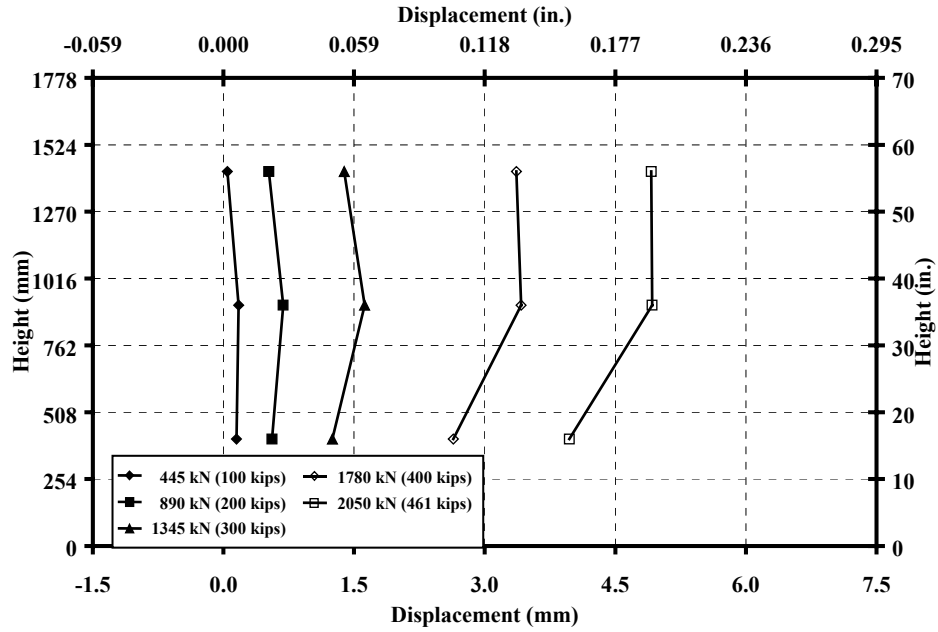
5.3.3 Longitudinal Profiles

The longitudinal profile of the specimen in the north-south direction is shown in Fig. 5.25(a). At load levels less than 1345 kN (300 kips) the hollow section showed the shape expected for an element subjected to uniform bending moment. At larger load levels the horizontal deflections measured near the top of the pier were similar to the deflections measured at mid-height. This behavior was observed in several specimens and is explained in Section 5.7.1.

The maximum horizontal deflection in the north-south direction occurred at mid-height and was equal to 5.0 mm (0.20 in.). At load levels less than 45% of the failure load the deflections at mid-height in the north-south direction were very small, less than 0.7 mm (0.03 in.).

The longitudinal profile in the east-west direction is shown in Fig. 5.25(b). The hollow section exhibited the curvature expected for a specimen subjected to uniform moment at all load levels. The maximum deflection in the east-west direction occurred at mid-height and was equal to 4.7 mm (0.19 in.). At load levels smaller than 65% of failure load the horizontal deflections were very small, 0.5 mm (0.02 in.). The deflections increased rapidly as the applied load was increased.

(a) Profile in North-South Direction



(b) Profile in East-West Direction

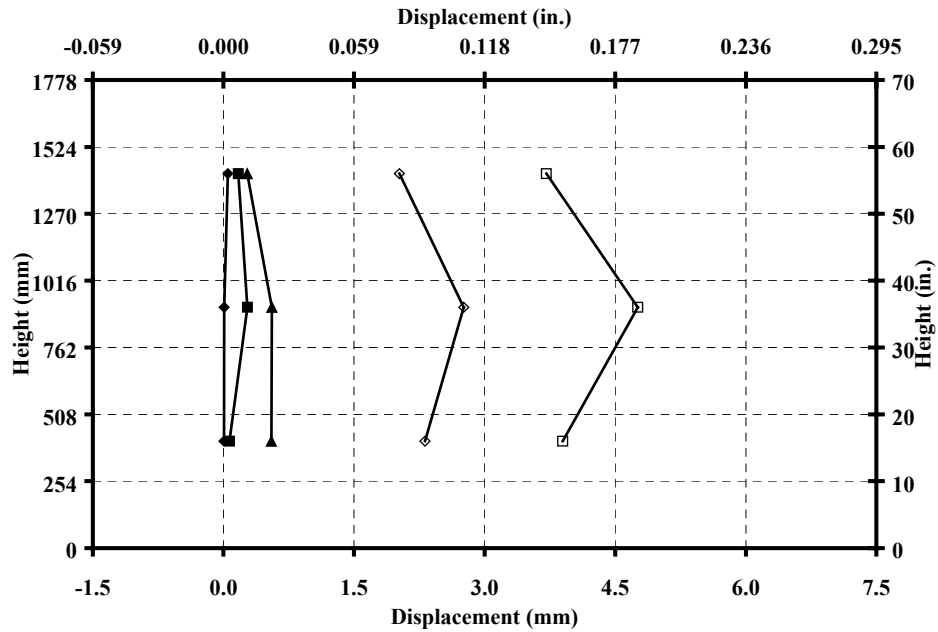


Figure 5.25 Specimen P8: Longitudinal Profile Measured Near the North-East Corner

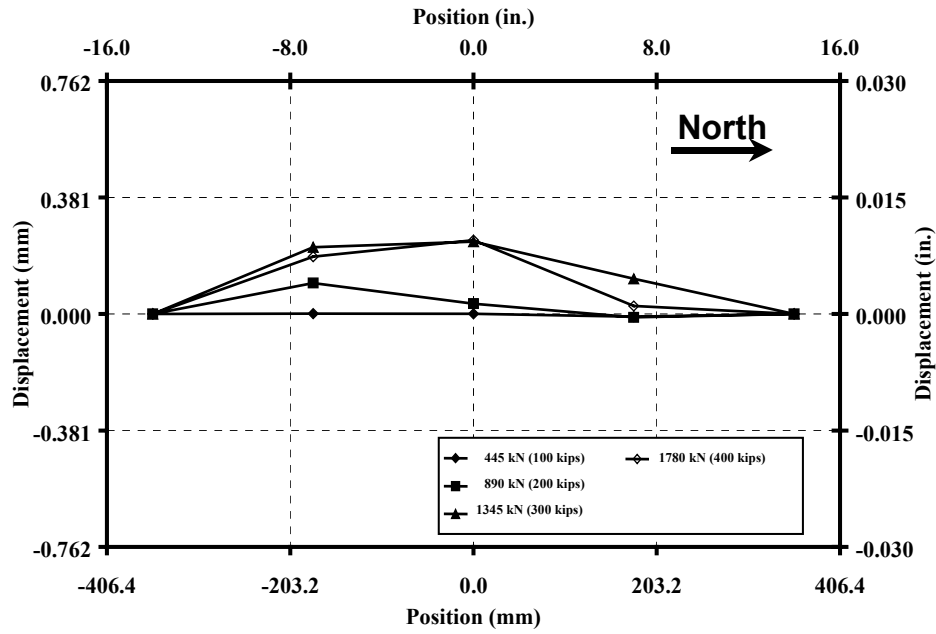
5.3.4 Profile of East Wall

Figure 5.26 shows the horizontal and vertical profiles of the east wall. At an applied load approximately equal to 65% of the capacity, the center of the wall panel had moved outward and the horizontal profile had deformed in single curvature. At the same load level the vertical profile also exhibited a single curvature.

Because the concrete crushed near mid-height of the specimen (Fig. 5.18), the relative profile of the east wall could not be determined near failure. The baseline position of the instruments was disturbed when the concrete crushed.

At load levels approximately 85% of the failure load, the maximum relative horizontal deflection occurred at three-quarters of the height of the wall, and was equal to 0.5 mm (0.02 in.).

(a) Horizontal Profile



(b) Vertical Profile

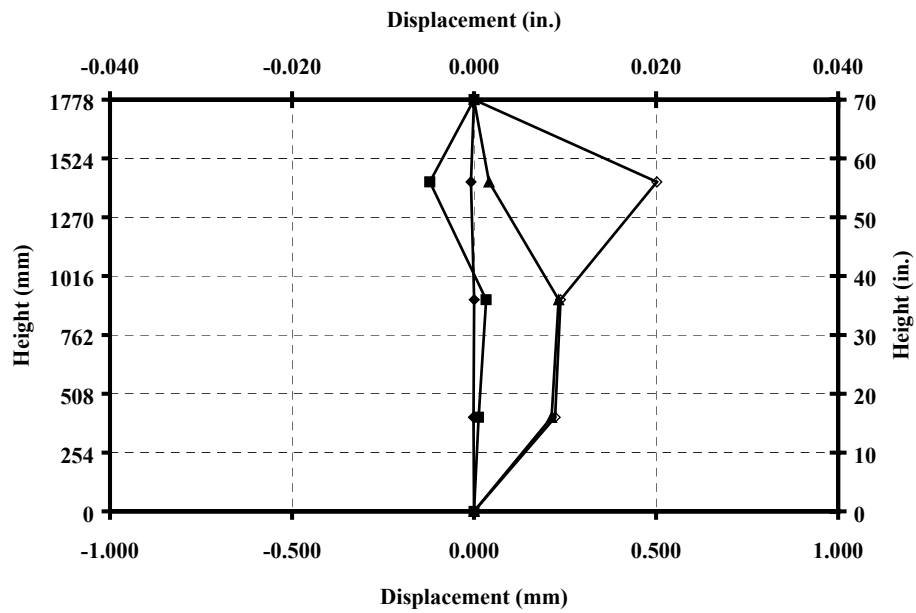


Figure 5.26 Specimen P8: Relative Displacements of the East Wall

5.3.5 Rotations of the End Blocks

The rotations of the end blocks are shown in Fig. 5.27. All rotations were positive. The rotations measured at the bottom block about the east-west axis were larger than the rotations of the top block about that axis. In contrast, the rotations of the bottom block about the north-south axis were smaller than the rotations of the top block about that axis for load levels less than 80% of the failure load. At larger load levels the top and end blocks had similar rotations about the north-south axis.

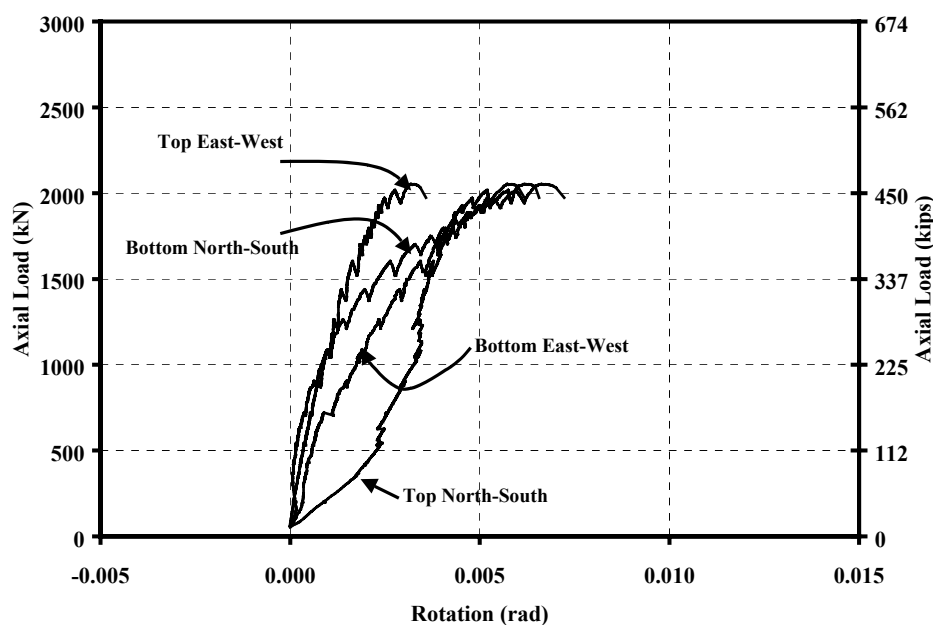


Figure 5.27 Specimen P8: Rotations of End Blocks

5.3.6 Vertical Deflections

The relative axial deflections of Specimen P8 are shown in Fig. 5.28. The response measured at the centroid of the specimen had a low initial slope that

increased as the applied axial load increased. The maximum shortening was 0.23 mm (0.009 in.), measured at an applied axial load of 780 kN (175 kips). At larger load levels the axial response decreased as the applied load increased, up to failure. At failure the measured relative axial deflection was approximately 0.03 mm (0.001 in.).

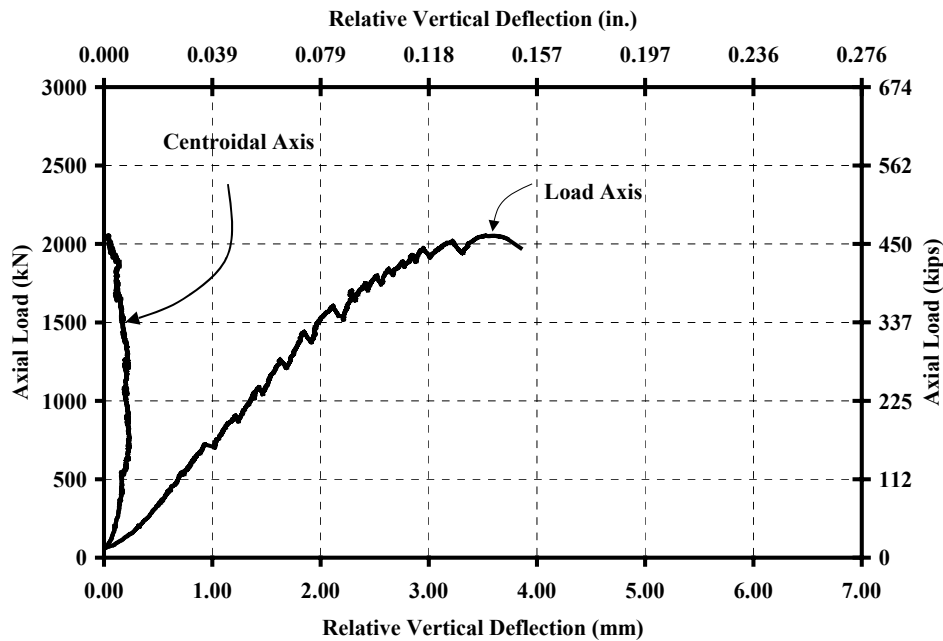


Figure 5.28 Specimen P8: Relative Vertical Deflections Measured at the Center of the End Blocks and at the Point of Application of the Axial Load

The relative vertical deflection measured at the point of application of the load was fairly linear up to an applied axial load of approximately 1700 kN (380 kips), approximately the load at which first crushing of the concrete in compression was observed. At higher loads, the specimen continued to shorten, although the slope of the response slightly decreased. The curve approached a

horizontal slope before failure. The maximum measured relative axial deflection was 3.8 mm (0.15 in.).

5.3.7 Curvature

The moment-curvature responses about the east-west and north-south axes respectively are plotted in Fig. 5.29 and 5.30. Instrument EB (Fig. B.15a) did not work properly; therefore, the moment-curvature response was not calculated about the north-south axis using measured strains. The moment-curvature responses about the east-west axis calculated using both methods had similar slopes. The curvatures calculated using end rotations were larger than the curvatures calculated using strains. Both curves approached a horizontal slope before failure.

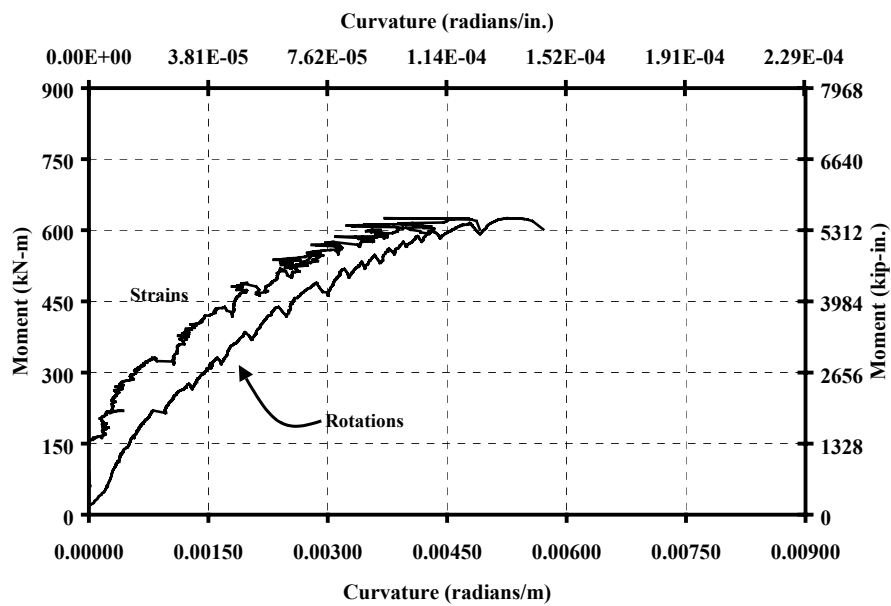


Figure 5.29 Specimen P8: Moment-Curvature Response about the East-West Axis

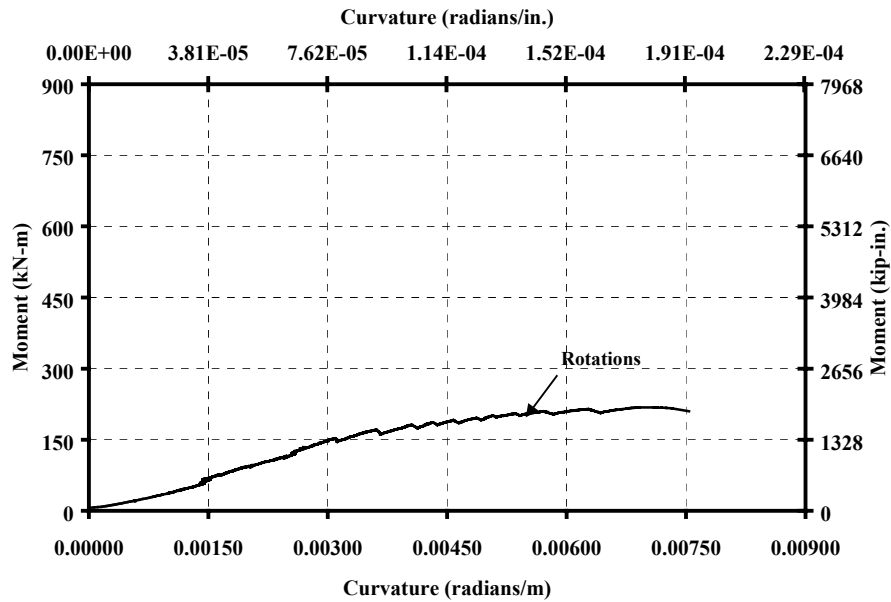


Figure 5.30 Specimen P8: Moment-Curvature Response about the North-South Axis

The maximum curvature about the east-west axis calculated using the measured longitudinal strains was 0.00491 radians/m (1.25×10^{-4} radians/in.), while the maximum curvature calculated using the rotations of the blocks was 0.00573 radians/m (1.45×10^{-4} radians/in.). The maximum calculated curvatures are summarized in Table 5.2.

The moment-curvature response about the north-south axis was linear up to approximately 1400 kN (310 kips). At larger loads the response slightly softened. The maximum calculated curvature was 0.00754 radians/m (1.92×10^{-4} radians/in.).

5.4 MEASURED RESPONSE OF SPECIMEN P10

Specimen P10 failed explosively at an applied load of 2370 kN (532 kips), during a loading step. A 125-mm (5-in.) zone of concrete, centered 115 mm (4.5in.) below the top block (Fig. 5.31 and 5.32), crushed and the longitudinal reinforcement buckled. The east wall broke through its entire thickness, exposing the interior curtain of reinforcement. The zone of crushed concrete extended along the entire length of the north wall and 735 mm (29 in.) along the east wall.

5.4.1 Observed Crack Patterns

The first three tension cracks were observed along the south and west walls, at an applied load of 530 kN (120 kips). The cracks extended from the southwest corner. One was located approximately at the midheight of the hollow section, while the other two were located at approximately three-quarters the height. Figures 5.33 and 5.35 show that the tension cracks extended along less than 70% of the east wall and along the entire length of the south wall. In general, the tension cracks were located at the elevations of the transverse reinforcement.

After the test, it was observed that the cracks extended through the entire thickness of the walls. Figure 5.34 shows the tension cracks converging towards the northwest corner of the specimen, close to the zone of spalled concrete. These cracks developed near the end of the test and were marked after the specimen failed.

Cracks were also observed at the end blocks. The first cracks in the end blocks were observed along the east side of both blocks, at an applied load of 1600 kN (360 kips). After the test, the top block exhibited four diagonal cracks

along the west side, three diagonal cracks along the north side and three vertical cracks along the east side. The bottom end block exhibited one vertical crack along the east side and one short crack along the north side. The crack patterns on all sides of the end blocks are shown in Fig. 5.36.

Crushing and cracking of concrete in the east and north walls were first observed at the northeast corner, 200 mm (8 in.) below the top end block, at an applied load of 1780 kN (400 kips). Near failure, at an applied load of 2180 kN (490 kips), crushing of the concrete was observed at the bottom of the pier, while at the top of the hollow section spalling and crushing of the concrete had extended along most of the length of the north and east walls.

5.4.2 Behavior of the Reinforcement

Spalling of concrete exposed two layers of transverse reinforcement. The transverse reinforcing details performed well, but some of the longitudinal bars buckled between two non-adjacent horizontal reinforcing bars, as can be seen in the two photographs in Fig. 5.37. The bars in the interior curtain buckled inward. The bars located farther from the northeast corner had less transverse deflection than the ones closer to the corner. One hairpin, located near the northeast corner, opened outward (Fig. 5.37b), but still constrained the longitudinal bars to buckle between adjacent layers of transverse reinforcing.

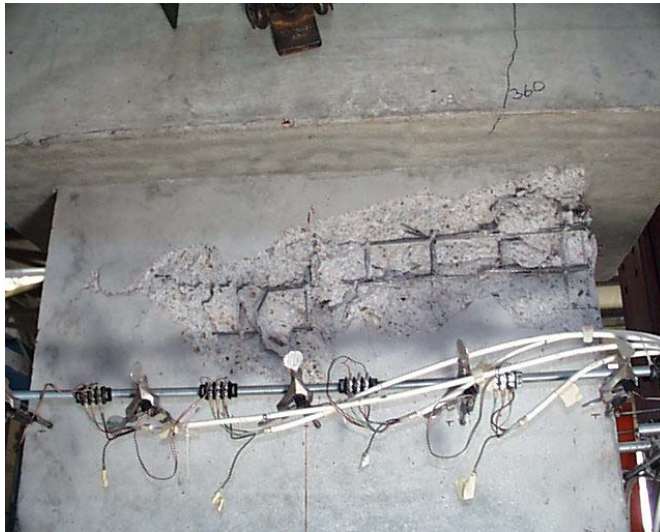


Figure 5.31 Specimen P10: Photo of East Wall at End of Test



Figure 5.32 Specimen P10: Photo of North Wall at End of Test

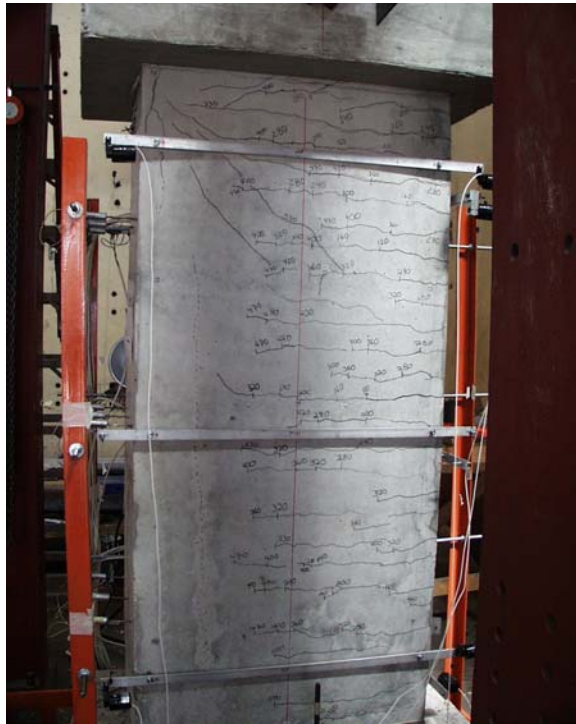


Figure 5.33 Specimen P10: Photo of West Wall at End of Test



Figure 5.34 Specimen P10: Photo of at Top of Northwest Corner at End of Test



Figure 5.35 Specimen P10: Photo of West and South Walls at End of Test

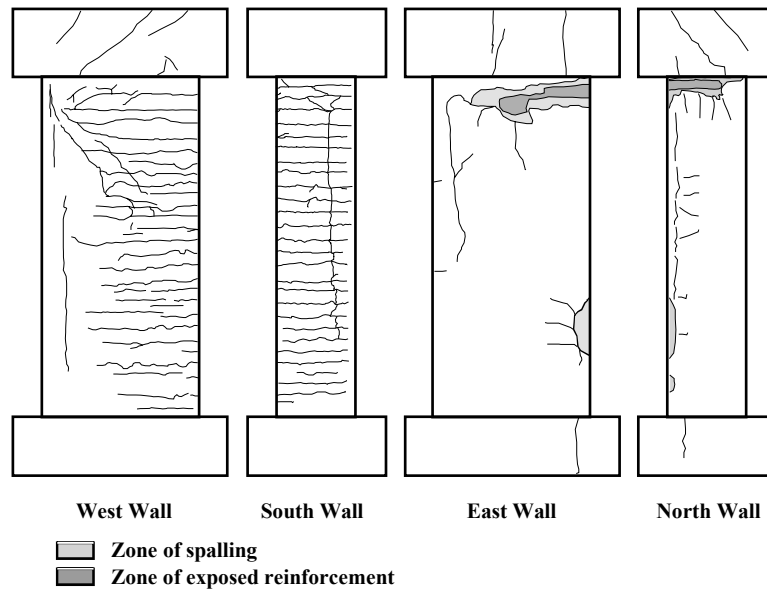


Figure 5.36 Specimen P10: Observed Crack Patterns

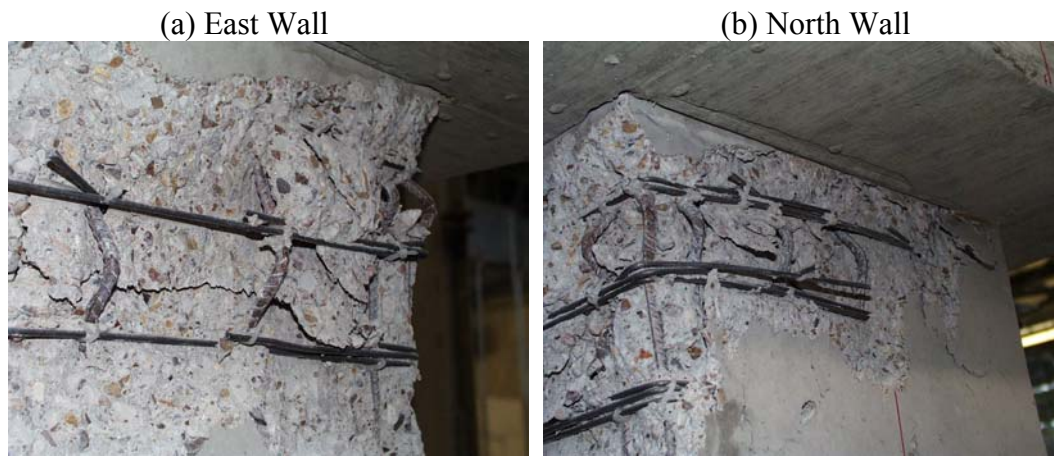


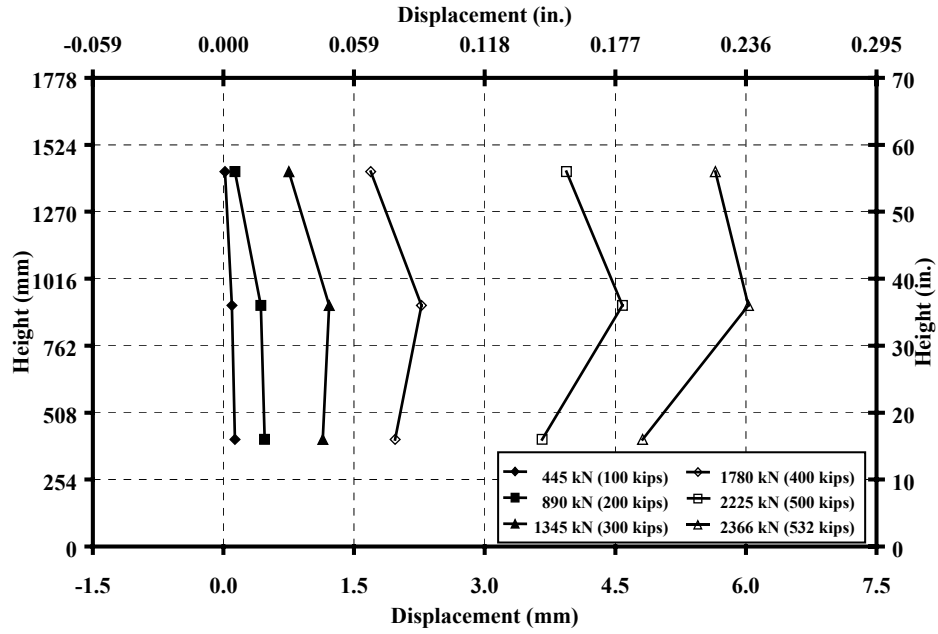
Figure 5.37 Specimen P10: Buckled Longitudinal Reinforcement near Top of Northeast Corner

5.4.3 Longitudinal Profiles

The longitudinal profile of the specimen in the north-south direction is shown in Fig. 5.38(a). The deflected shape is similar to that expected for an element subjected to uniform bending moment along its length. The maximum horizontal deflection in the north-south direction occurred at mid-height and was equal to 6 mm (0.24 in.). At load levels smaller than 40% of the failure load the deflections in the north-south direction were very small, less than 0.5 mm (0.02in.) measured at mid-height.

The horizontal deflection measured at mid-height in the north-south direction, at an applied load approximately equal to 75% of the failure load, was less than 40% of the maximum deflection at failure.

(a) Profile in North-South Direction



(b) Profile in East-West Direction

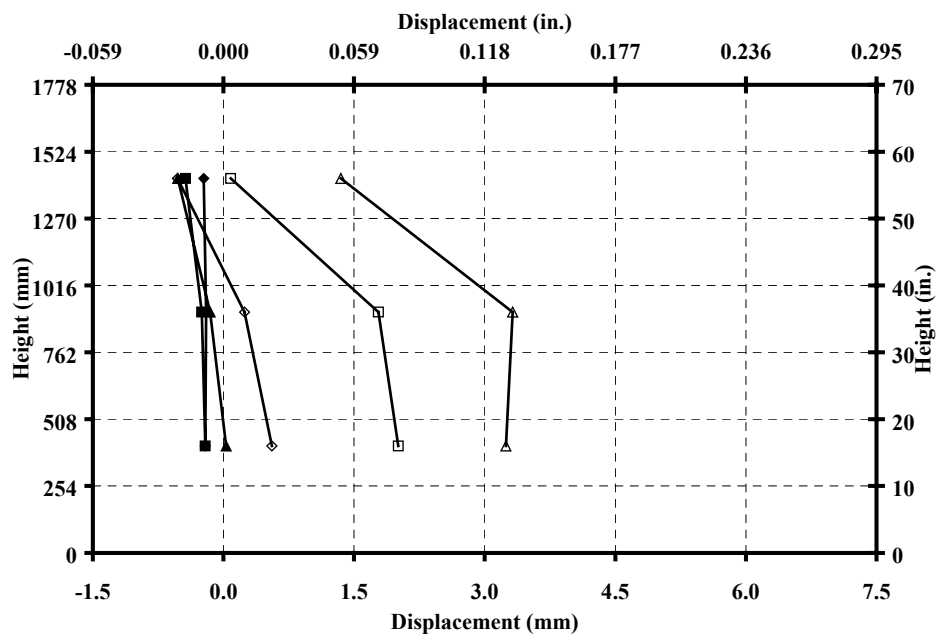


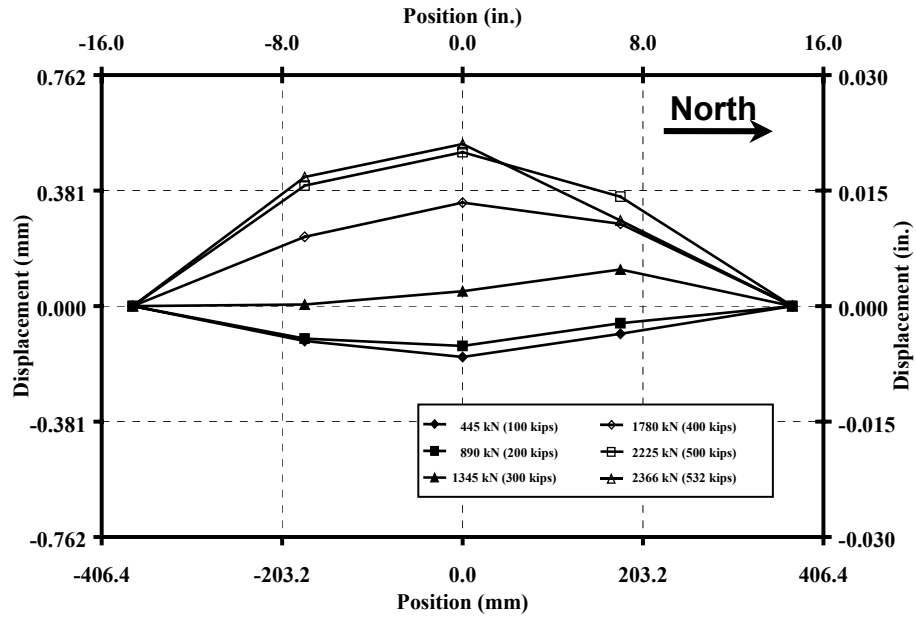
Figure 5.38 Specimen P10: Longitudinal Profile Measured Near the North-East Corner

The longitudinal profile in the east-west direction is shown in Fig. 5.38(b). The maximum deflection occurred at mid-height and was equal to 3.3 mm (0.13 in.). At load levels smaller than 55% of the capacity the horizontal deflections were negative and the longitudinal profiles of the pier did not have the curvature expected for a column subjected to uniform bending moment. At larger load levels the horizontal deflections increased rapidly and the deflection measured near the bottom of the pier was large, similar to the deflection measured at mid-height. This behavior was observed in several piers and is discussed in Section 5.7.1.

5.4.4 Profile of East Wall

Figure 5.39 shows the horizontal and vertical profiles of the east wall, measured at mid-height of the hollow section and at the center of the wall, respectively. Initially, the center of the wall moved inward, but as the applied load increased, the relative deflection shifted outward. The vertical profile had double curvature at load levels smaller than 75% of the failure load. At higher load levels the vertical profile had a single curvature. The maximum relative deflection was measured at the center of the wall and was 0.50 mm (0.02 in.), outward.

(a) Horizontal Profile



(b) Vertical Profile

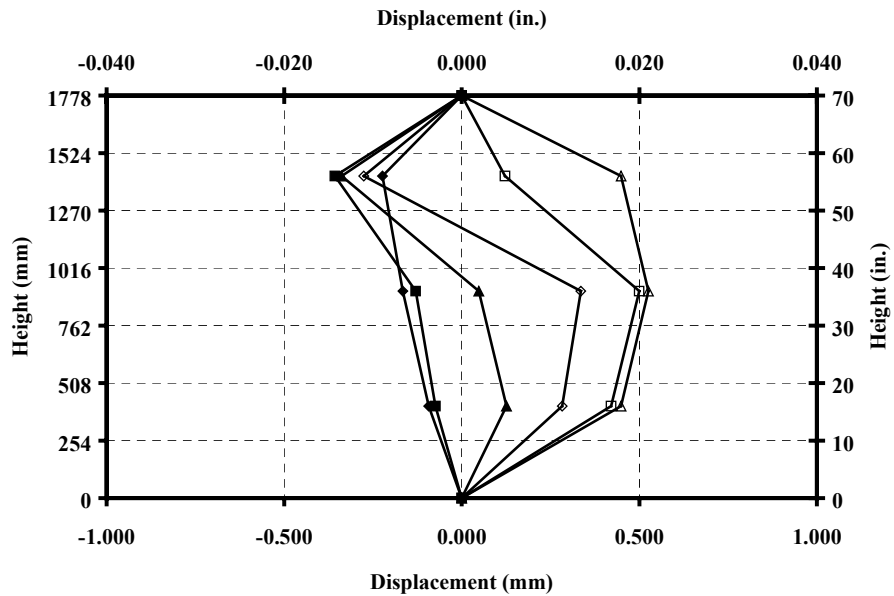


Figure 5.39 Specimen P10: Relative Displacements at Mid-height of East Wall

5.4.5 Rotations of the End Blocks

The rotations of the end blocks are shown in Fig. 5.40. All rotations were positive. Rotations about the east-west axis measured at the top block were slightly larger than at the bottom block. At all levels of applied axial load the rotations about the north-south axis measured at the bottom end were smaller than the rotations measured at the top. This behavior was observed in several specimens and is discussed in Section 5.7.1.

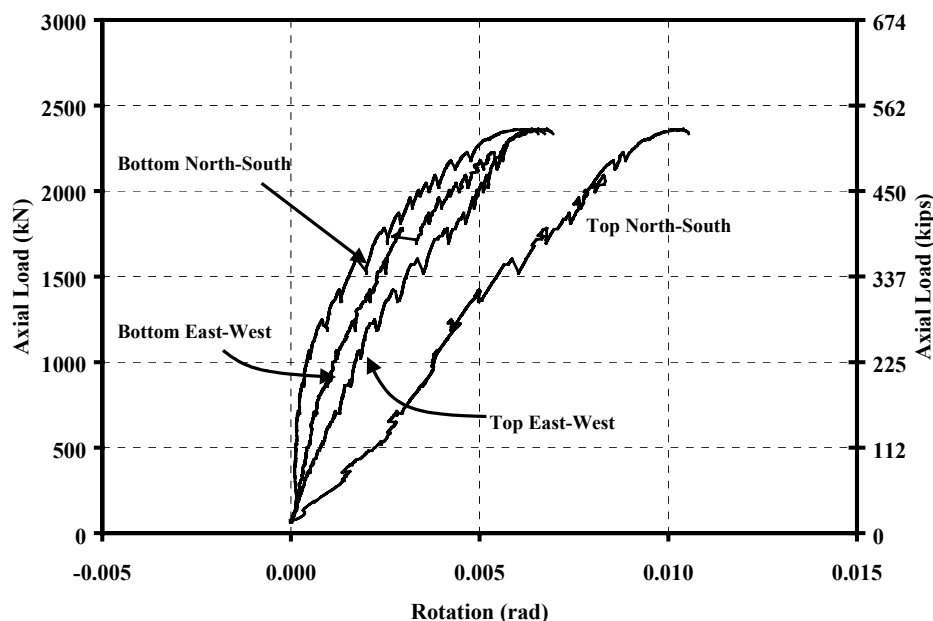


Figure 5.40 Specimen P10: Rotations of the End Blocks

5.4.6 Vertical Deflections

The relative vertical deflections of Specimen P10 are shown in Fig. 5.41. The response measured along the centroidal axis of the cross-section was somewhat linear up to an applied load of 720 kN (160 kips). The specimen

continued to shorten, at a reduced rate, up to an applied load of approximately 1800 kN (405 kips), the same load at which compression crushing of concrete was first observed. At larger loads the axial response decreased up to the failure load. The maximum measured shortening was 0.93 mm (0.037 in.).

The axial response measured at the point of application of the load was fairly linear and the curve approached to a horizontal slope before failure. The maximum measured relative axial deflection was 6.6 mm (0.26 in.).

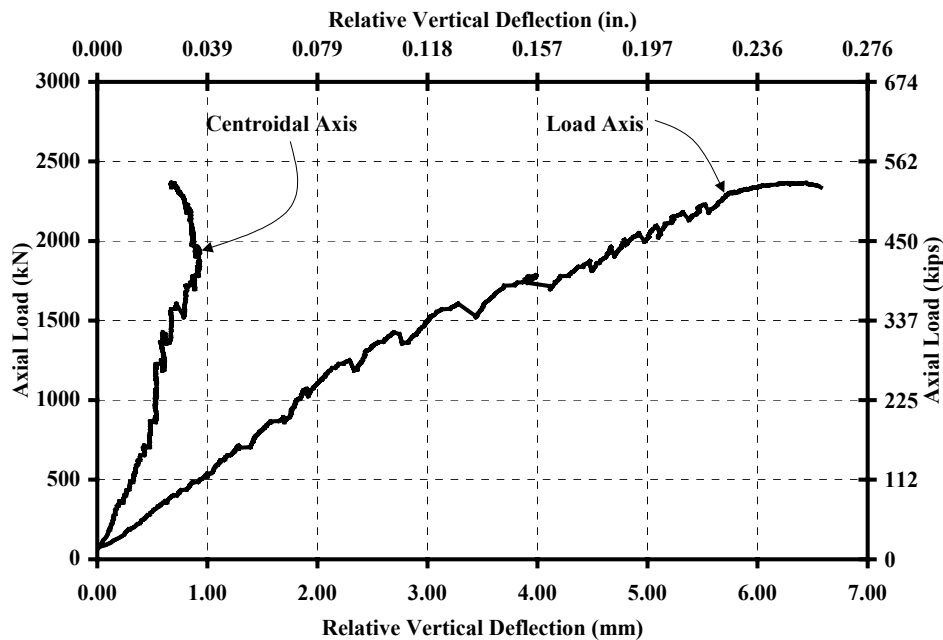


Figure 5.41 Specimen P10: Relative Vertical Deflections Measured at Center of End Blocks and at the Point of Application of Axial Load

5.4.7 Curvature

The moment-curvature relationships about the east-west and north-south axes, calculated using the two methods described in Section 5.1.4, are plotted in Fig. 5.42 and 5.43. Both curves calculated about the east-west axis had similar

slopes and tended to a horizontal slope before failure. The maximum curvature calculated using the measured longitudinal strains was 0.00658 radians/m (1.67×10^{-4} radians/in.), and the maximum curvature calculated using the rotations of the end block was 0.00769 radians/m (1.95×10^{-4} radians/in.). At all load levels the curvatures calculated using rotations were larger than the curvatures calculated using strains.

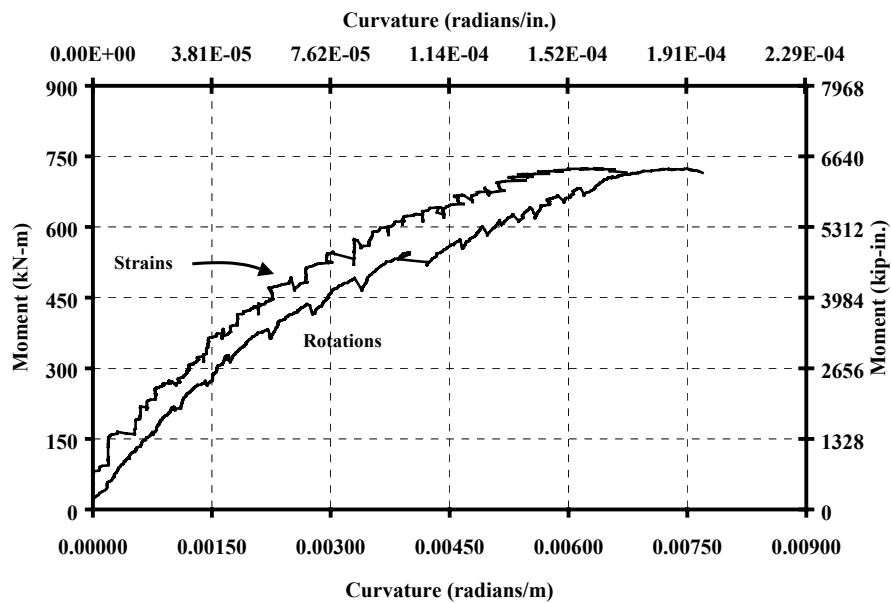


Figure 5.42 Specimen P10: Moment-Curvature Response about the East-West Axis

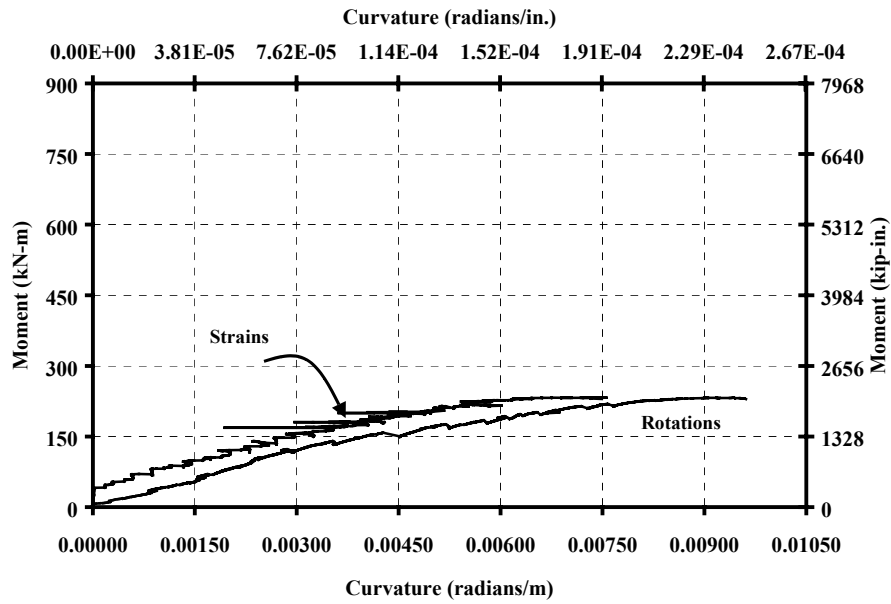


Figure 5.43 Specimen P10: Moment-Curvature Response about the North-South Axis

The observations made for the calculated relationships about the east-west axis were valid for the curves calculated about the north-south axis. The maximum curvature calculated using the measured longitudinal strains was 0.00749 radians/m (1.90×10^{-4} radians/in.), and the maximum curvature calculated using the rotations of the end block was 0.00961 radians/m (2.44×10^{-4} radians/in.).

5.5 MEASURED RESPONSE OF SPECIMEN P12

Specimen P12 failed explosively at an applied load of 2280 kN (513 kips), during a loading step. A 150-mm (6-in.) zone of concrete, centered 225 mm (9in.) above the bottom block (Fig. 5.44 and 5.45), crushed and the longitudinal reinforcement buckled between adjacent transverse bars. The zone of crushed concrete extended along the entire length of both the east and north walls and into the end of the west and south walls. In the 400 mm (16 in.) closer to the northeast corner the east wall broke through its thickness exposing the interior reinforcing curtain.

5.5.1 Observed Crack Patterns

The first two tension cracks were observed along the south and west walls, at an applied load of 710 kN (160 kips). The cracks extended from the southwest corner and were located approximately at one-half and three-quarters the height of the hollow section. Figures 5.46, 5.47 and 5.48 show that the cracks extended along approximately 60% of the west wall and along the entire length of the south wall. In general, the cracks were located at the elevations of the transverse reinforcement.

After the test, it was observed that the tension cracks extended through the entire thickness of the walls. Figure 5.47 shows the tension cracks converging towards the zone of spalled concrete in the west wall. These cracks developed at the end of the test and were marked after the specimen failed.

Cracks were also observed within the end blocks. The first crack in the top block was observed along the east side at an applied load of 1690 kN (380 kips). The first crack at the bottom block was also observed along the east side, at an applied load of 1890 kN (400 kips). A vertical crack was observed along the north side of the top block at a load of 1960 kN (440 kips). After the test, the top block showed one vertical crack along the east side, close to the point of application of the load, while two cracks were observed along the north side. The bottom block showed three cracks along the east and north sides and four cracks along the west side. Figure 5.49 shows photographs of the cracks on the east and north sides of the end blocks, while the crack patterns on all sides of both end blocks are shown in Figure 50.

Crushing and cracking of concrete in the hollow pier were first observed at the northeast corner of the specimen at an applied load of 2050 kN (460 kips), 380 mm (15 in.) above the bottom block. No crushing and spalling of concrete was observed in other parts of the northeast corner prior to failure.

5.5.2 Behavior of the Reinforcement

The transverse reinforcing details performed well, with the exception of the north side, where the short legs of the U-shaped, horizontal web reinforcement opened (Fig. 5.51). The longitudinal bars buckled with an effective length equal to or slightly larger than the vertical spacing of the transverse reinforcement (Fig. 5.52). The bars located farther from the northeast corner of the specimen had less horizontal deflection than the ones closer to the corner. After the test, it was observed that the bars that formed the interior curtain had buckled inward.

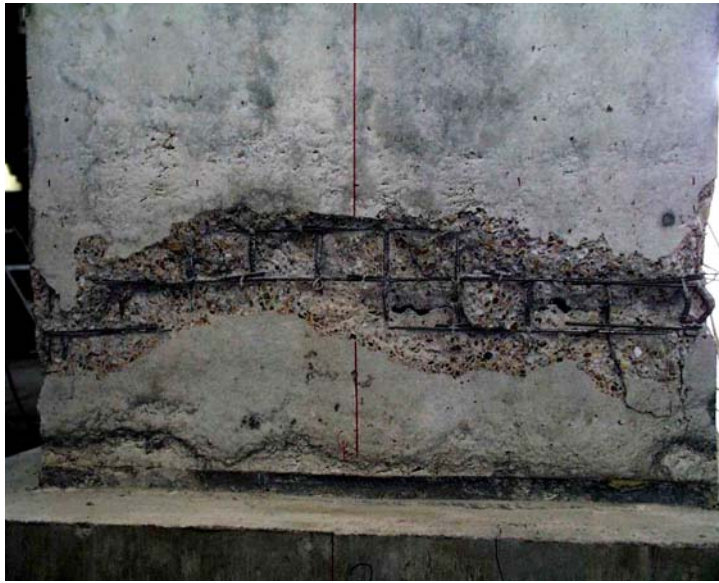


Figure 5.44 Specimen P12: Photo of East Wall at End of Test



Figure 5.45 Specimen P12: Photo of North Wall at End of Test



Figure 5.46 Specimen P12: Photo of West Wall at End of Test



Figure 5.47 Specimen P12: Photo of West and South Walls at End of Test



Figure 5.48 Specimen P12: Photo of South Wall at End of Test

(a) East Side of Bottom Block



(b) North Side of Top Block



Figure 5.49 Specimen P12: Cracks at the End Blocks

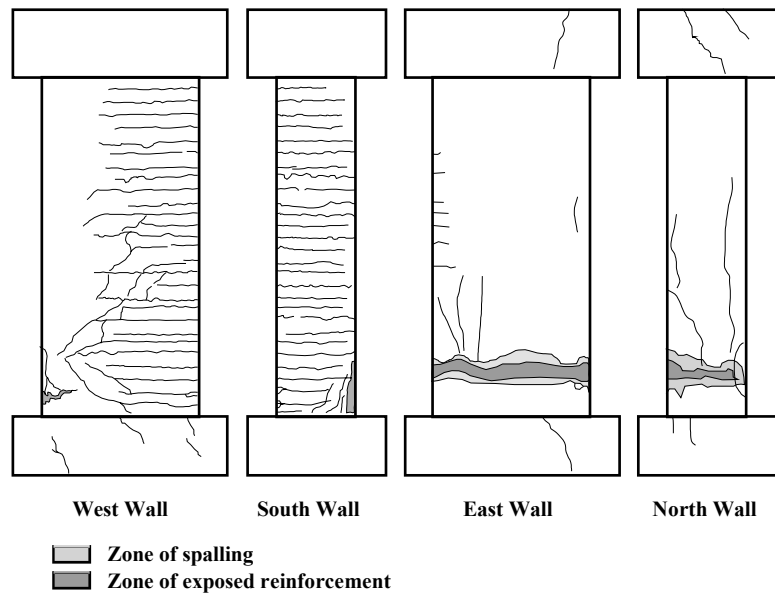


Figure 5.50 Specimen P12: Observed Crack Patterns



Figure 5.51 Specimen P12: Buckled Longitudinal Reinforcement along the North Wall and Opened Transverse Reinforcement



Figure 5.52 Specimen P12: Buckled Longitudinal Bars along the East Wall

5.5.3 Longitudinal Profiles

The longitudinal profile of the specimen in the north-south direction is shown in Fig. 5.53(a). The deflected shape is similar to that expected for an element subjected to uniform moment along its length. The maximum horizontal deflection in the north-south direction occurred at midheight and was equal to 4.3 mm (0.17 in.). At load levels less than 40% of the failure load the deflections in the north-south direction were very small, less than 0.5 mm (0.02 in.) at midheight.

At an applied load of 1780 kN (400 kips), the horizontal deflection at midheight in the north-south direction was less than 45% of the maximum deflection at failure.

The maximum deflection in the east-west direction (Fig. 5.53(b)) also occurred at midheight and was equal to 1.9 mm (0.07 in.). At loads smaller than 40% of the failure load the horizontal deflections were negative and the longitudinal profiles of the pier did not have the curvature expected for an element subjected to uniform moment. The deflection measured near the bottom of the hollow section was larger than the deflection at midheight. At larger loads, the deflections increased rapidly, but the deflected shape did not change.

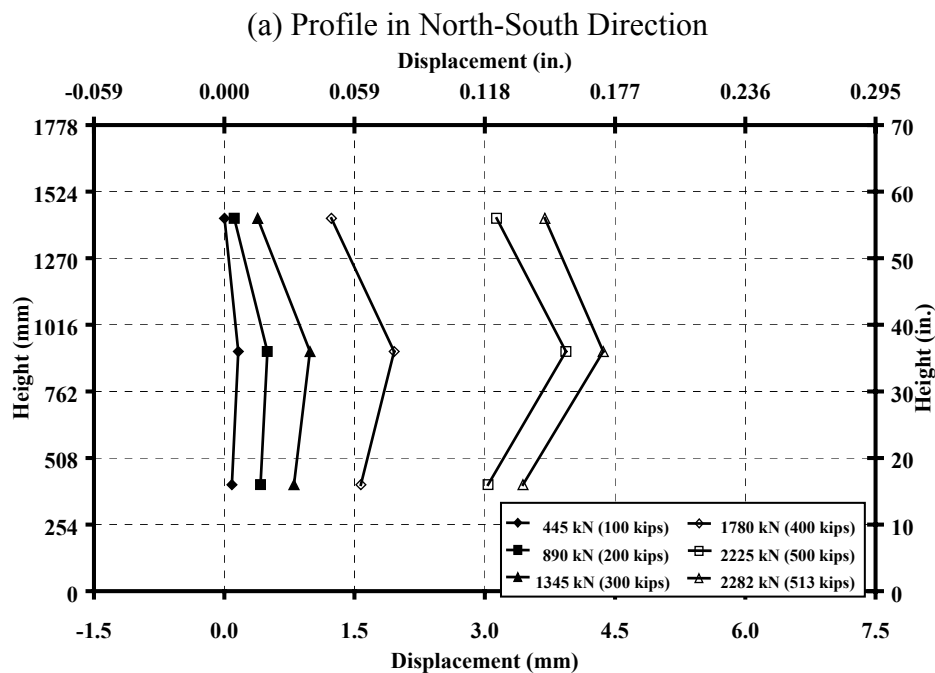


Figure 5.53 Specimen P12: Longitudinal Profile Measured Near the North-East Corner

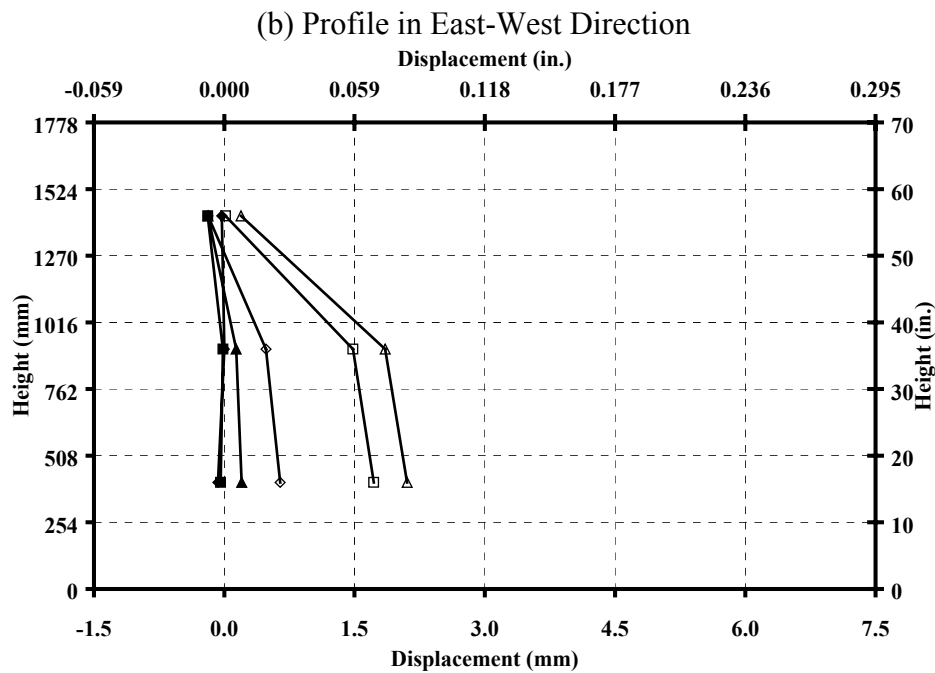
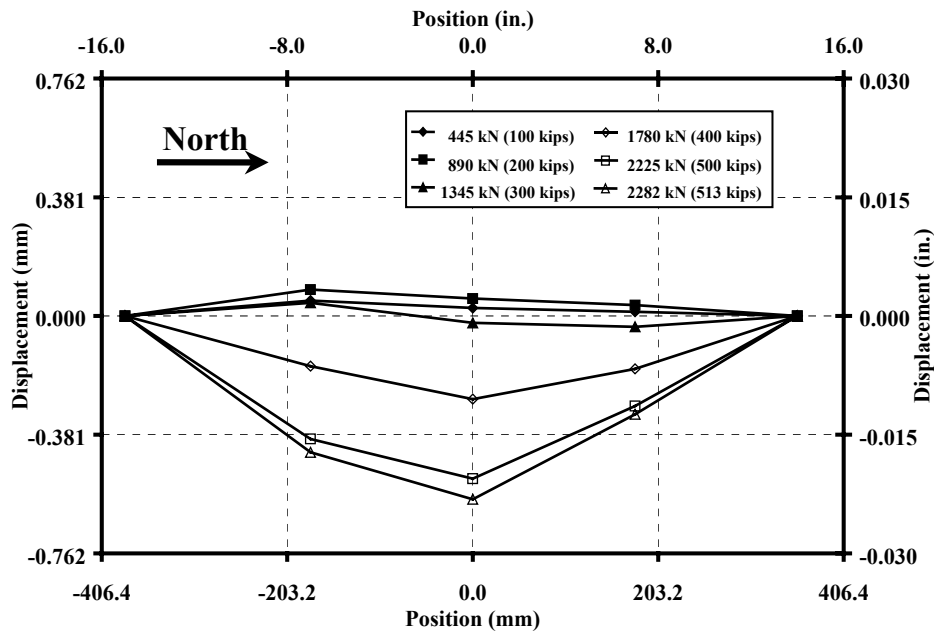


Figure 5.53 (cont.) Specimen P12: Longitudinal Profile Measured Near the North-East Corner

5.5.4 Profile of East Wall

Specimen P12 was the only test specimen in which the east wall moved inward at failure (Fig. 5.54). At load levels less than 50% of the ultimate load the wall moved slightly outward and the vertical profile exhibited double curvature shape. At larger levels of applied load the direction of the relative deflection changed inward, and the center of the wall deformed rapidly as the load increased. The maximum relative deflection occurred near the bottom of the wall and was equal to 0.75 mm (0.03 in.) inward. The maximum relative displacement at the center of the wall was equal to 0.58 mm (0.023 in.), inward.

(a) Horizontal Profile



(b) Vertical Profile

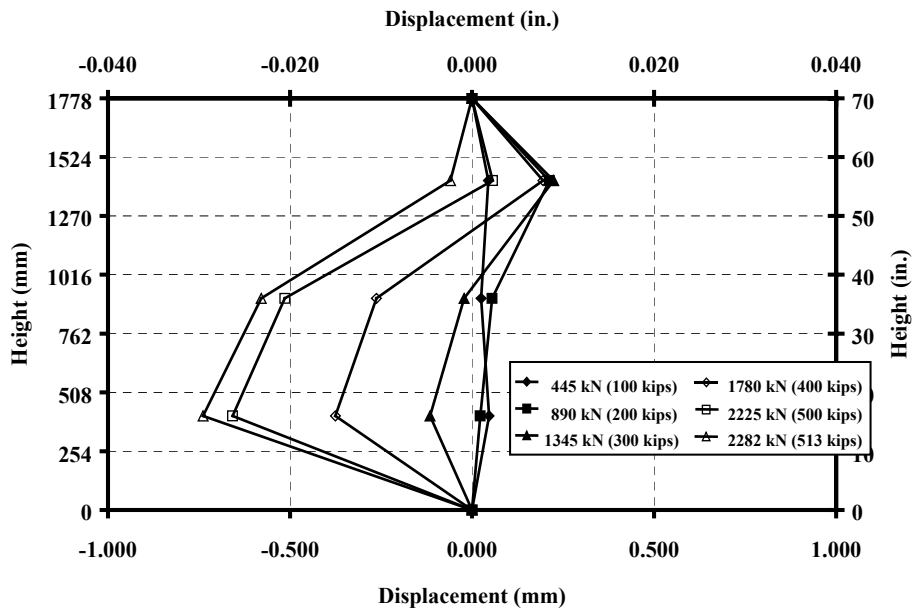


Figure 5.54 Specimen P12: Relative Displacements of East Wall

5.5.5 Rotations of the End Blocks

The rotations of the end solid blocks are shown in Fig. 5.55. All the measured rotations occurred in the expected directions. The rotations measured at the bottom about the east-west axis were similar to the rotations measured at the top. The rotations about the north-south axis of the top block were larger than the rotations measured at the bottom solid block. This was observed in several specimens and is discussed in Section 5.7.1.

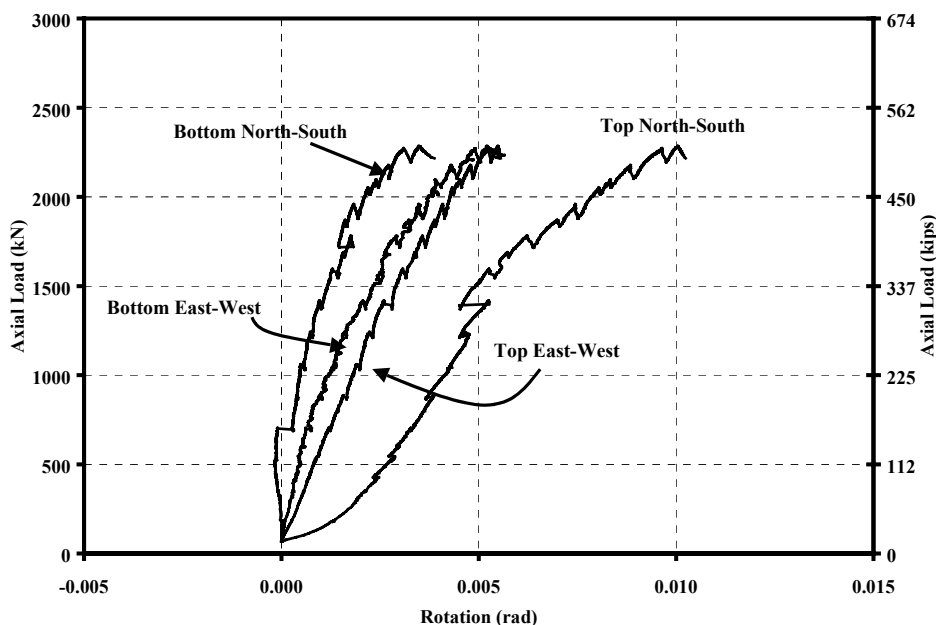


Figure 5.55 Specimen P12: Rotations of End Blocks

5.5.6 Vertical Deflections

The relative vertical deflections of Specimen P12 are shown in Fig. 5.56. The response measured along the centroidal axis of the cross-section was nearly linear up to an applied load of approximately 900 kN (200 kips), 25% larger than

the load at which first tension cracks were observed. The specimen continued to shorten, although at a reduced rate, up to an applied load of approximately 1600 kN (360 kips). At larger loads the response softened, with no reversal of the slope as the previous specimens exhibited. The maximum measured shortening was 1.4 mm (0.055 in.).

The axial shortening response measured at the point of application of the load exhibited a linear behavior up to a load near failure. The curve approached to a horizontal slope before failure. The maximum measured relative axial deflection was 6.4 mm (0.25 in.).

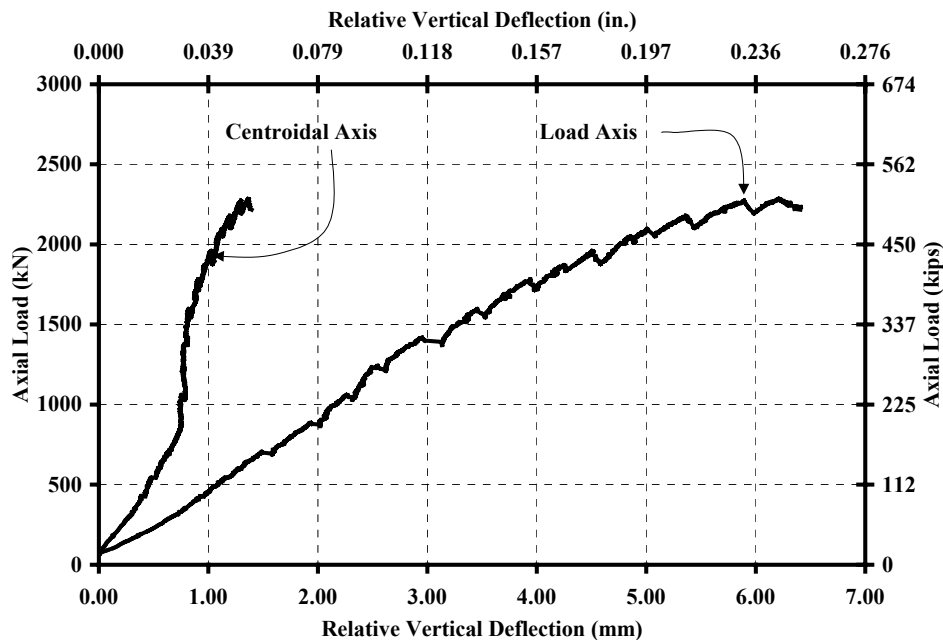


Figure 5.56 Specimen P12: Relative Vertical Deflections Measured at Center of End Blocks and at the Point of Application of Axial Load

5.5.7 Curvature

Measured relationships between moment and curvature are plotted in Fig. 5.57 and 5.58. At all load levels the curvatures about the east-west axis calculated using end rotations were larger than the curvatures calculated using longitudinal strains. Both moment-curvature responses showed very little softening at load levels near the failure load, which agrees with the failure mode that showed little damage of the concrete in compression before failure. The maximum curvature about the east-west axis calculated using the measured longitudinal strains was 0.00396 radians/m (1.00×10^{-4} radians/in.), smaller than the curvature calculated using the end rotations of the specimen, that was 0.00629 radians/m (1.60×10^{-4} radians/in.).

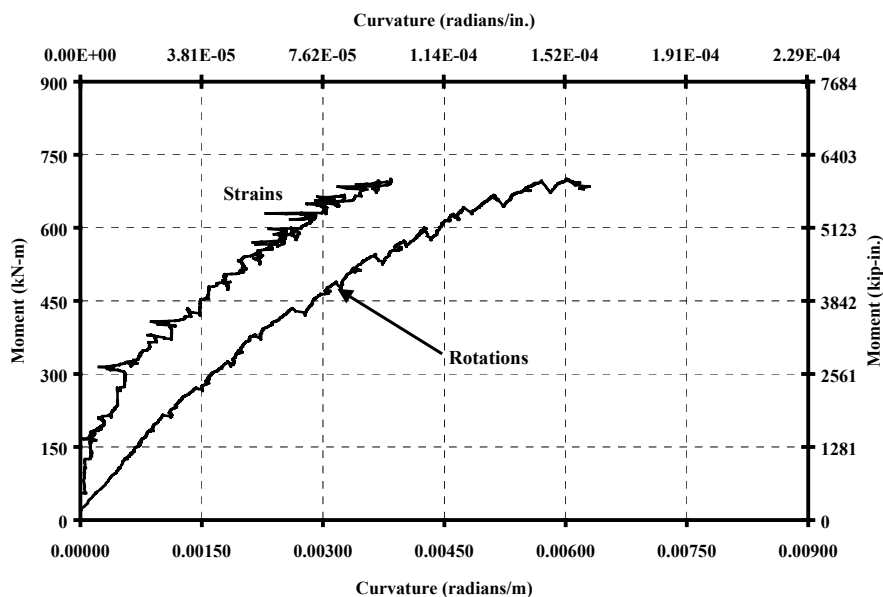


Figure 5.57 Specimen P12: Moment-Curvature Response about East-West Axis

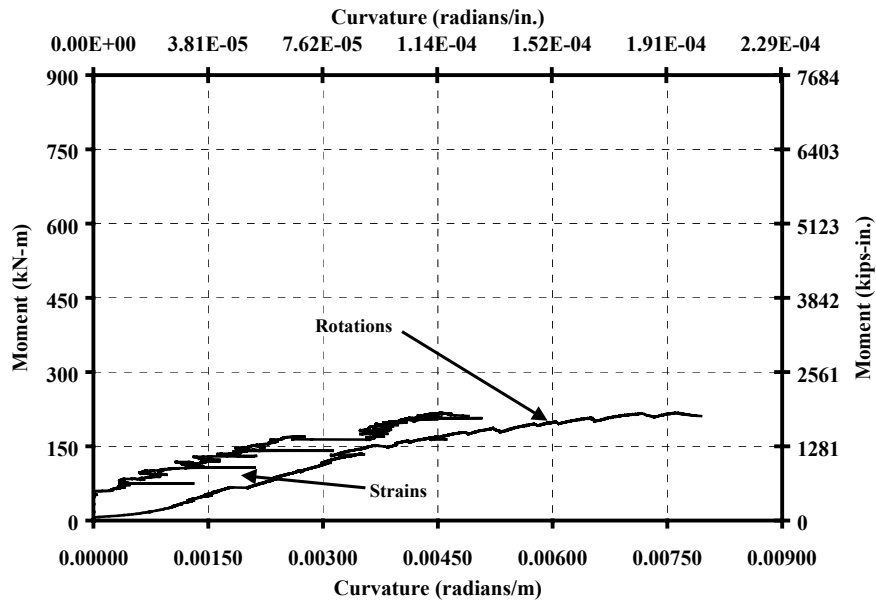


Figure 5.58 Specimen P12: Moment-Curvature Response about North-South Axis

The moment-curvature curves about the north-south axis calculated using both procedures were similar. The maximum curvature calculated using the measured longitudinal strains was 0.00507 radians/m (1.29×10^{-4} radians/in.), slightly larger than the curvature calculated using the rotations of the end blocks, which was 0.00474 radians/m (1.21×10^{-4} radians/in.).

5.6 MEASURED RESPONSE OF SPECIMEN P14

Specimen P14 failed explosively and without warning at an applied load of 1960 kN (440 kips), seconds after the last loading step was completed. A 125-mm (5-in.) zone of concrete, centered 90 mm (3.5 in.) below the top block, crushed (Fig. 5.59 and 5.60) and the longitudinal reinforcement buckled between adjacent transverse bars. The zone of crushed concrete extended 685 mm (27 in.)

along the east wall, along the entire length of the north wall, and 200 mm (8 in.) into the north end of the west wall.

5.6.1 Observed Crack Patterns

The first tension cracks were observed along the south and west walls, at an applied load of 530 kN (120 kips). The cracks extended from the southwest corner and were located at approximately one-half and one-quarter the height of the hollow section. Figures 5.61 and 5.62 show that the tension cracks extend along 50% the length of the west wall and along almost the entire length of the north wall. In general, the cracks were located at the elevations of the horizontal transverse reinforcement.

After the test, it was observed that the cracks extended through the entire thickness of the walls. Figure 5.61 shows the tension cracks converging towards the top of the northwest corner of the hollow section, close to the zone of spalled concrete. These cracks developed at the end of the test and were marked after the specimen failed.

Cracks were also observed in the end blocks. The first three cracks in the end blocks were observed along the east side of the top block and along the east and north sides of the bottom block, at an applied load of 1600 kN (360 kips). After the test, the top block exhibited four vertical cracks along the east side and two cracks along the north side. The bottom block exhibited one crack along the east side and one crack along the north side. Figure 5.63 shows photographs of the cracks on the east and north sides of the top end block, while the crack patterns on all sides of both end blocks are shown in Fig. 5.64.

Prior to failure the walls in compression had no signs of crushing of the concrete.

5.6.1 Behavior of the Reinforcement

The transverse reinforcing details at the northeast corner performed well, limiting the effective unbraced length of the longitudinal bars to the vertical spacing of the horizontal reinforcement in most locations. Figure 5.65 shows that in the east wall the longitudinal reinforcement buckled outward with an effective length between 1.5 to 2.0 times the vertical spacing of the transverse reinforcement. The interior of the pier could not be seen, but later examination showed that the longitudinal bars that formed the interior curtain had buckled inward.



Figure 5.59 Specimen P14: Photo of East Wall at End of Test



Figure 5.60 Specimen P14: Photo of North Wall at End of Test



Figure 5.61 Specimen P14: Photo of West Wall at End of Test

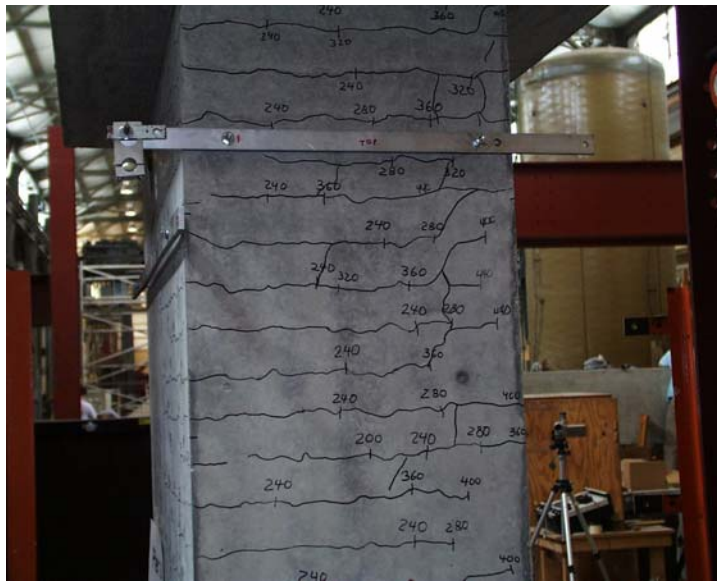


Figure 5.62 Specimen P14: Photo of South Wall at End of Test

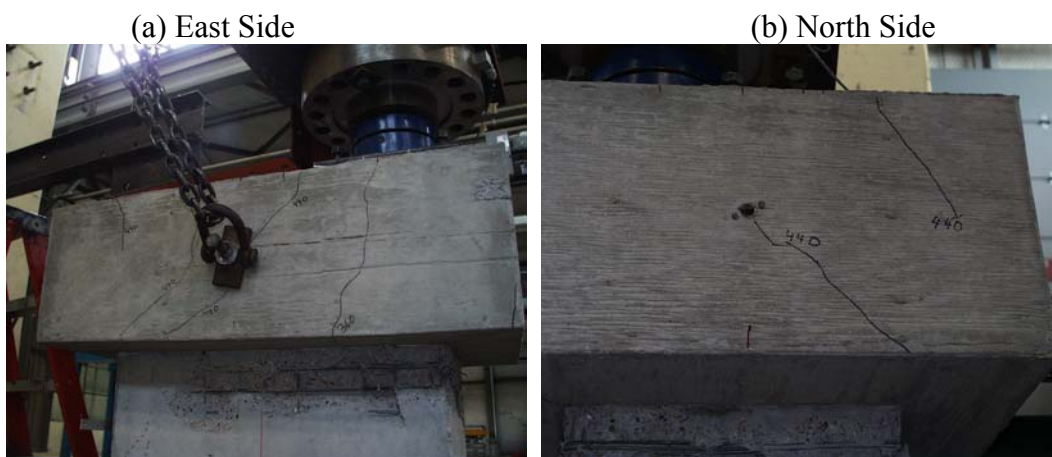


Figure 5.63 Specimen P14: Vertical Cracks at Top End Block

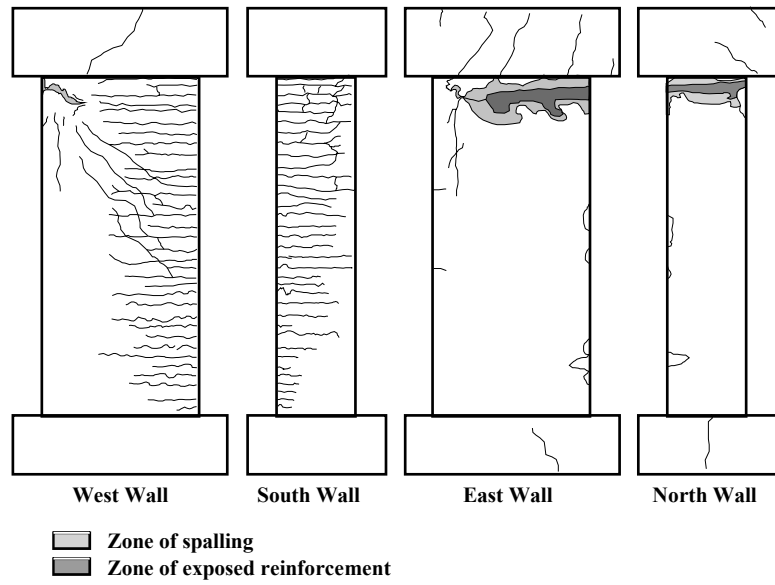


Figure 5.64 Specimen P14: Observed Crack Patterns



Figure 5.65 Specimen P14: Buckled Longitudinal Reinforcement near Top of East Wall

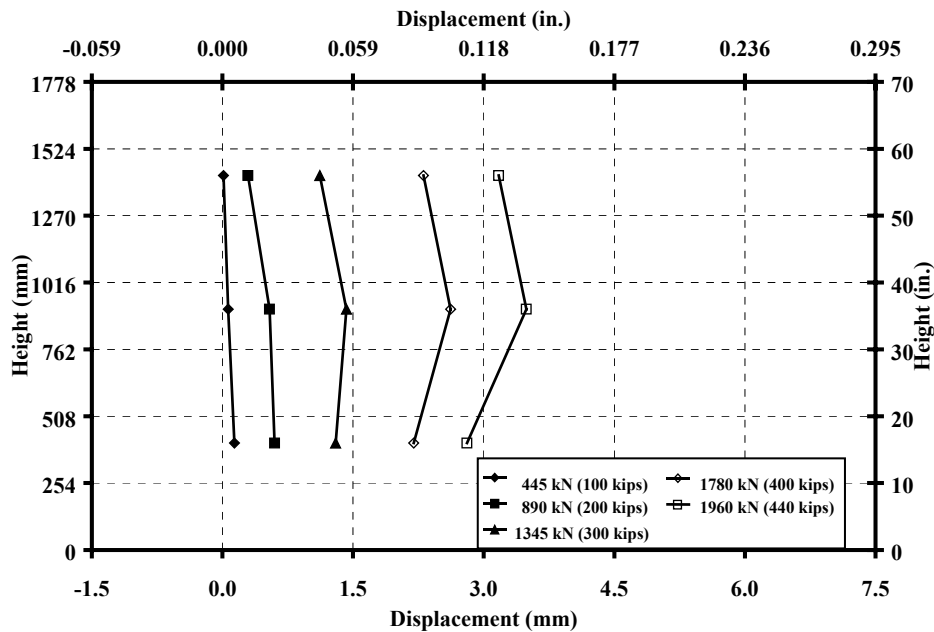
5.6.3 Longitudinal Profiles

The longitudinal profile of the specimen in the north-south direction is shown in Fig. 5.66(a). The deflected shape is similar to that expected for an element subjected to uniform bending moment along its length. The maximum horizontal deflection in the north-south direction occurred at midheight and was equal to 3.5 mm (0.14 in.). At load levels less than 45% of the failure load the deflections in the north-south direction were very small, less than 0.5 mm (0.02 in.) at midheight.

At an applied load of approximately 70% 1340 kN (300 kips), the horizontal deflection at midheight in the north-south direction, was approximately 40% of the maximum deflection at failure.

The maximum deflection in the east-west direction (Fig. 5.66(b)) occurred at midheight and was equal to 1.5 mm (0.06 in.). At load levels less than 890 kN (200 kips) the horizontal deflections were negative and the longitudinal profiles of the pier did not have the curvature expected for an element subjected to uniform moment. This behavior was observed in other specimens and is discussed in Section 5.3.1. At load levels near failure the deflections at midheight increased rapidly. The deflections in the east wall, measured near the bottom of the hollow section, were larger than the deflections measured at midheight of the specimen. This behavior was observed in several piers and is discussed in Section 5.7.1.

(a) Profile in North-South Direction



(b) Profile in East-West Direction

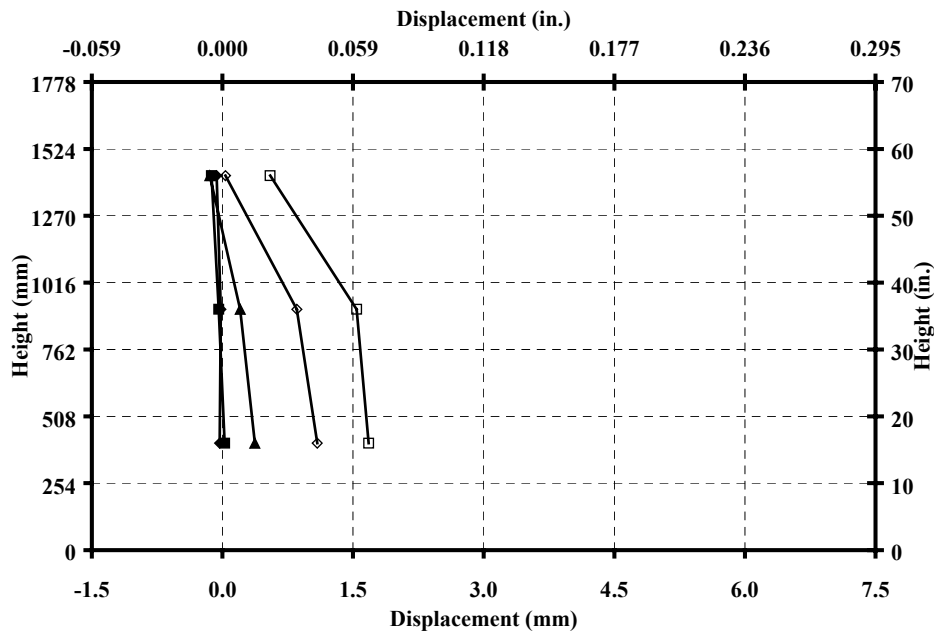


Figure 5.66 Specimen P14: Longitudinal Profile Measured Near North-East Corner

5.6.4 Profile of East Wall

Figure 5.67 shows the horizontal and vertical profiles of the east wall. At applied loads less than 50% of the capacity the center of the wall had very small relative deflection and the vertical profile exhibited double curvature shape. At larger load levels the relative deflection at the center of the wall panel increased rapidly outward and the vertical profile of the wall exhibited a single curvature shape. The maximum relative displacement occurred near the bottom of the wall and was equal to 0.8 mm (0.032 in.). The maximum relative deflection measured at the center of the wall was equal to 0.75 mm (0.03 in.).

(a) Horizontal Profile

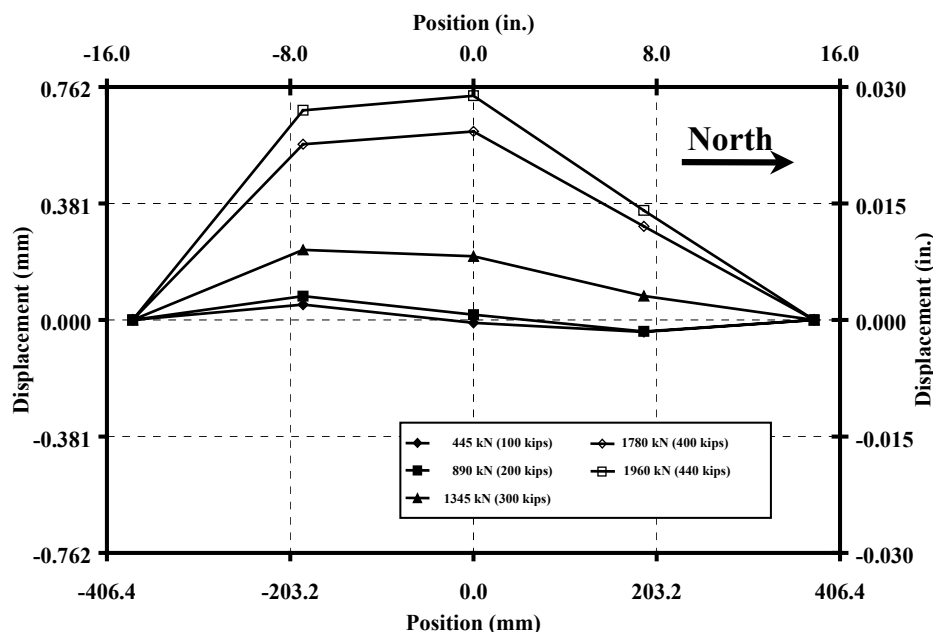


Figure 5.67 Specimen P14: Relative Displacements of East Wall

(b) Vertical Profile

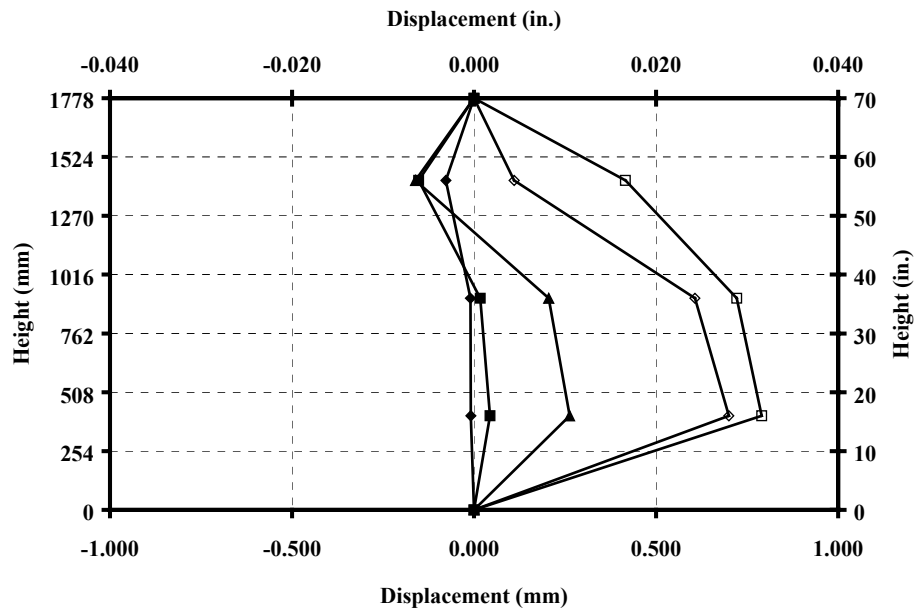


Figure 5.67 (Cont.) Specimen P14: Relative Displacements of East Wall

5.6.5 Rotations of the End Blocks

The rotations of the end solid blocks are shown in Fig. 5.68. All the measured rotations occurred in the expected directions. The rotations measured at the bottom about the east-west axis were similar to the rotations measured at the top. The rotations about the north-south axis of the top block were larger than the rotations measured at the bottom solid block. This was observed in several specimens and is discussed in Section 5.7.1.

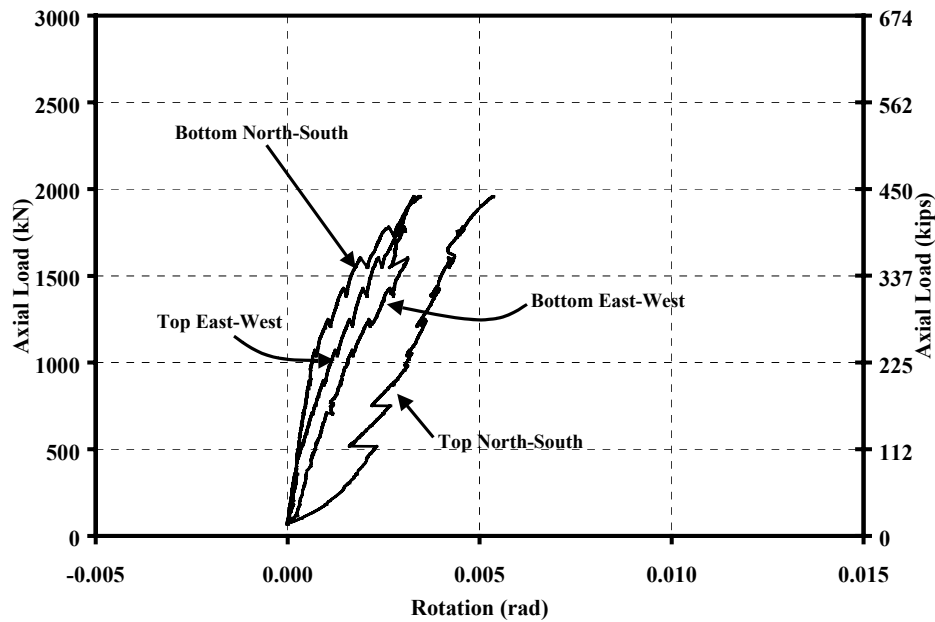


Figure 5.68 Specimen P14: Rotations of End Blocks

5.6.6 Vertical Deflections

The relative vertical deflections of Specimen P14 are shown in Fig. 5.69. The response measured at the centroid of the specimen was linear up to an applied load approximately equal to 95% of the capacity. At higher loads the slope of the response increased sharply and failure occurred shortly thereafter. The maximum measured shortening was 0.66 mm (0.026 in.).

The longitudinal shortening measured at the point of application of the load was linear, with constant slope, up to an applied axial load approximately equal to the capacity of the pier. The curve approached a horizontal slope before failure. The maximum measured relative axial deflection was 3.6 mm (0.14 in.).

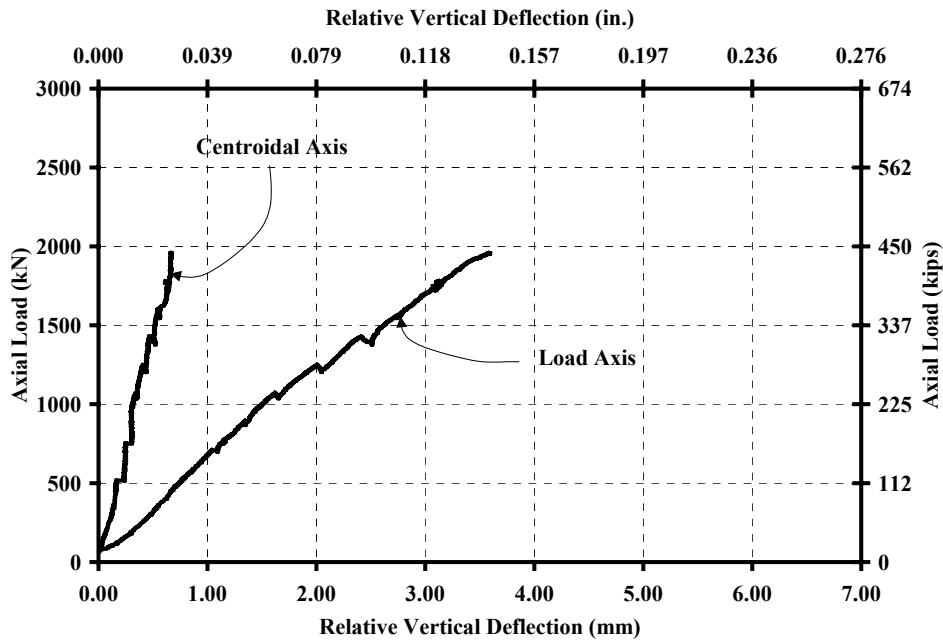


Figure 5.69 Specimen P14: Relative Vertical Deflections Measured at the Center of the End Blocks and at the Point of Application of the Axial Load

5.6.7 Curvature

The moment-curvature responses about the east-west and north-south axes are plotted in Fig. 5.70 and 5.71. The moment-curvature responses about the east-west axis were similar for the two methods used to calculate them. Both responses showed a slight softening at about 150 kN-m (1280 kip-in.), which corresponded to approximately to 450 kN (100 kips). That was very close to the load at which first tension cracks were observed. At larger loads the calculated responses were somewhat linear up to the failure load. This agrees with the observed failure mode, which was explosive failure of the walls in compression with no prior observed damage to the concrete.

The maximum curvature about the east-west axis, calculated using the measured longitudinal strains, was 0.00405 radians/m (1.04×10^{-4} radians/in.). The maximum curvature calculated using the rotations of the end blocks was 0.00380 radians/m (0.97×10^{-4} radians/in.).

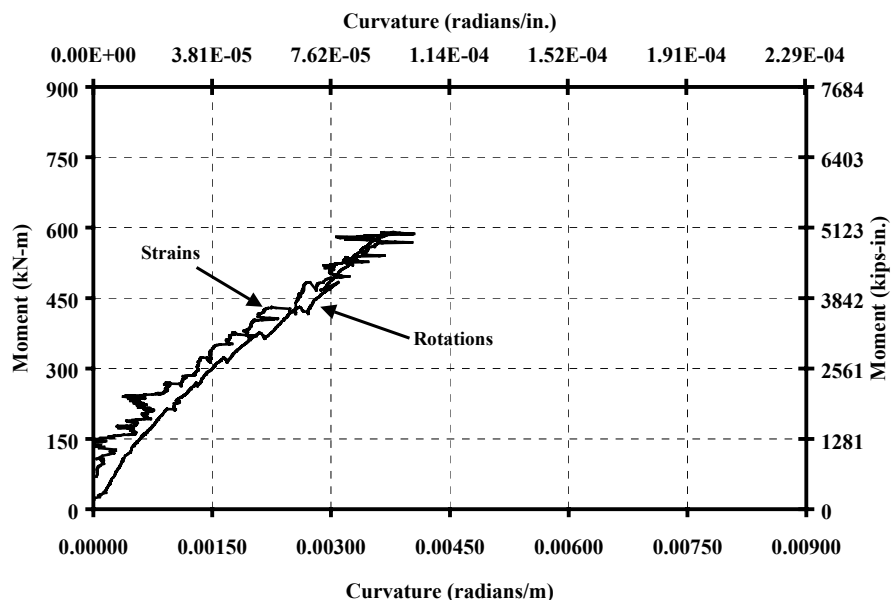


Figure 5.70 Specimen P14: Moment-Curvature Response about East-West Axis

Instruments ET and EB recorded no displacements up to load levels equal to 90% of failure load (Fig. 14e), suggesting that those instruments did not work properly; therefore, the moment-curvature response was not calculated about the north-south axis using measured strains. The response calculated using end rotations was linear up to failure load, which agrees with the explosive failure

mode observed. The maximum calculated curvature about the north-south axis was 0.00625 radians/m (1.59×10^{-4} radians/in.).

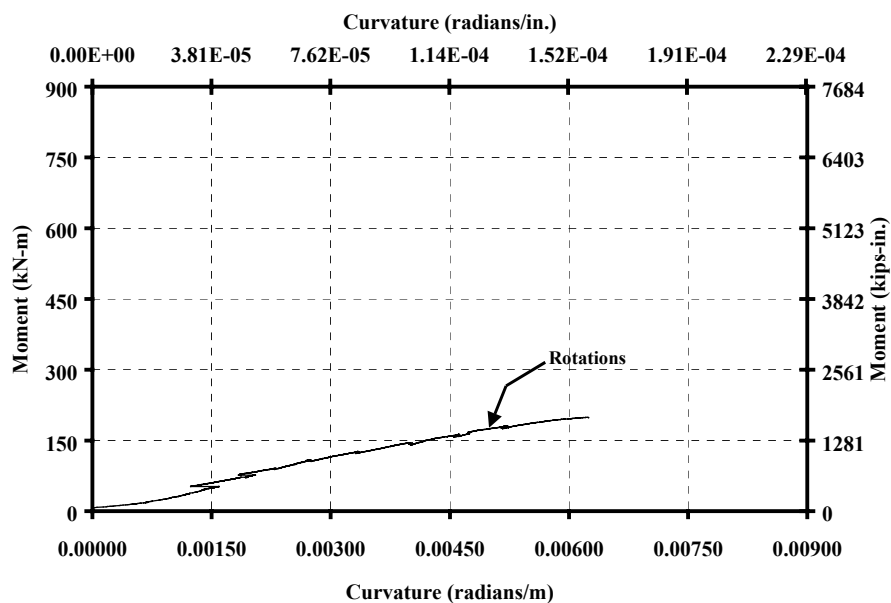


Figure 5.71 Specimen P14: Moment-Curvature Response about North-South Axis

5.7 DISCUSSION OF EXPERIMENTAL RESULTS

In this section the measured data and observed behavior of the five test specimens are summarized and compared. When the measured data do not agree with the expected response, possible explanations are provided.

5.7.1 Longitudinal Profiles

The longitudinal profiles of the piers, measured in the north-south and east-west directions, were shown in Fig. 5.12, 5.25, 5.38, 5.53, and 5.66. The key

load-deflection relationships for all specimens are summarized in Figures 5.72 and 5.73.

In the north-south direction, Specimens P10, P12, and P14 exhibited the expected deflected shape for members subjected to uniform bending moment. Specimens P6 and P8 exhibited different profiles: the horizontal deflections at the top were approximately the same as the deflections at midheight. The end block rotations about the east-west axis for these two specimens were also similar: the top blocks experienced less rotation than the bottom blocks (Fig. 5.14 and 5.27).

The maximum deflection occurred at midheight for all specimens and varied between 3.5 and 7.0 mm (0.14 and 0.28 in.). The north-south deflections at midheight recorded by instrument P19 for all specimens are plotted in Fig. 5.72. Except for P8, the maximum horizontal deflection tended to decrease as the wall slenderness ratio increased. Also, the stiffness of the specimens decreased at an applied load approximately equal to the load at which cracks were first observed in the south and west walls.

On average, the horizontal deflection was less than 45% of the maximum deflection at an applied load equal to 75% of the failure load. As the applied load increased, the deflections increased rapidly.

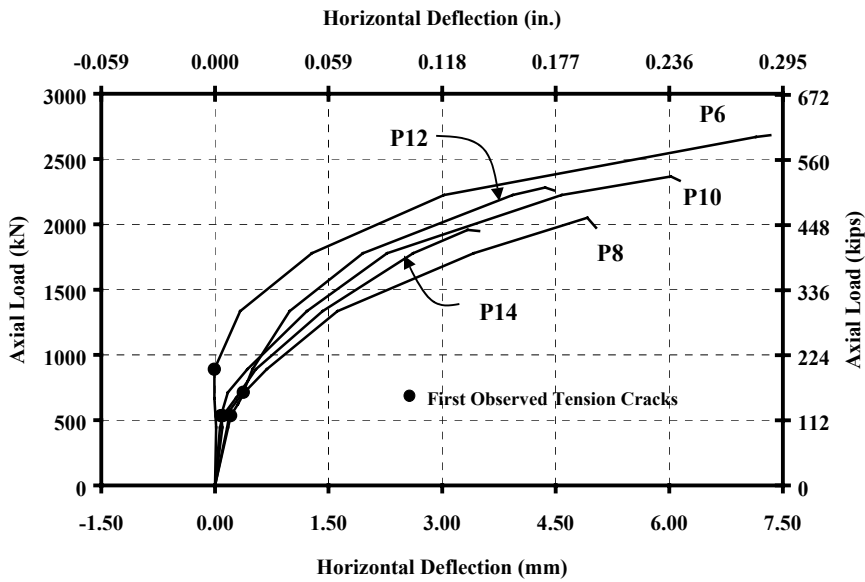


Figure 5.72 *Horizontal Deflection Measured at Midheight of the Piers in the North-South Direction*

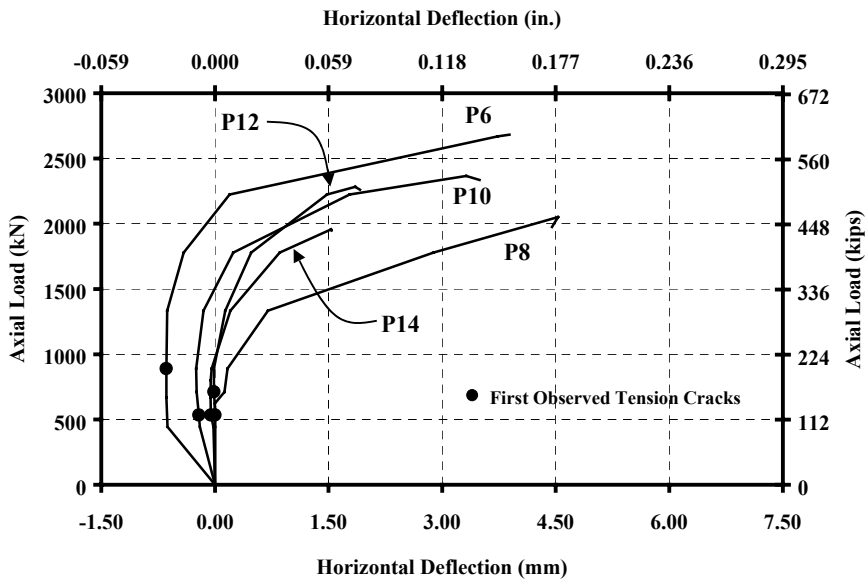


Figure 5.73 *Horizontal Deflection Measured at Midheight of the Piers in the East-West Direction*

In the east-west direction, the maximum deflection at midheight varied between 1.5 and 4.6 mm (0.06 and 0.18 in.). The east-west deflections at midheight for all specimens recorded by instrument P10 are plotted in Fig. 5.73. The deflections followed trends similar to those observed in the north-south direction.

In the east-west direction, piers P6 and P8 exhibited longitudinal profiles similar to those expected for a specimen loaded under uniform bending moment. Specimens P10, P12, and P14 exhibited different profiles. The horizontal deflections at the bottom were approximately the same as the deflections at midheight. The end block rotations about the north-south axis for these three specimens were also similar, the bottom blocks experienced less rotation than the top blocks (Fig. 5.40, 5.55, and 5.68).

The piers that experienced the expected deflected shape for members subjected to uniform bending moment exhibited almost equal end block rotations at the top and the bottom.

The shape of the measured longitudinal profiles can be explained by considering two possible hypotheses: (1) the top block translated while these specimens were tested, or (2) the specimens were misaligned before the tests. Under the first hypothesis, the piers would experience rigid-body rotations caused by translation of the top block. The resulting end rotations would differ at the top and bottom, but the rotations due to bending would be the same. Under the second hypothesis, the eccentricities at the two ends would be different. This condition

would lead to unequal rotations at top and bottom. Each hypothesis is investigated in the following paragraphs.

(a) Influence of Possible Lateral Translation of the Top Block

The possibility that the top blocks translated slightly during the tests is investigated in this section. Translations of the bottom blocks were not considered, because the bottom bearing plate was welded to a plate that was attached to the laboratory floor by bolts (Fig. 4.26). The top block of the specimens and the bottom end of the loading ram, however, were not restrained against horizontal displacements (Fig. 4.27). Therefore, it was possible for the top block to experience small horizontal translation during the tests.

The following discussion will demonstrate that the measured north-south and east-west displacement profiles and end block rotations could occur during the tests if the top of the specimens displaced to the south or to the east relative to the bottom of the specimens.

Figure 5.74 shows the idealized configuration of the test specimens, in the north-south direction. The pier is subjected to a uniform bending moment about the east-west axis. If there is no horizontal displacement at the top of the pier (Fig. 5.74 (a)), if the curvature is uniform along the length of the pier, and if the end blocks have infinite stiffness, the resulting rotations of the end blocks, θ , are equal and the horizontal deflection at any location along the length of the pier is given by

$$u(x) = \theta \left(x + H_b - \frac{x^2}{H} \right) \quad (5.10)$$

where $u(x)$ is the horizontal displacement of the east wall of the pier, x is the height above the bottom end block, H is the clear height of the pier, and H_b is the height of the end blocks.

The assumption of uniform curvature assumes that cracking was uniform along the height of the specimens. The cracking patterns of the specimens after failure (Fig. 5.10, 5.23, 5.36, 5.50, and 5.64) show that, at load levels close to the ultimate load, the cracks distributed evenly along the height of the specimens and had similar lengths. Therefore, it is reasonable to assume uniform curvature along the length of the specimens.

The same pier is shown in Fig. 5.74(b), but the top end block has been displaced horizontally a small distance to the south, Δ_{top} . The rigid-body rotation of the axis of the specimen is given by

$$\alpha = \frac{\Delta_{top}}{H + 2H_b} \quad (5.11)$$

Assuming the curvature is uniform along the length of the pier, the measured end block rotations, θ_{bot} and θ_{top} , would be given by

$$\theta_{bot} = \theta + \alpha \quad (5.12)$$

$$\theta_{top} = \theta - \alpha \quad (5.13)$$

The rigid body rotation of the axis of the specimen, α , can also be calculated from the measured end rotations, θ_{bot} and θ_{top} , as

$$\alpha = \frac{\theta_{bot} - \theta_{top}}{2} \quad (5.14)$$

For the case of translation to the south, the rotations at the top of the specimen are smaller than the rotations at the bottom. If the horizontal deflections are measured relative to the vertical axis, then deflections measured above

midheight will be larger than the deflections measured below midheight. These trends agree with the displacement measurements recorded during the tests. Therefore, it is possible that Specimens P6 and P8 experienced horizontal southward displacements at the top of the specimens during the tests.

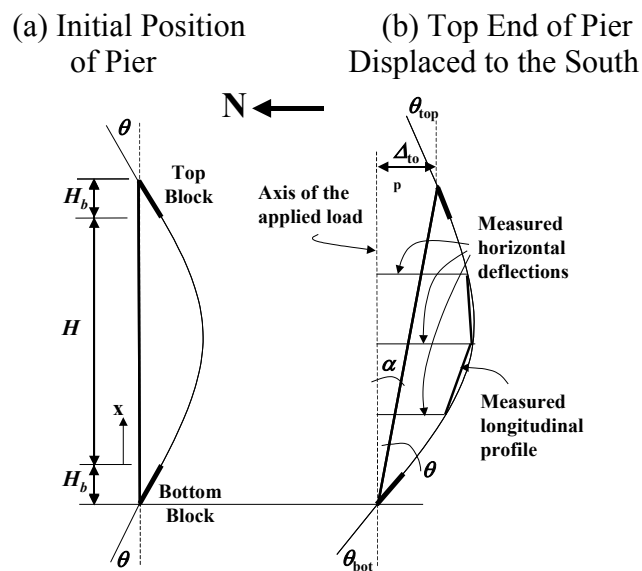


Figure 5.74 Longitudinal Displacement Profile for Pier without and with Horizontal Displacement of the Top Block in the South Direction

Figure 5.75 is similar to Fig. 5.74, but shows the idealized configuration of the test specimens in the east-west direction. The pier is subjected to a uniform bending moment about the north-south axis. If there is no horizontal displacement at the top of the pier, the resulting rotations of the end blocks, θ , are equal and the horizontal deflection at any location along the length of the pier is given by Eq. 5.10.

The same pier is shown in Fig. 5.75(b), but the top end block has been displaced horizontally a small distance to the east, Δ_{top} . The rigid body rotation of the axis of the specimen is given by Eq. 5.11. The measured end block rotations would be θ_{bot} and θ_{top} , given by

$$\theta_{bot} = \theta - \alpha \quad (5.15)$$

$$\theta_{top} = \theta + \alpha \quad (5.16)$$

The rigid body rotation of the axis of the specimen, α , can be calculated as

$$\alpha = \frac{\theta_{top} - \theta_{bot}}{2} \quad (5.17)$$

For this configuration, the rotations at the top are larger than the rotations at the bottom. The horizontal deflections measured below midheight are larger than those measured above midheight. These trends agree with the displacement measurements recorded during the tests of Specimens P10, P12, and P14. Therefore, it is possible that these specimens experienced horizontal displacements at the top in the east direction.

From Eq. 5.12 through 5.16, the rotation of the ends of the pier with respect to its own axis can be calculated as the average of the measured rotations:

$$\theta = \frac{\theta_{top} + \theta_{bot}}{2} \quad (5.18)$$

and the horizontal displacement of the top of the specimen, Δ_{top} , can be calculated as

$$\Delta_{top} = \alpha(H + 2H_b) \quad (5.19)$$

The horizontal displacement at any location along the length of the pier can then be calculated by adding or subtracting the horizontal displacement due to rigid-body rotation from the displaced shape for the idealized deflections

(Eq. 5.10). Equation 5.20 gives the resulting horizontal displacement at any location along the pier.

$$u(x) = \theta \left(x + H_b - \frac{x^2}{H} \right) \pm \alpha (x + H_b) \quad (5.20)$$

where the positive sign is used when the top of the specimen has translated to the south and the negative sign is used when the top of the specimen has translated to the east.

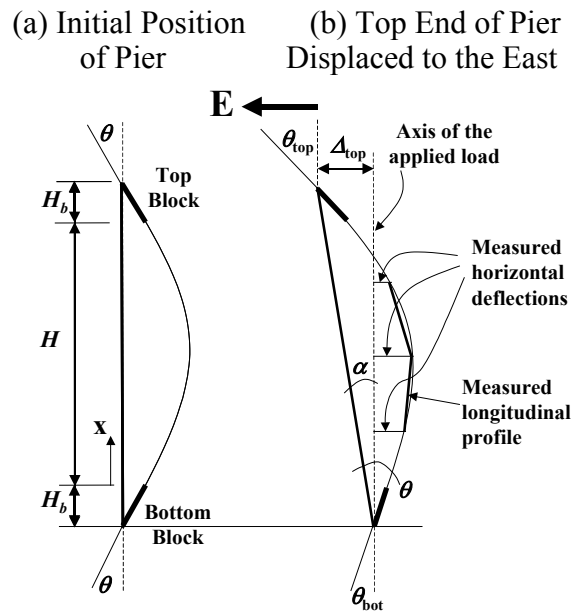


Figure 5.75 Longitudinal Displacement Profile for Pier without and with Horizontal Displacement of Top Block in the East Direction

Longitudinal profiles in the north-south and east-west directions were calculated assuming that the top of the specimens displaced horizontally during the tests. Equations 5.14, 5.17, 5.18, and 5.20, and the measured end rotations, θ_{bot} and θ_{top} , were used to calculate the rigid-body rotation and longitudinal profiles at the measured capacity of each specimen. The results of these analyses

are summarized in Table 5.2 and the calculated displacement profiles are compared with the measured profiles in Fig. 5.76 and 5.77.

The procedure used to calculate the longitudinal profiles in the north-south direction slightly underestimated the measured horizontal displacements of Specimens P8, P10, P12, and P14. The displacements of Specimen P6 were underestimated by approximately 35%. The measured horizontal displacements of Specimens P8, P10, and P14 in the east-west direction were slightly overestimated by the procedure, and the measured horizontal displacements of Specimen P6 were overestimated by more than 50%. The displacements in the east-west direction of Specimen P12 were slightly underestimated. All the calculated longitudinal profiles exhibited the same shape as the measured longitudinal profiles.

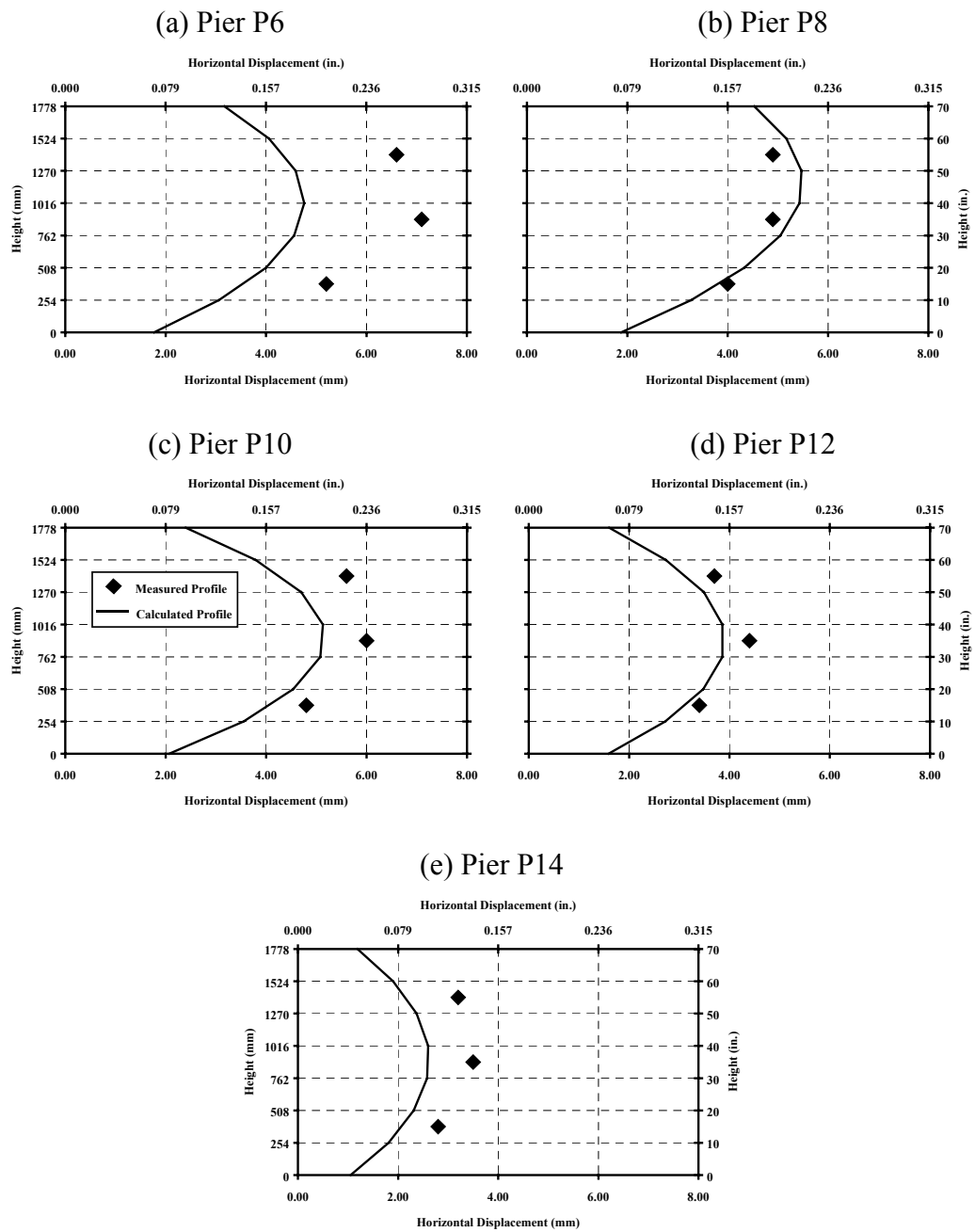


Figure 5.76 Measured and Calculated Longitudinal Profiles in the North-South Direction at Ultimate Load

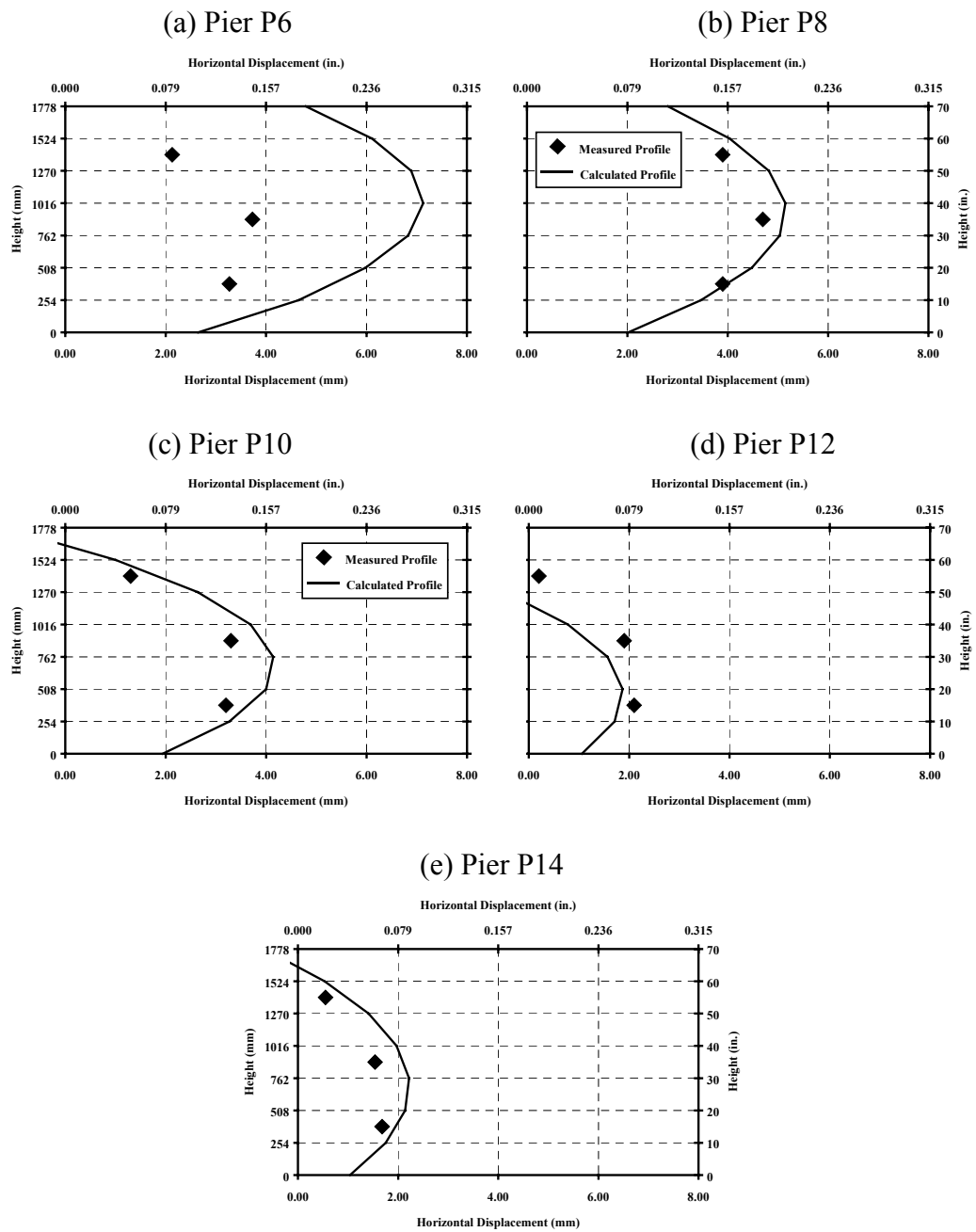


Figure 5.77 Measured and Calculated Longitudinal Profiles in the East-West Direction at Ultimate Load

Table 5.2 Calculated Rigid-Body Translations and Rotations of the Top Blocks at the Measured Capacity of the Piers

Specimen ID	Top Displacement in South Direction		Top Displacement in East Direction		Rigid Body Rotation About the East-West Axis rad.	Rigid Body Rotation About the North-South Axis rad.
	mm	(in.)	mm	(in.)		
P6	1.9	(0.075)	-2.9	(-0.11)	0.00077	-0.00120
P8	3.7	(0.15)	-1.1	(-0.04)	0.00149	-0.00045
P10	0.3	(0.012)	5.0	(0.20)	0.00010	0.00206
P12	-0.4	(-0.016)	8.0	(0.31)	-0.00014	0.00295
P14	0.2	(0.008)	2.4	(0.09)	0.00008	0.00096

The calculated horizontal translations at the top varied from 0.2 to nearly 4 mm (0.008 to 0.15 in.) in the north-south direction, and from 1 to 8 mm (0.04 to 0.3 in.) in the east-west direction. These displacement levels of the top end block correspond to less than a 1% change in the nominal eccentricity in the north-south direction, and between 1 and 8% change of the nominal eccentricity in the east-west direction. Because the calculated accidental eccentricities in the north-south direction are within expected experimental tolerances, the assumption of uniform moment and uniform curvature along the length of the piers appears reasonable. However, the calculated accidental eccentricities in the east-west direction are too large to be ignored.

(b) Influence of Possible Initial Misalignment of the Test Specimens

The possibility that the deflected longitudinal shape of the specimens was produced by an initial misalignment of the piers at the beginning of the tests was also studied. An initial misalignment could have led to unequal eccentricities at the top and bottom of the specimens. As a result, the moments and curvature would vary along the length. In this discussion, it is assumed that the base of the specimen was aligned correctly, and the curvature varied linearly along the length of the specimen. Therefore, if the curvature about either axis of the pier is ϕ_{bot} at the bottom, then the curvature about the same axis at the top can be written as:

$$\phi_{top} = (1 + \beta)\phi_{bot} \quad (5.21)$$

A positive value of β means that the misalignment at the top increases the eccentricity of the applied load. A negative value of β indicates that the misalignment at the top reduces the eccentricity. A value of β smaller than -1.0 represents a pier with double curvature. Figure 5.78 shows the deflected shape of a specimen and the variation of curvature along it. The end blocks were assumed to be infinitely stiff in bending.

The factor β and the end eccentricities are related through the moment-curvature relationship of the piers. If the relationship between moment and curvature is proportional, and the moment of inertia is assumed to be equal along the length of the pier, then the eccentricities are also related by β :

$$e_T = (1 + \beta)e_B \quad (5.22)$$

where e_T is the actual eccentricity at the top and e_B is the actual eccentricity at the bottom, which is assumed to be equal to the nominal eccentricity. At levels of

applied load near failure, moment and curvature are not proportional and Eq. 5.22 is not valid.

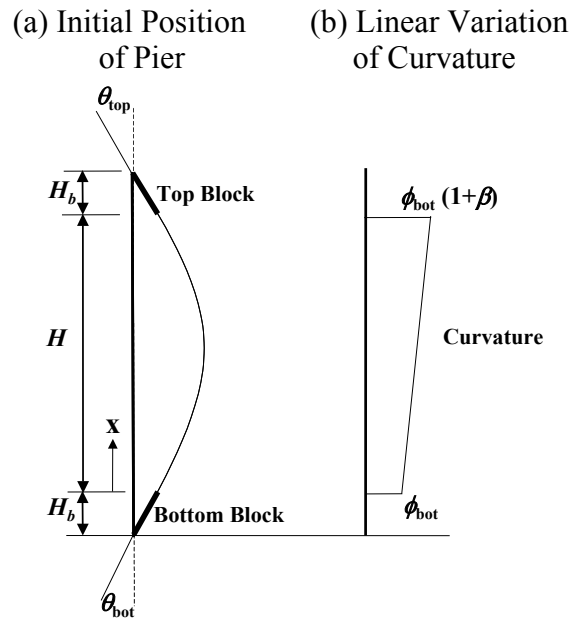


Figure 5.78 Longitudinal Displacement Profile for Pier without Horizontal Displacement of the Top Block, with Linear Variation of the Curvature Along the Specimen.

Using Eq. 5.21, the difference between the top and bottom curvatures can be calculated as:

$$\Delta\phi = (\phi_{top} - \phi_{bot}) = \beta\phi_{bot} \quad (5.23)$$

Figure 5.79 helps to explain how the eccentricities at the top can be determined using the calculated values of β at any level of applied load. The difference between the top and bottom moments, ΔM , can be calculated from the moment-curvature relationship using $\Delta\phi$ and the corresponding curvature at the bottom, ϕ_{bot} . Then, the corresponding eccentricity at the top, e_T , is given by:

$$e_T = e_B + \left(\frac{\Delta M}{M_{bot}} \right) e_B \quad (5.24)$$

where M_{bot} is the moment at the bottom corresponding to ϕ_{bot} . It can be seen that for a given value of ΔM , the value of β increases as the applied load increases.

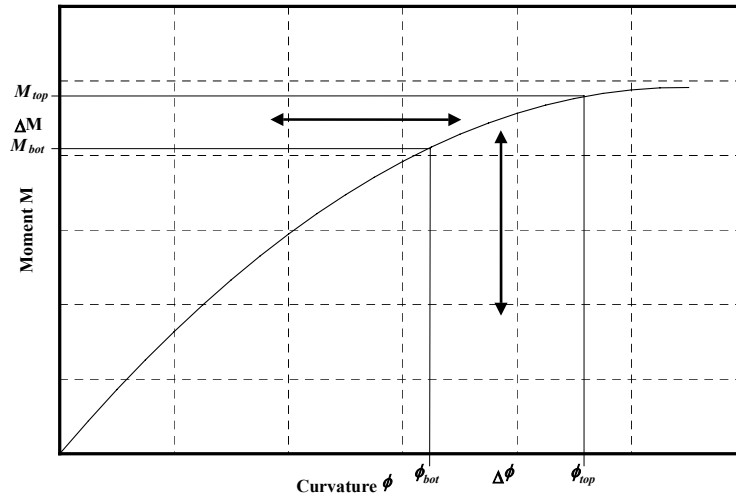


Figure 5.79 Determination of Changes in Moment due to Changes in Curvature

Integrating the curvature along the length of the member leads to the following rotations at the ends of the pier.

$$\theta_{bot} = -\frac{H}{2} \phi_{bot} \left(1 + \frac{\beta}{3} \left(\frac{H + 3H_b}{H + 2H_b} \right) \right) \quad (5.25)$$

$$\theta_{top} = -\frac{H}{2} \phi_{bot} \left(1 + \frac{\beta}{3} \left(\frac{2H + 3H_b}{H + 2H_b} \right) \right) \quad (5.26)$$

where θ_{bot} and θ_{top} are the measured end rotations. The ratio of the rotation of the top end to the rotation of the bottom end of the specimens, r_θ , can be calculated using Eq. 5.25 and 5.26 as

$$r_{\theta} = \frac{\theta_{top}}{\theta_{bot}} = \frac{3(H + 2H_b) + \beta(2H + 3H_b)}{3(H + 2H_b) + \beta(H + 3H_b)} \quad (5.27)$$

The value of β can be calculated using the measured end rotations from Eq. 5.27 as:

$$\beta = 3 \frac{(r_{\theta} - 1)(H + 2H_b)}{((2H + 3H_b) - r_{\theta}(H + 3H_b))} \quad (5.28)$$

Equation 5.28 is plotted in Fig. 5.80. The denominator of Eq. 5.28 is equal to zero for a ratio of end rotations given by:

$$r_{\theta} = \frac{(2H + 3H_b)}{(H + 3H_b)} = 1.66 \quad (5.29)$$

This represents a case in which the moment at the bottom is zero. For values of r_{θ} larger than 1.66, β is less than -1.0 , which requires that the specimen to loaded in double curvature. For values of r_{θ} close to 1.66 the corresponding values of β are large and can be unrealistic.

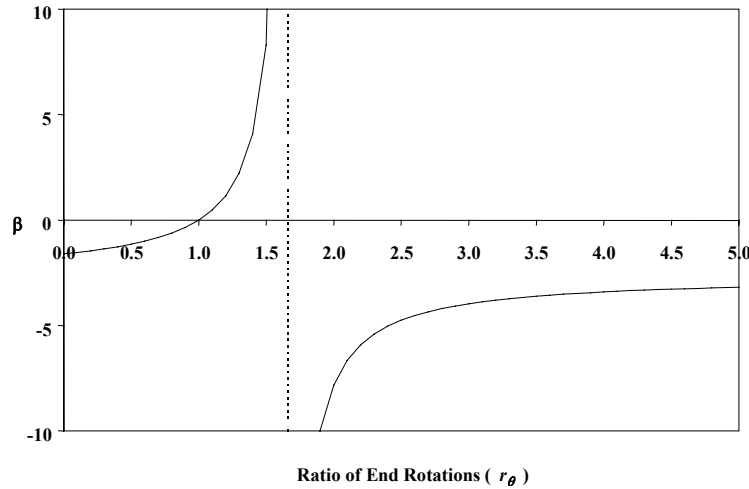


Figure 5.80 Variation of β as Function of the Ratio of Top to Bottom End Rotations (r_{θ})

The lateral deflection at any point along the length of the pier is obtained by integrating Eq. 5.21 and substituting into Eq. 5.25:

$$u(x) = \theta_{bot} \left(x + H_b - \left(\frac{x^2}{2} + \beta \frac{x^3}{6H} \right) \left(\frac{H + 2H_b}{H + 2H_b + \frac{\beta}{3}(H + 3H_b)} \right) \right) \quad (5.30)$$

Table 5.3 summarizes the values of β and e_T calculated using the measured end rotations at the measured axial capacity. With the exception of Specimens P10, P12, and P14 in the north-south direction, and Specimen P8 in the east-west direction, the values of β and the differences between the calculated and nominal eccentricities are too large to be feasible. Misalignments of this order of magnitude would have been obvious to the casual observer.

Table 5.3 Calculated Values of β at the Measured Capacity

Specimen ID	Calculated β		Top Eccentricity e_T mm (in.)	
	North-South Direction	East-West Direction	North-South Direction	East-West Direction
P6	-0.77	-0.76	115 (4.5)	57 (2.25)
P8	-1.13	-0.47	-40 (-1.56)	79 (3.10)
P10	-0.12	57.0	300 (11.8)	1024 (40.3)
P12	0.23	-4.1	335 (13.2)	-315 (-12.4)
P14	-0.13	5.1	279 (11.0)	620 (24.4)

Longitudinal profiles in the north-south and east-west directions were calculated using Eq. 5.27, 5.28, and 5.30 and the measured end rotations, θ_{bot} and

θ_{top} . The calculated displacement profiles are compared with the measured profiles in Fig. 5.81 and 5.82.

The procedure used to calculate the longitudinal profiles based on the assumption of an initial misalignment underestimated the horizontal displacements in the north-south direction and overestimated the displacements in the east-west direction. Profiles based on the assumption of an initial misalignment of the calculated longitudinal profiles differed significantly from the measured profiles. The hypothesis of an initial misalignment leads to unrealistic values of β (Table 5.3).

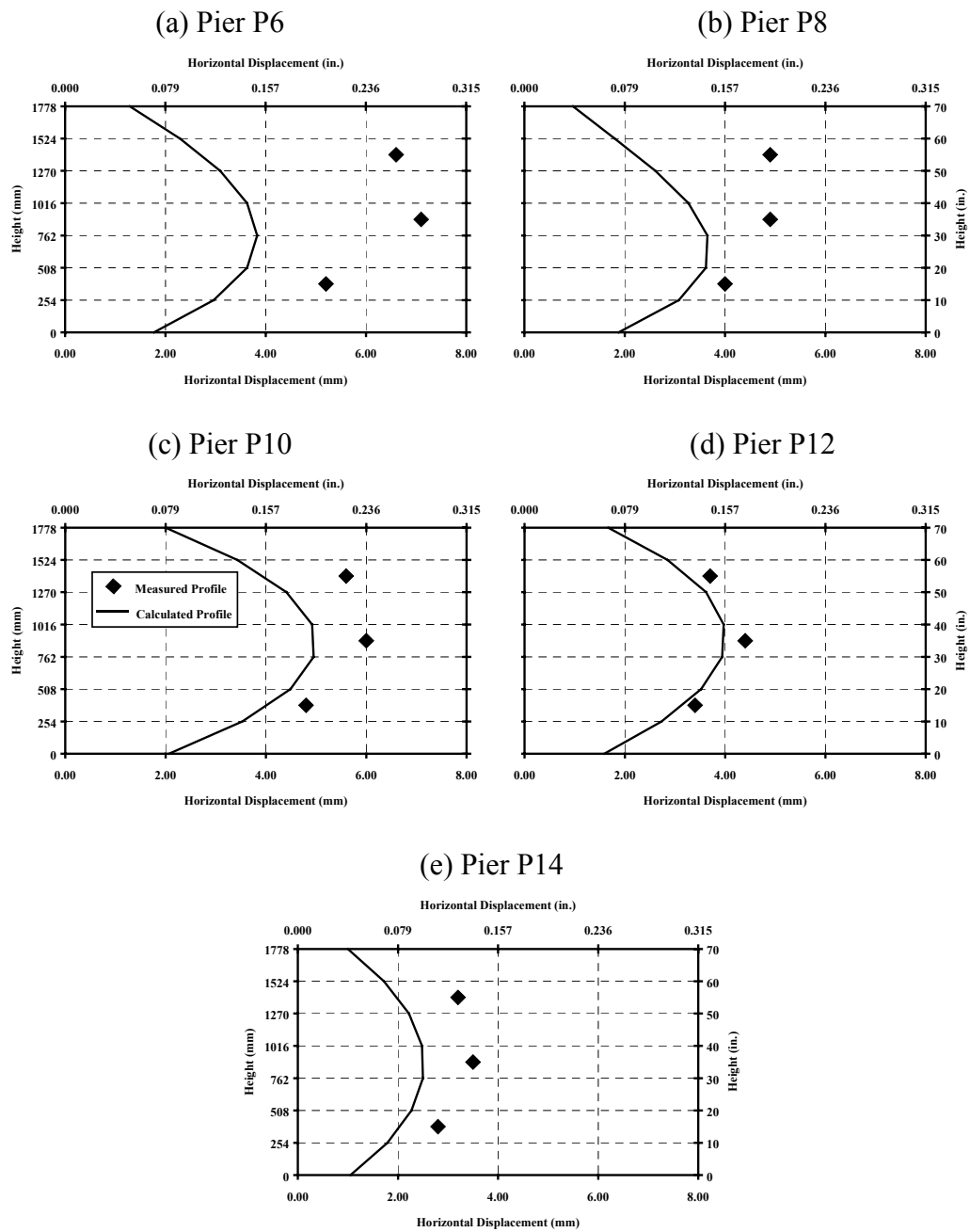


Figure 5.81 Measured and Calculated Longitudinal Profiles in the North-South Direction at Ultimate Load

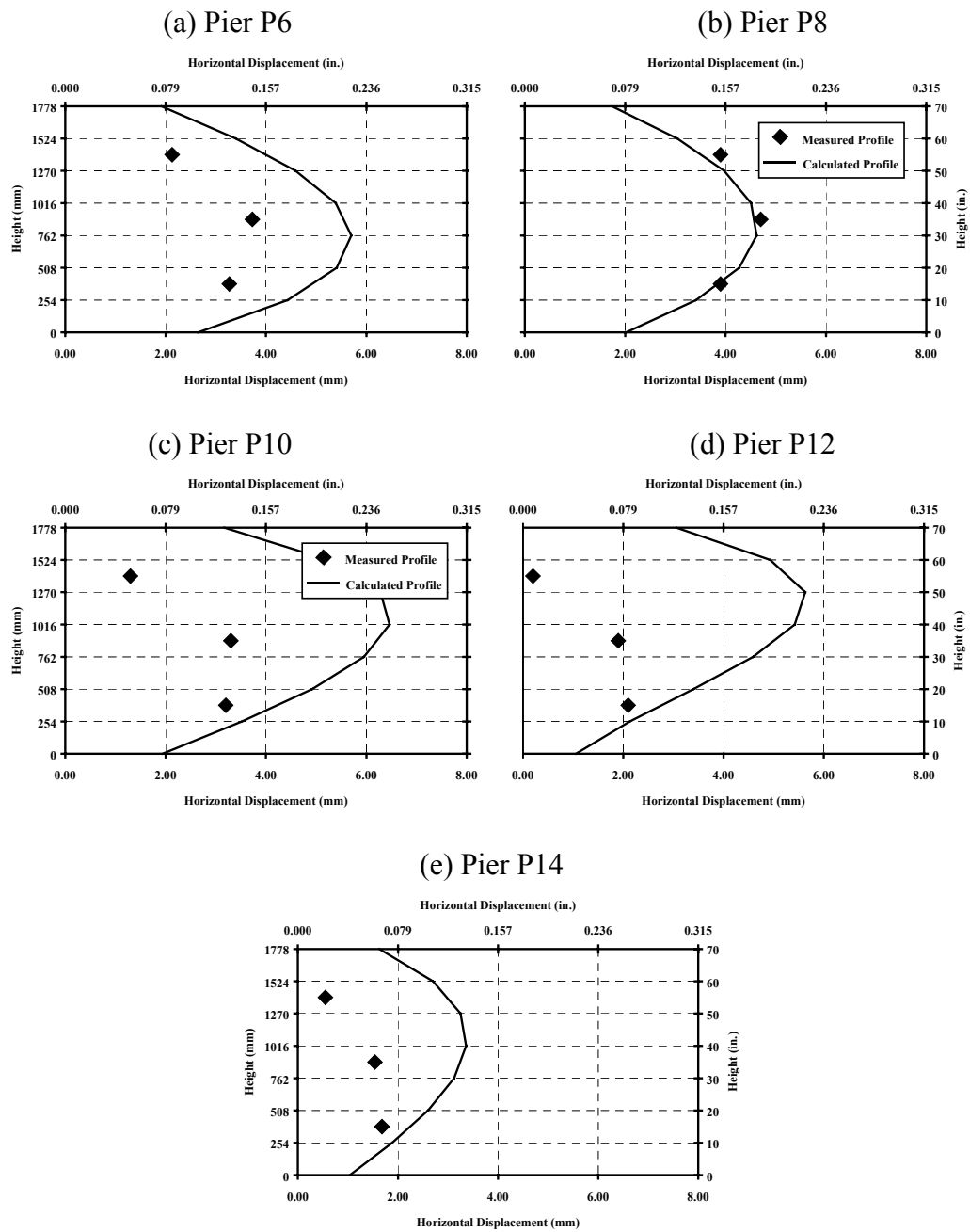


Figure 5.82 Measured and Calculated Longitudinal Profiles in the East-West Direction at Ultimate Load

(c) Influence of Simultaneous Varying Curvature and Translation of the Top Block

In Section 5.7.1(a), the longitudinal profiles of the piers are calculated assuming that the specimens exhibited a horizontal translation of the top block and their curvature was uniform along their height. Calculated translations in the east-west direction at the top of the pier, however, are considered too large to satisfy the assumption of uniform curvature.

In Section 5.7.1(b), the piers are analyzed assuming that misalignment of the specimens produced a linear variation of the curvature along the height, and that the piers did not experience translation of the top. In that section, the calculated values of the initial misalignment are judged too large to be feasible.

In this section the displacement profiles are calculated assuming that the specimens experienced horizontal translation in the east-west direction, and that the curvature varied linearly along the height of the piers (Eq. 5.21).

Assuming that the tops of the piers did not translate, the rotations at the ends of the piers are given by Eq. 5.25 and 5.26.

$$\theta_B = -\frac{H}{2}\phi_{bot}\left(1 + \frac{\beta}{3}\left(\frac{H + 3H_b}{H + 2H_b}\right)\right) \quad (5.31)$$

$$\theta_T = -\frac{H}{2}\phi_{bot}\left(1 + \frac{\beta}{3}\left(\frac{2H + 3H_b}{H + 2H_b}\right)\right) \quad (5.32)$$

For the purpose of this discussion, θ_B and θ_T will be used to represent the end rotations without translation and θ_{bot} and θ_{top} will be used to represent the end rotations due to combined translation and varying curvature (Fig. 5.83).

The ratio of the rotation of the top end to the rotation of the bottom end of the specimens, r_θ , can be calculated using Eq. 5.31 and 5.32 as

$$r_\theta = \frac{\theta_T}{\theta_B} = \frac{3(H + 2H_b) + \beta(2H + 3H_b)}{3(H + 2H_b) + \beta(H + 3H_b)} \quad (5.33)$$

If the specimen also experienced horizontal translation of the top block to the east during the tests (Fig. 5.83), then the rotations at the two ends are given by:

$$\theta_{bot} = \theta_B - \alpha \quad (5.33)$$

$$\theta_{top} = \theta_T + \alpha \quad (5.34)$$

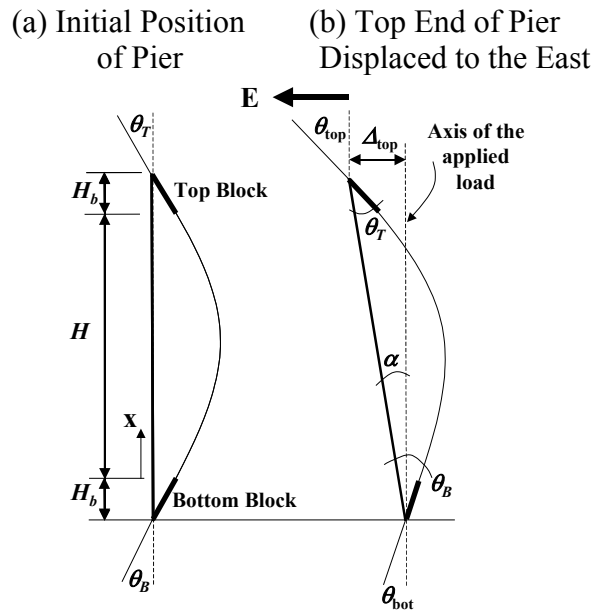


Figure 5.83 Longitudinal Displacement Profile for Pier without and with Horizontal Displacement of the Top Block in the East Direction and with Linear Variation of the Curvature Along the Height

As in the previous discussions, the measured rotations are used to evaluate the assumed displaced shape of the piers. Therefore, using the measured rotations of the end blocks, θ_{bot} and θ_{top} , the rotations due to the varying curvature, θ_B and θ_T , can be calculated as:

$$\theta_B = \frac{\theta_{bot} + \theta_{top}}{(1 + r_\theta)} \quad (5.35)$$

$$\theta_T = r_\theta \frac{\theta_{bot} + \theta_{top}}{(1 + r_\theta)} \quad (5.36)$$

The rigid-body rotation, α , is obtained from Eq. 5.33, Eq. 5.34, and 5.35 and is given by

$$\alpha = \frac{\theta_{top} - r_\theta \theta_{bot}}{(1 + r_\theta)} \quad (5.37)$$

Because r_θ depends only on β and the geometrical properties of the pier, the rotations due to the varying curvature, θ_B and θ_T , and the rigid-body rotation, α , can be calculated using the measured rotations and an assumed value of β .

The horizontal displacement at any location along the length of the pier can then be calculated by adding or subtracting the horizontal displacement due to the rigid body rotation from the displaced shape calculated from the assumed curvature distribution (Eq. 5.30). Equation 5.38 gives the horizontal displacements at any location along the pier.

$$u(x) = \theta_B \left(x + H_b - \left(\frac{x^2}{2} + \beta \frac{x^3}{6H} \right) \left(\frac{H + 2H_b}{H + 2H_b + \frac{\beta}{3}(H + 3H_b)} \right) \right) - \alpha(x + H_b) \quad (5.38)$$

To estimate the value of β to be used in the analysis it is necessary to know the difference between the bottom and top eccentricities. It is assumed that the change in eccentricity was produced by the translation of the top end. Therefore, the horizontal displacements calculated in Section 5.7.1(a) in the east direction (Table 5.2) are used as the difference in eccentricity between the bottom and top ends. The maximum displacement calculated represents an increase of 8% in the eccentricity in the east direction. The values of β are determined as shown in Fig. 5.79, using the moment-curvature relationships about the north-south axis (Fig. 5.17, 5.30, 5.43, 5.58, and 5.71) and the eccentricities estimated with the horizontal translation of the top end.

It was found that changes in the eccentricity at the top of 3% or less produced changes of approximately 10% in the values of the measured curvatures at the top of the pier. Changes of eccentricity of 5% and 7% produced changes of 20% and 30% in the top curvature, respectively. These values of β are used in the analyses and the calculated displacements of the top end in the east direction are listed in Table 5.4. The horizontal translations listed in Table 5.4 are similar to those calculated assuming uniform curvature along the height of the piers and listed in Table 5.2.

Also, longitudinal profiles in the east-west direction were calculated using Eq. 5.33 through 5.39 for values of β ranging from -0.3 to 0.3 . The calculated horizontal displacements were within 10% of the horizontal displacements calculated assuming β equal to zero and plotted in Fig. 5.77.

Table 5.4 Calculated Translations of the Top Blocks in the East Direction Assuming Linear Variation of the Curvature Along the Length of the Piers at the Measured Capacity

Specimen ID	β	Translation at the Top of Pier in East Direction mm (in.)		Change of Eccentricity with Respect to the Nominal Eccentricity (%)
P6	-0.1	-2.7	(-0.11)	-2.6
P8	-0.1	-0.9	(-0.04)	-1.0
P10	0.2	4.4	(0.17)	4.3
P12	0.3	7.6	(0.30)	7.5
P14	0.1	2.1	(0.08)	2.1

(d) Possible Explanation of the Shape of the Measured Longitudinal Profiles

It was shown in the previous sections that the assumption that the top of the piers translated slightly during the tests is plausible. The longitudinal profiles calculated using the measured end rotations exhibited the same shape as the measured profiles.

It was also shown that the observed response was probably not due to an initial misalignment of the specimens, because misalignments calculated from the measured rotations were extremely large. Misalignments of this magnitude would have been obvious from the photographic records.

Finally, it was shown that the longitudinal profiles calculated under the assumption that the top of the piers translated slightly during the tests and that the curvature varied linearly along the height of the specimens, differed by less than 10% from the profiles calculated assuming uniform curvature.

Therefore, it is concluded that small horizontal displacements of the top of the piers that occurred during loading, changed the measured longitudinal profiles. In addition, the assumption that the curvature was uniform along the height of the specimens is apparently reasonable. Therefore, the moment-curvature response calculated using measured end block rotations represents a reasonable estimate of the actual response of the specimens in bending.

A possible explanation for the lateral displacement of the top end block in the east-west direction may be found in the lateral stiffness of the testing frame. The test apparatus was not braced against horizontal displacements. An initial misalignment between the applied load and the floor reaction of the specimens would result in a horizontal force applied at the top spherical bearings. The horizontal reaction, V , applied at the top spherical bearing at a given load level P can be calculated as:

$$V = \frac{\delta}{(H + 2H_b)} P \quad (5.39)$$

where δ is the misalignment of the vertical end reactions and H and H_b are the height of the pier and the end blocks, respectively, and are defined in Fig. 5.83.

Simplifying, the horizontal displacement in the east-west direction of the testing frame can be calculated assuming one end of the columns fixed and the other free. The displacement of the frame, Δ_{frame} , is given by:

$$\Delta_{frame} = \frac{V_{col}L^3}{3EI} \quad (5.40)$$

where V_{col} is the applied horizontal load in each column, which is equal to 1/4th of the force applied at the end of the ram; L is the height of the column (5.08 m (200 in.)); E is the modulus of elasticity of the steel (2000 MPa (29000 ksi)); and I is the moment of inertia about the weak axis of the columns (70000000 mm⁴ (168in⁴)). Equation 5.40 is evaluated for Specimen P12, using a value of misalignment equal to the translation of the top block calculated in the previous section and listed in Table 5.4 (δ equal to 7.6 mm (0.30 in.)); and the ultimate measured load P equal to 2280 kN (513 kips). The horizontal displacement of the testing frame is estimated to be 5.6 mm (0.22 in.), which is very similar to the estimated displacement of the top end block mentioned before, 7.6 mm (0.30 in.).

Therefore, horizontal translation of the testing frame due to possible misalignment of the line of action of the applied vertical load and the floor reaction may be a reasonable explanation of the horizontal displacement estimated at the top end block of the test specimens.

5.7.2 Profiles of the East Walls

The horizontal displacements were measured at fifteen locations along the east walls. The relative horizontal profile at midheight and vertical profile at the center of the walls were plotted in Fig. 5.13, 5.26, 5.39, 5.54, and 5.67.

At failure, the horizontal and vertical profiles exhibited shapes representative of single curvature. Specimens P6, P8, P10, and P14 exhibited outward relative deflection, while Specimens P12 experienced inward relative deflection prior to failure. The maximum relative horizontal displacement was not linked to the location of the failure. The same trends in the shape of the profiles and the location of the maximum relative displacement can be found in the results of Taylor et al. (1990). In most of the specimens tested by Taylor et al., the profiles for the walls in compression exhibited outward deflections in single curvature. The profile of the compression wall in one specimen, 11ML34, exhibited double curvature.

The maximum relative horizontal deflections measured in this research were very small, ranging from 0.45 to 0.8 mm (0.018 to 0.032 in.). These values are quite similar to those measured by Taylor et al. (1990), which varied between 0.5 and 2.0 mm (0.02 and 0.08 in.). In both studies the maximum relative horizontal deflection tended to increase with increasing wall slenderness ratio (Fig. 5.84).

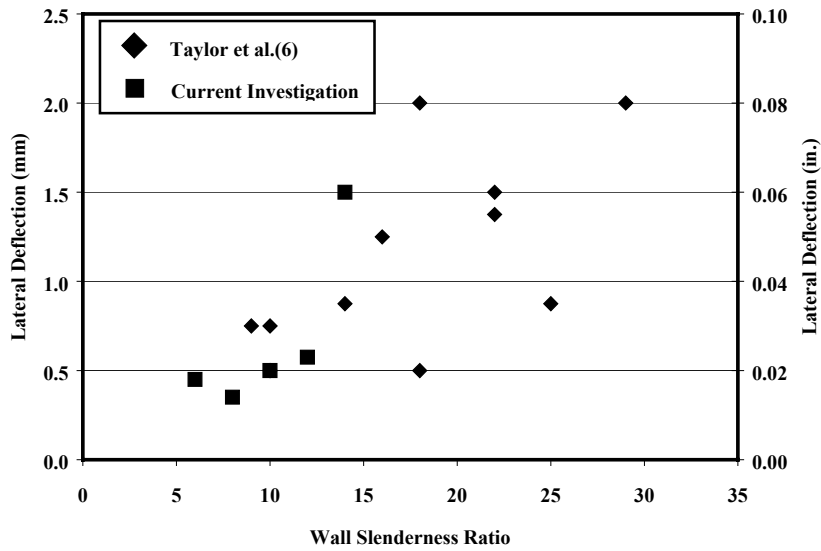


Figure 5.84 Maximum Relative Horizontal Displacement of East Walls

5.7.3 Rotations of the End Blocks

The rotations of the end blocks were plotted in Fig 5.14, 5.27, 5.40, 5.55, and 5.68. All specimens experienced similar behavior. The stiffness of the measured response decreased as the applied load was increased. At loads near failure, the slope of the response was nearly zero. Specimen P14 was the only specimen that failed before experiencing a significant reduction in stiffness. The differences in the measured rotations of the top and bottom blocks were explained in Section 5.7.1.

The average end-block rotations, θ , were calculated about each axis using Eq. 5.16, and are plotted in Fig. 5.85 and 5.86. The average rotations of the end blocks of Specimens P8, P10, P12, and P14 were similar, while those of Specimen P6 were slightly lower.

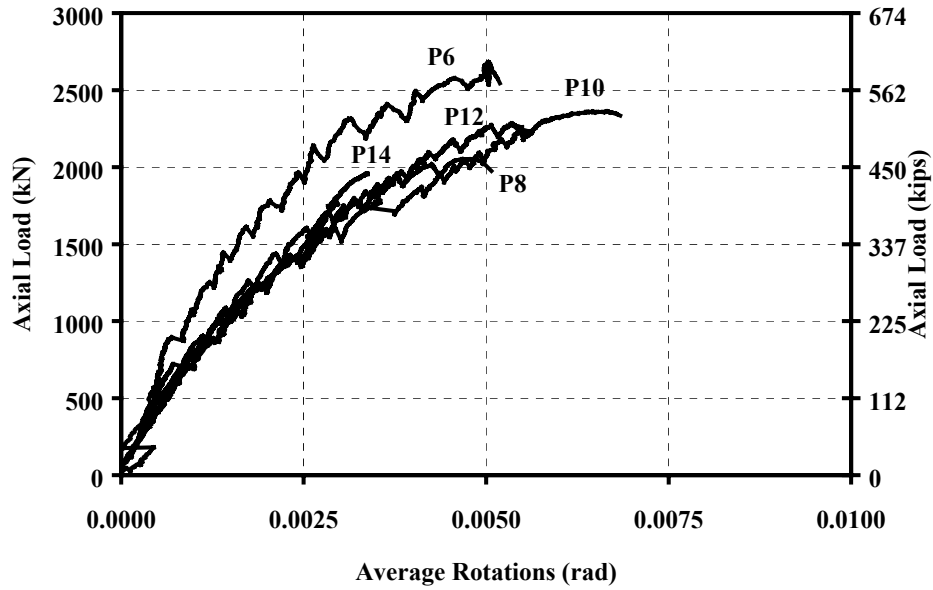


Figure 5.85 Average End-Blocks Rotations about the East-West Axis

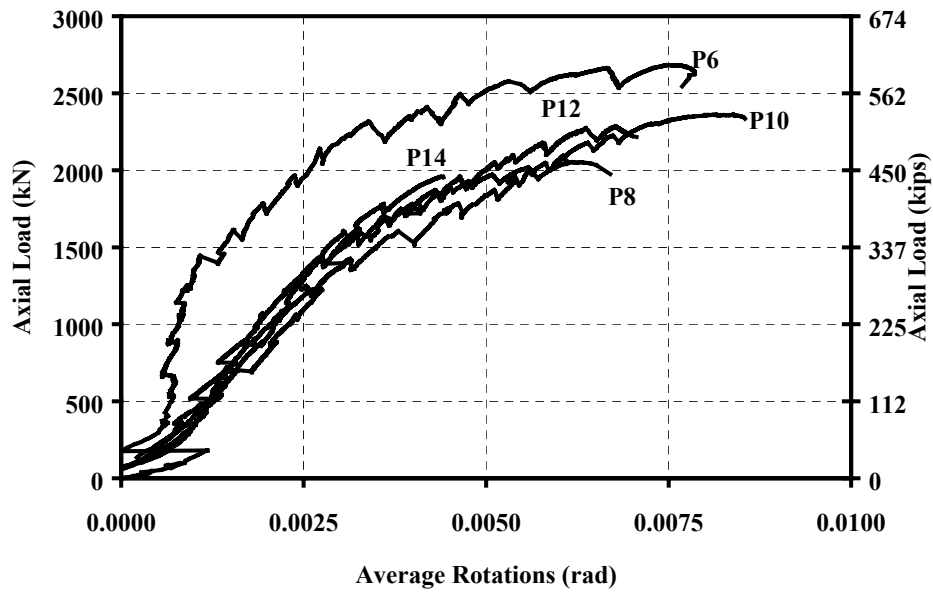


Figure 5.86 Average End-Blocks Rotations about the North-South Axis

The maximum end-block rotations about the north-south axis were larger than those about the east-west axis. While the rotations about the north-south axis varied between 0.0044 to 0.0085 radians, while the rotations about the east-west axis ranged from 0.0034 and 0.0068 radians.

No clear trend was observed between the maximum average rotation of the end blocks and the wall slenderness ratio.

5.7.4 Vertical Deflections

Relative vertical deflections were calculated at two locations: (1) along the centroidal axis of the cross-section; and (2) along the line of application of the load.

The maximum measured axial shortening of the centroidal axis varied between 0.23 and 1.4 mm (0.009 and 0.055 in.). No clear trends are observed between the maximum axial deflections along the centroidal axes and the wall slenderness ratios. The relative axial deflections are very small if compared with the axial deformations of the piers subjected to concentric axial load. Assuming a strain in the concrete equal to 0.003 at the maximum load, the deflection would have been 5.3 mm (0.21 in.). The smaller axial deflection can be explained by looking at the shape of the measured response.

All the specimens exhibited similar response: axial stiffness was very low at low loads, and increased after the walls cracked (with the exception of P6, which experienced a sharp increase in slope before any cracks were observed). At higher levels of applied load, axial stiffness continued to increase. Specimen P8

experienced a reversal of the axial deflection curve, and the relative axial deflection decreased as the load increased (Fig. 5.87).

At a load near 85% of the crushing load, the response curves exhibited a second change of slope. In Specimens P6, P8 and P10 the slope of the response became negative (reversal of the axial deflection curve), while for P14 the curve became almost vertical. This change in the slope of the response was not observed in Specimen P12.

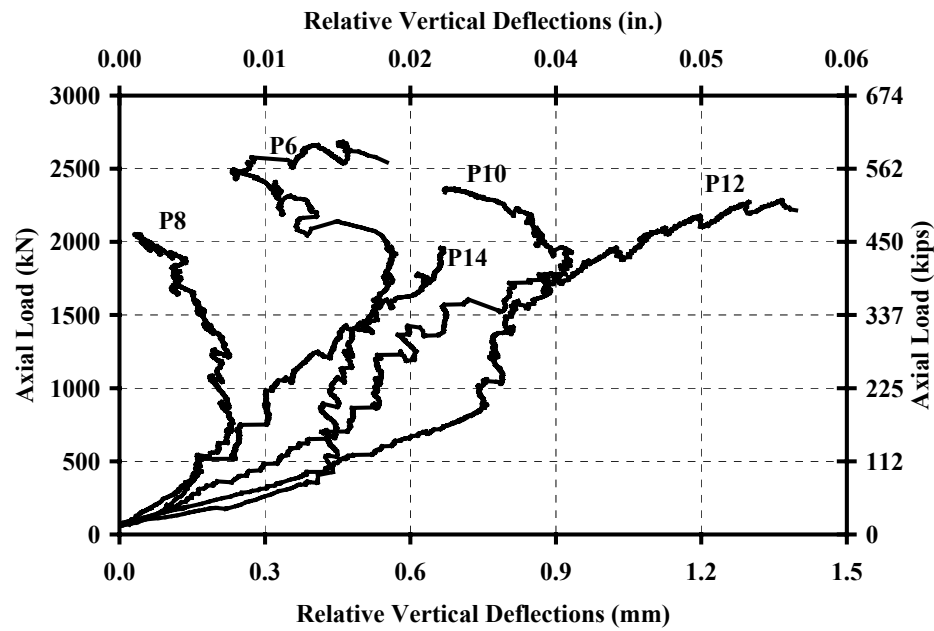


Figure 5.87 Relative Axial Deflections Measured at the Center of End Blocks

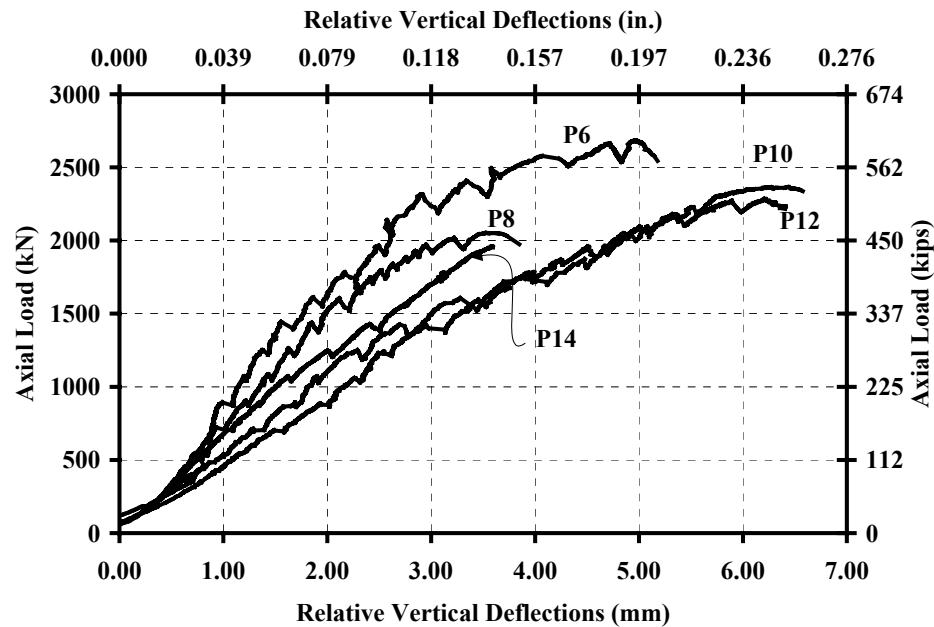


Figure 5.88 *Relative Axial Deflections Measured on the Line of Application of the Axial Load*

The apparent axial stiffening described above was produced by the shift of the location of the neutral axis toward the point of application of the load after the south and west walls cracked. The axis located at the centroid of the specimen experienced axial elongation due to bending, which reduced the axial shortening due to compression and decreased the total measured shortening of the specimens.

The differential displacement of the axis along the line of action of the applied loads varied from 3.6 to 6.6 mm (0.14 to 0.26 in.), with no clear trend between the variation of the maximum relative deflection (Fig. 5.88) and the wall slenderness ratio. The relative axial deflections at the point of application of the load are similar to the deformations of the piers subjected to concentric axial load.

All specimens exhibited similar behavior: the axial response was linear up to an applied axial load equal to or larger than the load at which first crushing of the concrete was observed. At higher loads, the stiffness decreased.

The maximum differential displacement measured at the point of application of the axial load was 5 to 16 times larger than the maximum shortening measured along the centroidal axis of the cross-section. That ratio decreased as the wall slenderness ratio increased. This occurred because the piers with smaller wall slenderness ratios tended to experience larger rotations of the end blocks.

5.7.5 Moment-Curvature Response

Average curvatures were calculated using two types of measured data. Using the first method, the average curvatures were calculated from the measured longitudinal strains measured along the south and west walls (Fig. 5.89). Using the second method, the curvatures were calculated from the measured rotations of the end blocks (Fig. 5.90). In both cases, the curvature was assumed to be uniform along the height of the pier.

It was shown in Section 5.3.1 that, even if the measured rotations of the end blocks were different, it was possible to calculate the curvature in the specimens by assuming that the end rotations were equal to the average of the measured end-block rotations (Eq. 5.16). The average of the end-block rotations was used in Eq. 5.9 to calculate the curvatures of the piers.

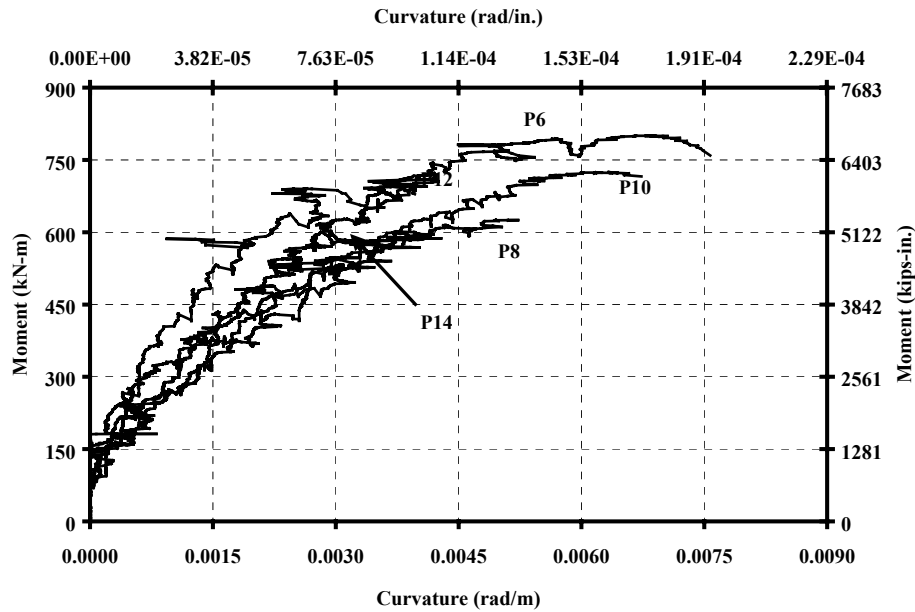


Figure 5.89 *Moment-Curvature Relationships about the East-West Axis Calculated Using the Measured Longitudinal Strains along the West Walls*

The curvatures about the east-west axis calculated using rotations were larger than the curvatures calculated using longitudinal strains (Fig. 5.27, 5.39, 5.53, and 5.65) for all five specimens. However, the curves obtained from both methods were similar.

From Fig. 5.89 and 5.90, for load levels less than 50% the capacity, all specimens had similar bending stiffness about the east-west axis. The initial bending stiffness of Specimen P6 was slightly larger than the others, while the stiffness of Specimen P14 was slightly smaller. This agrees with the calculated elastic bending stiffness EI of the specimens, where E is the initial modulus of

elasticity of the concrete (Table A.2) and I is the gross moment of inertia of the cross-section with respect to the east-west axis.

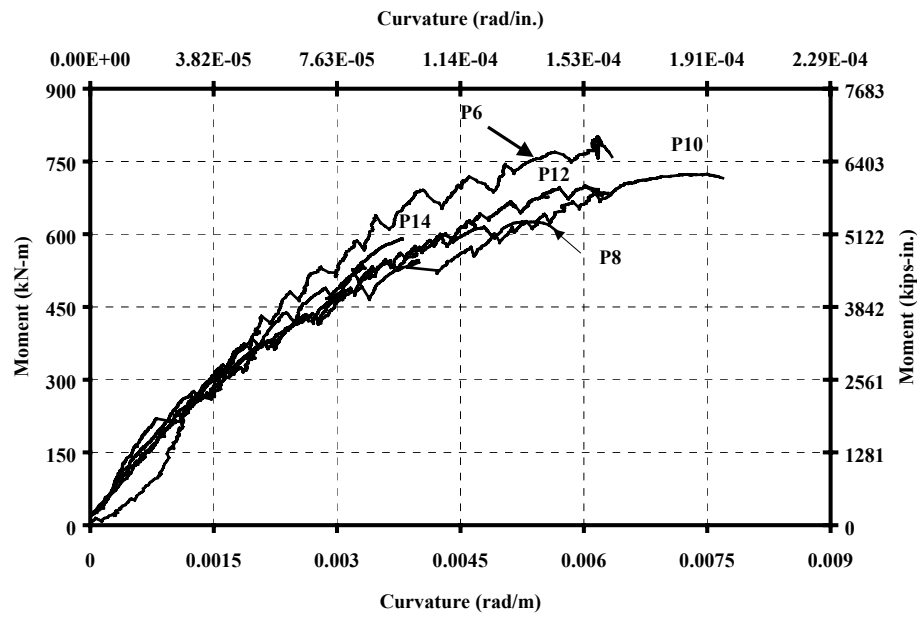


Figure 5.90 *Moment-Curvature Relationships about the East-West Axis Calculated Using the Average Rotations of the End Blocks*

Table 5.5 summarizes the elastic bending stiffness about the east-west axis of the hollow sections. Values of EI were similar for all specimens. The values of EI for P6 and P14 were, respectively, 23% larger and 20% smaller than the average EI .

In Fig. 5.90 the slope of the moment-curvature response of the specimens that exhibited crushing of the concrete prior to failure (P6, P8, P10 and P12) was nearly horizontal immediately before failure. The moment-curvature response of Specimen P14, which failed without warning, did not exhibit the same horizontal slope.

Table 5.5 Elastic Bending Stiffness about the East-West Axis

Specimen ID	Wall Slenderness Ratio (λ_w)	Moment of Inertia with respect to the East-West Axis mm^4 (in^4)	Modulus of Elasticity MPa (ksi)	Elastic Bending Stiffness EI $\text{MN}\cdot\text{m}^2$ ($\text{kip}\cdot\text{in}^2$)
P6	5.70	10060×10^6 (24168)	21720 (3150)	218 (7.61×10^7)
P8	7.85	7676×10^6 (18442)	23100 (3350)	177 (6.18×10^7)
P10	9.64	6684×10^6 (16059)	27600 (4000)	184 (6.42×10^7)
P12	12.22	5657×10^6 (13520)	30300 (4400)	170 (5.95×10^7)
P14	14.0	5074×10^6 (12191)	28300 (4100)	143 (5.00×10^7)

Table 5.6 summarizes the maximum curvatures calculated using end-block rotations. Curvatures about the north-south axis could not be calculated using measured strains because some instruments malfunctioned. Specimens P6, P8, P10, and P12 had less than 20% difference between the maximum curvatures about the east-west axis calculated using both procedures. The maximum curvature of Specimen P12, calculated using rotations, was 20% larger than the curvature calculated using strains.

The ultimate curvatures about the north-south axis, calculated using end rotations, were between 25% and 65% larger than the curvatures about the east-west axis. The curvatures calculated using strains were 14% and 28% larger about the north-south axis than about the east-west axis.

Table 5.6 Curvatures Measured at Failure

Specimen ID	End-Block Rotations		Longitudinal Strains	
	About East-West Axis rad/m (rad/in.)	About North-South Axis rad/m (rad/in.)	About East-West Axis rad/m (rad/in.)	About North-South Axis rad/m (rad/in.)
P6	0.00752 (1.91x10 ⁻⁴)	0.00883 (2.24x10 ⁻⁴)	0.00629 (1.60x10 ⁻⁴)	-
P8	0.00573 (1.46x10 ⁻⁴)	0.00754 (1.92x10 ⁻⁴)	0.00491 (1.25x10 ⁻⁴)	-
P10	0.00769 (1.95x10 ⁻⁴)	0.00961 (2.44x10 ⁻⁴)	0.00658 (1.67x10 ⁻⁴)	0.00749 (1.90x10 ⁻⁴)
P12	0.00629 (1.60x10 ⁻⁴)	0.00794 (2.02 x10 ⁻⁴)	0.00396 (1.00x10 ⁻⁴)	0.00507 (1.29x10 ⁻⁴)
P14	0.00380 (0.97x10 ⁻⁴)	0.00625 (1.59x10 ⁻⁴)	0.00405 (1.04x10 ⁻⁴)	-

5.7.6 Cracking

Three types of cracks were observed in the specimens during the tests: horizontal cracks in sections of the walls subjected to tensile stresses, vertical cracks in sections of the walls subjected to high compressive stresses where crushing of the concrete was observed, and vertical and diagonal cracks in the end blocks.

All specimens exhibited similar patterns of flexural cracks: the cracks started in the southwest corner and extended along the south and west walls. In most cases, the locations of the horizontal cracks coincided with the locations of the horizontal reinforcement.

Vertical cracks appeared near the northeast corner of Specimens P6, P8, P10, and P12. Vertical cracks did not form in Specimen P14. After the tests, all

specimens exhibited similar crack patterns in the north and east walls: vertical cracks close to the northeast corner along most of the height of the specimens produced by failure of the concrete in the cover that was not confined by the transverse reinforcement.

Several vertical and diagonal cracks were observed in the north, east and west sides of the top solid blocks of all specimens. They were first observed at applied loads between 1420 and 1780 kN (320 and 400 kips).

Those cracks can be explained by considering the location of the compressive and tensile stress fields within the end blocks. Similar analyses are used to evaluate likely crack patterns in the anchorage zones of post-tensioned beams. The transition from concentrated longitudinal compressive stresses in the anchorage zone (at the end of the beam) to distributed stresses within the hollow pier produces transverse tensile strains that may cause longitudinal cracks. Similarly, the transition between the concentrated compressive stresses in the end blocks to distributed stresses in the walls of the piers produced tensile strains perpendicular to the orientation of the compression field.

Figure 5.91 shows the approximate distribution of stresses in the walls of the piers, as well as the approximate stress trajectories in the end-blocks and the typical orientation of the cracks observed during the tests in each face of the blocks. The east and north walls were mostly in compression, with cracks oriented approximately parallel to the compressive stresses. This agrees with the orientation of cracks in a compression field.

Most of the west wall was in tension, and therefore the cracks were orientated roughly perpendicular to the direction of the tensile stresses.

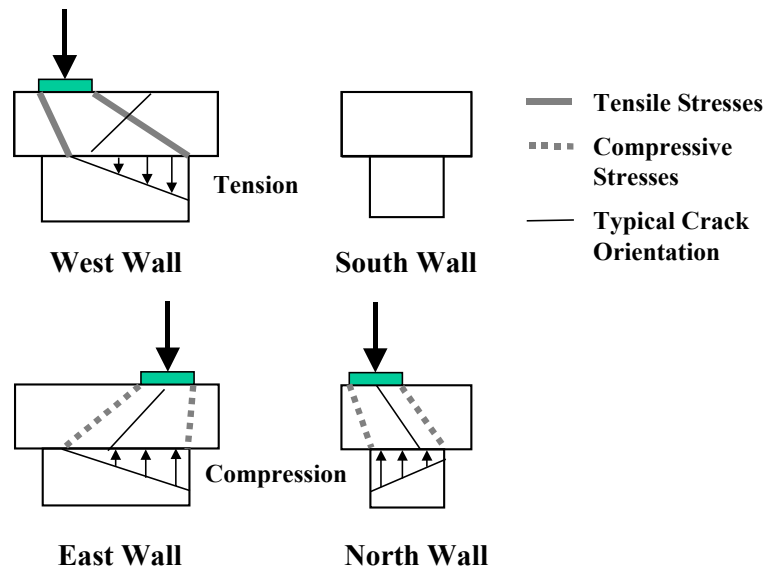


Figure 5.91 Stress Trajectories and Crack Orientation in End Blocks

5.7.7 Location of Failure

The five specimens failed at three different locations. Specimens P6, P10 and P14 failed near the top of the pier; Specimen P12 failed near the bottom of the pier; and Specimen P8 failed near midheight.

Two conditions can explain the observed failures near the top of Specimens P6, P10, and P14. First, it has been shown⁽²⁷⁾ that a zone of weaker concrete forms at the top of vertically cast columns due to the upward migration of free water that increases the water-cement ratio at the top of the column, producing concrete of lower strength.

Second, the walls were thinnest at the top. As shown in Fig. 4.22, the north and east walls in Specimens P10 and P14 were thinnest near the tops of the hollow piers. In Specimen P6, the east wall maintained a uniform thickness, while the north wall was almost 12 mm (0.5 in.) thinner at the top than at the bottom.

The concrete in Specimen P12 exhibited first signs of crushing near the bottom, and crushing at the top was observed only immediately before failure. The location of the failure coincided with the thinnest part of the east wall (Fig. 4.22).

The location of the failure zone at midheight in Specimen P8 can also be explained by the thickness of the walls. Figure 4.22 shows that both the north and east walls were thinnest near midheight.

5.7.8 Confinement of the Concrete

Crushing of the concrete spread at different rates in each specimen. In Specimens P6, P8 and P10, crushing and spalling of concrete was observed along the east and north walls prior to failure, so the specimens gave warning before failing. Minor crushing and spalling of concrete near the northeast corner of Specimen P12 was observed prior to failure, but no damage was observed along the north or east walls. The last specimen, P14, showed no signs of crushing of concrete before it failed. Table 5.7 summarizes those observations. Specimens P6, P8, P10 and P12 were able to carry additional load (11 to 33%) after the first signs of crushing were observed.

Table 5.7 Ratio of Measured Strength to Load of First Observed Crushing in Concrete

Specimen ID	Wall Slenderness Ratio (λ_w)	Measured Strength (P_{meas}) kN (kips)	Measured First Observed Crushing kN (kips)	Ratio of Measured Strength to Load of First Observed Crushing
P6	5.70	2670 (600)	2315 (520)	1.15
P8	7.85	2050 (461)	1735 (390)	1.18
P10	9.64	2370 (532)	1780 (400)	1.33
P12	12.22	2280 (513)	2050 (460)	1.11
P14	14.0	1960 (440)	1960 (440)	1.00

These observations suggest that after the cover concrete began to crush and spall, the concrete confined by the transverse reinforcement continued to carry the load. The specimens that contained larger areas of confined concrete were able to carry additional axial load before failure occurred. This subject is discussed in detail in Chapter 6.

5.7.9 Reinforcing details

The reinforcing details used to construct the specimens were selected to comply with the specifications for concrete piers from the AASHTO Specifications (1996) and the AASHTO Specifications (1998). The only requirements that were not followed in the test specimens were the ones related to cross-ties.

As discussed in Section 4.2.1, to avoid obstructions in the walls during casting, the cross-ties were made with 90-degree hooks at both ends. Also, because of the small size of the details of the specimens the hooks of cross-ties enclosed only the longitudinal reinforcing bars, and not the transverse reinforcement, as the specifications require.

Despite not following the requirement mentioned above, the cross-ties performed very well. Some of the 90-degree hooks of the cross-ties opened (Fig. 5.24, 5.37, and 5.65) after failure, but the cross-ties restrained most of the longitudinal bars against horizontal deflection and helped to confine the concrete in compression.

The cross-ties were distributed in a checkerboard pattern over each face of the piers. As a result, most longitudinal bars had an effective unbraced length equal to the vertical spacing of the horizontal reinforcement. Bars with longer effective unbraced lengths (1.25 to 2.0 times the spacing of the horizontal reinforcement) may have been better restrained if the cross-ties had also enclosed the transverse reinforcement.

The horizontal transverse reinforcement consisted of two U-shaped bars, spliced along the north and south walls. The legs of the exterior layer of transverse reinforcement did open within the zone of crushed concrete in Specimen P12 (Fig. 5.51 and 5.92). This highlights the need for the cross-ties to enclose the transverse reinforcement.

The pairs of U-shaped hairpins used as confinement reinforcement in the corners of the specimens performed very well. All corner longitudinal bars buckled between layers of horizontal reinforcement.



Figure 5.92 Pier P12: Separation of Spliced Transverse Reinforcement along the North Wall

5.7.10 Plane Sections

No strains were measured in the specimens to verify if plane sections were distorted during loading and to assess the possible effects of shear-lag. Average strains were measured at four points along the west and south walls (Fig. 4.35), however. The measured responses are presented in Section B.4. Those strains can be used to get an idea of the distortions produced in the cross sections.

Figure 5.93 shows the distances from the locations where the average strains were measured to a line parallel to the neutral axis. The orientation of the

neutral axis is calculated using the end block rotations. A plot of those distances versus the measured strains represents a straight line if the cross section remains plane during loading.

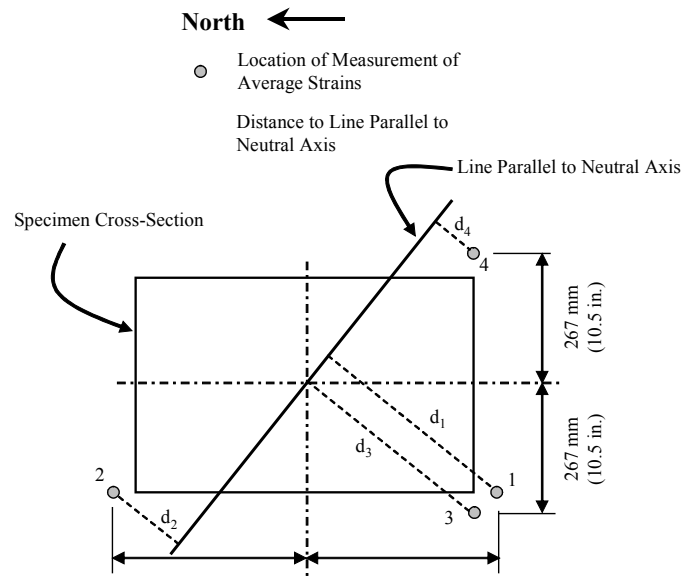


Figure 5.93 Locations of Four Measurements of Average Strains

In Figure 5.94 are plotted the average strains measured at the top and bottom halves of each specimen and the distances from those strains to a line parallel to the neutral axis. Dark markers represent strains at 50% of the ultimate load and white markers represent 100% of the ultimate load.

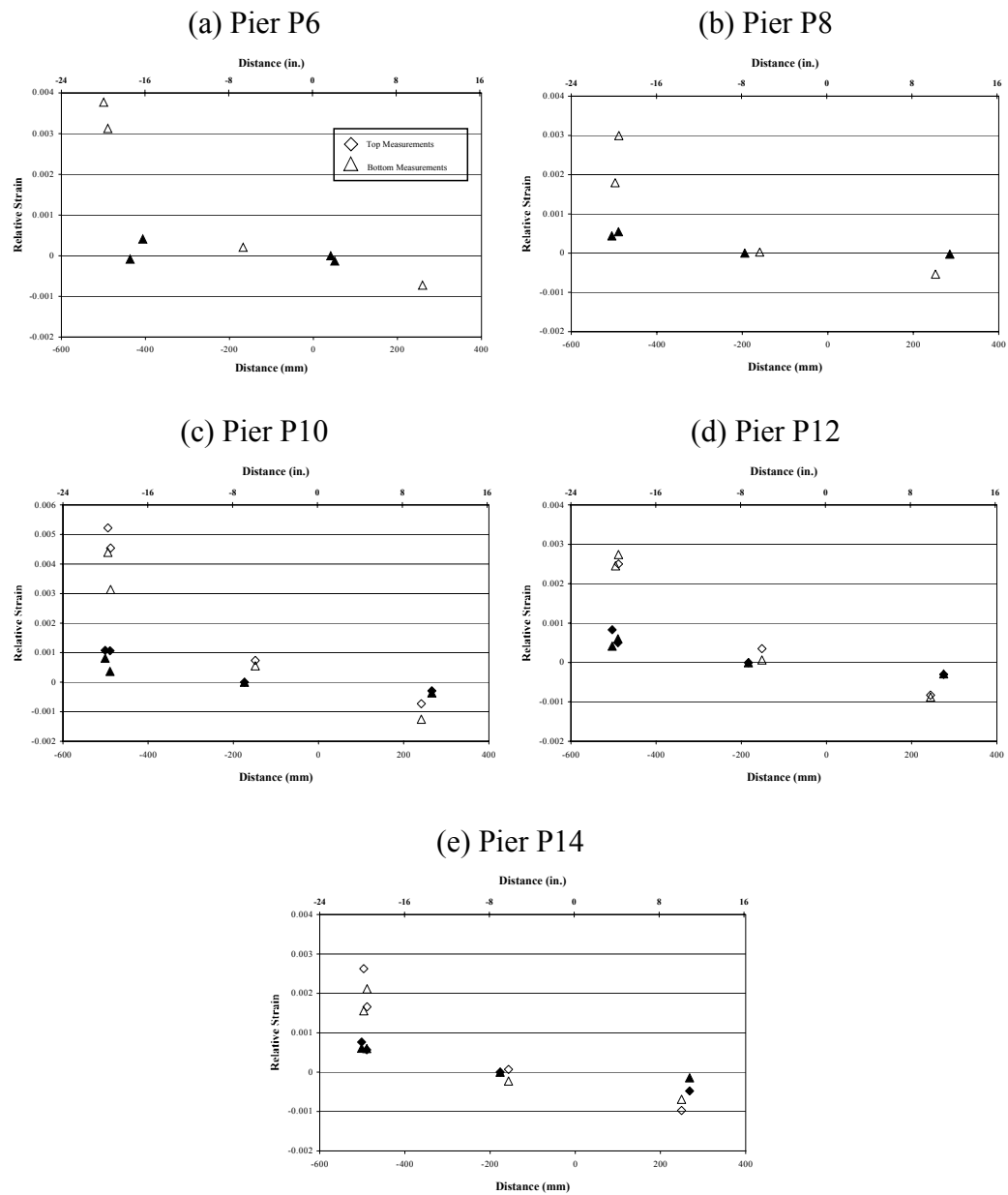


Figure 5.94 Average Strains Measured at the Top Half and Bottom Half of the Specimens, at 50% and 100% of the Ultimate Load

At a load level of 50% of the ultimate load the points are very close to a straight line, indicating that the cross-sections may have remained plane at that load level. At ultimate load the strains tend to form a line slightly bowed downward. The number of points available at each cross-section is small (only four) and most of the time three of them are tensile strains. Therefore, it is not possible to be certain that plane sections remain plane, but it seems to be a reasonable approximation of the response of the specimens.

5.8 SUMMARY

The results from the experiments were presented and each test was described and analyzed. General trends in the behavior of the specimens were also observed when available. Through analysis of the measured data it was possible to show that the measurements were reliable.

Some observed trends in the behavior of the specimens were: (1) the shape of the measured longitudinal profiles of the specimens could be explained by small horizontal displacements of the top block of the piers; (2) the assumption of uniform curvature along the length of the specimen is reasonable; (3) the maximum relative horizontal deflection increases with increasing wall slenderness ratio increases; (4) the wall slenderness ratio and the confinement provided by the transverse reinforcement to the concrete in the walls in compression were important to explain the strength and the behavior of the specimens; (5) the amount of damage prior to failure (warning) with decreasing wall thicknesses; and (6) the location of the failure zone was very sensitive to variations in the thickness of the walls in compression.

The reinforcing details performed very well. The requirements from the AASHTO Specifications (1996) and for hollow compression members in the AASHTO Specifications (1998) contribute to a good behavior of the specimens. The requirements that the cross-ties must have 135-degree hooks and enclose the transverse and longitudinal bars are of importance to ensure that the longitudinal bars are restrained to lateral deflection.

The influence of the wall slenderness ratio and the confinement provided by the transverse reinforcement to the concrete in the walls in compression in the behavior and the strength of the specimens are analyzed in Chapter 6.

Chapter 6 Analytical Evaluation of the Capacity of the Test Specimens

Various approaches were used to calculate the axial capacity of the test specimens based on their nominal eccentricity. The first approach used the approximate method for the design of hollow, rectangular concrete compression members introduced in the AASHTO Specifications (1998) and discussed in Section 3.2.2. Using this design method, if the wall slenderness ratio is less than or equal to 15 the nominal axial capacity, P_n , is calculated using standard design procedures, including an equivalent rectangular compressive stress block for concrete and axial and flexural capacities in terms of an interaction diagram.

In the second approach, three analytical material models were used to represent the stress-strain response of the concrete. Because four of the five piers failed at applied loads exceeding those at which crushing of the concrete was first observed, two material models for confined concrete were used. The third material model was a stress-strain relationship for unconfined concrete based in principles originally proposed by Hognestad (1951, 1952) and described in Section A.1.2.2. The peak stress of the model was made equal to the measured peak compressive stress of the specimens.

6.1 CALCULATION OF THE AXIAL CAPACITY AT NOMINAL ECCENTRICITY OF THE TESTED SPECIMENS USING APPROXIMATE DESIGN PROCEDURE

The nominal axial capacity, P_n , at nominal eccentricity, e_n , of the specimens was calculated using an equivalent rectangular stress block for concrete in compression and column interaction curve theory (Fig. 6.1). This approach is

consistent with Sections 5.7.2 and 5.7.4 of the AASHTO Specifications (1998) and the ACI-318 (1999) for members subjected to axial loading and bending. Local buckling effects were not considered because the wall slenderness ratios did not exceed 15. The details of this procedure for calculating the nominal capacity are summarized in Section 3.1. The limiting compressive strain in the concrete was considered to be 0.003 and the compressive strength was equal to the measured cylinder strengths reported in Appendix A. The strength reduction factor, ϕ , was taken equal to 1.0 (Section 9.3.2, ACI-318 (1999)).

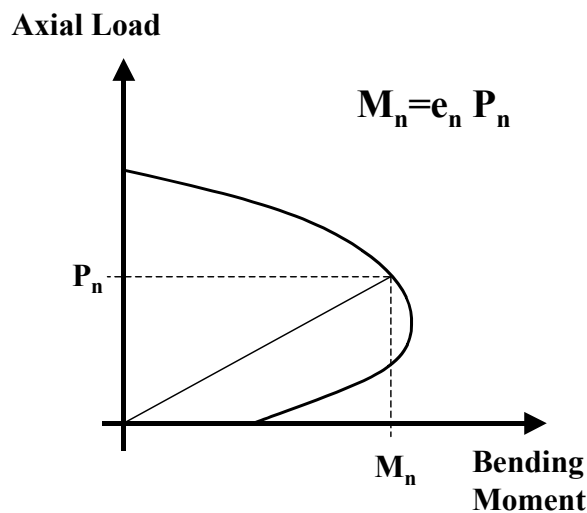


Figure 6.1 *Calculated Axial Capacity of Test Specimens at Nominal Eccentricity*

When calculating the nominal capacity, it was assumed that all walls in the specimens had a uniform thickness, equal to the wall thickness measured at the location of the observed failure in the individual specimens. Also, the eccentricity of the axial load measured immediately before testing was used to

relate the applied axial load and moment. Measured material properties were used in all calculations.

Table 6.1 lists the measured strength, P_{meas} , the nominal capacity calculated as described above, P_n , and the strength ratio, defined as the ratio of the measured strength to the calculated nominal capacity, for each specimen tested in this investigation. The load at which concrete crushing was first observed is also indicated.

The strength ratio also indicates the level of safety of current design procedures.

The measured strengths of all piers exceeded the nominal capacities. The measured strengths of Specimens P6, P8, P10, and P12 were 11 to 26% larger than the corresponding nominal capacities. This can be explained by two factors: (1) the equivalent rectangular stress block produces conservative estimates of the strength of a section when the compression area is not rectangular at failure (Furlong 1979) and (2) the observed response of the specimens indicates that the transverse reinforcement provided confinement to the concrete. Crushing and spalling of concrete was observed along the east and north walls prior to failure in four of the specimens. The specimens that contained larger areas of confined concrete were able to carry additional axial load before failure occurred. These observations suggest that after the cover concrete began to crush and spall, the transverse reinforcement provided some confinement to the concrete that resulted in increase of the concrete strength.

The ratio of the load at which concrete crushing was first observed to the nominal capacity is also given in Table 6.1. The nominal capacity provides a good estimate of the load corresponding to the onset of crushing of the concrete near the extreme compression fiber.

Table 6.1 Measured and Calculated Capacities of Tested Specimens

Specimen ID	Measured Strength (P_{meas}) kN (kips)	Measured First Observed Crushing Load kN (kips)	Nominal Capacity (P_n) kN (kips)	Ratio of Crushing Load to Nominal Capacity	Ratio of Measured to Nominal Capacity
P6	2670 (600)	2310 (520)	2070 (465)	1.12	1.29
P8	2050 (461)	1730 (390)	1680 (379)	1.03	1.22
P10	2370 (532)	1780 (400)	1870 (419)	0.95	1.27
P12	2280 (513)	2050 (460)	1940 (436)	1.06	1.18
P14	1960 (440)	1960 (440)	1870 (420)	1.05	1.05

Ratios of measured to nominal capacities are plotted in Fig. 6.2. They tend to decrease as the wall slenderness ratio increased. For this set of test results (piers with a nominal ratio of strong-axis to weak-axis eccentricity equal to 3.0, a nominal strong-axis eccentricity equal to 305 mm (12 in.), and an aspect ratio of the cross section equal to 2.0), local buckling of the walls may limit the capacity of hollow piers with wall slenderness ratios larger than 15.

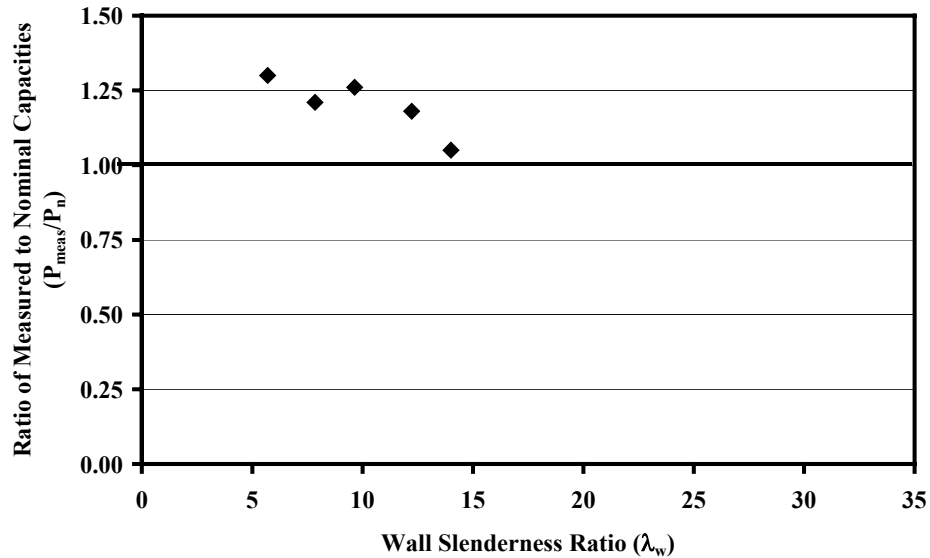


Figure 6.2 Ratios of Measured to Calculated Nominal Capacity of Test Specimens

6.2 INFLUENCE OF TRANSVERSE REINFORCEMENT ON THE COMPRESSIVE STRENGTH OF THE CONCRETE

Many experimental investigations have shown that confinement provided by transverse reinforcement increases the compressive strength and deformation capacity of concrete (Kent and Park 1971, Kaar et al. 1978, Mander, Priestley and Park, 1988a). Several empirical stress-strain curves have been proposed for confined concrete (Mander, Priestley and Park, 1988b, Park, Priestley and Gill 1982, Saatcioglu, M. and Razvi, S. R. 1992, Sheikh and Uzumeri 1980). In these material models the increase in compressive strength is related to the confining stresses provided by the transverse steel.

Most available material models have been verified using the measured response of circular and square columns subjected to uniaxial compression. Mander et al. (1988b) and Saatcioglu, M. and Razvi, S.R. (1992) developed procedures that also consider rectangular columns and situations with unequal confining stresses in perpendicular directions. In the following discussion, the material model developed by Mander et al. (1988b) will be called model M, and that developed by Saatcioglu, M. and Razvi, S.R. (1992) will be called model S. These material models were developed to represent confined concrete, and do not address buckling of the longitudinal reinforcement or buckling of the thin walls of the pier.

To describe the stress-strain relationship of confined concrete, the material models consider: (1) the transverse reinforcement ratio; (2) the yield stress of the transverse reinforcement; (3) the vertical spacing of transverse reinforcement; (4) the horizontal spacing of the longitudinal reinforcement; and (5) the compressive strength of the unconfined concrete.

In rectangular hollow concrete piers, the corners of the cross section and the walls can have different ratios of confining reinforcement. Section 5.10.12.5 of the AASHTO Specifications (1998) requires that closed hoops enclose the longitudinal reinforcing bars in the corners of the cross section of hollow rectangular compression members. This tends to produce larger transverse reinforcement ratios in the corners than along the walls. Therefore, separate stress-strain relationships had to be determined for the confined concrete in the corner and along the walls in compression.

The application of the two material models to the hollow pier specimens is described in detail in Appendix C.

It was assumed that all horizontal bars (the cross-ties, the hairpins and the horizontal web reinforcement) described in Section 4.2.2 contributed to confining the concrete in compression.

Table 6.2 summarizes the ratios of confined to unconfined concrete compressive strength calculated in Appendix C using material Models M and S. As a general trend, the ratio of the measured to calculated capacity decreased as the wall thickness decreased. The ratios of confined to unconfined compressive strength calculated using Model M varied between 1.00 and 1.55. The east and north walls had the same ratios of confined to unconfined compressive strength for each pier, while the ratios of confined to unconfined compressive strength in the northeast corners were 20 to 55% larger than the ratios for the walls.

The ratios of confined to unconfined compressive strength calculated using Model S varied between 1.10 and 1.20. The ratios along the east walls were slightly higher than the ratios along the north walls for piers P6 and P8. The ratios in the northeast corners were similar to the smaller ratios calculated along the walls.

The calculated ratios of confined to unconfined concrete compressive strength were larger for Specimen P14 than P12 using both material models. This is because the vertical spacing of the transverse reinforcement was smaller in Specimen P14.

Table 6.2 *Calculated Ratios of Confined to Unconfined Compressive Strength of the Concrete Calculated in Appendix C*

Specimen ID	Model M		Model S		
	East and North Walls	Northeast Corner	East Wall	North Wall	Northeast Corner
P6	1.10	1.35	1.20	1.15	1.14
P8	1.05	1.42	1.17	1.15	1.14
P10	1.00	1.38	1.11	1.12	1.12
P12	1.00	1.44	1.11	1.10	1.11
P14	1.00	1.55	1.12	1.15	1.12

6.3 MOMENT-CURVATURE RESPONSE

Relationships between moment and curvature were calculated for each test specimen using the stress-strain relationships of material Models M and S for confined concrete. The measured material properties are reported in Appendix A and were used to calculate the idealized stress-strain relationships for confined and unconfined concrete. The stress-strain relationship of the unconfined concrete is described in Appendix A.

The limiting strain in the unconfined concrete was assumed to be 0.0038. Above this strain, the stress in the unconfined concrete was assumed to be zero. The maximum strains in the confined concrete were calculated using the procedures described in Appendix C.

Each cross section was divided into regions with different concrete properties, as shown in Fig. 6.3. The centerline of the transverse reinforcement was used to define the boundaries between the zones. The wall thickness

measured at the location of the observed failure in the individual specimens and the nominal depths to the reinforcement were used. Measured material properties were used in all calculations.

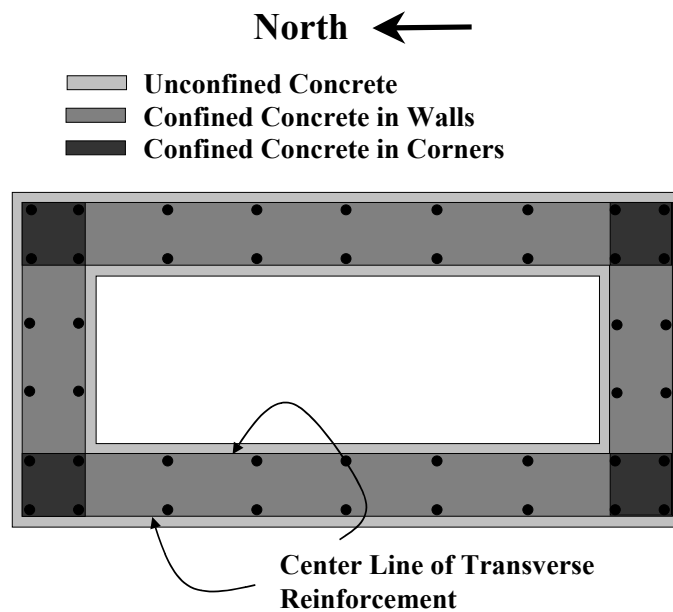


Figure 6.3 Idealized Distribution of Confined Concrete within the Test Specimens

Each concrete zone within the cross section was then divided into small square or rectangular fibers. Each fiber had a corresponding concrete material model. Each longitudinal reinforcement bar was defined as a steel fiber located at the position of the bar. The steel fibers had a cross section equal to the area of the longitudinal bars and were modeled as elastic-perfectly plastic, with the yield stress reported in Appendix A.

A typical fiber model used to calculate moment-curvature response is shown in Fig. 6.4. Three lines of fibers were used through the thickness of the unconfined concrete; 16 lines of fibers were used through the thickness of the

walls; and 96 and 32 lines of fibers were used along the long and short walls, respectively.

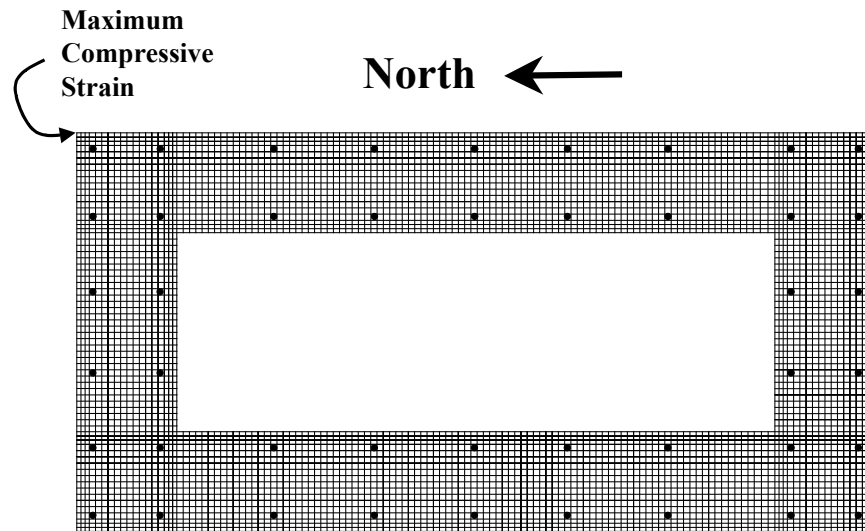


Figure 6.4 Typical Distribution of Fibers used to Calculate Moment-Curvature Response of Piers

An iterative procedure used to calculate the moment-curvature relationship for each specimen. A value for compressive strain, ϵ_{max} , in the concrete in the northeast corner was assumed (Fig. 6.4 and 6.5), and then the depth of the neutral axis, c , and orientation of the neutral axis, θ , were assumed. Plane sections were assumed to remain plane after loading, and the distribution of strains over the cross section can be calculated as shown in Fig. 6.5.

The strain at the centroid of each fiber could be calculated from the assumed strain distribution. The stress at those locations was calculated using the appropriate stress-strain relationship (Fig. 6.5). The axial force in each fiber was

calculated by multiplying the area of the fiber by the stress in the appropriate material.

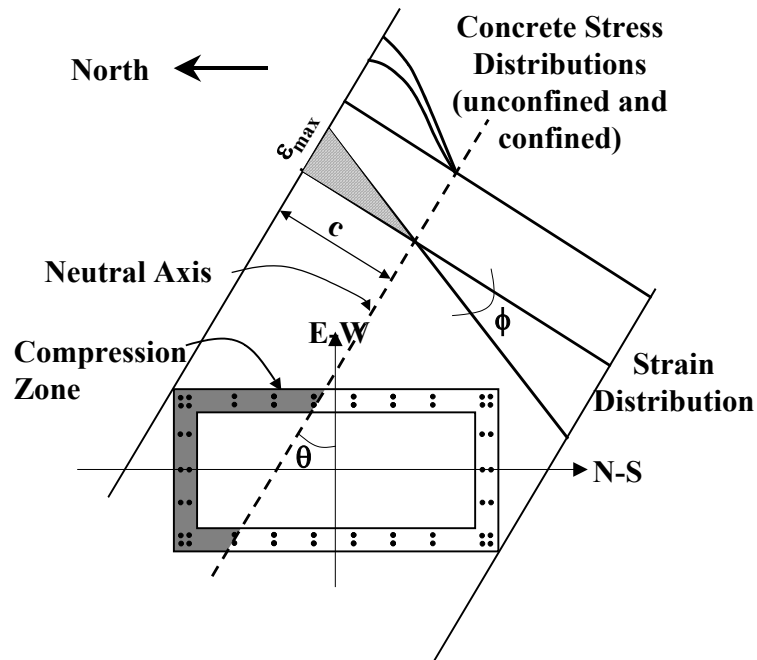


Figure 6.5 Strain and Stress Distributions Over Cross-Section

The total axial load was then calculated by summing the axial forces in each of the fibers. To simplify the calculations, moments were calculated about the principal axes of the cross section (north-south and east-west axis in Fig. 6.5). The eccentricities in the principal directions were then calculated by dividing these moments by the axial load.

If the eccentricities and the ratios of eccentricities did not match the known values that were measured during the tests (Table 5.1), then the neutral axis depth and orientation were adjusted, and the axial load and bending moments were re-calculated. If the eccentricities were within 0.25% of the nominal values,

then the solution was considered to satisfy equilibrium and correspond to the applied loading. The curvatures about the two principal axes were then computed.

Because curvature is a vector the curvatures about two given directions are the components of the total curvature in those directions. The following is a derivation of the components about the two principal axes of a hollow section. From Fig. 6.5, the total curvature of the cross-section may be calculated as:

$$\phi = \frac{\varepsilon_{\max}}{c} \quad (6.1)$$

Figure 6.6 helps to explain how the curvatures about the east-west and the north-south axes were calculated. The curvatures about the east-west and north-south axes may be defined as:

$$\phi_{E-W} = \frac{\varepsilon_{\max}}{a} \quad (6.2)$$

$$\phi_{N-S} = \frac{\varepsilon_{\max}}{b} \quad (6.3)$$

where a and b are related to the neutral axis depth and the orientation of the neutral axis as follows:

$$c = b \sin \theta \quad (6.4)$$

$$c = a \cos \theta \quad (6.5)$$

Substituting the expressions for a and b into Eq. 6.2 and 6.3 give the following relationships for curvature about the two principal axes of the column:

$$\phi_{E-W} = \phi \cos \theta \quad (6.6)$$

$$\phi_{N-S} = \phi \sin \theta \quad (6.7)$$

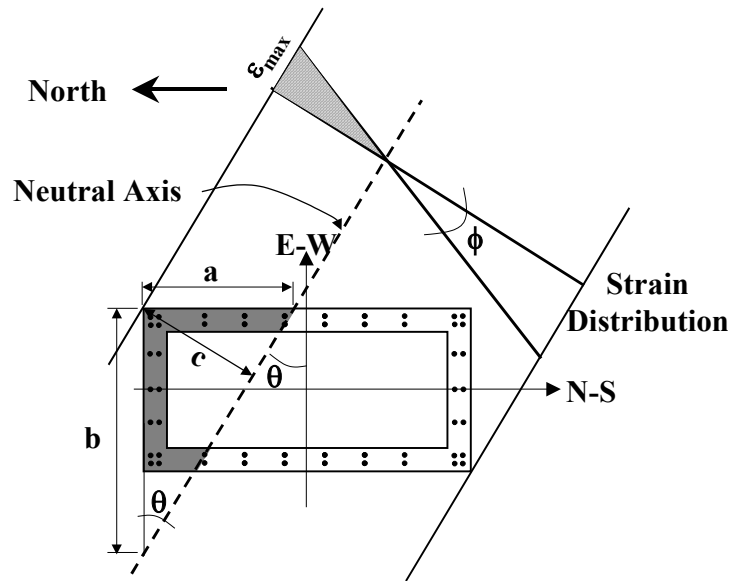


Figure 6.6 Calculation of Curvatures About East-West and North-South Axes in a Cross Section Loaded Under Biaxial Eccentricity

Therefore, two moment-curvature relationships were calculated for each pier, one about the east-west axis and one about the north-south axis. These calculations were performed using both material models for confined concrete. The calculated moment-curvature relationships are compared in Fig. 6.7 through 6.11 with the responses obtained from the measured end block rotations.

One of the main assumptions in the fiber model described above is that the Bernoulli-Euler hypothesis, that plane sections remain plane after being subjected to bending (Fig. 6.5 and 6.6), is valid.

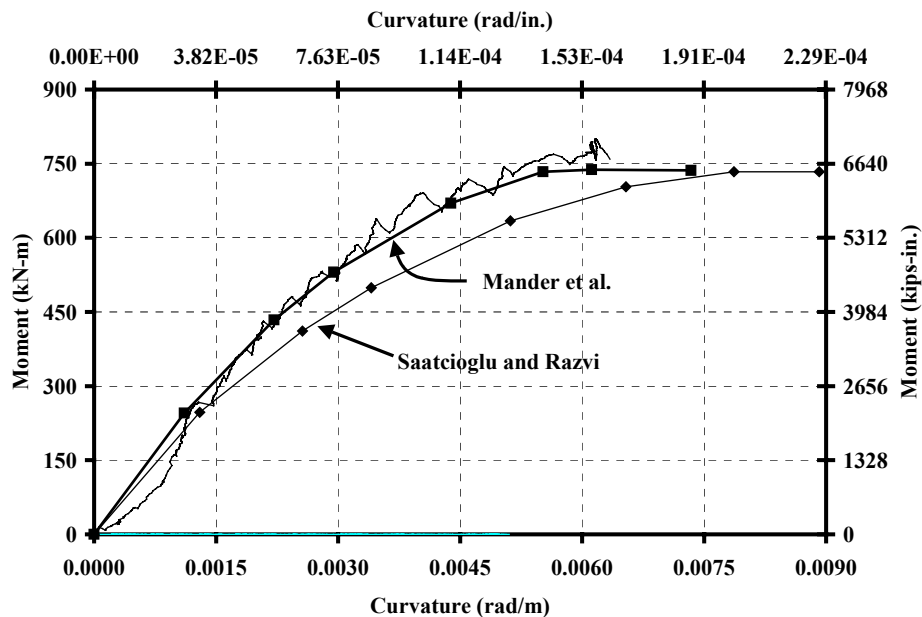
Taylor et al. (1990) measured strains in longitudinal bars to test the hypothesis of plane sections. He reported that at 50% of the ultimate the strain distribution of all the specimens were very close to planar. At ultimate load,

however, only four of 12 specimens had planar strain distributions. In the other specimens the strain distributions were approximately planar, but with large local deviations from planar in the walls in compression. The wall slenderness ratios of the specimens tested by Taylor et al. (1990) ranged from 9 to 34, larger than in this investigation.

The specimens tested in this investigation showed a response similar to that observed by Taylor et al. (1990) (see Section 5.7.10). At load levels of 50% of the ultimate load the cross-sections are very close to planar, but at ultimate load the strains tend to be slightly deviated from planar.

Current design practice can help to determine if the Bernoulli-Euler is a reasonable hypothesis for the specimens tested in this investigation. The cross-section of a pier can be represented as two L-beams. The slender walls of the piers correspond to the flanges of the beams, while the short walls correspond to the webs of the beams. The effective overhanging flange is recommended not to exceed six times the thickness of the slabs (ACI-318 1999). Therefore, using those provisions, the effective length of the slender wall should be reduced only for piers with wall slenderness ratios larger than 12. Because the stresses in the biaxially loaded specimens are concentrated near the corner of the piers it seems reasonable to do calculations using the full length of the walls even for Specimen P14, which has a wall slenderness ratio of 14. The observations by Taylor et al. (1990) and this investigation lead to conclude that the hypothesis of plane sections appears to be valid for load levels up to 50% of ultimate load and a reasonable approximation at loads close to ultimate.

a) Moment-Curvature Curves About the East-West Axis



b) Moment-Curvature Curves About the North-South Axis

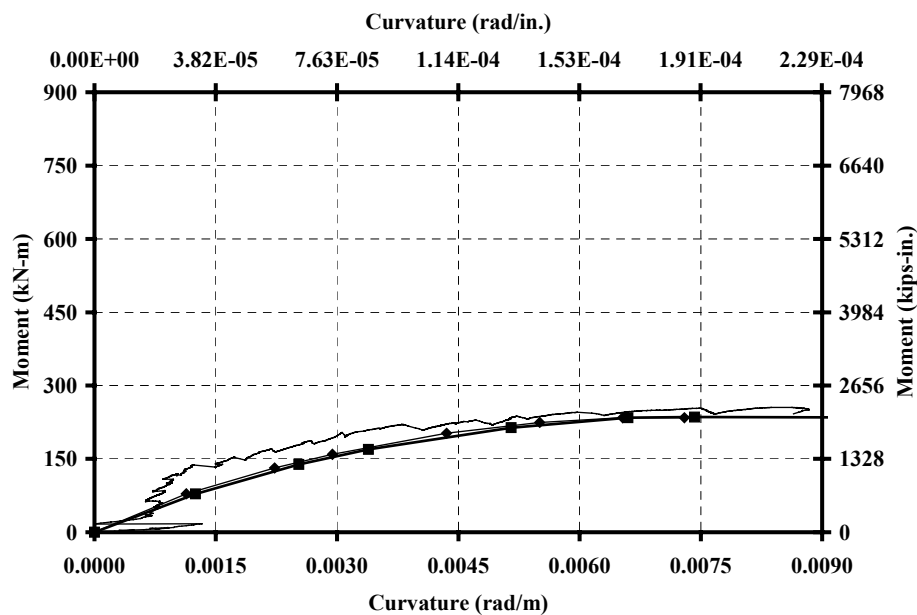
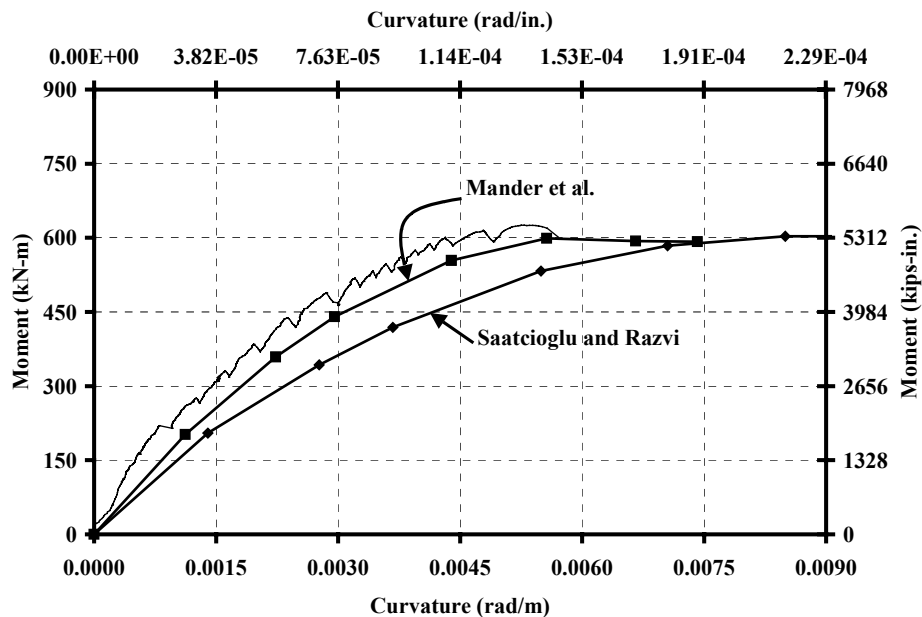


Figure 6.7 Specimen P6: Comparison of Moment-Curvature Response from End-Block Rotations and Calculated Moment-Curvature Response

a) Moment-Curvature Curves About the East-West Axis



b) Moment-Curvature Curves About the North-South Axis

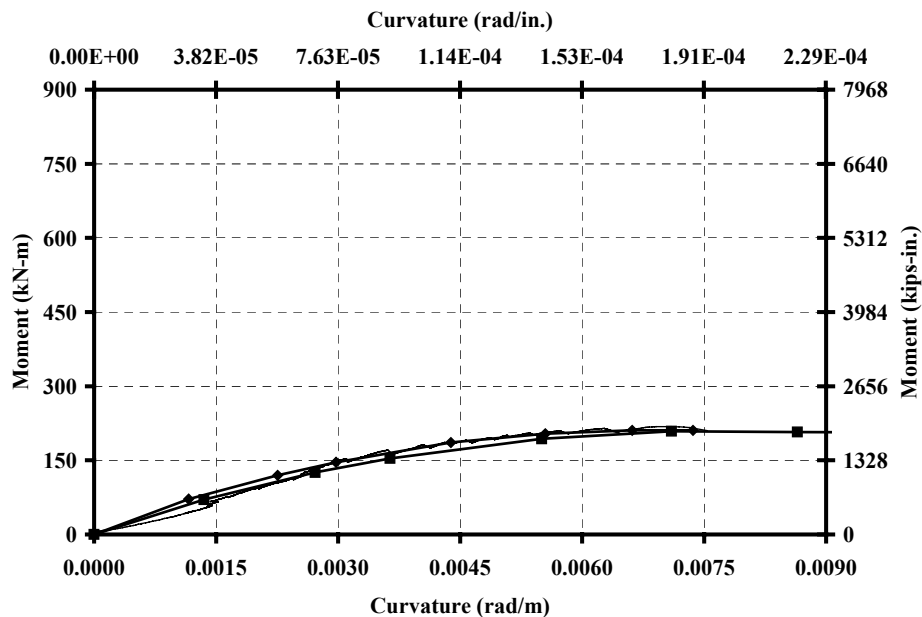
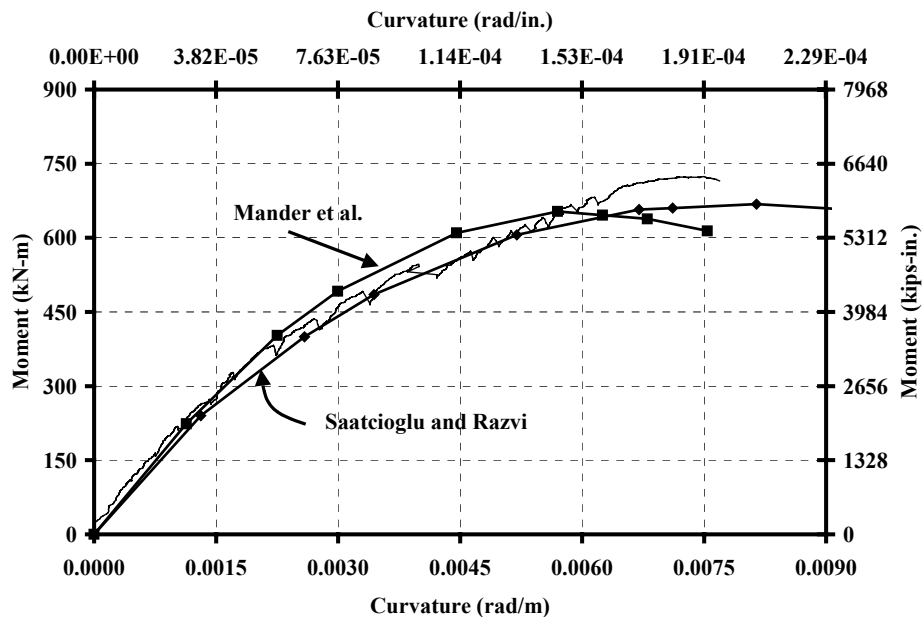


Figure 6.8 Specimen P8: Comparison of Moment-Curvature Response from End-Block Rotations and Calculated Moment-Curvature Response

a) Moment-Curvature Curves About the East-West Axis



b) Moment-Curvature Curves About the North-South Axis

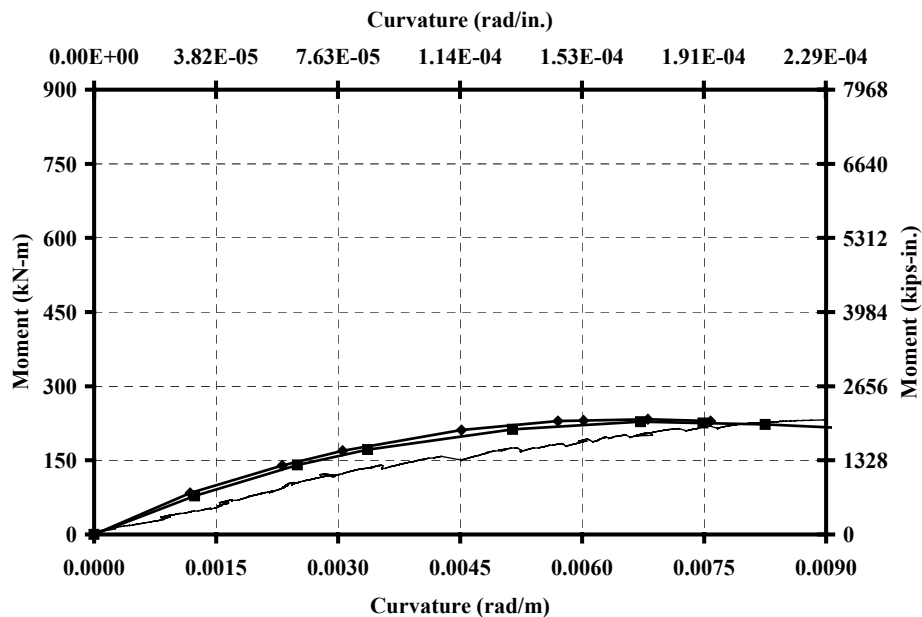
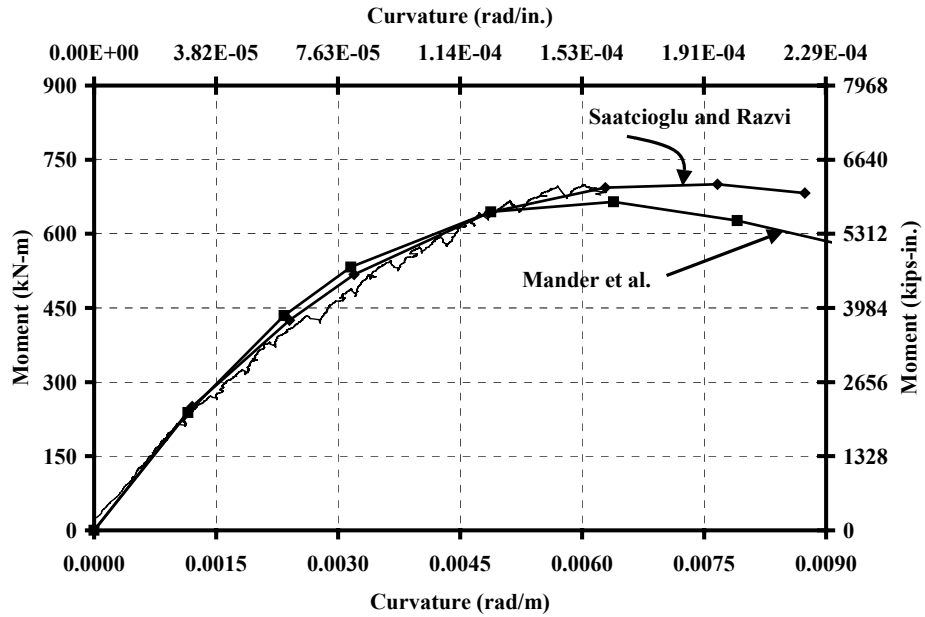


Figure 6.9 Specimen P10: Comparison of Moment-Curvature Response from End-Block Rotations and Calculated Moment-Curvature Response

a) Moment-Curvature Curves About the East-West Axis



b) Moment-Curvature Curves About the North-South Axis

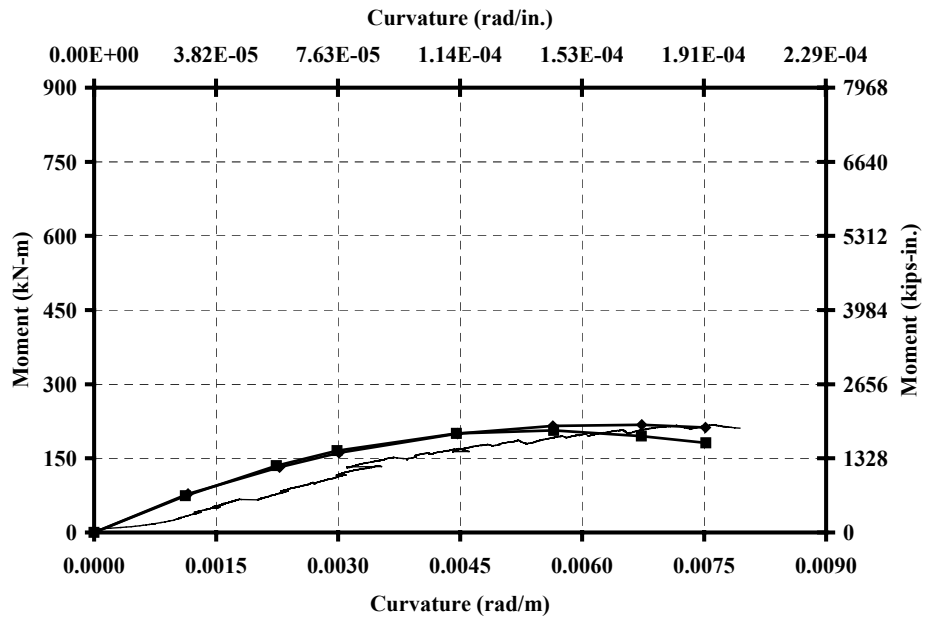
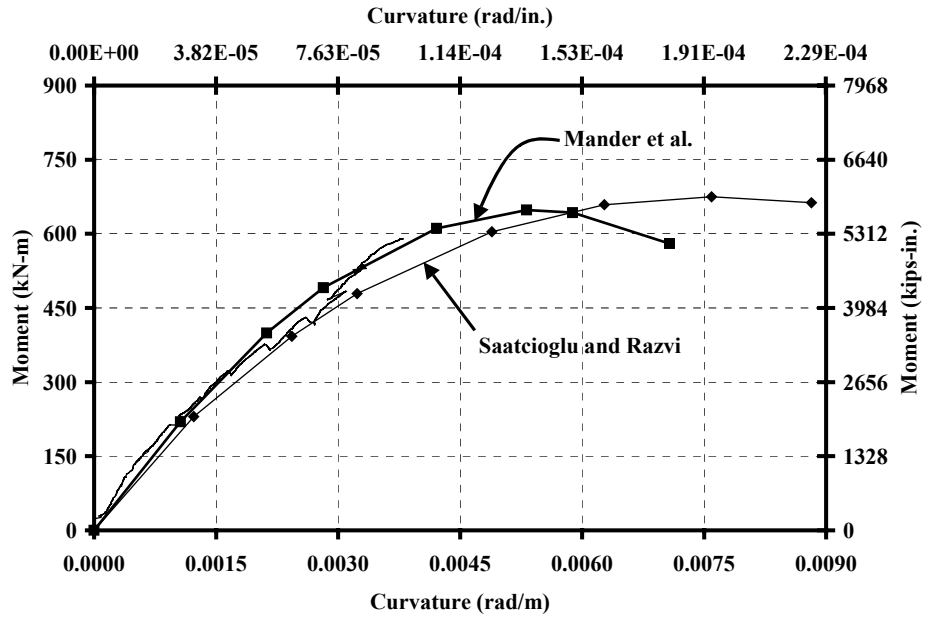


Figure 6.10 Specimen P12: Comparison of Moment-Curvature Response from End-Block Rotations and Calculated Moment-Curvature Response

a) Moment-Curvature Curves About the East-West Axis



b) Moment-Curvature Curves About the North-South Axis

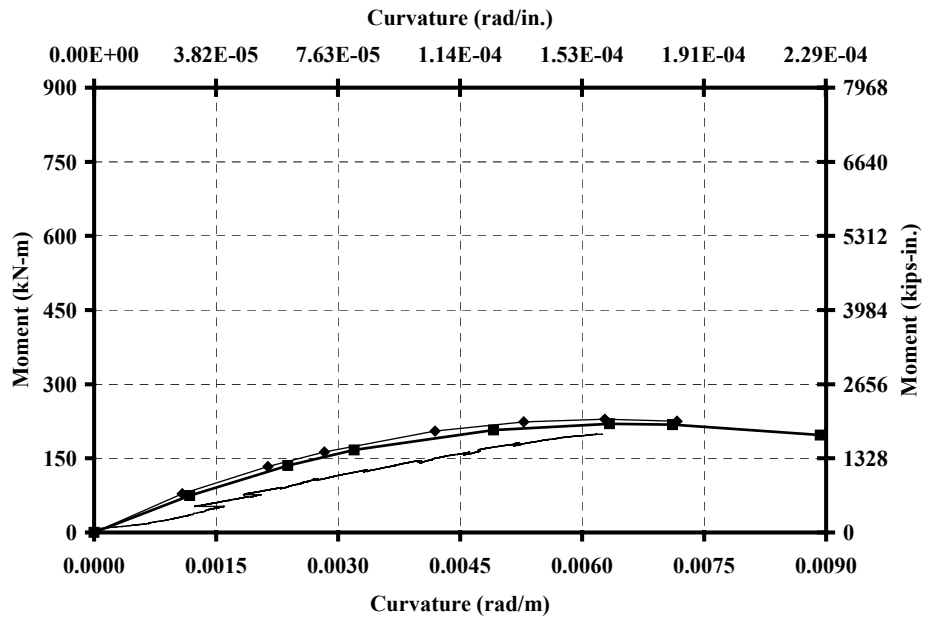


Figure 6.11 Specimen P14: Comparison of Moment-Curvature Response from End-Block Rotations and Calculated Moment-Curvature Response

The response calculated using material Model M reproduced the moment-curvature response measured from end-block rotations about the east-west axis extremely well. The calculated response using Model S was slightly softer than the measured response for Specimens P6 and P8. Both models gave very similar responses about the north-south axis, and the calculated responses agreed well with the measured moment-curvature relationship.

Table 6.3 shows the calculated curvatures at the peak calculated axial load, and the ratios of the measured to calculated curvatures. The ratios of measured to calculated curvatures at maximum capacity ranged from 0.89 to 1.30 and from 0.84 to 1.42 for material models A and B, respectively.

Table 6.3 Measured Ultimate Curvatures and Curvatures Calculated at the Maximum Load

Specimen ID	Curvatures			Ratios of Measured to Calculated Curvatures	
	Measured rad/m (rad/in.)	Model M rad/m (rad/in.)	Model S rad/m (rad/in.)	Model M	Model S
P6	0.0110 (2.79 x 10 ⁻⁴)	0.0104 (2.64 x 10 ⁻⁴)	0.0131 (3.33 x 10 ⁻⁴)	1.06	0.84
P8	0.00947 (2.41 x 10 ⁻⁴)	0.0104 (2.64 x 10 ⁻⁴)	0.0102 (2.60 x 10 ⁻⁴)	0.91	0.93
P10	0.0123 (3.12 x 10 ⁻⁴)	0.00944 (2.40 x 10 ⁻⁴)	0.00866 (2.20 x 10 ⁻⁴)	1.30	1.42
P12	0.0101 (2.57 x 10 ⁻⁴)	0.00854 (2.17 x 10 ⁻⁴)	0.00840 (2.13 x 10 ⁻⁴)	1.18	1.21
P14	0.00731 (1.86 x 10 ⁻⁴)	0.00831 (2.09 x 10 ⁻⁴)	0.00827 (2.07 x 10 ⁻⁴)	0.89	0.90
			Average	1.07	1.06
			St. Dev	0.18	0.25
			COV	0.16	0.23

6.4 AXIAL CAPACITIES OF THE TESTED SPECIMENS CALCULATED AT THE MEASURED ECCENTRICITIES USING MODELS FOR CONFINED CONCRETE

The axial capacities calculated using two material models for confined concrete and the stress-strain relationship proposed for unconfined concrete are reported in Table 6.4. In each case, the axial capacity is defined as the axial load corresponding to the maximum calculated moment. The axial capacities calculated using the expression for unconfined concrete were calculated using the same procedure described in Section 6.3, but assuming that all the concrete in the cross section was unconfined. The nominal axial capacity of each pier is listed in Table 6.4.

All four procedures provided conservative estimates of the axial capacity of Specimens P6, P8, P10, and P12. In most of these specimens, the calculations based on confined concrete models provided closer estimates of measured strengths than did calculations based on unconfined material properties.

The strength ratios calculated using the unconfined material model and the nominal capacity followed the same trend: strength ratios decreased as the wall slenderness ratios increased. Also, the nominal capacity provided a conservative estimate of the measured strength of all the tested piers, while the material model for unconfined concrete led to an unconservative estimate of the capacity of Specimen P14.

Table 6.4 Capacities of Piers Calculated Using Models for Confined and Unconfined Concrete

Spec. ID	Measured Strength (P_{meas}) kN (kips)	Calculated Capacity				Ratio of Measured to Calculated Capacity			
		Nominal (P_n) kN (kips)	Unconf. kN (kips)	Model M kN (kips)	Model S kN (kips)	Nominal	Unconf.	Model M	Model S
P6	2670 (600)	2070 (465)	2290 (515)	2510 (565)	2360 (546)	1.29	1.17	1.06	1.10
P8	2050 (461)	1680 (379)	1860 (419)	2030 (456)	1970 (443)	1.22	1.10	1.01	1.04
P10	2370 (532)	1870 (419)	2160 (485)	2080 (472)	2220 (500)	1.27	1.10	1.13	1.06
P12	2280 (513)	1940 (436)	2170 (488)	2220 (498)	2260 (508)	1.18	1.05	1.03	1.01
P14	1960 (440)	1870 (420)	2050 (460)	2080 (467)	2120 (477)	1.05	0.96	0.94	0.92
Average						1.20	1.07	1.03	1.03
St. Dev						0.10	0.08	0.07	0.07
COV						0.08	0.07	0.07	0.07

Both material models for confined concrete provided excellent estimates of the strength of Specimen P6, P8, P10, and P12, but overestimated the strength of Specimen P14. The average strength ratio for all piers was 1.03 calculated using Models M and also S. Using material Model M, the calculated capacities of Specimens P6, P8, and P12 were less than 6% below measured strengths, and the calculated capacity of Specimen P10 was about 13% less than the measured strength. Using material Model S, the calculated capacities of Specimens P6, P8, P10, and P12 were underestimated by less than 10%.

The capacity of Specimen P10 calculated using the unconfined concrete model was slightly larger than the capacity calculated using Model M. This result is explained by comparing the stress-strain curves of the unconfined concrete and confined concrete along the north and east walls (Fig. C.10(a)). Both material models have the same peak stress, but the descending branch of Model M is steeper than that of the unconfined concrete, resulting in a smaller stress in Model M at the ultimate strain.

The capacity of Specimen P14 was overestimated using both material models for confined concrete and the material model for unconfined concrete. One possible explanation is described below.

6.4.1 Evaluation of Pier P14

Pier P14 failed explosively and without warning. This suggests that the maximum compressive strain in the concrete immediately before failure was smaller than the strain corresponding to peak stress in the unconfined concrete. The possibility that failure occurred due to buckling of the longitudinal reinforcement as soon as it reached the yield stress will be investigated in this section. The strength calculated under this hypothesis represents a lower bound of the calculated values of the strength.

The longitudinal bar that exhibited the longest unbraced length was located 105 mm (4.125 in.) from the northeast corner along the east wall. It was hypothesized that the strain in this bar may have reached the yield strain immediately before failure. The corresponding maximum compressive strain in the concrete was determined from the data used to calculate the moment-

curvature response (Section 6.3). This calculated maximum compressive strain was 0.003 when both models for confined concrete were used. The corresponding values of axial capacity and curvature are reported in Table 6.5. The calculated values are very close to the measured response and indicate that the stability of the longitudinal bars must be investigated in more detail.

Table 6.5 Capacities and Maximum Curvatures for Specimen P14 Calculated using Material Models M and S assuming the Maximum Compressive Strain in the Unconfined Concrete Equal to 0.003

	Measured Data	Model M	Model S	Ratio of Measured to Calculated Data using Model M	Ratio of Measured to Calculated Data using Model S
Axial Capacity KN (kips)	1960 (440)	1970 (443)	1960 (440)	0.99	1.00
Ultimate Curvature Rad/m (rad/in.)	0.00731 (1.86×10^{-4})	0.00646 (1.64×10^{-4})	0.00642 (1.63×10^{-4})	1.13	1.14

The maximum measured compressive strains at ultimate load, ϵ_c , listed in Table 6.6, were estimated from the average strain measured using Instruments ST and SB at the south-west corner along the west wall (Fig. 4.35). The data from those instruments was used in the calculations because was available for all specimens. The maximum compressive strains were estimated using curvatures calculated with end-block rotations and geometric compatibility, assuming plane sections. The maximum compressive strain in the concrete of Specimen P14 is 0.0032, which agrees with the value calculated before.

6.4.2 Stability of Longitudinal Bars

The material models for confined concrete did not consider the possibility of buckling of the longitudinal reinforcement. Therefore, the calculated moment-curvature relationships exhibited long descending branches because the material models were based on the assumption that the reinforced concrete member could sustain extremely large compressive strains. During the tests of the hollow piers, however, none of the specimens experienced a reduction in axial capacity prior to failure. Failure may have occurred when the longitudinal reinforcement buckled in all cases. In this section, a possible limitation to capacity based on the buckling behavior of the longitudinal reinforcing bars is studied.

All the buckled longitudinal bars in Pier P6 failed with an effective length equal to the vertical spacing of the transverse reinforcement (Fig. 5.11). Most of the longitudinal bars in piers P8, P10, P12, and P14 also buckled with an effective length equal to the spacing of the transverse reinforcement. Some longitudinal bars along the east wall, however, exhibited buckled lengths that varied between 1.25 and 2.0 times the vertical spacing of the transverse reinforcement (Fig. 5.24, 5.37, 5.52, and 5.65). This occurred because the checkerboard pattern of the cross-ties makes possible effective unbraced lengths as large as twice the spacing of the transverse reinforcement. The maximum observed effective buckled lengths of longitudinal bars at the northeast corner and along the east wall are reported in Tables 6.6 and 6.7, respectively. The calculated maximum compressive strains in the concrete at the peak calculated axial load, ε_{max} , the calculated axial strains in

the longitudinal bars, ϵ_s , and the nominal distances of those longitudinal bars to the northeast corner of the piers are also listed in Tables 6.6 and 6.7.

The calculated axial compressive strains at failure in the bars located at the northeast corner varied between 0.0029 and 0.0051. Most of the calculated strains were smaller than 0.0042. The calculated axial strains in the bars along the east wall varied between 0.0025 and 0.0041. The yield strain, ϵ_y , of the longitudinal reinforcement used to construct the specimens was 0.0026, similar to the lower bound of calculated axial strains of the longitudinal bars with longest buckled length. Also, the stress-strain curve of the longitudinal bars (Fig. A.6) had a well-defined yield plateau up to a strain equal to 0.0075, larger than the calculated strains in those bars. Therefore, strains in the longitudinal bars were within the yield plateau of the measured stress-strain curve at the load corresponding to failure of the piers.

The measured maximum compressive strains of Specimens P6, P8, and P14 are within 10% of the maximum compressive strains calculated using the models for confined concrete, while the measured maximum compressive strains of Specimens P10 and P12 are approximately 50% larger than the calculated strains (Table 6.6). This supports the previous assumption that the bars with longer unbraced length at failure had strains larger than the yield strain of the steel.

Table 6.6 Calculated Compressive Strain in the Concrete and in Longitudinal Bars in Northeast Corner at Peak Axial Load

Spec. ID	Measured Maximum Compressive Strain in Concrete ϵ_c	Calculated Maximum Compressive Strain in Concrete ϵ_{max}		Calculated Axial Strain in Longitudinal Bars ϵ_s		Distance from North-East Corner to Buckled Bar mm (in.)	Observed Buckled Length of Longitudinal Bar mm (in.)
		Model M	Model S	Model M	Model S		
P6	0.0041	0.0045	0.0055	0.0041	0.0051	19 (0.75)	63.5 (2.50)
P8	0.0042	0.0045	0.0043	0.0042	0.0041	19 (0.75)	63.5 (2.50)
P10	0.0056	0.0038	0.0038	0.0036	0.0036	19 (0.75)	63.5 (2.50)
P12	0.0060	0.0038	0.0038	0.0036	0.0036	19 (0.75)	63.5 (2.50)
P14	0.0032	0.0030	0.0030	0.0029	0.0029	16 (0.625)	51.0 (2.00)

Table 6.7 Calculated Compressive Strain in the Concrete and in Longitudinal Bars Along East Wall with Largest Buckled Length at Peak Axial Load

Spec. ID	Calculated Maximum Compressive Strain in Concrete ϵ_{max}		Calculated Axial Strain in Longitudinal Bars ϵ_s		Distance from North-East Corner to Buckled Bar mm (in.)	Observed Buckled Length of Longitudinal Bar mm (in.)
	Model M	Model S	Model M	Model S		
P6	0.0045	0.0055	0.0033	0.0041	146 (5.75)	63.5 (2.50)
P8	0.0045	0.0043	0.0034	0.0033	140 (5.50)	95.3 (3.75)
P10	0.0038	0.0038	0.0030	0.0030	140 (5.50)	95.3 (3.75)
P12	0.0038	0.0038	0.0026	0.0026	203 (8.00)	95.3 (3.75)
P14	0.0030	0.0030	0.0026	0.0026	105 (4.125)	102.0 (4.00)

A commonly used procedure to determine the critical buckling stress of a longitudinal reinforcing bar is to use the Euler buckling theory, but substituting the modulus of elasticity by the tangent modulus, E_t (Bresler. and Gilbert 1961, Mau 1990, Pantazopoulou. 1998, Popov 1999).

$$\sigma_{cr} = \frac{\pi^2 E_t I_b}{S^2 A_b} = \frac{\pi^2 E_t}{16} \left(\frac{d_b}{S} \right)^2 \quad (6.8)$$

where d_b , A_b , and I_b are the diameter, the cross section and moment of inertia of the longitudinal bar, and S is the vertical spacing of the transverse reinforcement or the unsupported length of the bar.

From Eq. 6.8, the critical spacing, S_{cr} , is calculated as:

$$S_{cr} = \frac{\pi d_b}{4} \sqrt{\frac{E_t}{\sigma_{cr}}} \quad (6.9)$$

The tangent modulus is the slope of the tangent to the stress-strain curve at a given compressive stress. If a bar reaches the yield stress then the critical spacing is calculated using Eq. 6.9, taking σ_{cr} equal to the yield stress. In the yield plateau the tangent modulus is equal to zero, which results in the critical spacing equal to zero. Therefore, the bars would buckle as soon as yielding is reached. But it is well known that longitudinal reinforcement can sustain strains larger than the yield strain.

One approach to evaluate the critical spacing is to take the tangent modulus equal to the modulus at onset of strain-hardening. The values of the yield stress and the strain-hardening modulus of the 6-mm (#2) bars used in this investigation are 510 MPa (74 ksi) and 2260 MPa (330 ksi), respectively (Appendix A). Evaluating Eq. 6.9 it is found that the critical spacing of the

transverse reinforcement, S_{cr} , is 3.5 times the bar diameter, which corresponds to 21 mm (0.83 in.) for the longitudinal reinforcement used in this research.

Mau (1990) showed that if the transverse reinforcement spacing is less than a critical value, the longitudinal bars are able to sustain axial strains in the strain-hardening region before buckling. The critical spacing is a function of the shape of the steel stress-strain curve and the diameter of the longitudinal bars. The parameters that define a steel stress-strain curve are: the yield strain, ϵ_y ; the strain at the onset of strain hardening, ϵ_h ; the yield stress, f_y ; the peak stress, f_{su} ; the hardening modulus of elasticity, E_h ; and the modulus of elasticity, E_s . Mau calculated the hardening modulus of elasticity by replacing the hardening curve by a straight line.

Using a finite element model, Mau (1990) calculated contour curves of the critical value of S/d_b . Elastic unloading due to bending of the bars during post-buckling behavior was also considered.

The parameters used to describe the stress-strain characteristics of the longitudinal bars used in the piers were reported in Appendix A: $\epsilon_y = 0.0026$; $\epsilon_h = 0.0059$; $f_y = 510$ MPa (74 ksi); $f_{su} = 600$ MPa (87 ksi); $E_s = 200000$ MPa (29000 ksi); $E_h = 2260$ MPa (330 ksi).

A value of the critical S/d_b approximately equal to 4 was determined using the contour curves developed by Mau (1990) and the material properties for the longitudinal steel. This value agrees with the value obtained using Eq. 6.9. The critical spacing of the transverse reinforcement was approximately $S_{cr} = 25$ mm (1.0 in.) for the 6-mm (#2) longitudinal bars used in this investigation. The

vertical spacing of the transverse reinforcement in all the specimens was larger than S_{cr} . Therefore, Mau's model and Eq. 6.9 suggest that the longitudinal bars will buckle before the onset of strain hardening. This result is consistent with the calculated strain values reported in Tables 6.6 and 6.7.

Also, it has been shown experimentally that in confined columns buckling of the longitudinal reinforcement in confined concrete can occur at strains larger than the yield strain of the bars (Kaar et al. 1978, Mander et al. 1988a).

Mau (1990) and Pantazopoulou (1998) showed that the buckling strain might exceed the yield strain for bars with transverse reinforcement spaced at distances that exceed the critical spacing. After initial buckling at yield strain, the steel may regain its load carrying capacity and buckle at a larger strain. For large values of S/d_b larger than the critical ratio, the bars will buckle immediately after reaching the yield strain and rapidly lose their load carrying capacity. For values of S/d_b close to the critical ratio, the bars lost their load carrying capacity but sustaining large axial strains.

Figure 6.12 shows results from finite element analysis by Mau and El-Mabsout (1989) of bars with perfectly-plastic stress-strain relationship and yield stress equal 415 MPa (60 ksi). Bayrak and Sheikh (2001) obtained similar curves by from compression tests of reinforcing bar specimens. Curves of the ratio of the axial capacity to the yield strength of the reinforcing bars for three values of slenderness ratio, L/r , are plotted, where L corresponds to one-half the spacing of the transverse ties. Therefore, the value of the ratio S/d_b is given by

$$\frac{S}{d_b} = \frac{1}{2} \frac{L}{r} \quad (6.10)$$

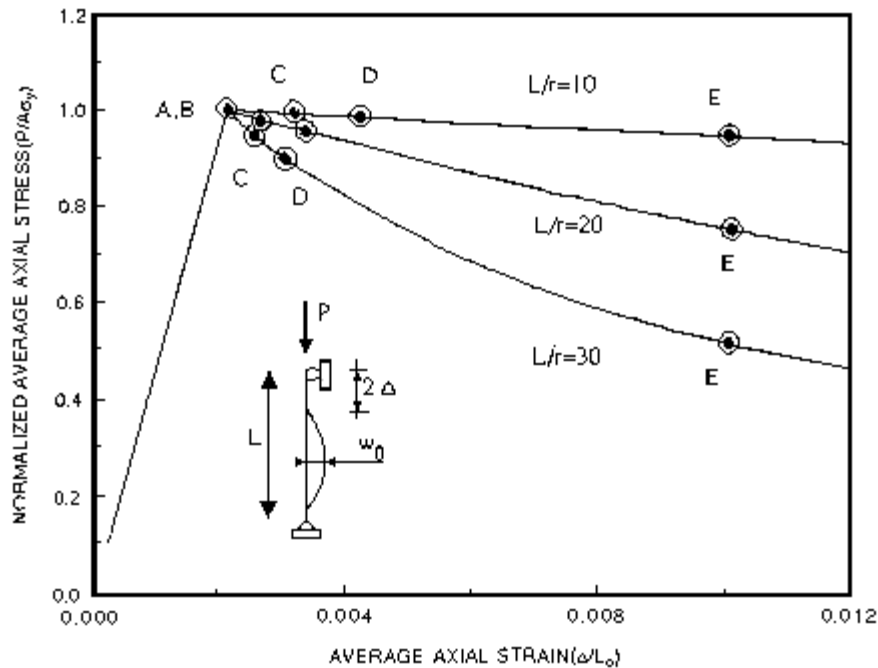


Figure 6.12 Post-Buckling Behavior of Perfectly Plastic Bars (Mau and El-Mabsout 1989)

Points A, B, C, D, and E represent various stages of stress-strain changes in the bar. Point A is yielding of the bar; B is initial unloading; C is the point where tension stress occurs; D is the point where tension yielding occurs; and E represents the point at which the average axial strain is 0.01.

This plot can be used to estimate the loss in axial load capacity of the bars used to construct the piers. The actual yield strain was 25% larger than the yield strain used to calculate the curves.

The ratios of transverse reinforcing spacing to the longitudinal bar diameter, S/d_b , for the critical bars along the east wall and for bars located at the north-east corner are listed in Table 6.8. The values of S/d_b ranged from 8 to 16.

Table 6.8 Ratios S/d_b of Longitudinal Bars with Largest Buckled Length and Bars Located at the Northeast Corner of the Piers

Specimen ID	Ratio S/d_b		Increase of Concrete Compressive Stress in Bars with Largest Buckled Length MPa (psi)
	Bars with Largest Buckled Length	Bars Located at Northeast Corner	
P6	10	10	0.83 (120)
P8	15	10	0.97 (140)
P10	15	10	1.17 (170)
P12	15	10	2.07 (300)
P14	16	8	2.48 (360)

The bars located at the northeast corner have values of S/d_b that correspond to L/r equal 20. In Fig. 6.12 these longitudinal bars can sustain axial compressive strains as large as 0.005 and maintain an axial strength equal to 90% of their yield strength. The bars located along the east wall have values of S/d_b that correspond to L/r equal 30. These bars can sustain axial compressive strains as large as 0.003 and maintain an axial strength equal to 90% of their yield strength (Fig. 6.12).

A 10% decrease of axial capacity of the bars corresponds to 1.6 kN (0.37 kips), which has to be transferred to the concrete in the core. The increase of compressive stress in the confined concrete due to a decrease in the axial capacity of the longitudinal bars that buckled with largest length along the east wall are also reported in Table 6.8. The increase in concrete compressive stress was

calculated as the decrease in steel capacity divided by the area of confined concrete around the bar.

The piers that had the largest increase in compressive stress in the core concrete, P12 and P14, also had strains at buckling of the bars along the east wall equal to the yield strain.

The calculated increase in compressive stress corresponds to less than 6% of the compressive strength of the concrete in the walls, which can be redistributed within the concrete. Therefore, the longitudinal bars could sustain axial compressive strains larger than the yield strain of the bars before failure occurred.

6.4.3 Hypothesized Failure Sequence of the Test Specimens

From the previous discussion, the likely failure sequence for the specimens can be described as follows. As the axial load increased the stresses in the cover concrete also increased until reaching a limiting value. At this level of stress, the cover concrete cracked and spalled. After the longitudinal bars located at the northeast corner reached the yield strain, the large amount of transverse reinforcement and the effective spacing of that reinforcement helped those bars to sustain larger axial compressive strains.

The axial load was increased until the longitudinal bars located along the east wall reached the yield strain. At this level of strain the bars could buckle due to two factors. First, the longitudinal bars along the walls had cross ties distributed in a checkerboard pattern, and therefore, the length effectively restrained by the cross-ties was as large as two times the vertical spacing of the

transverse reinforcement. The longitudinal bars were also restrained at mid-length between cross-ties by the bending stiffness of the transverse reinforcement. However, the bending stiffness of the transverse bars is negligible compared with the axial stiffness of the cross-ties.

The second factor is that the cross-ties had 90-degree hooks. In the photographs (Fig. 5.24, 5.37, 5.52, and 5.65) the 90-degree hook in the cross ties opened outward in Specimens P8, P10, P12, and P14.

In Specimens P12 and P14 the calculated axial strain of the bar with longest buckled length (Table 6.7) was equal to the yield strain. Also, these piers had the smallest thickness of confined concrete and the largest increase in compressive stresses due to a loss in capacity of the bars. Therefore, the bars buckled as soon as they reached the yield strain and the confined concrete could not resist the increase of compressive stresses, and failure occurred explosively.

The other piers could resist the increase in compressive stresses, and the longitudinal bars along the east walls therefore sustained larger axial strains before the confinement in the concrete core of the walls was lost. Then the axial load could not be redistributed and the concrete walls failed explosively.

6.5 SUMMARY

Four procedures were used to estimate the axial capacity of piers. One procedure was a design method and the other three consisted in the use of material models to represent the concrete behavior.

The equivalent rectangular stress block method described in Sections 5.7.2 and 5.7.4 of AASHTO Specifications (1998) and Sections 10.2 and 10.3 of

ACI-318 (1999) coupled with ordinary column interaction curve theory provided a conservative estimate of the axial capacity of the rectangular hollow piers tested in this investigation. All specimens had a wall slenderness ratio less than 15 and were subjected to combined axial loading and biaxial bending. The nominal capacity of hollow piers provided a good estimate of the load corresponding to the onset of crushing of the concrete near the extreme compression fiber. The ratios of measured axial strength to nominal axial capacity decreased, as the wall slenderness increased.

Two material models for confined concrete were used to calculate the response of the five hollow, concrete piers tested in this investigation. The models did not include local buckling effects.

Both material models exhibited very good agreement with the measured moment-curvature response of the piers about the north-south axis, but by Mander et al. (1988b) more closely reproduced the moment-curvature response of the specimens about the east-west axis. Both models overestimated the limiting strains of the specimens. In both models the maximum compressive strain on the concrete at the peak calculated axial load was less than 0.0055.

Buckling of the longitudinal bars apparently controlled the limiting strain on the specimens. The checkerboard distribution of the cross ties resulted in effective unbraced lengths of the longitudinal bars along the east and north walls larger than the vertical spacing of the transverse reinforcement. Also, cross-ties with 135-degree hooks helped delay the buckling of the longitudinal bars by better restraining their lateral deflection.

Based on a definition of failure load calculated using the material models for confined concrete as the peak calculated load, both material models accurately estimated the capacity and the ultimate curvature of the specimens.

Chapter 7 Overall Analytical Model

A finite element model that was developed to study the behavior of reinforced concrete members with thin walls subjected to compression and bending is presented in this chapter. The model is first evaluated by comparing the calculated response with the measured response of thin concrete panels subjected to in-plane compression and later using the measured response of the hollow piers tested in this and previous investigations.

7.1 FINITE ELEMENT MODEL

The general-purpose finite element program ABAQUS (Hibbitt 1994a, 1994b) was used to formulate a finite element model to analyze thin concrete panels and rectangular hollow concrete piers. The material models that are included in the program, the elements used in the model, the loading procedures, and the boundary conditions are described in this section.

7.1.1 Materials

The program ABAQUS includes a constitutive model for plain concrete (Section 4.5.1 from Hibbitt et al. 1994a and Section 8.9.7 from Hibbit et al. 1994b) that can be combined with bar elements to model reinforced concrete. With this approach, the concrete behavior is considered independently of the reinforcement.

The compressive response of the concrete is modeled using an elastic-plastic model to define a compression yield surface. The tensile response of the

concrete is modeled using tension-stiffening and a surface defining the onset of cracking.

The cracking model is based on the assumption of non-rotating, smeared cracks. Therefore, after cracking occurs the orientation of the crack is fixed for all future loading steps and the model does not track individual cracks. The cracked concrete is represented using a damaged elasticity model, which is defined with a reduced modulus of the concrete at the location of the cracks.

The steel was modeled as an elastic-plastic material. In the following sections the material models are presented and their characteristics and parameters are discussed in relation with this investigation.

(a) Concrete

The compression yield surface used to model the concrete is defined in Eq. 7.1 as a line in terms of two stress invariants: the equivalent or hydrostatic stress, p , and the Von Mises equivalent deviatoric stress, q . The hydrostatic stress is defined in Eq. 7.2 and the Von Mises stress is defined in Eq. 7.3.

$$f = q - \sqrt{3}a_0p - \sqrt{3}\tau_c = 0 \quad (7.1)$$

$$p = -\frac{(\sigma_1 + \sigma_2 + \sigma_3)}{3} \quad (7.2)$$

$$q = \sqrt{\frac{1}{2}\{(\sigma_1 - \sigma_2)^2 + (\sigma_2 - \sigma_3)^2 + (\sigma_3 - \sigma_1)^2\}} \quad (7.3)$$

where σ_1 , σ_2 , and σ_3 are the principal stresses of the stress tensor, a_0 is a constant that is function of the ratio of the ultimate stress in biaxial compression to the

ultimate stress in uniaxial compression, and τ_c is a hardening parameter calculated from the uniaxial stress-strain response of the concrete in compression.

Isotropic hardening and an associated flow rule are used. An isotropic hardening rule represents an expansion of the yield surface, with no change of its shape. Under uniaxial stress the isotropic hardening rule predicts that, after a stress σ has been reached as a result of work-hardening, the yield stress obtained on stress reversal will be $-\sigma$. An associated flow rule is a plastic flow rule in which the plastic strain rates are determined by differentiating the yield surface.

The tensile response of the concrete is modeled using a crack-detection surface, also described in terms of the stress invariants p and q , as shown in Eq. 7.4.

$$f = q - \left(3 - b_0 \frac{\sigma_t}{\sigma_t^u} \right) p - \left(2 - \frac{b_0}{3} \frac{\sigma_t}{\sigma_t^u} \right) \sigma_t = 0 \quad (7.4)$$

The stress σ_t^u is the uniaxial tensile strength of the concrete. The constant b_0 is a function of the uniaxial tensile strength of the concrete and the tensile strength of the concrete at the intersection of the crack-detection surface and the compression yield surface (Point A in Fig. 7.1).

The compression-yield surface and the crack-detection surface are shown in Fig. 7.1 in terms of plane stresses, and in Fig. 7.2 terms of the hydrostatic and the Von Mises stress. In this second representation, straight lines represent both failure surfaces. The uniaxial and biaxial compressive and tensile strengths of the concrete are also shown in Fig. 7.1.

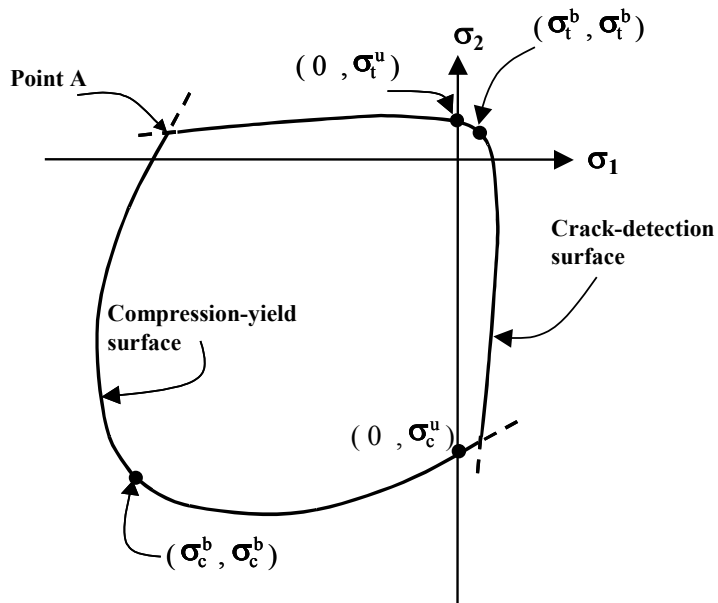


Figure 7.1 Concrete Failure Surfaces in Plane Stresses (Hibbitt et al. 1994a)

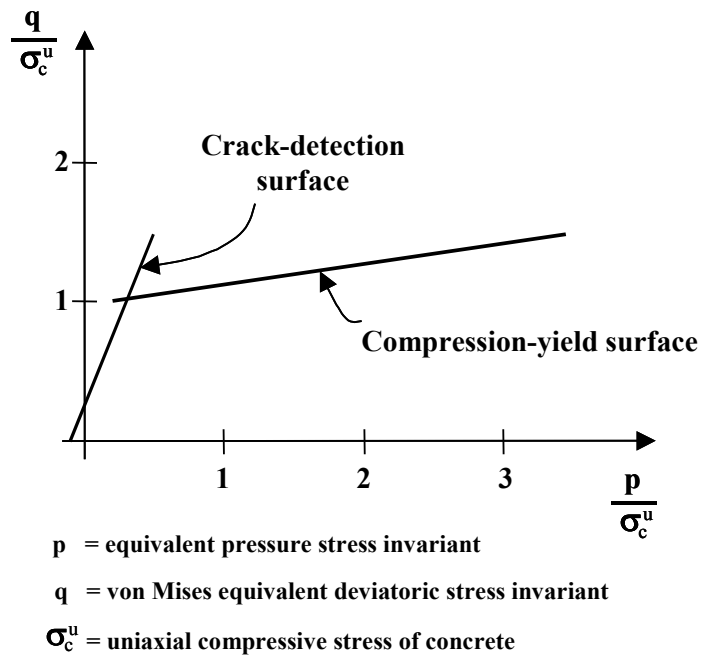


Figure 7.2 Concrete Failure Surfaces in the (p-q) Plane (Hibbitt et al. 1994a)

The properties of the concrete are defined using the uniaxial stress-strain relationship of the concrete (Hibbitt et al. 1994b) shown in Fig. 7.3. The material model assumes elastic behavior in uniaxial compression up to the proportional limit, f_p . The softening of the stress-strain relationship, including the descending branch of the curve, is defined using straight lines.

The uniaxial tensile response of the concrete is assumed to be elastic, with a modulus of elasticity equal to the initial compressive modulus of elasticity, up to the maximum tensile stress, f_t . The softening of the tension curve is defined using the tension-stiffening model.

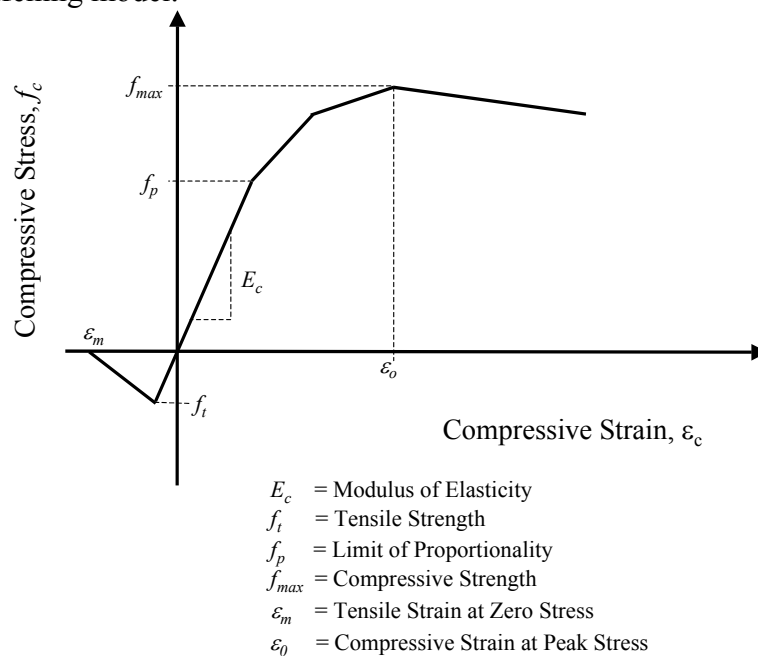


Figure 7.3 Unconfined Concrete Uniaxial Stress-Strain Relationship

A well-known uniaxial compression stress-strain relationship for concrete is the curve developed by Hognestad (1951). The stress-strain curve consists of a parabolic ascending branch and a linear descending branch, as shown in Fig. 7.4.

The uniaxial compressive strength, f'_c , can be determined by testing 150-mm diameter by 300-mm long (6-in. diameter by 12-in. long) concrete cylinders, following ASTM C39 (1999). It was assumed that the compressive strength of the concrete obtained from the cylinders, reported in Appendix A, represents the strength of the concrete in the piers ($k_3 = 1.0$).

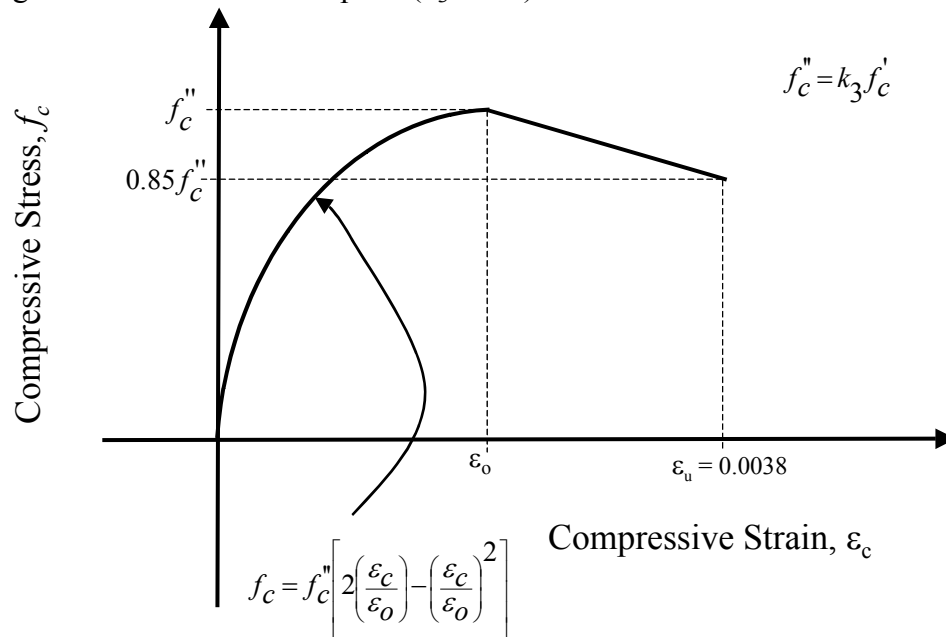


Figure 7.4 Uniaxial Compression Stress-strain Relationship for Unconfined Concrete Proposed by Hognestad (1951, 1952)

The measured stress-strain response for all the piers tested in this investigation and the stress-strain relationships calculated using a expression based in the material model by Hognestad are plotted in Fig. A.1 through A.5. The ascending branch of the measured curves is well represented by the Hognestad relationship, but taking the value of k_3 equal to 1.0, and therefore a stress-strain relationship based in the curve proposed by Hognestad is a good

representation of the uniaxial compressive response of the concrete used in the test specimens. The stress-strain relationship described in Fig. 7.3 was defined using a curve based in Hognestad's.

The ACI 318 (1999) specifies a maximum concrete compressive strain equal to 0.003 for design. This corresponds to a lower fractile of available test data (Kaar et al. 1978, Mac Gregor 1988). Larger strains have been measured in tests of plain and reinforced concrete members. However, the capacities calculated using the finite element model were not sensitive to the ultimate compressive strain of the concrete, for strains in the range of 0.0038 and 0.0050. Therefore, the limiting strain suggested by Hognestad ($\varepsilon_u = 0.0038$) was used for the calculations.

The tensile strength of concrete is low, about 8% to 15% of the compressive strength. It has a high variability among specimens and depends on the testing procedure used and on the compressive strength of the concrete. Two tests are widely used to determine the tensile strength of the concrete: the modulus of rupture or flexural test (as specified in ASTM C78 (1994) or C293 (1994)) and the split-cylinder test (as specified in ASTM C496 (1996)). The flexural test gives values that exceed the direct tensile strength of the concrete, while the split cylinder test values are more conservative and were used to define the tensile strength in the model.

The tension-stiffening model includes the interaction between concrete and reinforcement by specifying a post-cracking strain to simulate load transfer across cracks through the reinforcement. The tension-stiffening model used

defines a post-cracking stress-strain relationship in the concrete^(52,53) and is shown in Fig. 7.5. The shape of the tension-stiffening relationship depends on a diverse set of factors such as the reinforcing pattern, quality of the bond between steel and concrete, loading type, and support conditions.

ABAQUS (Section 4.5.1 (Hibbitt et al. 1994a)) recommends the following relationship for strains in the tension-stiffening model (Fig. 7.5): ϵ_m equal to 10 times ϵ_t . For normal concrete, ϵ_t is approximately 10^{-3} , so ϵ_m would be around 10^{-2} . Chang et al. (1987) also found that tension stiffening in reinforced concrete panels could be adequately modeled using the linear unloading scheme shown in Fig. 7.5, with ϵ_m equal to 10^{-2} . On the other hand, Pagnoni et al. (1992) suggested using the yield strain of the reinforcement as an upper bound for ϵ_m . For the specimens tested in this investigation, the yield strain was 2.6×10^{-3} .

Various values of ϵ_m , ranging from 10^{-3} to 10^{-2} , were used to analyze the hollow piers. It was found that the calculated capacity decreased as the value of ϵ_m increased. However, for values of ϵ_m above 5×10^{-3} , the calculated capacity was essentially constant. Therefore, it was decided to use a value of ϵ_m equal to 5×10^{-3} in all calculations.

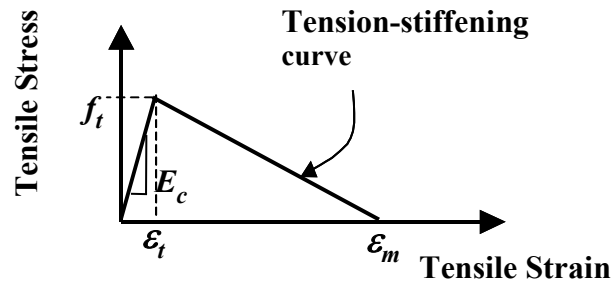


Figure 7.5 Tension-Stiffening Model

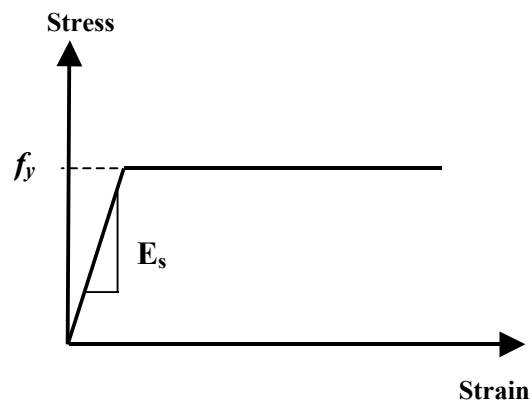
To define the shape of the failure surfaces in the multiaxial stress state, the following ratios of stresses defined in Fig. 7.1 must be specified:

1. The ratio of the ultimate biaxial compressive stress (a state of stress with two equal compressive stresses), σ_c^b , to the uniaxial compressive strength, σ_c^u . A value equal to 1.16 (Hupfer, Hilsdorf and Rusch, 1969) was used in the model.
2. The ratio of the principal tensile stress at the intersection of the crack-detection surface and the compression-yield surface (Point A in Fig. 7.1) to the uniaxial tensile strength, σ_t^u . The default value from ABAQUS (Hibbit 1994b) is 1/3, which was used in this investigation.
3. The ratio of the magnitude of the plastic strain in a principal direction at the ultimate stress in biaxial compression, (σ_c^b, σ_c^b) in Fig. 7.1, to the plastic strain at ultimate stress in uniaxial compression, $(\sigma_c^u, 0)$ in Fig. 7.1. The ABAQUS (Hibbit 1994b) default value is 1.28, which was used in this investigation.

The confinement provided by the transverse reinforcement was not included in the finite element model. The increase in strength due to the confinement is included through the ratio of the ultimate biaxial compressive stress to the uniaxial compressive strength, which was considered to be 1.16. The biaxial state of stresses is induced by the transverse reinforcement that is assumed to be bonded perfectly to the concrete in the model.

(b) Steel Reinforcement

To model steel reinforcement in ABAQUS (Section 2.2.3, Hibbit 1994b) uses uniaxial elements superposed on the mesh of plain concrete elements. Dowel action of the reinforcement is not modeled, and the reinforcement is assumed to have perfect bond with the concrete. The steel was modeled as an elastic-plastic material as shown in Fig. 7.6. Strain hardening was neglected.



E_s = Modulus of elasticity of steel
 f_y = Yield stress of steel reinforcement

Figure 7.6 Assumed Stress-Strain Behavior of Steel Reinforcement

7.1.2 Element

First-order, solid, isoparametric, hexahedral, three-dimensional elements were used to model the walls of the panels and the hollow piers. The element is a fully integrated 8-node brick (Section 3.2.1 Hibbit 1994b), meaning that the stiffness matrix of an element with uniform material properties and parallel opposing faces is integrated exactly. Two 8-node elements were used through the

thickness of all the plates and walls discussed in this chapter. All elements were defined with parallel opposing faces.

The sensitivity of the calculated response of the panels and the hollow piers to the number of elements used to model the walls was also studied and is reported in Sections 7.2 and 7.3.

7.1.3 Loading Method

ABAQUS has two control algorithms for loading: load control, in which the load is applied in various steps; and displacement control, in which changes in displacement are imposed on the member and changes in deformation, stresses, and reactions are calculated so equilibrium is satisfied. In cases in which the load-displacement response exhibits a maximum load and then experiences a softening of the response, the load-controlled method has to be used simultaneously with an algorithm that can follow the solution. ABAQUS uses the modified Riks (Section 2.2.2 Hibbit 1994b) method to solve that problem.

To follow the path of the load-displacement response, the Riks algorithm calculates a point by defining an arc increment tangent to the current solution point. Then, the algorithm searches for equilibrium in a plane passing through the new point and orthogonal to that tangent. It was observed that the load-control algorithm was sensitive to the parameters that define the Riks method, and may not converge.

Figure 7.7 shows calculated deflection response of Specimen P14 calculated using both loading methods. The calculated displacements shown are

the vertical shortening measured at the point of application of the load, and the horizontal deflection in the east direction, measured at mid-height of the east wall.

The only difference in the calculated responses is that the load-controlled method follows the response from very low loads, while the first load calculated by the displacement-controlled method is close to the point where the stiffness of the structure decreases (in this case, at approximately 50% of the ultimate load). It was also observed that the load-controlled method needed more increments and more computation time to reach the final solution, and therefore, the displacement-controlled method was preferred.

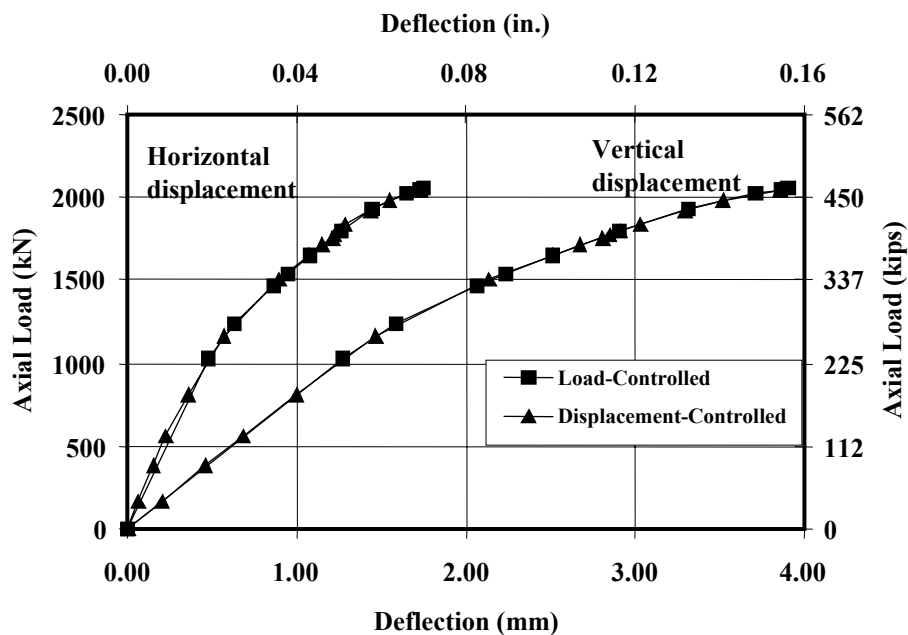


Figure 7.7 Vertical Deflection and Horizontal Load-Deflection Responses of Pier P14 Calculated Using Displacement Controlled and Load Controlled Loading

Two bounds to the loading paths can be followed while loading a column in bending. In Taylor et al. (1990) and in the current study, the piers were loaded with a constant eccentricity, as shown in Fig. 7.8(a). This can be modeled using displacement-controlled or load-controlled loading.

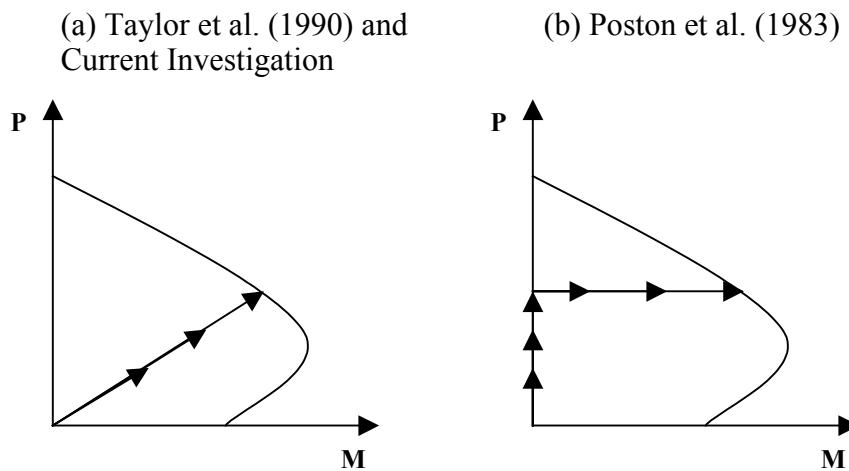


Figure 7.8 Load Paths Followed in Different Testing Programs

Poston et al. (1983) loaded the specimens axially up to a given load and then introduced bending, holding the axial load constant (Fig. 7.8(b)). In this case, the eccentricity was varied from zero to a maximum at failure, keeping the ratio of strong to weak axis eccentricity constant. In the finite element analysis, the displacement-controlled method could not be used to calculate the specimens tested by Poston et al. because the deflection path followed by the specimens was unknown. Therefore, those specimens were analyzed using the load-controlled method.

7.1.4 Local Buckling

To include local buckling effects in the analysis two steps were taken. First, a first-order, linear buckling analysis (Section 2.4.1 Hibbit 1994a and Section 10.2.2 Hibbit 1994b), was performed. The analysis takes into account the loading and boundary conditions, but assumes that the materials are elastic. The results obtained are the elastic buckling load and the first buckling mode shape for the specimen. The buckling mode shape is then added to the geometry of the piers as an initial imperfection. An imperfection ratio, defined as the initial horizontal deflection of the piers with respect to the non-deformed geometry divided by the wall thickness, δ_w/t_w , is used to define the size of the imperfection.

Geometric nonlinearities (Hibbit 1994b), were included to consider large-displacement effects by using the actual geometry of the specimen to calculate the stiffness matrix of the elements and the equilibrium equations during each step of the solution algorithm.

The same approach was used to model buckling effects for the thin plates and the hollow piers.

7.2 CALCULATION OF BUCKLING IN THIN CONCRETE PANELS

Before studying the behavior of hollow rectangular concrete sections, the model was used to investigate the behavior of thin concrete panels. The objective was to find if the model could reliably calculate the local buckling load of thin concrete members.

The responses of the thin concrete panels discussed in Chapter 2 (Ernst 1952, Swartz et al. 1974, and Saheb and Desayi 1990) were calculated using the

procedures discussed in Section 7.1. Reported concrete and steel strengths were used to define the material properties.

The concrete tensile strengths were not reported; therefore, the tensile strength was approximated as (Mirza, Hatzinikolas and MacGregor 1979):

$$f_t = 0.53\sqrt{f'_c} \text{ (MPa)} \quad (7.5a)$$

$$f_t = 6.4\sqrt{f'_c} \text{ (psi)} \quad (7.5b)$$

where f_t and f'_c are in MPa (psi). Equation 7.5 provides an estimate of the split cylinder strength of the concrete.

The modulus of elasticity, E_c , was assumed to be:

$$E_c = 4730\sqrt{f'_c} \text{ (MPa)} \quad (7.6a)$$

$$E_c = 57,000\sqrt{f'_c} \text{ (psi)} \quad (7.6b)$$

where E_c and f'_c are in MPa (psi), as defined in the ACI-318 (1999).

Three values of the imperfection ratio, δ_w/t_w , were used in the analyses: 0.16, 0.24 and 0.32. These values correspond to initial deformations of the panels equal to approximately 1/6 to 1/3 of the thickness of the panels. The initial deflection varied between 2 and 12 mm (0.08 and 0.48 in.) for the specimens tested by Ernst and by Swartz et al. The specimens tested by Saheb and Desayi were thicker, so their maximum initial deflection varied between 8 and 16 mm (0.32 and 0.64 in.). These imperfection ratios are unrealistic.

Five panels tested by Ernst were modeled to study the sensitivity of the calculated buckling load to the size of the elements of the models. The specimens

were modeled using 10 to 32 elements along the width of the panels. The aspect ratio of the elements in the plane of the plate was 1.0, and the imperfection ratio was equal to 0.32. The calculated capacities are reported in Table 7.1. The calculated capacities decrease as the number of elements in the model increase. The calculated capacities converge slowly. To avoid needing too long computing time it was decided to use between 20 and 25 elements along the width of the panels

Table 7.1 Capacity of Concrete Panels Tested by Ernst (1952) Calculated Using Various Numbers of Elements

Number of Elements Along the Width	Calculated Capacity KN (kips)				
	Specimen ½x40x40	Specimen ¾x40x40	Specimen 1x40x40	Specimen 1 ¼ x40x40	Specimen 1 ½x40x40
10	352 (79.1)	534 (120.0)	747 (168.0)	1000 (225.0)	1220 (274.0)
16	345 (77.6)	419 (94.1)	587 (132.0)	796 (179.0)	974 (219.0)
25	272 (61.2)	338 (76.0)	480 (108.0)	672 (151.0)	859 (193.0)
32	237 (53.3)	304 (68.3)	431 (97.0)	618 (139.0)	823 (185.0)
40	209 (47.0)	262 (59.0)	414 (93.0)	591 (133.0)	796 (179.0)

The typical finite-element mesh used to analyze the panels is shown in Fig. 7.9. Each mesh was based on a rectangular grid of 20 to 25 elements along the width of the plates, and as many elements as were needed along the height of the plates, so the aspect ratio of the elements was approximately equal 1.0. The aspect ratio of the elements through the thickness varied between 1.5 and 6.0. The

dimensions of the sides of the elements varied between 32 mm (1.25 in.) to 45 mm (1.75 in.).

The boundary conditions used in the physical tests were also used in the finite element models. Simply supported edges were modeled by assuming that each node along the central of edge nodes was constrained against horizontal displacement. Nodes located along the bottom line of edge nodes were also restrained against vertical displacements.

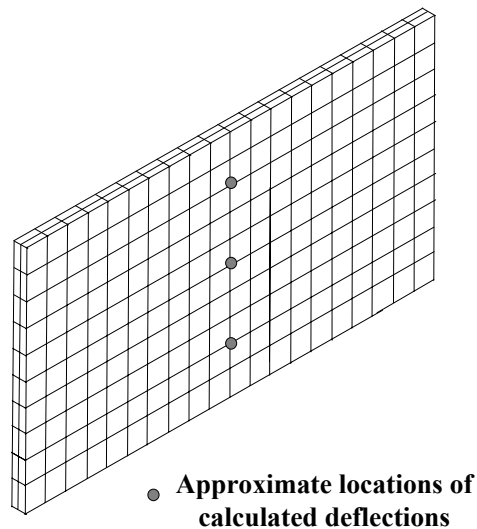


Figure 7.9 Finite Element Mesh used for Panels

7.2.1 Responses of Thin Concrete Panels Calculated using Finite Element Model

The panels tested by Saheb and Desayi (1990) had slenderness ratios between 6 and 18, similar to the range of slenderness ratios in the hollow piers tested in this investigation. The panels tested by Ernst (1952) and Swartz et al. (1974) were more slender, with slenderness ratios ranging from 26 to 72.

Detection of the onset of buckling is one of the critical issues that must be addressed in order to interpret the results of the finite element analyses. Shanley (1947) tested an aluminum-alloy column in compression and measured the strains on opposite sides of the specimen. He observed that the strains diverged sharply at a load very close to the onset of buckling. Mikhail and Guralnick (1971) studied the response of folded aluminum plates subjected to transverse load and made similar observations. As the critical buckling load was approached, the compressive stresses on one surface of the plate increased at a higher rate than the compressive stresses on the opposite surface. At the critical load, the compressive stresses decreased on the surface that originally was subjected to higher stresses, and increased rapidly on the other surface.

Swartz et al. (1974) observed the same trend in the measured compressive strains at the center of rectangular concrete panels subjected to uniaxial compression. The buckling load was determined by Swartz et al. (1974) as the last load prior to a decrease in the measured compressive strain on one surface of the plate. On the opposite surface of the plate, the compressive strains increased rapidly. The same trend was observed in some of the compressive strains measured by Ernst (1952).

The calculated compressive strains on opposite surfaces of three panels modeled using finite elements are plotted in Fig. 7.10 through 7.12. The calculated strain response was similar to the measured response of the concrete panels. As the axial load approached the buckling load, compressive strains on one surface increased rapidly while decreasing, or remaining constant on the

opposite surface. These trends were more apparent for analytical models with larger initial imperfection ratios.

Lateral deflections were calculated using an imperfection ratio equal to 0.24 along the vertical centerline of the plates, approximately at mid-height and at the quarter-points of that line (Fig. 7.9). The largest calculated deflections for the three panels are plotted in Fig. 7.13. These data indicate that the decrease in the compressive strains corresponded to a sharp increase in the lateral deflection of the panels.

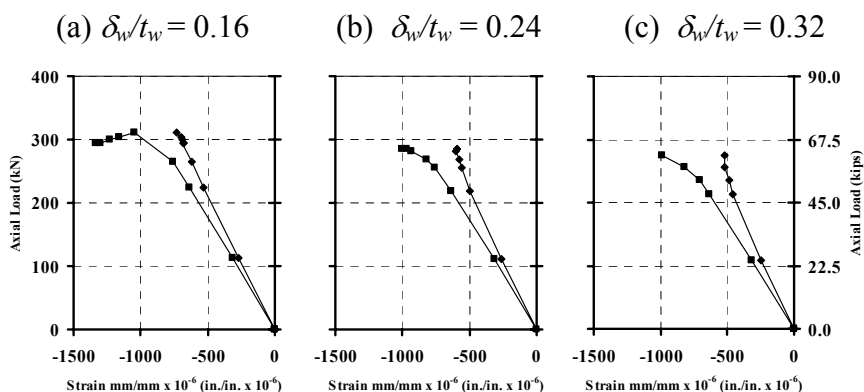


Figure 7.10 Calculated Response of Panel $\frac{1}{2} \times 40 \times 40$ Tested by Ernst (1952)

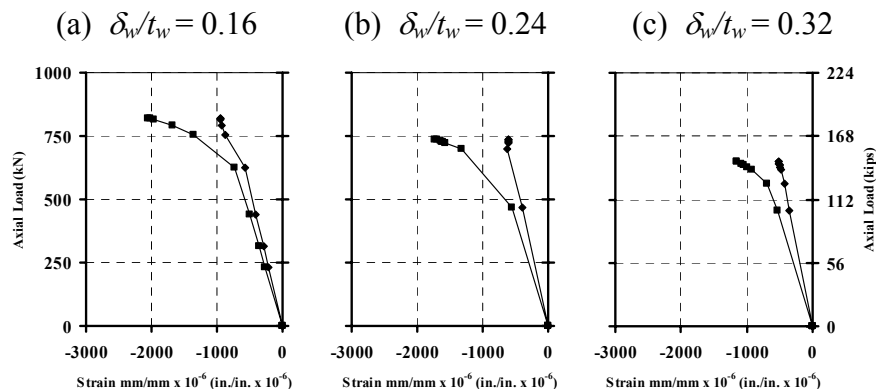


Figure 7.11 Calculated Response of Panel 15 Tested by Swartz et al. (1974)

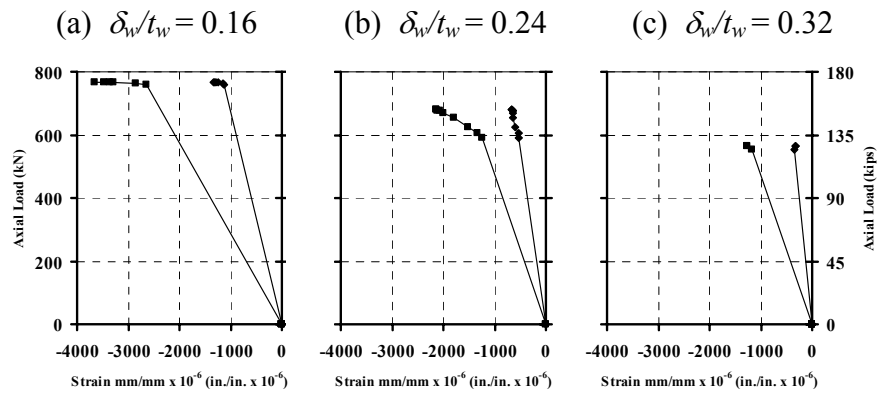
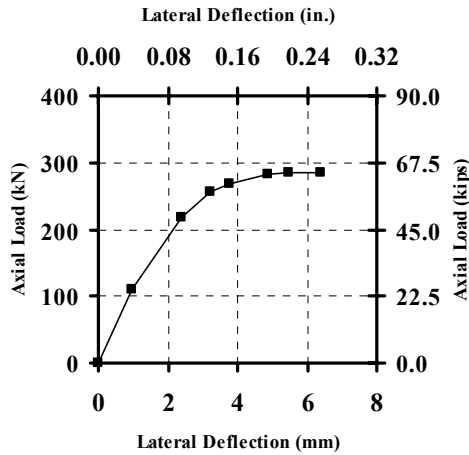


Figure 7.12 *Calculated Response of Panel 10 Tested by Saheb and Desayi (1990)*

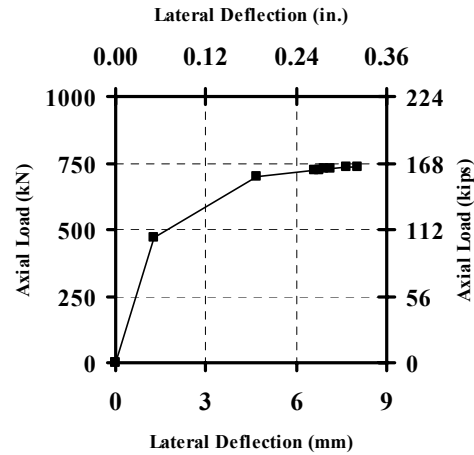
Based on these comparisons, the finite element model was successful in reproducing the buckling behavior of the reinforced concrete panels. As shown in Fig. 7.10 through 7.12, however, the calculated buckling load was extremely sensitive to the size of the initial imperfection used in the analysis. In all cases, the calculated buckling load decreased as the initial imperfection ratio increased.

The sensitivity of the calculated buckling load to the initial imperfection is documented in Tables 7.2, 7.3 and 7.4, which summarize the capacities calculated using the three assumed initial imperfection ratios. The ratios of the measured to calculated capacities are also listed in those tables.

(a) Panel 1/2x40x40
Tested by Ernst (1952)



(b) Panel 15 Tested
by Swartz et al. (1974)



(c) Panel 10 Tested by Sahed and Desayi (1990)

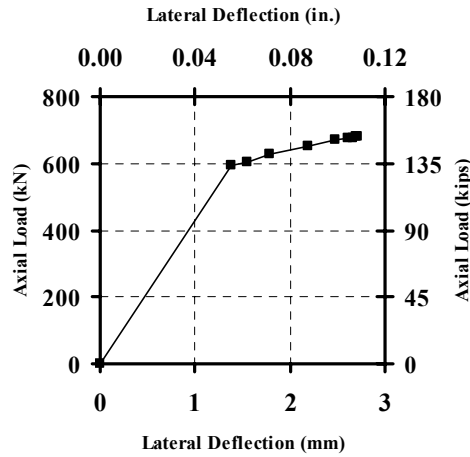


Figure 7.13 Calculated Lateral Deflections for Panels Shown in Figures 7.10 through 7.12

The ratios of measured to calculated capacities for all the plates, are plotted in Fig. 7.14 for the three values of imperfection ratio. The points are widely scattered. However, two trends can be observed. The first trend is that for

plates with a given wall slenderness ratio, the ratio of measured to calculated capacities tends to increase as the imperfection ratio increases. The second observed trend is that the ratio of measured to calculated capacities decreases as the wall slenderness ratio increases.

From the observations described in the previous paragraph was concluded that the imperfection ratio that produces best estimates of the capacity of a concrete plate increases as the wall slenderness ratio of the plate increases. The plates tested by Ernst (1962) and by Swartz et al. (1974) had large wall slenderness ratios (between 25 and 70, approximately), while the plates tested by Saheb and Desayi (1990) had wall slenderness ratios less than 20. The parameters that yielded the best estimates of the capacity were obtained for different values of imperfection ratio for the different test programs, as is shown in the following paragraphs.

The calculated capacities for the majority of the panels tested by Ernst were unconservative. The average of the ratios of the measured strength to calculated capacities closest to 1.0 was obtained using an imperfection ratio equal to 0.32. The average was 0.83, with standard deviation equal to 0.38. In Table 7.2 the plates with a thickness less than 25 mm (1.0 in.) had very low measured capacities, which the model overestimated by a factor close to 2. In the case of plates thicker than 25 mm (1.0 in.), the calculated capacities were closer to the measured capacities.

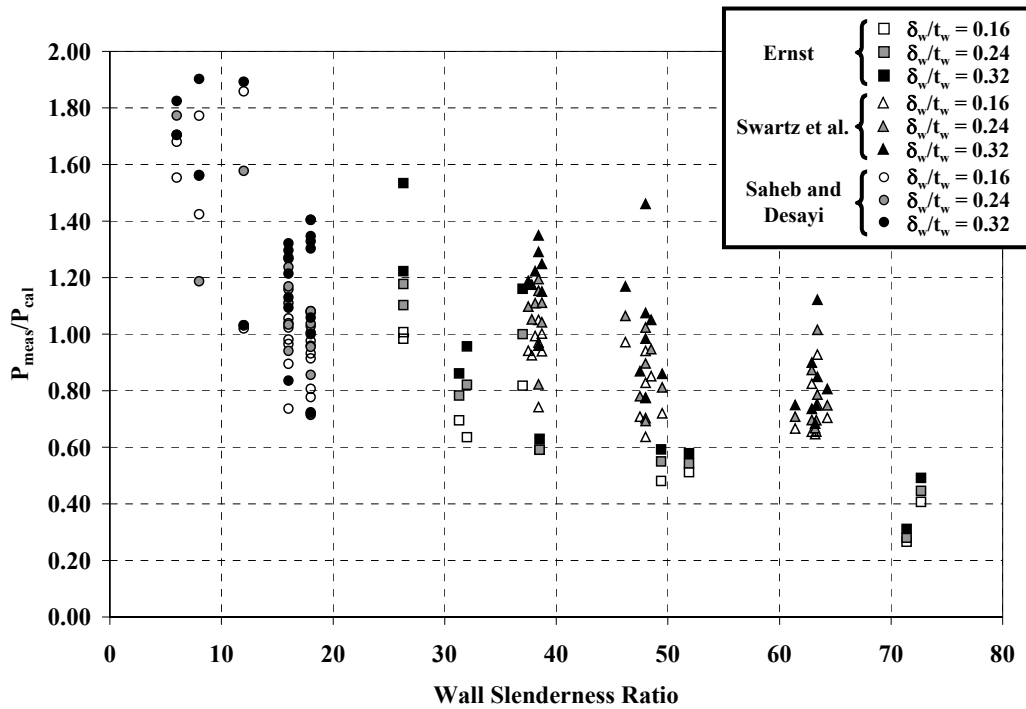


Figure 7.14 Ratios of Measured to Calculated Capacities of all the Plate Results Available for Three Values of Imperfection Ratio

The imperfection ratio that gave best estimates of the strengths reported by Swartz et al. was 0.32. The average ratio of the measured strengths to the calculated capacities was 1.02, with standard deviation equal to 0.22.

The imperfection ratio that gave best estimates of the strengths reported by Saheb and Desayi was 0.16. The average ratio of the measured strength to the calculated ultimate load was 1.08, with a standard deviation equal to 0.34.

All the test specimens were grouped by their wall slenderness ratios and the average ratio of measured to calculated capacities were computed. These, and the values of the imperfection ratios that produced best estimates (average ratio of

measured to calculated capacity equal 1.0) of the strength of the plates are listed in Table 7.5. The average ratios of measured to calculated capacities of the specimens with wall slenderness ratios less than or equal to 12 were larger than 1.45. The capacities of those panels were calculated using an imperfection ratio equal to 0.0 (Table 7.6). The average ratio of measured to calculated capacities was 1.30, which is closer to 1.0 than the values obtained using larger imperfection ratios and listed in Table 7.5. Therefore, it was decided that an imperfection ratio of 0.0 yields best estimates of capacity for panels with small wall slenderness ratio.

To obtain best estimates of the capacity of the panels, the imperfection ratio of specimens with small slenderness ratios (less than 12) should be 0.0, while the imperfection ratio of specimens with wall slenderness ratios in the range between 12 and 40 should be approximately 0.24. The wall slenderness ratios of the hollow piers tested in this and previous investigations ranged from 2 to 35. Therefore, values of the imperfection ratios between 0 and 0.24 will be used to estimate the capacity of those piers.

In conclusion, the finite element model was able to estimate a reduction in the capacity of the panels by introducing an initial imperfection in the finite element geometry. The estimated capacity of the plates was very sensitive to the value of the initial imperfection and to the size of the elements used in the model.

The value of the imperfection ratio that produced the best estimates of the capacity of the panels increased as the wall slenderness ratio increased.

Table 7.2 Comparison of Measured and Calculated Capacity for Specimens tested by Ernst (1952)

Panel ID	Panel Slenderness Ratio	Measured Capacity kN (kips)	Imperfection Ratio 0.16		Imperfection Ratio 0.24		Imperfection Ratio 0.32	
			Calculated Capacity kN (kips)	Ratio of Measured to Calc. Capacity	Calculated Capacity kN (kips)	Ratio of Measured to Calc. Capacity	Calculated Capacity kN (kips)	Ratio of Measured to Calc. Capacity
½x40x40	72.7	129 (29)	311 (70)	0.41	285 (64)	0.45	258 (58)	0.50
¾x40x40	51.9	196 (44)	383 (86)	0.51	360 (81)	0.54	338 (76)	0.58
1x40x40	38.5	302 (68)	512 (115)	0.59	512 (115)	0.59	480 (108)	0.63
1¼x40x40	31.3	578 (130)	832 (187)	0.70	738 (166)	0.78	672 (151)	0.86
1½x40x40	26.3	1050 (236)	1068 (240)	0.98	952 (214)	1.10	859 (193)	1.22
½x40x20	71.4	76 (17)	276 (62)	0.27	262 (59)	0.28	236 (53)	0.31
¾x40x20	49.4	173 (39)	356 (80)	0.48	311 (70)	0.55	289 (65)	0.59
1x40x20	37.0	578 (130)	707 (159)	0.82	578 (130)	1.00	498 (112)	1.16
1¼x40x20	32.0	489 (110)	770 (173)	0.64	596 (134)	0.82	512 (115)	0.96
1½x40x20	26.3	903 (203)	894 (201)	1.01	787 (177)	1.14	587 (132)	1.53
Average				0.64	0.73		0.83	
St. Dev.				0.24	0.29		0.38	
COV				0.38	0.40		0.46	

Table 7.3 Comparison of Measured and Calculated Capacity for Specimens tested by Swartz et al. (1974)

Panel ID	Panel Slenderness Ratio	Measured Capacity kN (kips)	Imperfection Ratio 0.16		Imperfection Ratio 0.24		Imperfection Ratio 0.32	
			Calculated Capacity kN (kips)	Ratio of Measured to Calc. Capacity	Calculated Capacity kN (kips)	Ratio of Measured to Calc. Capacity	Calculated Capacity kN (kips)	Ratio of Measured to Calc. Capacity
1	48.0	490 (110)	770 (173)	0.64	707 (159)	0.69	632 (142)	0.78
2	48.0	507 (114)	721 (162)	0.70	654 (147)	0.77	472 (106)	1.07
3	47.5	444 (100)	627 (141)	0.71	569 (128)	0.78	512 (115)	0.87
4	48.0	524 (120)	645 (145)	0.83	596 (134)	0.90	543 (122)	0.98
5	48.0	634 (140)	663 (149)	0.94	609 (137)	1.02	427 (96)	1.46
6	46.2	692 (156)	712 (160)	0.97	649 (146)	1.07	592 (133)	1.17
7	48.5	640 (144)	752 (169)	0.85	676 (152)	0.95	609 (137)	1.05
8	49.5	455 (102)	632 (142)	0.72	560 (126)	0.81	529 (119)	0.86
9	38.4	626 (141)	645 (145)	0.97	543 (122)	1.15	485 (109)	1.29
10	38.4	696 (157)	663 (149)	1.05	583 (131)	1.19	512 (116)	1.35
11	38.1	636 (143)	641 (144)	0.99	574 (129)	1.11	520 (117)	1.22
12	38.7	640 (144)	681 (153)	0.94	614 (138)	1.04	556 (125)	1.15
13	38.4	512 (115)	689 (155)	0.74	623 (140)	0.82	534 (120)	0.96
14	37.8	716 (161)	774 (174)	0.93	681 (153)	1.05	609 (137)	1.18
15	37.5	766 (172)	814 (183)	0.94	698 (157)	1.10	645 (145)	1.19
16	38.7	722 (162)	721 (162)	1.00	649 (146)	1.11	578 (130)	1.25
17	63.4	429 (97)	463 (104)	0.93	423 (95)	1.02	383 (86)	1.12
18	62.9	396 (89)	480 (108)	0.83	454 (102)	0.87	440 (99)	0.90
19	63.4	378 (85)	503 (113)	0.75	480 (108)	0.79	445 (100)	0.85
20	64.3	373 (84)	529 (119)	0.70	498 (112)	0.75	463 (104)	0.81
21	63.2	368 (83)	569 (128)	0.65	552 (124)	0.67	538 (121)	0.68
22	63.3	356 (80)	543 (122)	0.66	512 (115)	0.70	476 (107)	0.75
23	62.9	347 (78)	529 (119)	0.66	498 (112)	0.70	472 (106)	0.74
24	61.4	400 (90)	601 (135)	0.67	565 (127)	0.71	534 (120)	0.75
			Average	0.82			0.91	1.02
			St. Dev.	0.14			0.17	0.22
			COV	0.17			0.19	0.22

Table 7.4 Comparison of Measured and Calculated Capacity for Specimens tested by Saheb and Desayi (1990)

Panel ID	Panel Slenderness Ratio	Measured Capacity kN (kips)	Imperfection Ratio 0.16		Imperfection Ratio 0.24		Imperfection Ratio 0.32	
			Calculated Capacity kN (kips)	Ratio of Measured to Calc. Capacity	Calculated Capacity kN (kips)	Ratio of Measured to Calc. Capacity	Calculated Capacity kN (kips)	Ratio of Measured to Calc. Capacity
1	18.0	556 (125)	689 (155)	0.86	649 (146)	0.84	556 (125)	1.00
2	12.0	413 (93)	405 (91)	1.03	400 (90)	1.01	400 (90)	1.03
3	8.0	285 (64)	200 (45)	1.19	240 (54)	1.16	182 (41)	1.56
4	6.0	235 (53)	151 (34)	1.70	138 (31)	1.67	138 (31)	1.70
5	6.0	284 (64)	169 (38)	1.77	160 (36)	1.74	156 (35)	1.82
6	8.0	347 (78)	196 (44)	1.56	222 (50)	1.53	182 (41)	1.90
7	12.0	463 (104)	249 (56)	1.58	294 (66)	1.55	245 (55)	1.89
8	18.0	534 (120)	747 (168)	0.72	743 (167)	0.70	738 (166)	0.72
10	18.0	587 (132)	770 (173)	0.95	627 (141)	0.94	565 (127)	1.06
11	18.0	694 (156)	761 (171)	1.03	689 (155)	1.01	534 (120)	1.33
12	18.0	823 (185)	818 (184)	1.08	765 (172)	1.05	632 (142)	1.30
13	16.0	498 (112)	676 (152)	0.94	529 (119)	0.92	596 (134)	0.84
14	16.0	613 (138)	685 (154)	1.16	529 (119)	1.13	560 (126)	1.09
15	16.0	717 (161)	743 (167)	1.03	694 (156)	1.01	543 (122)	1.32
16	16.0	790 (178)	761 (171)	1.11	712 (160)	1.09	609 (137)	1.30
18	18.0	712 (160)	743 (167)	1.08	658 (148)	1.06	507 (114)	1.40
19	18.0	712 (160)	730 (164)	1.08	658 (148)	1.06	507 (114)	1.40
20	18.0	683 (154)	747 (168)	1.04	658 (148)	1.02	507 (114)	1.35
22	16.0	598 (134)	609 (137)	1.17	512 (115)	1.15	529 (119)	1.13
23	16.0	648 (146)	614 (138)	1.27	512 (115)	1.24	534 (120)	1.21
24	16.0	633 (142)	618 (139)	1.24	512 (115)	1.21	498 (112)	1.27
			Average	1.10			1.17	1.32
			St. Dev.	0.34			0.27	0.32
			COV	0.31			0.23	0.25

Table 7.5 Summary of Averages of Ratios of Measured Strengths to Calculated Capacities Calculated Using All the Available Panel Tests, Grouped in Ranges of Wall Slenderness Ratios

Range of Wall Slenderness Ratios	Average Wall Slenderness Ratios	Standard Deviation Wall Slenderness Ratios	Number of Plates	Ratios of Measured to Calculated Capacities			Best Imperfection Ratio
				Imperfection Ratio = 0.16	Imperfection Ratio = 0.24	Imperfection Ratio = 0.32	
6 – 12	8.7	2.7	6	1.55	1.47	1.65	0.00
16 – 18	17.1	1.0	15	0.92	1.05	1.18	0.21
25 – 32	29.0	3.1	4	0.83	0.97	1.14	0.25
37 – 40	37.4	2.2	10	0.91	1.04	1.16	0.22
47 – 52	48.5	1.5	10	0.74	0.81	0.94	0.36
61 – 73	64.9	3.9	10	0.65	0.69	0.74	0.72

Table 7.6 Averages of Ratios of Measured to Calculated Capacities of Panels with Wall Slenderness Ratio Between 6 and 12 and Calculated Using an Imperfection Ratio Equal to 0.0

Panel ID Saheb and Desayi ⁽¹⁶⁾	Panel Slenderness Ratio	Measured Capacity kN (kips)	Calculated Capacity kN (kips)	Ratio of Measured to Calc. Capacity
2	12.0	413 (93)	400 (90)	1.04
3	8.0	285 (64)	270 (60)	1.08
4	6.0	235 (53)	190 (42)	1.26
5	6.0	284 (64)	160 (36)	1.79
6	8.0	347 (78)	270 (59)	1.33
7	12.0	463 (104)	340 (77)	1.35
Average				1.31
St. Dev.				0.27

7.3 COMPARISON OF THE MEASURED AND CALCULATED RESPONSE OF HOLLOW PIERS TESTED IN THIS INVESTIGATION

The responses of the five hollow piers tested in this investigation were calculated using the finite element model described in Section 7.1. The model was also used to calculate the capacities of hollow rectangular piers tested in previous investigations (Procter 1977, Poston et al. 1983, and Taylor et al. 1990).

7.3.1 Verification of the Finite Element Model Using Test Results from Current Investigation

The measured geometry of the hollow piers and the nominal size and location of the reinforcing bars were used to define the finite element models. The cross-section of each specimen was modeled using the measured thickness of the walls in the zone of failure, and this critical wall thickness was assumed to be uniform along the entire height of the specimens.

To study the sensitivity of the finite element to the size of the elements Specimen P14 was modeled using three different meshes along the longer wall. The number of elements used along the width of the longer walls in each model and the calculated capacities are listed in Table 7.7. The element aspect ratios in the plane of the wall were maintained as close to 1.0 as possible.

The calculated capacity decreased as the number of elements increased from 12, but it was almost the same for 16 and 20 elements. In Section 7.2 the concrete panels were modeled using between 20 and 25 elements along the width of the panels. However, it was decided to use 16 elements in this phase of the investigation to decrease the amount of computational time.

Table 7.7 Calculated Capacities of Specimen P14 using Models with Different Meshes in the Longer Walls and Imperfection Ratio of 0.24

Number of Elements	Calculated Capacity kN (kips)
12	2030 (457)
16	1630 (366)
20	1645 (370)

A typical finite element mesh used to model the piers is shown in Fig. 7.15. Two layers of elements were used through the thickness of the walls. The longer walls were modeled using 10 to 12 elements along the clear length of the wall, while the short walls were modeled with 4 to 6 elements. Four elements were used in each corner. Thirty-five elements were used along the height of each of the piers. The aspect ratio of the elements through the thickness varied between 0.9 and 1.8, while the aspect ratio of the sides of the elements ranged from 0.83 to 1.0. The size of the elements varied from 51 by 51 mm (2.0 by 2.0 in.) to 61 by 51 mm (2.4 by 2.0 in.), depending of the dimensions of the walls.

As discussed in Section 7.2, the imperfection ratio that produced reasonable estimates of the capacity of panels with wall slenderness ratios less than 40 varied between 0.0 and 0.24. Therefore, three values of the imperfection ratio were used to calculate the capacity of the piers: 0.0, 0.16, and 0.24. A value

of the imperfection ratio equal to zero represents an estimate of the capacity of the piers without considering the possibility of buckling.

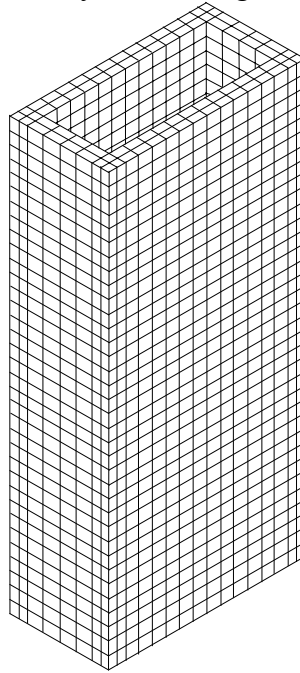


Figure 7.15 Finite Element Mesh of a Pier

To define the boundary conditions and apply the loads, the top and bottom blocks were modeled as rigid planes. To model this behavior, two reference nodes were defined, one at each end of the pier, to which the nodes along those end planes were rigidly connected, as shown in Fig. 7.16. These nodes were used to define the boundary conditions of the columns. The coordinates of the reference node define the eccentricity of the applied load. During a displacement-controlled loading step, the reference node at the bottom was restrained against vertical displacement, while the top reference node displaced vertically. Both reference nodes were restrained against horizontal movement.

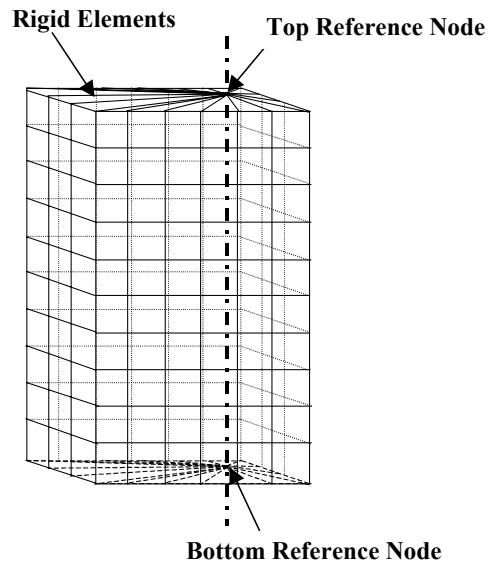


Figure 7.16 Definition of Infinitely Rigid Plane and Reference Nodes

The calculated and measured capacities, failure modes, crack patterns, axial deformation curves, and moment curvature curves were compared to evaluate the performance of the model.

7.3.1.1 Comparison of Measured and Calculated Capacities

Table 7.8 shows the calculated axial load capacity using the corresponding eccentricities measured during the tests (Table 5.1), and the ratio of the measured strength to the calculated capacity for the three assumed imperfection ratios. The calculated capacity of the specimens was very sensitive to the size of the assumed imperfection. The axial capacity decreased as the assumed imperfection ratio increased.

The model estimated fairly well the strength of the specimens if buckling effects were not considered. The average strength ratio calculated using the

imperfection ratio equal to 0.0 was 1.08, with a standard deviation of 0.11. The average strength ratios obtained using assumed values of imperfection ratio equal to 0.16 and 0.24 were 1.16 and 1.26, respectively, with a standard deviation of 0.15. This agrees with the observations made in Section 7.2 about the imperfection ratios that produced best estimates of the capacities of the concrete panels. From Table 7.5, the imperfection ratio should be assumed as 0.0 for plates with slenderness ratios less than 12.

If the assumed imperfection ratio was less than 0.24, the model overestimated the capacity of Specimen P14, while with an assumed imperfection ratio of 0.24 the model underestimated the capacity of Specimen P14 by approximately 20%. This also agrees with the values of imperfection ratios from Table 7.5. For a panel with slenderness ratio of 14 the imperfection ratio used in the model should be less than 0.2. In this case, using an imperfection ratio of 0.16 produced the best estimate of the capacity of Specimen P14.

Table 7.8 Calculated Capacity Using Finite Elements for the Specimens from the Current Investigation

ID	Wall Slenderness Ratio	Measured Strength kN (kips)	Imperfection Ratio 0.0		Imperfection Ratio 0.16		Imperfection Ratio 0.24	
			Calculated Capacity kN (kips)	Ratio of Measured to Calculated Capacity	Calculated Capacity kN (kips)	Ratio of Measured to Calculated Capacity	Calculated Capacity kN (kips)	Ratio of Measured to Calculated Capacity
P6	5.7	2670 (600)	2206 (496)	1.21	1930 (434)	1.38	1837 (413)	1.45
P8	7.8	2050 (461)	1900 (427)	1.08	1886 (424)	1.09	1886 (424)	1.09
P10	9.6	2370 (532)	2046 (460)	1.16	1939 (436)	1.22	2010 (387)	1.37
P12	12.2	2280 (513)	2215 (498)	1.03	1988 (447)	1.15	1944 (437)	1.17
P14	14	1960 (440)	2104 (473)	0.93	2002 (450)	0.98	1628 (366)	1.20
Average			1.08	Average	1.16	Average	1.26	
Std. Dev.			0.11	Std. Dev.	0.15	Std. Dev.	0.15	
COV			0.10	COV	0.13	COV	0.12	

An imperfection ratio of 0.16 in Pier P14 represents an initial out of plane displacement of 8 mm (0.32 in.). This corresponds to approximately, 1/220 of the height of the pier. This imperfection is slightly larger than the largest measured difference between the nominal and the actual thickness of the walls, which was 5 mm (0.2 in.) (Fig. 4.22).

Table 7.9 lists the ratios of measured to calculated capacities calculated using the concrete material models for unconfined concrete, Mander et al. (1988b) and Saatcioglu, M. and Razvi, S.R. (1992) using finite elements with an assumed

imperfection ratio equal to zero, and using design provisions to determine the nominal capacities of the piers. An assumed imperfection ratio equal to zero was used for comparison because it produced the best estimates of the capacity of the piers.

Ratios of measured to calculated capacities obtained using finite elements but neglecting initial imperfections were similar to the ratios calculated using unconfined concrete. The strength ratio calculated using finite elements for Specimen P6, which was the specimen in which the confinement reinforcement was most effective, was larger than the strength ratios calculated using the material models for confined concrete. These observations suggest that the finite element model did not reproduce the confinement provided by the transverse reinforcement.

Table 7.9 Ratios of Measured to Calculated Capacities

Spec. ID	Nominal	Unconfined Concrete	Mander et al. (1988b)	Saatcioglu, M. and Razvi, S.R. (1992)	Finite Elements
P6	1.29	1.17	1.06	1.10	1.21
P8	1.22	1.10	1.01	1.04	1.08
P10	1.27	1.10	1.13	1.06	1.16
P12	1.18	1.05	1.03	1.01	1.03
P14	1.05	0.96	0.94	0.92	0.93
Average	1.20	1.08	1.03	1.03	1.08
St. Dev.	0.10	0.07	0.07	0.07	0.11
COV	0.08	0.07	0.07	0.07	0.10

7.3.1.2 Local Buckling

Figure 7.17 shows plots of the compressive strains computed from the finite element model on both surfaces of the east wall of each pier, calculated at the point of maximum lateral deflection using an assumed imperfection ratio equal to 0.24.

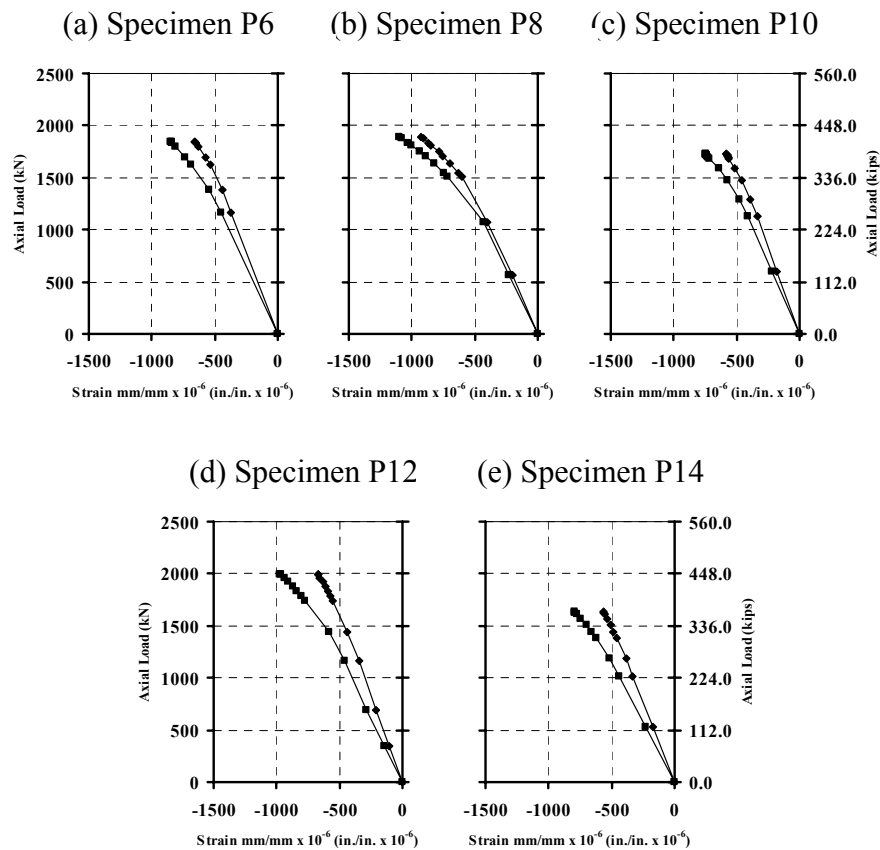


Figure 7.17 Compressive Strains on Both Surfaces of East Walls of Test Specimens

None of the calculated responses exhibited the behavior observed in buckled plates (Section 7.2.1). This observation, added to the fact that the

calculated axial capacities were closest to the measured response using an imperfection value equal to zero, led to the conclusion that local buckling did not occur.

7.3.1.3 Comparison of Failure Modes

All tested in this research specimens failed explosively in compression. Compressive failure of the concrete was followed by buckling of the longitudinal reinforcement in the north and east walls. Three specimens failed at the top; one failed at the bottom; and one failed at midheight.

7.3.1.4 Comparison of Crack Patterns

Because the finite element model is a smeared crack model, it does not track the formation of individual cracks, and therefore, the model cannot reproduce the location of each crack. But the analyses can be used to estimate the load at which the first cracks formed, and the approximate location and orientation of the cracks.

In the test specimens, the tension cracks formed parallel to the transverse reinforcement (Fig. 5.7, 5.16, 5.25, 5.35, and 5.45) and propagated from the southwest corner (the corner where the maximum tensile stress occurred) towards the east and north walls. In the finite element model, the first elements to crack were also located at the southwest corner. The orientation of the cracks was very close to horizontal and the calculated direction of growth of those cracks was toward the north and east walls.

Table 7.10 summarizes the loads at which the first tension cracks were observed, and the cracking loads calculated by the finite element model. The

observed cracking loads were 20 to 100% larger than the cracking load obtained from the model. But because the cracks in the test specimens were marked at the end of a load step, the actual cracking loads may have been up to 180 kN (40 kips) smaller than the observed cracking loads reported in Table 7.9. Therefore, the error in the estimate of the cracking load could be as little as 0 to 60%.

Table 7.10 Observed Cracking Loads and Computed Cracking Loads

Specimen Identification	Load of First Observed Cracks kN (kips)	Calculated Cracking Load kN (kips)	Ratio of Observed to Calculated Cracking Load
P6	890 (200)	445 (100)	2.0
P8	530 (120)	445 (100)	1.2
P10	530 (120)	445 (100)	1.2
P12	710 (160)	445 (100)	1.6
P14	530 (120)	445 (100)	1.2

7.3.1.5 Comparison of Vertical Deflections

Figures 7.18 to 7.22 are plots of the measured relative vertical deflection of the specimens and the relative vertical deflection computed with the finite element model. The relative vertical deflection was calculated at the centroidal axis of the piers and at the point of application of the load. The responses shown were calculated using the models with an imperfection ratio equal to zero.

The model was most successful in calculating both differential deflection responses of Specimen P14. The relative axial deflections measured at the point

of application of the load were well reproduced by the finite element model in Specimens P6 and P8. The model underestimated the relative axial deflection measured at the point of application of the load of Specimens P10 and P12, but the slope of the calculated response was similar to that of the measured response.

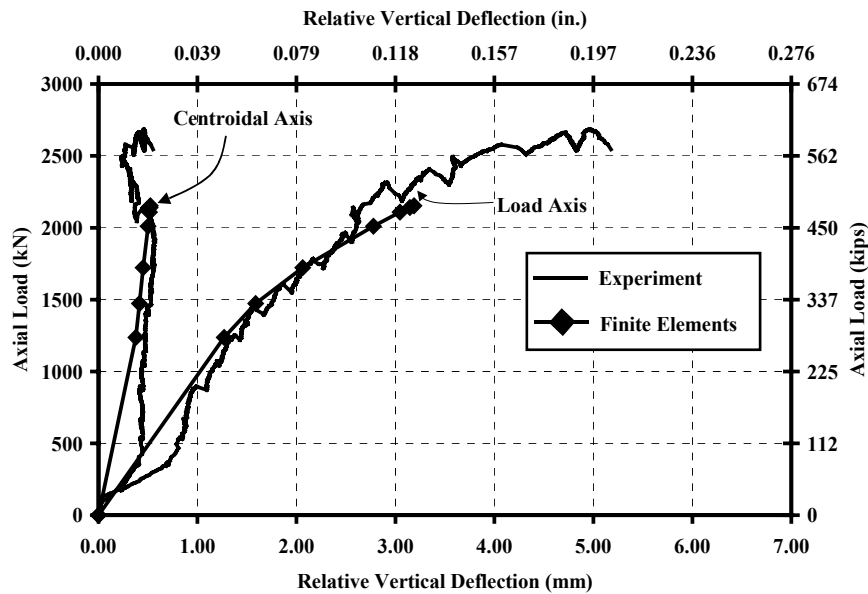


Figure 7.18 Specimen P6: Relative Vertical Deflections Measured at Centroid of the Cross-Section and at Point of Application of the Load

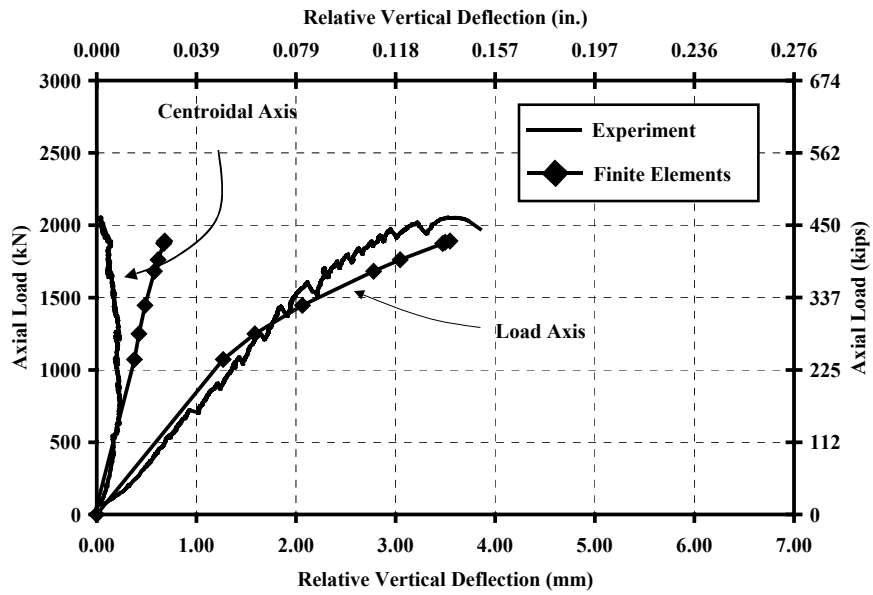


Figure 7.19 Specimen P8: Relative Vertical Deflections Measured at Centroid of the Cross-Section and at Point of Application of the Load

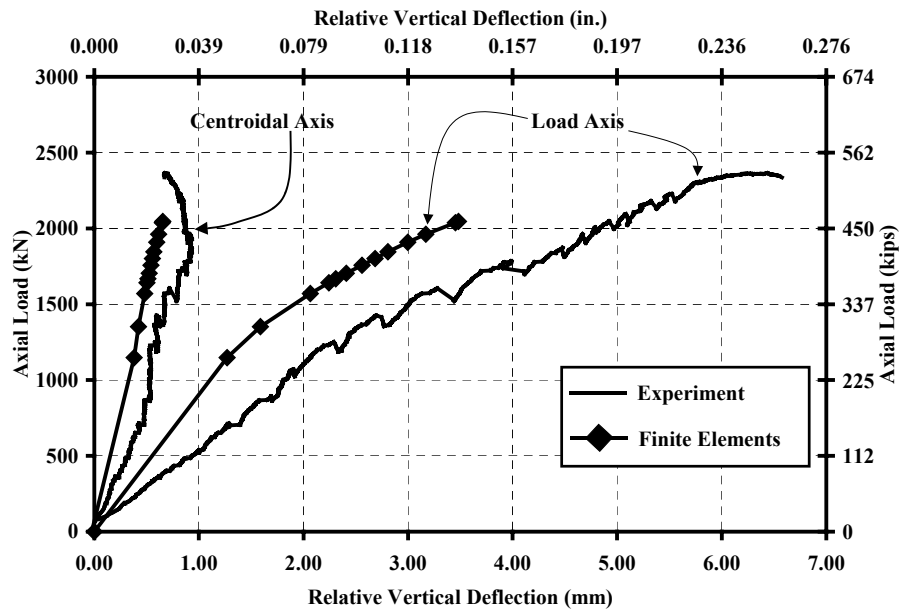


Figure 7.20 Specimen P10: Relative Vertical Deflections Measured at Centroid of the Cross-Section and at Point of Application of the Load

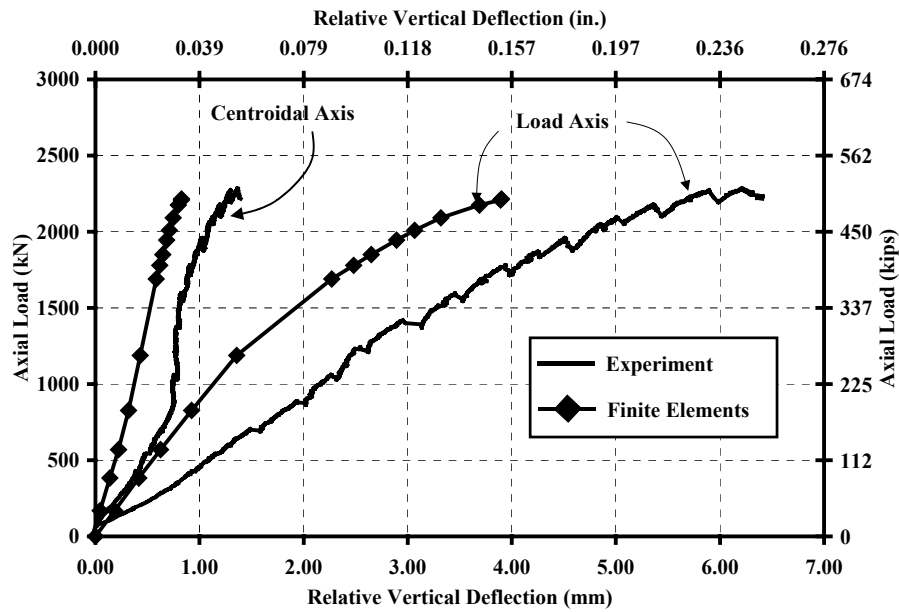


Figure 7.21 Specimen P12: Relative Vertical Deflections Measured at Centroid of the Cross-Section and at Point of Application of the Load

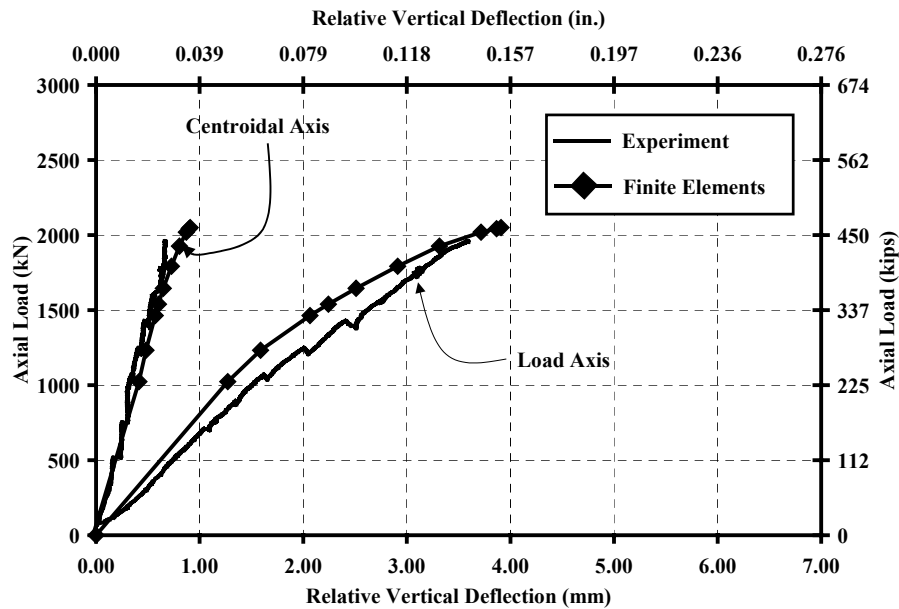


Figure 7.22 Specimen P14: Relative Vertical Deflections Measured at Centroid of the Cross-Section and at Point of Application of the Load

The differential deflections along the centroidal axis of Specimens P6, P10, and P12 were slightly underestimated, but the model reproduced well the slopes of the curves. The response of Specimen P8 was reproduced at low load levels, but relative axial deflection was overestimated at large levels of applied loads.

7.3.1.6 Comparison of Moment–Curvature Responses

Figures 7.23 to 7.32 are plots of the measured moment-curvature response calculated using end-block rotations and the moment-curvature response calculated using the finite element model with an imperfection ratio equal to zero.

The initial slopes of the moment-curvature response about the east-west axis were reproduced fairly well. The curvatures were underestimated at all load levels for all piers, however, and the ultimate curvature was underestimated for all specimens but P14, for which it was overestimated. The model did not reproduce the fact that some of the measured responses were almost horizontal near failure.

The model for Specimen P6 reproduced the moment-curvature response about the north-south axis, but underestimated the maximum curvature by 50%. The slopes of the moment-curvature response of the other four piers were reproduced by the model at load levels larger than 50% of the ultimate load, but were overestimated at lower load. With the exception of Specimen P14, the ultimate curvatures were underestimated.

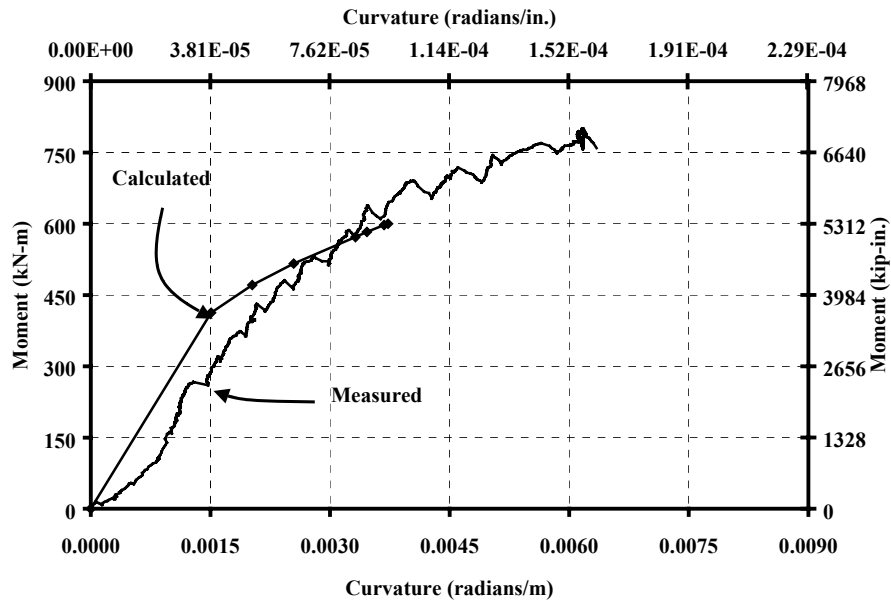


Figure 7.23 Pier P6: Moment-Curvature Responses about the East-West Axis

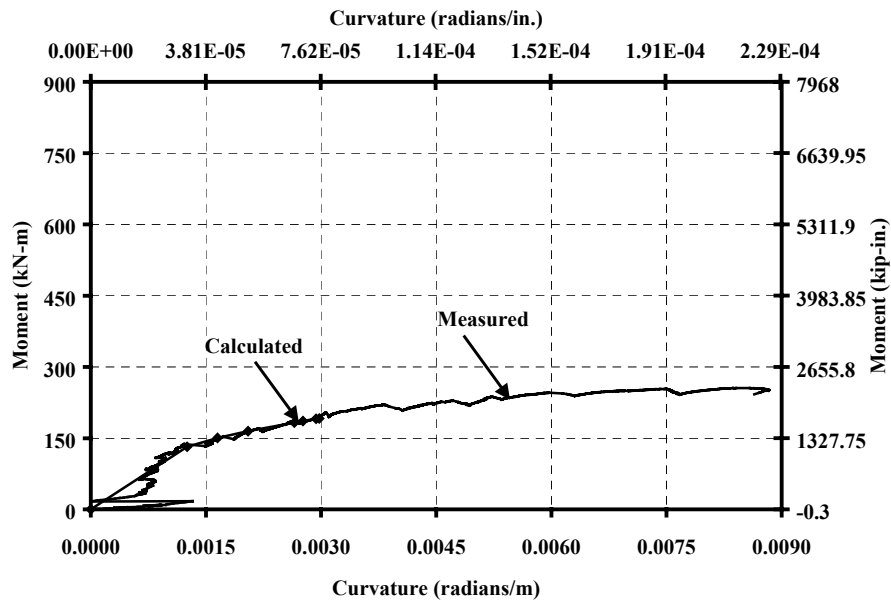


Figure 7.24 Pier P6: Moment-Curvature Responses about the North-South Axis

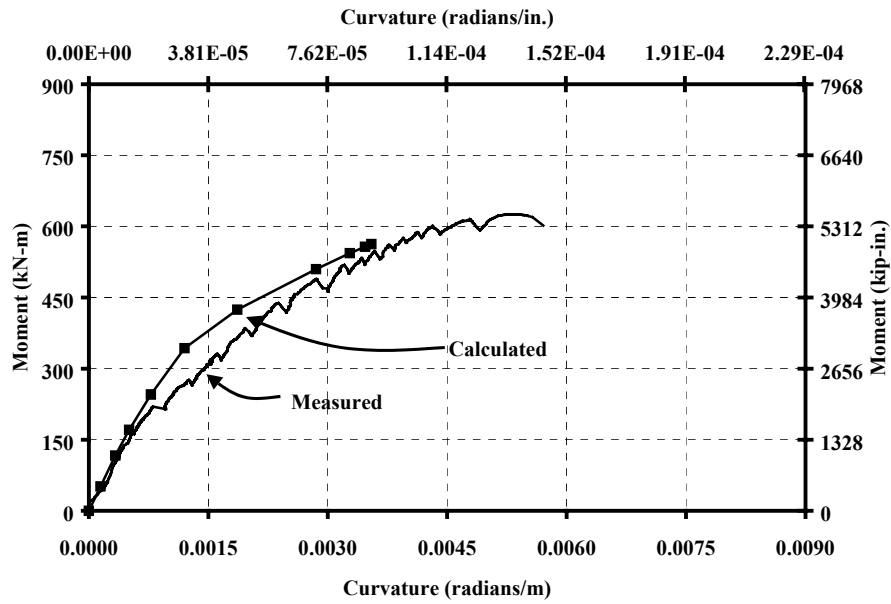


Figure 7.25 Pier P8: Moment-Curvature Responses about the East-West Axis

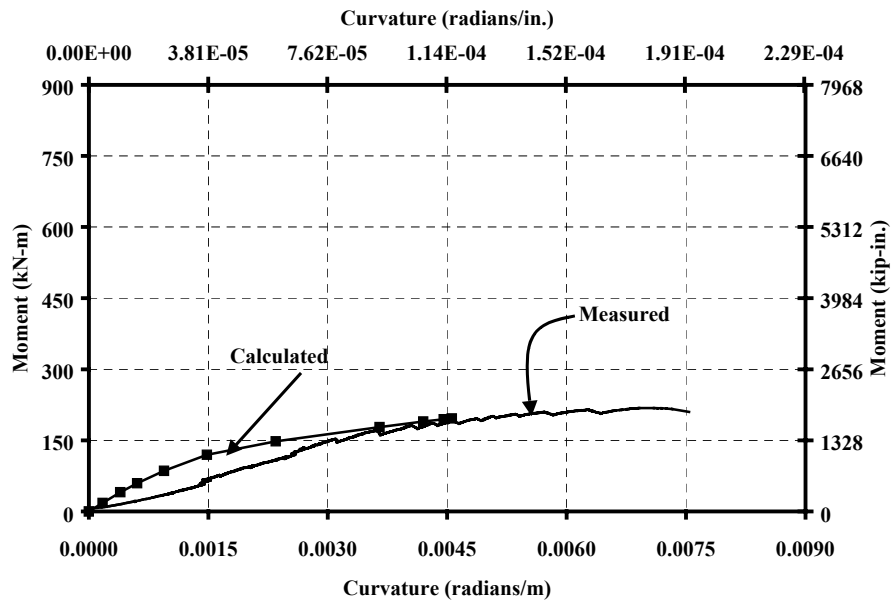


Figure 7.26 Pier P8: Moment-Curvature Responses about the North-South Axis

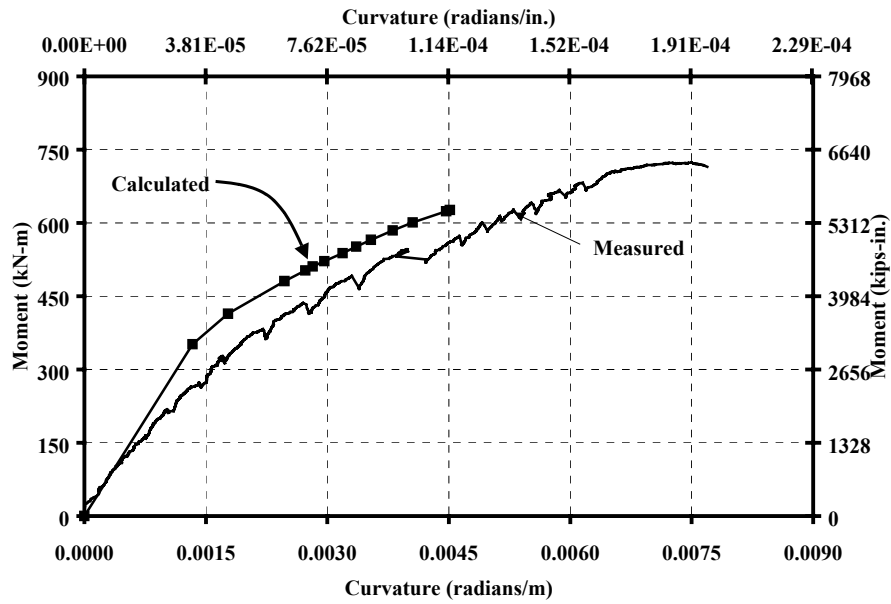


Figure 7.27 Pier P10: Moment-Curvature Responses about the East-West Axis

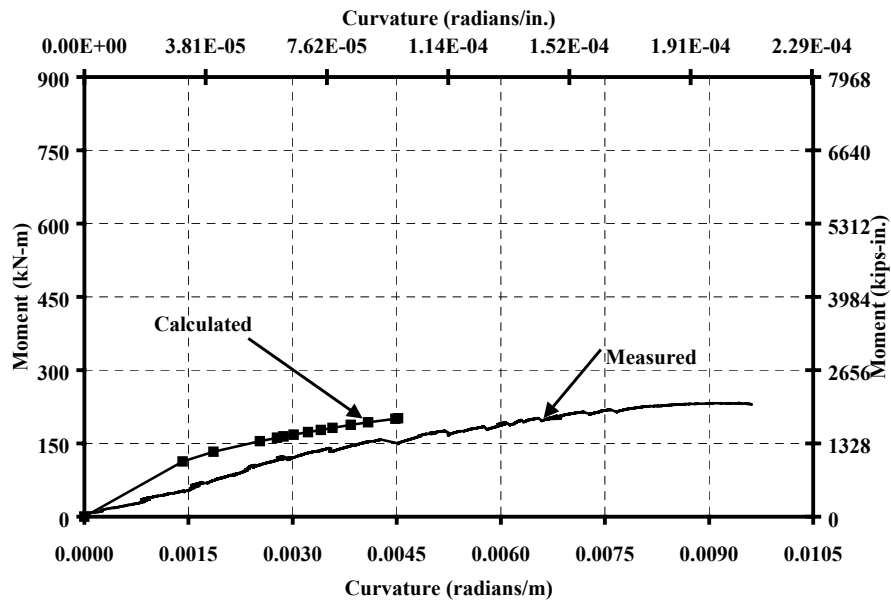


Figure 7.28 Pier P10: Moment-Curvature Responses about the North-South Axis

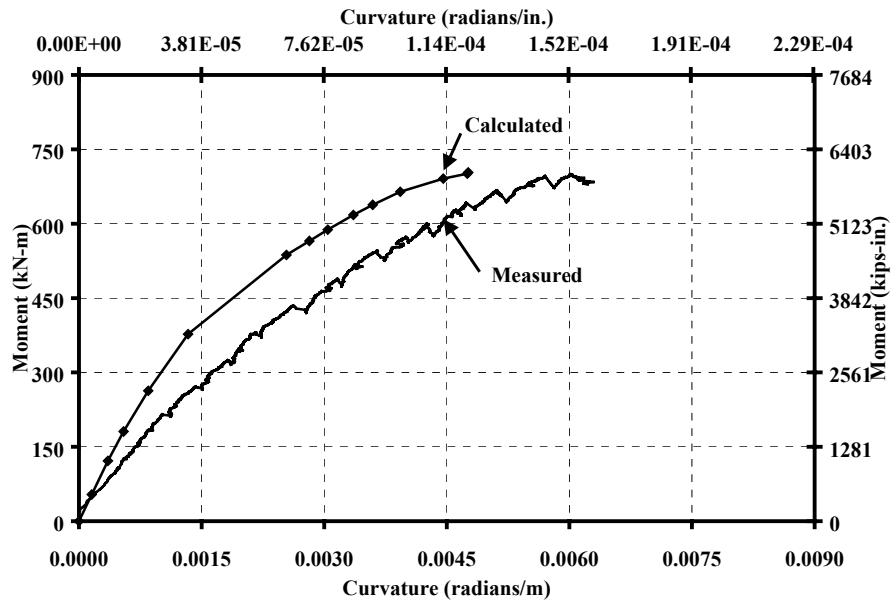


Figure 7.29 Pier P12: Moment-Curvature Responses about the East-West Axis

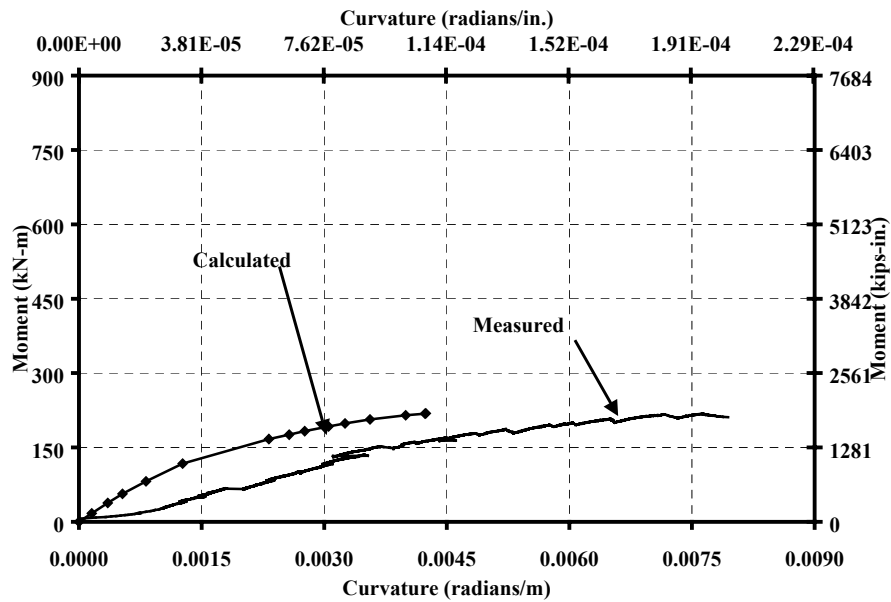


Figure 7.30 Pier P12: Moment-Curvature Responses about the North-South Axis

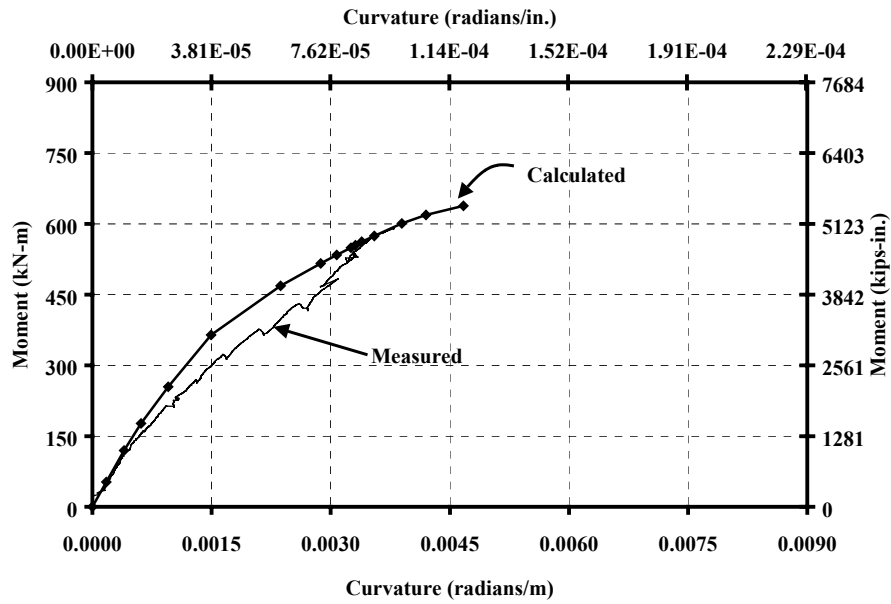


Figure 7.31 Pier P14: Moment-Curvature Responses about the East-West Axis

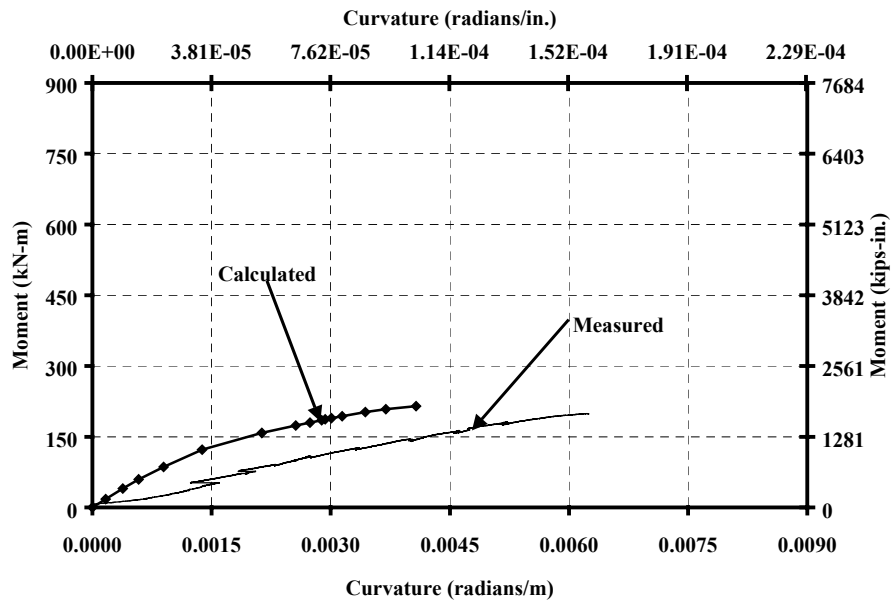


Figure 7.32 Pier P14: Moment-Curvature Responses about the North-South Axis

7.3.1.7 Summary of Observations

The finite element model reproduced the crack pattern and the failure mode of all specimens tested here. The axial capacities were estimated fairly well if local buckling effects were ignored (imperfection ratio equal to zero). The capacities were underestimated significantly using larger values of the initial imperfection ratio, however. To safely estimate the capacity of the piers it is necessary to use some non-zero imperfection ratio in the model; however, the correct value is unknown. Estimated values of imperfection ratios that gave good agreement with test results were reported in Section 7.2. Those values are not reliable, however, because the actual imperfections in those test specimens were not measured, and the physical significance of the imperfection ratios from Table 7.5 could not be assessed.

The finite element model did not reproduce the increase in strength due to confinement of the concrete, so the calculated capacities were similar to the nominal capacities and to the capacities calculated using the material model for unconfined concrete. The model detected no local buckling along the east walls of the specimens.

The model accurately reproduced the axial shortening response of Specimens P6 and P14, for an imperfection ratio equal zero. For Specimens P10 and P12 the model slightly underestimated the axial response. The model underestimated the ultimate shortening of all specimens except Specimen P14.

The moment-curvature responses were approximately reproduced by the model, but the curvatures at a given load level and the ultimate curvature were underestimated.

7.3.2 Comparison of the Measured and Calculated Capacity of Hollow Piers Tested by other Researchers

The capacities of the specimens tested by Procter (1977), Poston et al. (1983) and Taylor et al. (1990) were also calculated using the finite element model. The nominal cross-sectional dimensions and the reported material properties were used to model the piers.

The concrete tensile strength was not reported for those specimens, so it was estimated using Eq. 7.5. The modulus of elasticity of the concrete was estimated using Eq. 7.6.

A stress-strain relationship based in the Hognestad constitutive model, but using k_3 equal to 1.0, was used to represent the compressive uniaxial stress-strain relationship of the concrete of all the specimens modeled.

The other parameters needed to define the model were taken equal to the values indicated in Section 7.1. The displacement-controlled method was used to calculate the capacity of the specimens tested by Procter and by Taylor. Because of how the piers were loaded during the tests, the load-controlled method was used to calculate the specimens tested by Poston. Specimens with post-tensioned reinforcement were not modeled.

Three values of assumed imperfection ratio were used: 0.0, 0.16, and 0.24. A value of 0.24 corresponds to imperfections of 7 to 15 mm (0.27 to 0.60 in.) for the specimens tested by Taylor et al. (1990). Taylor estimated that the largest

possible value of crookedness of those specimens was less than 4 mm (0.16 in.). Therefore, the values of assumed imperfection ratios used are up to 100% larger than the probable initial imperfection of the specimens.

Tables 7.11 through 7.13 list the measured and calculated capacities and their ratios for all specimens from previous investigations and from this study.

As expected, the calculated capacity of the specimens was very sensitive to the assumed value of the imperfection ratio used in the model in the entire range of wall slenderness ratios studied. The calculated capacity decreased with increasing assumed imperfection ratios.

Table 7.11 Comparison of Measured Capacity and Calculated Capacity Using Finite Elements for all the Available Test Results (Imperfection Ratio Equal 0.0)

Specimen ID	Wall Slenderness Ratio λ_w	Measured Strength kN (kips)	Calculated Capacity kN (kips)	Ratio of Measured to Calculated Capacity
Procter R8	7.5	405 (91)	414 (93)	0.98
Procter R9	5.7	556 (125)	498 (112)	1.12
Procter R10	4.3	618 (139)	578 (141)	0.99
Procter R11	3.5	721 (162)	689 (155)	1.05
Procter R12	2.8	725 (163)	738 (166)	0.98
Procter R13	2.4	738 (166)	738 (166)	1.00
Poston 1 Cell*	7.6	163 (1440)	190 (1680)	0.86
Poston 2 Cells*	3.3	200 (1770)	169 (1494)	1.18
Poston 3 Cells*	1.9	236 (2085)	186 (1649)	1.33
Taylor 1M10	10.0	2344 (527)	2304 (518)	1.02
Taylor 2M10	10.0	2091 (470)	2113 (475)	0.99
Taylor 3M14	14.0	4172 (938)	5044 (1134)	0.83
Taylor 4M18	18.0	4172 (938)	6374 (1433)	0.65
Taylor 8ML25	24.7	4021 (904)	4440 (998)	0.91
Taylor 10ML18	18.0	4506 (1013)	5630 (1266)	0.80
Taylor 11ML34	33.6	2771 (623)	3720 (836)	0.74
P6	5.7	2669 (600)	2206 (496)	1.21
P8	7.8	2051 (461)	1900 (427)	1.08
P10	9.6	2366 (532)	2046 (460)	1.16
P12	12.2	2282 (513)	2215 (498)	1.03
P14	14	1957 (440)	2104 (473)	0.93
Average				0.99
St. Dev.				0.16
COV				0.16
Number of Specimens				21

* The capacity of Poston's specimens corresponds to the strong-axis moment capacity, in kN-m (kip-in.).

Table 7.12 Comparison of Measured Capacity and Calculated Capacity Using Finite Elements for all the Available Test Results (Imperfection Ratio Equal 0.16)

Specimen ID	Wall Slenderness Ratio λ_w	Measured Strength kN (kips)	Calculated Capacity kN (kips)	Ratio of Measured to Calculated Capacity
Procter R8	7.5	405 (91)	414 (93)	0.98
Procter R9	5.7	556 (125)	498 (112)	1.12
Procter R10	4.3	618 (139)	627 (141)	0.99
Procter R11	3.5	721 (162)	681 (153)	1.06
Procter R12	2.8	725 (163)	738 (166)	0.98
Procter R13	2.4	738 (166)	738 (166)	1.00
Poston 1 Cell*	7.6	163 (1440)	145 (1285)	1.12
Poston 2 Cells*	3.3	200 (1770)	145 (1284)	1.38
Poston 3 Cells*	1.9	236 (2085)	186 (1649)	1.33
Taylor 1M10	10.0	2344 (527)	1677 (377)	1.40
Taylor 2M10	10.0	2091 (470)	1890 (425)	1.11
Taylor 3M14	14.0	4172 (938)	3728 (838)	1.12
Taylor 4M18	18.0	4172 (938)	5663 (1273)	0.74
Taylor 8ML25	24.7	4021 (904)	5102 (1147)	0.79
Taylor 10ML18	18.0	4506 (1013)	4786 (1076)	0.94
Taylor 11ML34	33.6	2771 (623)	3167 (812)	0.77
P6	5.7	2669 (600)	1930 (434)	1.38
P8	7.8	2051 (461)	1886 (424)	1.09
P10	9.6	2366 (532)	1939 (436)	1.22
P12	12.2	2282 (513)	1988 (447)	1.15
P14	14	1957 (440)	2002 (450)	0.98
Average				1.08
St. Dev.				0.19
COV				0.18
Number of Specimens				21

* The capacity of Poston's specimens corresponds to the strong-axis moment capacity, in kN-m (kip-in.).

Table 7.13 Comparison of Measured Capacity and Calculated Capacity Using Finite Elements for all the Available Test Results(Imperfection Ratio Equal 0.24)

Specimen ID	Wall Slenderness Ratio λ_w	Measured Strength kN (kips)	Calculated Capacity kN (kips)	Ratio of Measured to Calculated Capacity
Procter R8	7.5	405 (91)	360 (81)	1.12
Procter R9	5.7	556 (125)	525 (118)	1.06
Procter R10	4.3	618 (139)	565 (127)	1.09
Procter R11	3.5	721 (162)	645 (145)	1.12
Procter R12	2.8	725 (163)	672 (151)	1.08
Procter R13	2.4	738 (166)	627 (141)	1.18
Poston 1 Cell*	7.6	163 (1440)	133 (1177)	1.22
Poston 2 Cells*	3.3	200 (1770)	141 (1251)	1.42
Poston 3 Cells*	1.9	236 (2085)	186 (1649)	1.33
Taylor 1M10	10.0	2344 (527)	1753 (394)	1.34
Taylor 2M10	10.0	2091 (470)	2019 (454)	1.04
Taylor 3M14	14.0	4172 (938)	3665 (824)	1.14
Taylor 4M18	18.0	4172 (938)	5673 (1273)	0.74
Taylor 8ML25	24.7	4021 (904)	3990 (897)	1.01
Taylor 10ML18	18.0	4506 (1013)	4244 (954)	1.06
Taylor 11ML34	33.6	2771 (623)	3002 (675)	0.92
P6	5.7	2669 (600)	1837 (413)	1.45
P8	7.8	2051 (461)	1886 (424)	1.09
P10	9.6	2366 (532)	2010 (387)	1.37
P12	12.2	2282 (513)	1944 (437)	1.17
P14	14	1957 (440)	1628 (366)	1.20
Average				1.15
St. Dev.				0.17
COV				0.15
Number of Specimens				21

* The capacity of Poston's specimens corresponds to the strong-axis moment capacity, in kN-m (kip-in.).

The average ratio of measured to calculated capacity for the model with an assumed imperfection ratio equal to zero was 0.99, with a standard deviation of 0.16. Strength ratios ranged from 0.65 to 1.33. With imperfection ratios equal to 0.16 and 0.24 the average ratios were 1.08 and 1.15, respectively. The models with an imperfection ratio equal to 0.24 underestimated the capacity of all but 2 specimens.

The strength ratios calculated using the imperfection ratios from Table 7.5 corresponding to the wall slenderness ratio of each pier are reported in Table 7.3. The specimens for which the quality of the concrete was questioned in Section 3.3.1 were excluded. The average strength ratio is 1.06, with a standard deviation of 0.10. The capacities of only two piers were overestimated by more than 5%. The assumed initial imperfection is also listed in Table 7.14. For the specimens tested by Taylor et al. (1990), the assumed initial imperfection was 70 to 200% larger than the maximum probable lateral imperfection reported by Taylor.

Table 7.14 Comparison of Measured Capacity and Calculated Capacity Using Finite Elements for all the Test Results (Imperfection Ratio From Table 7.5)

Specimen ID	Wall Slenderness Ratio λ_w	Imperfection Ratios	Initial Imperfection mm (in.)	Ratio of Measured to Calculated Capacity
Procter R9	5.7	0.00	0.00	1.12
Procter R10	4.3	0.00	0.00	0.99
Procter R11	3.5	0.00	0.00	1.05
Procter R12	2.8	0.00	0.00	0.98
Procter R13	2.4	0.00	0.00	1.00
Poston 1 Cell*	7.6	0.00	0.00	0.86
Poston 2 Cells*	3.3	0.00	0.00	1.18
Poston 3 Cells*	1.9	0.00	0.00	1.33
Taylor 1M10	10.0	0.00	0.00	1.02
Taylor 2M10	10.0	0.00	0.00	0.99
Taylor 3M14	14.0	0.16	10 (0.40)	1.12
Taylor 8ML25	24.7	0.24	9 (0.36)	1.01
Taylor 10ML18	18.0	0.24	12 (0.48)	1.06
Taylor 11ML34	33.6	0.24	7 (0.27)	0.92
P6	5.7	0.00	0.00	1.21
P8	7.8	0.00	0.00	1.08
P10	9.6	0.00	0.00	1.16
P12	12.2	0.00	0.00	1.03
P14	14	0.16	8 (0.32)	0.98
Average				1.06
St. Dev.				0.11
COV				0.10

* The capacity of Poston's specimens corresponds to the strong-axis moment capacity, in kN-m (kip-in.).

The specimen with the lowest ratio of measured to nominal capacity was Specimen 11ML34 (Table 2.6). Taylor et al. (1990) observed that the profile of

the wall in compression of the specimen at failure exhibited double curvature, suggesting local buckling had occurred. To check if the finite element model could detect local buckling in that pier, the compressive strains calculated on both surfaces of the wall in compression are plotted in Fig. 7.32. The results are from the model with imperfection ratio equal to 0.24, and strains were calculated at the point of the wall with maximum lateral displacement. The shape of the calculated compressive strain response in the wall in compression does not exhibit the behavior observed in experiments and models with buckling of thin concrete panels, indicating that no local buckling was found by the finite element model.

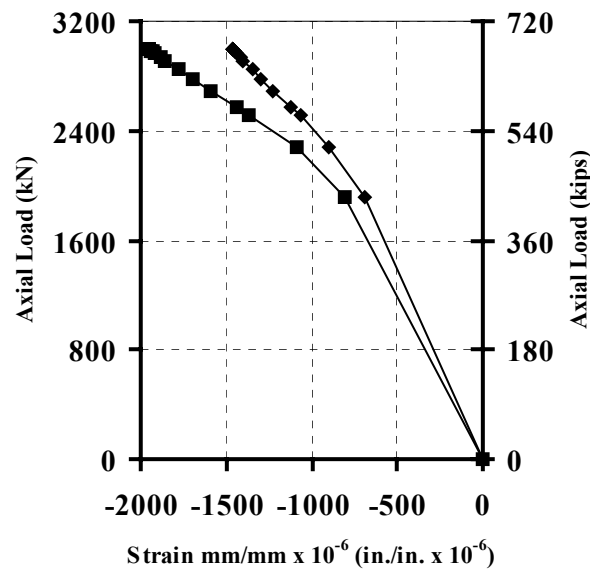


Figure 7.33 *Compressive Strains on both Surfaces of the Wall in Compression of Specimen 11ML34, Calculated at the Point of Maximum Lateral Deflection*

7.4 SUMMARY

A finite element model was used to calculate the capacity of the hollow pier specimens tested in this investigation. The model used two layers of 8-node, 3-dimensional solid elements through the thickness of the walls. Reinforcing bars were modeled using uniaxial elements with elasto-plastic material properties. The concrete model used a fixed, smeared crack approach. The stress-strain relationship based in principles originally proposed by Hognestad (1951) was used to model the uniaxial behavior of the concrete in compression.

The calculated axial capacities of thin concrete panels and rectangular hollow-concrete piers were very sensitive to the value of the imperfection ratio assumed in the model. The value of the imperfection ratio that produced estimates of the capacity closest to the measured strength increased as the wall slenderness ratio of the panel or the hollow pier increased. This indicates that the specimens with large wall slenderness ratio had a decrease in strength due to buckling.

Using the imperfection ratio equal to zero, the finite element model was able to reproduce fairly well the response of the specimens tested in this investigation. The model accurately estimated the capacity of the test specimens, while underestimating their axial and moment-curvature responses. Using larger assumed imperfection ratios the model underestimated the capacities of the piers. The finite element model was not able to reproduce the increase in strength due to the confinement provided to the concrete by the transverse reinforcement. Sectional analysis of the piers using material models for unconfined and confined

concrete provided as good estimates of the capacities of the piers as the finite element model.

The model was also used to calculate the axial capacity of test specimens from previous studies. Again, calculated capacities were very sensitive to the assumed imperfection ratio. To obtain good estimates of the capacity of the piers different values of imperfection ratios had to be used, depending on the wall slenderness ratio of each specimen. Those assumed values of initial imperfection were larger than the maximum value reported by Taylor et al. (1990).

Because the capacity of hollow piers calculated using the finite element model was very sensitive to the assumed imperfection ratio the capacity of hollow, rectangular concrete piers should not be predicted using this model.

The 8-node, 3-dimensional solid elements may have been a poor choice of elements. Less stiff elements with better rate of convergence, like solid elements with incompatible modes, may have produced better estimates of the measured responses and the axial capacity of concrete panels and hollow, rectangular concrete piers.

Chapter 8 Design Considerations

The AASHTO Specifications (1998) provide an approximate method for the design of hollow, rectangular concrete compression members. The nominal capacity of a hollow rectangular member subjected to axial load and bending with a wall slenderness ratio larger than 15 is multiplied by a reduction factor ϕ_w , whose value depends on the wall slenderness ratio λ_w , as described in Section 3.2. The nominal axial capacity of a hollow rectangular member, P_n , subjected to combined axial compression and bending, is calculated using an equivalent rectangular stress block for concrete, an elasto-plastic stress-strain relationship for steel, and a linear distribution of strain over the depth of the cross-section (Fig. 6.1). This design approach was discussed in Section 3.2.

The calculated strength ratios of 23 specimens tested in previous investigations (Procter 1977, Poston et al. 1983, Jobse and Moustafa 1984, and Taylor et al. 1990) and the five specimens tested in this investigation are listed in Tables 3.1 and 6.1 respectively. The strength ratios were calculated as the measured strength, P_{meas} , divided by the nominal strength, P_n , each. The actual eccentricity of the applied load was used to calculate the nominal capacity.

As discussed in Section 3.3.1, poor-quality concrete could explain the low strength ratios for Specimens R8 and 4M18 tested by Procter (1977) and Taylor et al. (1990, 1995) respectively. Also, the strength ratio for Specimen 12S29, tested by Taylor et al. (1990, 1995), was unusually high. The strength ratios for those three specimens were excluded in the studies described below. Therefore, all

results discussed in this chapter are based on the measured response of 25 specimens.

In this chapter the influence of various parameters on these strength ratios is studied. The current design procedures for hollow, rectangular piers are then evaluated using the results from this investigation (Table 6.1) and the strength ratios calculated in Section 3.3.2 (Table 3.1).

8.1 PARAMETERS INFLUENCING THE STRENGTH OF HOLLOW, RECTANGULAR CONCRETE PIERS

The strength ratios listed in Tables 3.1 and 6.1 are used to study the influence of various parameters on the strength of hollow concrete piers. Those parameters are the wall slenderness ratio, the confinement provided by the transverse reinforcement, the maximum compressive strain in the concrete, and the eccentricity of the applied load. Eccentricities along one and two principal axes of the cross-section were considered.

8.1.1 Wall Slenderness Ratio

The results from this investigation have demonstrated that the strength ratio of rectangular, hollow concrete piers subjected to simultaneous axial load and biaxial bending, decreased as the wall slenderness ratio increased (Chapter 6). Taylor et al. (1990) made the same observation for hollow piers tested under simultaneous axial load and uniaxial bending. Test results examined in this study corresponded to specimens with wall slenderness ratios ranging from 2 to 34.

From the plot in Fig. 8.1 the strength ratio for specimens subjected to axial load and uniaxial bending exhibit the same trend as in the specimens subjected to

axial load and biaxial bending: the strength ratio decreases as the wall slenderness ratio increases.

Also, strength ratios for piers subjected to combined axial load and biaxial bending tend to be larger than those for piers loaded under uniaxial bending. This observation agrees with results reported by Furlong (1979), that showed that the equivalent rectangular stress block method tend to be more conservative in nonrectangular than in rectangular sections.

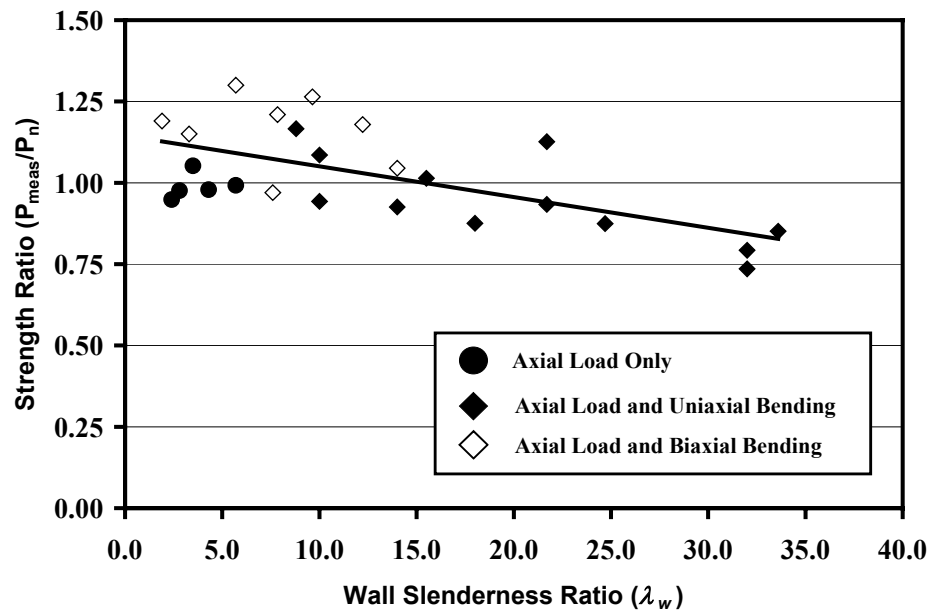


Figure 8.1 Influence of the Wall Slenderness Ratio on the Strength Ratio

Strength ratios for specimens loaded under pure compression are constant, close to one, and smaller than the strength ratios specimens with similar wall slenderness ratios and subjected to uniaxial or biaxial bending. This could be because that the specimens loaded under uniform load were constructed with a

single layer of reinforcement in the walls, and therefore, the effective strength of the concrete was not influenced by confinement provided by the transverse reinforcement.

8.1.2 Confinement Provided by the Transverse Reinforcement

In Chapters 5 and 6 was found that the confinement effects might be important in the behavior of hollow piers with thin walls. Therefore, those effects may be important for design and it is necessary to examine them in more detail.

Two material models for confined concrete were used to calculate the capacity of the test specimens (Chapter 6) at the measured eccentricities. Both models indicated that the specimens with wall slenderness ratios less than 12 were able to carry increased axial loads due to the confinement provided by the transverse reinforcement. The main parameters that influenced the increase in compressive strength and deformation capacity of the concrete were the amount of transverse reinforcement and the arrangement of that reinforcement.

The volumetric ratio of transverse reinforcement, defined as the total volume of transverse steel per unit volume of confined concrete, is commonly used as a nondimensional index of the amount of transverse reinforcement. In addition, the analyses described in Chapter 6 indicated that the amount of transverse reinforcement oriented through the thickness of the wall, A_y , has a larger influence on the strength of the confined concrete than the transverse reinforcement oriented along the length of the wall, A_x , (Fig. 8.2). This observation is expressed in symbolic form in Eq. 8.1 from Saatcioglu and Razvi (1992). The equivalent lateral pressure for a rectangular section, f_{le} , depends on

the dimensions of the confined core, b_c and t_c , and the equivalent uniform confining pressures in the x and y directions, f_{lex} and f_{ley} .

$$f_{le} = \frac{f_{ley}b_c + f_{lex}t_c}{b_c + t_c} \quad (8.1)$$

The equivalent uniform confining pressures are calculated from the average lateral pressures, f_{lx} and f_{ly} , which depend on the amount of transverse reinforcement:

$$f_{lx} = \frac{A_x f_{yh}}{s t_c} \quad (8.2)$$

$$f_{ly} = \frac{A_y f_{yh}}{s b_c} \quad (8.3)$$

where s is the vertical spacing of the transverse reinforcement, f_{yh} is the yield stress of the reinforcement, A_x is the total area of transverse reinforcement oriented parallel to the axis of the wall, and A_y is the total area of transverse reinforcement oriented through the thickness of the wall.

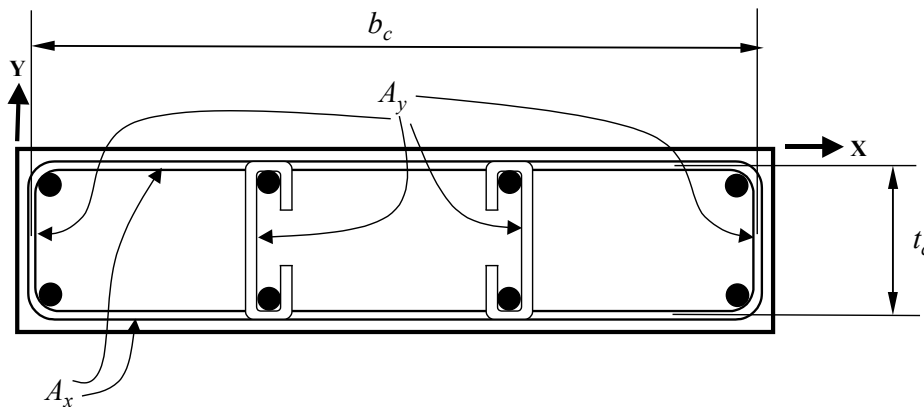


Figure 8.2 Effectively Confined Core for Rectangular Hoop Reinforcement

Therefore, the influence of the volumetric reinforcement ratio and the area of transverse reinforcement oriented through the thickness of the walls on the

observed strength ratios was studied. Only the transverse reinforcement within the unsupported length of the walls was considered.

The volumetric reinforcement ratio, ρ_v , was defined as:

$$\rho_v = \frac{A_y t_c + A_x b_c}{s t_c b_c} \quad (8.4)$$

where A_x and A_y are the total areas of transverse reinforcement oriented parallel and perpendicular to the length of the wall, respectively; t_c is the thickness of the confined core; b_c is the unsupported length of the confined concrete core of the wall; and s is the vertical spacing of the transverse reinforcement. The thickness of the core was measured between centerlines of the transverse reinforcement (Fig. 8.3).

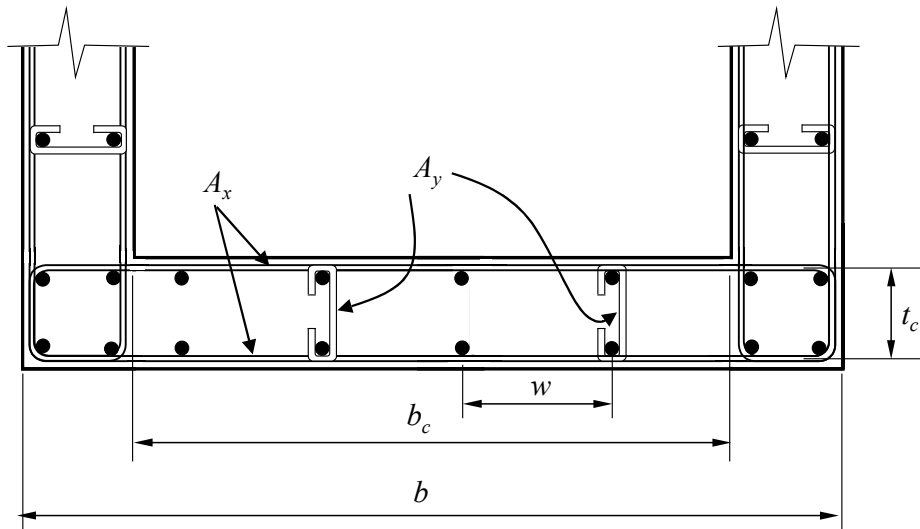


Figure 8.3 Geometry of the Slender Wall Subjected to Compression

The ratio of transverse reinforcement oriented through the thickness of the wall, ρ_w , was calculated as

$$\rho_w = \frac{A_y}{sb_c} \quad (8.5)$$

Specimens without two layers of reinforcement in the walls were considered to have ratios of transverse reinforcement equal to zero.

The second parameter that had a significant influence on the strength of the confined concrete was the arrangement of the transverse reinforcement. The vertical spacing of the transverse reinforcement and the horizontal spacing of the longitudinal bars are both important. In the material model by Saatcioglu, M. and Razvi, S. R. (1992) the effect of the arrangement of the transverse reinforcement is represented by the efficiency factors, k_{2x} and k_{2y} . The expressions (Eq. C.26 and C.27) used to calculate the efficiency factors were derived from regression analysis of test data.

Mander et al. (1988b) used the coefficient of effectiveness, k_e , to represent the influence of the arrangement of the longitudinal and transverse reinforcement. The expression used to define the coefficient, Eq. 8.6, was derived from the geometry of the effectively confined core of rectangular walls.

$$k_e = \frac{\left(1 - \sum_{i=1}^n \frac{(w'_i)^2}{6b_c t_c}\right) \left(1 - \frac{s'}{2b_c}\right) \left(1 - \frac{s'}{2t_c}\right)}{(1 - \rho_{cc})} \quad (8.6)$$

The term t_c is the thickness of the confined core, b_c is the length of the confined core, w'_i is the clear distance between adjacent longitudinal bars, s' is the vertical clear spacing between hoops (Fig. 8.4), and ρ_{cc} is the ratio of the area of longitudinal steel to the area of the confined core ($b_c * t_c$). The coefficient of effectiveness has the disadvantage its value can be negative for certain

arrangements of the transverse reinforcement. Although Eq. 8.6 is very complicated, a simpler expression will be developed in the following paragraphs to calculate the relationship between the arrangement of the reinforcement and the coefficient of effectiveness.

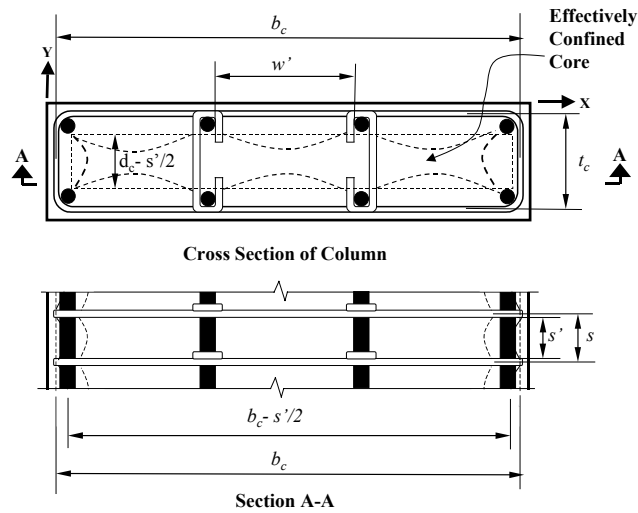


Figure 8.4 Effectively Confined Core for Rectangular Hoop Reinforcement (Mander et al. 1988b)

If the distances w_i are approximately equal between all vertical bars, then an average spacing, w' , can be used, and the sum of the first term in the numerator of Eq. 8.6 can be approximated as:

$$\sum_{i=1}^n \frac{(w_i')^2}{6b_c t_c} = \frac{nw'^2}{6b_c t_c} \quad (8.7)$$

where n is the number of spaces between vertical bars in the confined core. If nw' is approximated as the unsupported length of the confined core, b_c , then the sum in Eq. 8.7 can be approximated as:

$$\sum_{i=1}^n \frac{(w_i')^2}{6b_c t_c} = \frac{nw'^2}{6b_c t_c} \approx \frac{b_c w'}{6b_c t_c} = \frac{w'}{6t_c} \quad (8.8)$$

Also, for walls with unsupported lengths, b_c , that exceed the clear vertical spacing of the transverse reinforcement, s' , the second term in the numerator of Eq. 8.6 may be approximated as 1.0. Therefore, Eq. 8.6 can be rewritten as:

$$k_e \approx \frac{\left(1 - \frac{w'}{6t_c}\right) \left(1 - \frac{s'}{2t_c}\right)}{(1 - \rho_{cc})} \quad (8.9)$$

The coefficient of effectiveness increases as the ratio of the core thickness to the clear spacing of the longitudinal bars increases, and as the ratio of the core thickness to the clear vertical spacing of the transverse reinforcement increases. Therefore, a new coefficient, k_c , can be defined as:

$$k_c = \left(\frac{t_c}{s}\right) \left(\frac{t_c}{w}\right) \quad (8.10)$$

where s is the vertical spacing of the transverse reinforcement and t_c and w are as shown before in Fig. 8.3. This coefficient is easy to calculate and, as demonstrated above, it can be used to represent the effectiveness of the confinement provided by the transverse reinforcement.

In Section 6.4.3, a hypothesis was presented to describe the observed mode of failure of Specimens P12 and P14: after the concrete cover crushed, the confined concrete core was too thin and was not able to redistribute the increase in compressive stresses. Therefore, another parameter that could be used to represent the effects of the confinement is the ratio t_c/t_w , where t_c is the thickness of the confined core of the walls and t_w is the wall thickness, t_c/t_w .

The confined core thickness is defined as the distance between centerlines of the transverse reinforcement oriented parallel to the walls (Fig. 8.5). The distance from the centerline of the transverse reinforcement to the face of the wall, c , is calculated as:

$$c = \frac{t_w - t_c}{2} \quad (8.11)$$

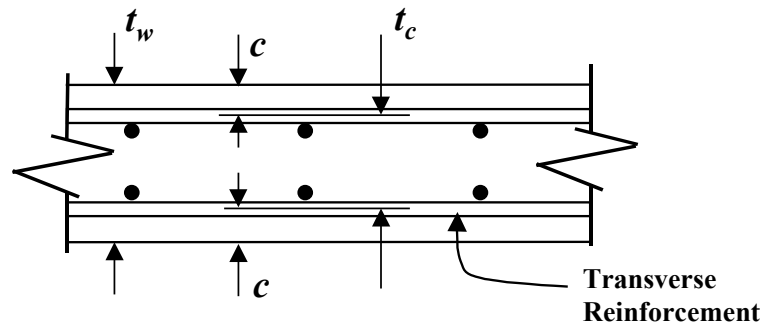


Figure 8.5 Definition of Thickness of the Confined Concrete Core

Therefore, the wall thickness ratio can be rewritten as:

$$\frac{t_c}{t_w} = \frac{t_w - 2c}{t_w} = 1 - \frac{2c}{t_w} \quad (8.12)$$

The minimum required size of the transverse reinforcement bars is 10 mm (#3), with a minimum clear cover of 38 mm (1 ½ in.). Therefore, the distance from the exterior surface of an actual wall to the centerline of the transverse reinforcement, c , is approximately 45 mm (1 ¾ in.). If the thicknesses of actual walls vary between 200 mm (8 in.) and 500 mm (20 in.) then the ratios of confined core thickness to wall thickness vary between 0.55 and 0.82.

In rectangular hollow piers with uniform wall thicknesses the wall slenderness ratio, λ_w , is:

$$\lambda_w = \frac{b - 2t_w}{t_w} \quad (8.13)$$

where b is the longest exterior dimension of the cross-section. Using Eq. 8.13, the wall thickness, t_w , can be written in terms of the wall slenderness ratio:

$$t_w = \frac{b}{(2 + \lambda_w)} \quad (8.14)$$

Substituting Eq. 8.14 into Eq. 8.12, the wall thickness ratio is calculated as:

$$\frac{t_c}{t_w} = 1 - \frac{2c}{b}(2 + \lambda_w) \quad (8.15)$$

If the exterior dimension, b , and the cover measured to the centerline of the transverse reinforcement, c , are constant, then there is a direct correlation between the wall thickness ratio and the wall slenderness ratio. The test specimens in this investigation were designed with constant values of b and c . Only Specimen P14 had a slightly smaller concrete cover.

Strength ratios of the specimens with transverse reinforcement are compared with the volumetric ratio of transverse reinforcement in Fig. 8.6(a). The results exhibit a trend similar to that of Fig. 8.1: strength ratios decrease as volumetric reinforcement ratios increase. This seems to contradict results from previous investigations that show that the effective compressive concrete strength

increases as the volumetric ratio of transverse reinforcement increases. This trend can be explained by rearranging Eq. 8.4 and separating the equation for the volumetric reinforcement ratio, ρ_v , into two terms.

$$\rho_v = \frac{A_y}{sb_x} + \frac{A_x}{st_c} \quad (8.16)$$

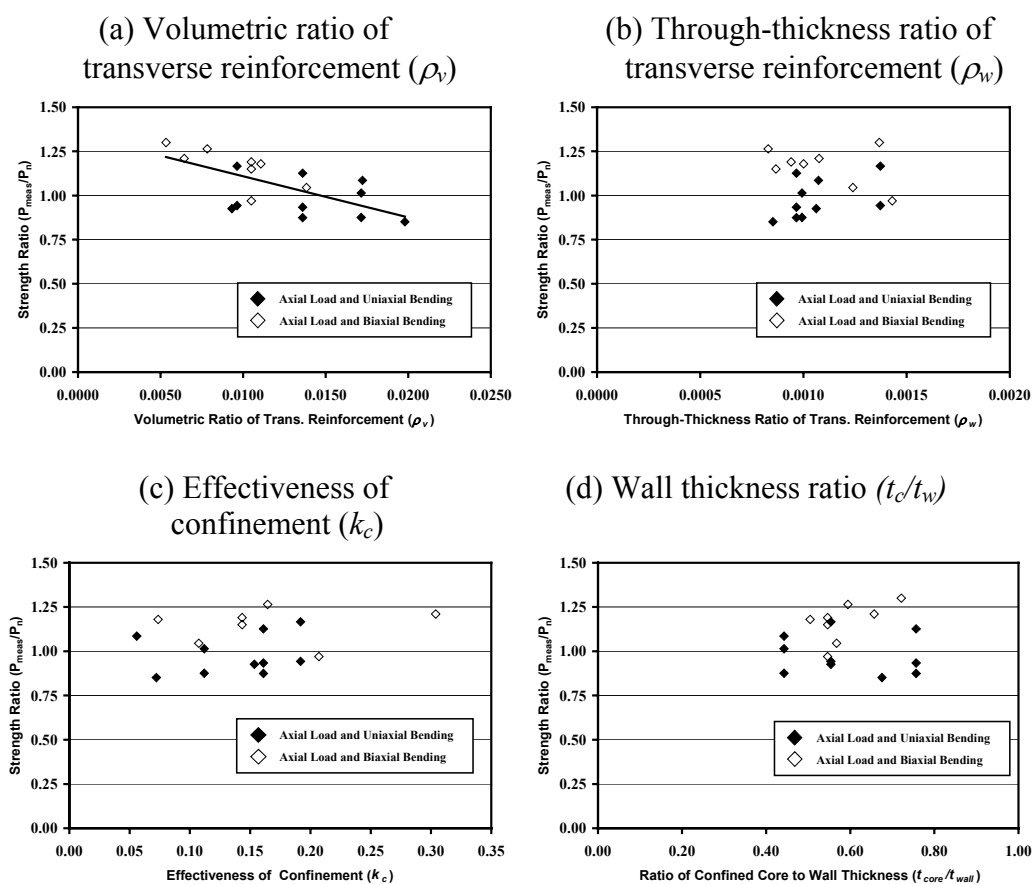


Figure 8.6 Relationship Between Measured Strength Ratios of Various Parameters

Table 8.1 Values of Various Parameters that Influence Strength Ratios

Specimen ID	λ_w	ρ_v	ρ_w	k_c	t_c/t_w	Loading Pattern	Strength Ratios
Procter R9	5.7	0.00	0.00	0.00	0.00	Axial	0.99
Procter R10	4.3	0.00	0.00	0.00	0.00	Axial	0.98
Procter R11	3.5	0.00	0.00	0.00	0.00	Axial	1.05
Procter R12	2.8	0.00	0.00	0.00	0.00	Axial	0.98
Procter R13	2.4	0.00	0.00	0.00	0.00	Axial	0.95
Jobse 1	32.0	0.00	0.00	0.00	0.00	Uniaxial	0.74
Jobse 2A	32.0	0.00	0.00	0.00	0.00	Uniaxial	0.79
Poston 1 Cell	7.6	0.0105	0.0009	0.14	0.55	Biaxial	0.97
Poston 2 Cells	3.3	0.0105	0.0009	0.14	0.55	Biaxial	1.15
Poston 3 Cells	1.9	0.0105	0.0014	0.21	0.55	Biaxial	1.19
Taylor 1M10	10.0	0.0096	0.0014	0.19	0.55	Uniaxial	0.94
Taylor 2M10	10.0	0.0172	0.0011	0.06	0.44	Uniaxial	1.09
Taylor 3M14	14.0	0.0093	0.0011	0.15	0.55	Uniaxial	0.93
Taylor 5S9	8.8	0.0096	0.0014	0.19	0.55	Uniaxial	1.17
Taylor 6S16	15.5	0.0172	0.0010	0.11	0.44	Uniaxial	1.01
Taylor 7S22	21.7	0.0136	0.0010	0.16	0.76	Uniaxial	1.13
Taylor 8ML25	24.7	0.0136	0.0010	0.16	0.76	Uniaxial	0.87
Taylor 9MLP22	21.7	0.0136	0.0010	0.16	0.76	Uniaxial	0.93
Taylor 10ML18	18.0	0.0172	0.0010	0.11	0.44	Uniaxial	0.88
Taylor 11ML34	33.6	0.0198	0.0009	0.07	0.68	Uniaxial	0.85
P6	5.7	0.0053	0.0014	0.74	0.72	Biaxial	1.29
P8	7.8	0.0064	0.0011	0.30	0.66	Biaxial	1.22
P10	9.6	0.0078	0.0008	0.16	0.59	Biaxial	1.27
P12	12.2	0.0111	0.0010	0.07	0.50	Biaxial	1.18
P14	14	0.0138	0.0012	0.11	0.57	Biaxial	1.05

The values of the volumetric reinforcement ratio, ρ_v , vary between 0.0053 and 0.0198 (Table 8.1). The largest value of the volumetric reinforcement ratio corresponded to the specimen with thinnest walls. The values of the ratio of the reinforcement oriented through the wall thickness, ρ_w , varied between 0.0008 and 0.0014. The values of the through thickness reinforcement ratio are an order of magnitude smaller than the values of the volumetric reinforcement ratio.

Therefore, in thin walls, the first term of Eq. 8.16 can be neglected and the volumetric ratio can be approximated as the ratio of the transverse reinforcement parallel to the walls.

$$\rho_v \approx \frac{A_x}{st_c} \quad (8.17)$$

In thin walls, the volumetric reinforcement ratio is strongly correlated to the thickness of the confined core, as is the wall slenderness ratio. The wall slenderness ratio increases when the volumetric ratio is increased. The plot in Fig. 8.6(a) does not provide new information compared with Fig. 8.1.

To investigate the influence of the transverse reinforcement on the strength ratio, the reinforcement oriented through the thickness of the walls has to be considered. A plot of the strength ratio as a function of the through thickness reinforcement ratio, ρ_w , is shown in Fig. 8.6(b). The strength ratio does not depend of the value of the ratio of reinforcement through the wall thickness.

The effectiveness of the confinement, k_c , is plotted in Fig. 8.6(c). Only the strength ratios of the specimens with transverse reinforcement are plotted. The value of the coefficient k_c for Pier P6 was 0.74, which is much larger than the values for the other specimens (Table 8.1). Therefore, Pier P6 was not included in

Fig. 8.6(c). Again, the plotted results exhibit no clear trend between the strength ratio and k_c .

The observations made about the influence of the through-thickness reinforcement ratio and the effectiveness of confinement on the value of the strength ratio can be explained as follows. It has been shown that the increase in concrete strength due to the transverse reinforcement results from the simultaneous effects of the transverse reinforcement and the arrangement of that reinforcement. It was shown in Appendix C that the confined concrete for the test specimens with thick walls, P6 and P8, had a larger increase in strength than the confined concrete of the specimens with thinner walls. This was because the arrangement of the reinforcement lead to a larger effectively confined core in the thicker walls. That explains why Specimen P8, which had a smaller through-thickness reinforcement ratio than Specimen P14 (Table 8.1), had an axial strength larger than the calculated nominal capacity (Table 6.4), while the axial strength of Specimen P14 was similar to its nominal capacity.

Figure 8.6(c) also shows that specimens loaded under biaxial bending tend to have higher strength ratios than specimens loaded under uniaxial bending. The strength ratios for the specimens with values of the coefficient k_c between 0.15 and 0.16 are plotted in Fig. 8.7. The strength ratio decreased as the wall slenderness ratio increased, showing that the main parameter that controls the variations of the value of the strength ratios is the wall slenderness ratio.

The ratios of wall thicknesses, t_c/t_w are plotted in Fig. 8.6(d), for only those specimens with transverse reinforcement. Thickness ratios ranged from 0.44

to 0.76 (Table 8.1), similar to the range of values expected in actual walls. The specimens subjected in this investigation to biaxial bending exhibited a clear trend: strength ratios increased as thickness ratios increased. This is explained by Eq. 8.15, which shows that in those specimens the wall thickness ratio and the wall slenderness ratio are correlated. The specimens subjected to uniaxial bending show no clear trend.

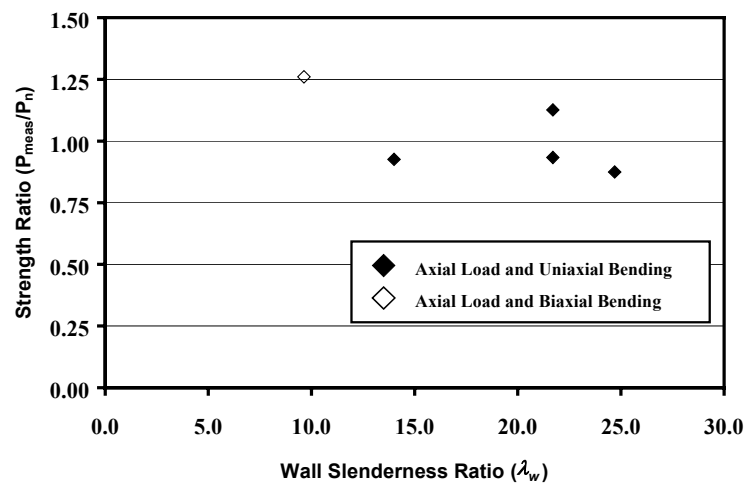


Figure 8.7 Relationship Between Wall Slenderness Ratio and Strength Ratio for Test Specimens with Coefficient k_c between 0.15 and 0.16

8.1.3 Maximum Compressive Strain in the Concrete

The maximum compressive strain in the concrete was calculated in Chapter 6 using two material models for confined concrete. It was found that the maximum compressive strain decreased as the wall slenderness ratio increased (Table 6.7). The calculated maximum compressive strains were equal to or larger than 0.003 for wall slenderness ratios less than 15. Taylor et al (1990) found that the maximum compressive strains in the concrete of hollow rectangular piers with

wall slenderness ratios of 15 or greater, subjected to combined axial load and uniaxial bending, were less than 0.003, the typical value of maximum compressive strain used with the equivalent rectangular stress block (AASHTO 1998, ACI-318 1999). Specimens tested by Taylor et al. (1990, 1995) had wall slenderness ratios less than 15. In three of those specimens the maximum compressive strain was larger than 0.003. In one specimen, however, with wall slenderness ratio of 10, the compressive strain at failure was 0.0027.

It was shown in Chapter 6 that the maximum compressive strain of the specimens tested in this investigation was limited by buckling of the longitudinal reinforcement. The vertical spacing of the transverse reinforcing bars that restrain the longitudinal reinforcement against lateral displacement was critical in controlling the buckling strain of the longitudinal bars.

The longitudinal bars located at the corners of the test specimens, which were heavily confined by hairpins, had an effective length equal to the vertical spacing of the transverse reinforcement (Table 6.6). On the other hand, the bars located in the walls, outside the corners, had longer effective lengths (Table 6.7). Those effective unbraced lengths increased as the wall thickness decreased. The longitudinal bars in the walls were restrained against lateral deflection by cross-ties placed in a checkerboard pattern, so the maximum possible effective length was twice the vertical spacing of the transverse reinforcement. Therefore, to increase the value of the maximum compressive strain in the concrete, the maximum possible effective unbraced length of the longitudinal bars located along the walls, and subjected to the largest compressive stresses, has to be

limited to the vertical spacing of the transverse reinforcement. To that end, cross-ties should be provided to the longitudinal bars located along the walls, near the corners, at every level of transverse reinforcement.

Additional cross-ties have three positive effects: (1) the through-thickness reinforcement is increased; (2) effectiveness of confinement is improved; and (3) the maximum possible unbraced length of the longitudinal bars subjected to the largest stresses is minimized, increasing the possibility that the maximum compressive strain in the concrete can equal or exceed 0.003.

8.1.4 Loading Pattern

Three different methods for applying loads were used to test the 25 hollow rectangular piers: (1) uniform compression (Procter 1977); (2) simultaneous axial compression and uniaxial bending (Jobse and Moustafa 1984 and Taylor et al. 1990); and (3) simultaneous axial compression and biaxial bending (Poston et al. 1983 and this investigation). Initially, the specimens tested by Poston et al. were subjected to uniform compression, and later biaxial eccentricity was added, maintaining constant axial load. However, those specimens were subjected to axial load and biaxial bending at failure.

The following discussion assumes elastic material. The elastic buckling capacity of the slender walls increases with increasing rotational stiffness of their edge restraint. The short transverse walls of the hollow piers provide rotational restraint to the edges of the longer and more slender walls. But compressive stresses decrease the stiffness of the transverse walls, increasing the possibility of local buckling of the slender wall. The capacity of the transverse walls to restrain

the edges of the slender wall decreases, depending on the stress distribution in such walls. This can be critical in specimens with square, hollow cross-sections subjected to uniform compression, in which all walls tend to buckle simultaneously.

In specimens subjected to axial load and uniaxial bending, with eccentricity in the direction of the shorter dimension of the cross-section, the short walls that provide edge restraint to the slender walls have stress gradient, and therefore, the decrease in the rotational stiffness of the short walls may be less critical than for specimens subjected to uniform compression stress.

To calculate the critical buckling stress of a plate using elastic plate buckling theory (Timoshenko 1936) the aspect ratio and the boundary conditions of the plate are taken into account using a buckling coefficient, k . The critical buckling stress, f_{cr} , is calculated as:

$$f_{cr} = k \frac{\pi^2 D}{bt^2} \quad (8.18)$$

$$D = \frac{Et^3}{12(1-\nu^2)} \quad (8.19)$$

where E is the modulus of elasticity, ν is the Poisson's ratio, t is the plate thickness, and b is the plate width.

The aspect ratios of the walls of the test specimens in this and in previous investigations were larger than 1.0. In addition, the cases of a wall with the edges free to rotate and a wall with clamped edges correspond to the limits of the actual elastic restraint of the edges of the slender wall. The buckling coefficients, k , of

plates with aspect ratios larger than 1.0 for those two edges conditions are approximately 4.0 and 7.7 (Timoshenko 1936), respectively.

In specimens subjected to axial load and biaxial bending no wall was subjected to uniform compression. The stress distribution on the transverse walls depends of the eccentricity of the applied load. In the specimens tested in this investigation one transverse wall was subjected to tension, while the other transverse wall was subjected to compression. The assumption of both edges free to rotate is conservative.

It can be assumed that the slender walls of the test specimens had one edge subjected to maximum compression stress and the other edge with no stress. This assumption agrees with the tension cracks that were observed in the test specimens. Those cracks extend along the south wall and into part of the east wall, the slender wall subjected to compression. The buckling coefficient, k , of plates with aspect ratios larger than 1.0, with edges free to rotate, and within the compressive stress distribution described above are larger than 7.8 (Timoshenko 1936).

The previous discussion corresponds to elastic behavior of the material. For piers subjected to axial load and uniaxial bending the stiffness of the transverse walls decreases as the compressive stresses on those walls increase, and therefore, the value of the buckling coefficients tends to be closer to 4.0, which is the lower bound of the values of k .

Therefore, the walls of the specimens loaded under axial load and biaxial bending may have larger critical stresses than walls in hollow piers subjected to other loading patterns..

Table 8.2 lists the number of specimens used in the investigations described in Chapter 2 and in this study subjected to each loading pattern. The specimens tested by Poston et al. (1983) were included in the column of simultaneous axial compression and biaxial bending because they failed under those conditions.

Table 8.2 Number of Tests Conducted Under Each Loading Pattern in Different Ranges of Wall Slenderness Ratio (λ_w)

	Uniform Compressive Load	Simultaneous Axial Compression and Uniaxial Bending	Simultaneous Axial Compression and Biaxial Bending
$\lambda_w \leq 5$	4	0	2
$5 < \lambda_w \leq 15$	2	4	6
$15 < \lambda_w \leq 25$	0	6	0
$25 < \lambda_w \leq 35$	0	4	0
$35 < \lambda_w$	0	0	0

The tested specimens with wall slenderness ratios larger than 15 have been subjected only to simultaneous axial load and uniaxial bending. Specimens with wall slenderness ratios equal or less than 5 have been primarily tested under uniform compression. Only in the range of wall slenderness ratios between 5 and 15 have specimens been tested under the three loading patterns.

It was shown in Section 8.1.1 that specimens subjected to simultaneous axial load and biaxial bending and the specimens subjected to axial load and uniaxial bending exhibited the same trends in strength ratios. Also, it was shown in Section 8.1.2 that specimens with wall slenderness ratios less than 15 loaded under biaxial bending have higher strength ratios than specimens loaded under uniaxial bending.

Both loading patterns that the maximum compressive strain in the concrete of piers with wall slenderness ratios less than 15 was probably larger than or equal to 0.003, which means that those specimens could reach that strain before local buckling occurred. Therefore, in those test specimens the critical stress corresponded to the compressive strength, regardless of the loading pattern.

It was discussed above that specimens subjected to axial load and biaxial bending have larger critical stresses than specimens subjected to axial load and uniaxial bending. This should be verified by further testing of specimens with wall slenderness ratios larger than 15, for which it has been shown that local buckling produced a decrease in the strength of the piers subjected to axial load and uniaxial bending.

The specimens subjected to uniform loading had smaller strength ratios. These specimens, however, did not have transverse reinforcement to confine the concrete, which explains their smaller strength ratios.

8.1.5 Results from Linear Regression Analyses

Linear regression analyses were performed to identify possible statistical relationships between the parameters described above and the strength ratios. The

parameters considered were: the wall slenderness ratio (λ_w), the volumetric ratio of transverse reinforcement (ρ_v), the ratio of transverse reinforcement through the thickness of the walls (ρ_w), a coefficient for effectiveness of confinement (k_c), the ratio of confined core thickness to the thickness of the wall (t_c/t_w), and the loading pattern.

The results from the linear regression analyses are summarized in Table 8.3. The t -test was used to find if the coefficients of the linear regressions are statistically significant. The coefficients are significant with 95% confidence if the calculated t values are larger than 2.07 (Gujarati 1995). As expected from the previous discussion only the coefficients from the regressions performed using the wall slenderness ratio and the volumetric reinforcement ratio are significant. The results estimated from the linear regressions were plotted only for those two parameters in Fig 8.1 and Fig. 8.6(a).

The coefficient of determination of the linear regressions was 0.39 and 0.42 for the wall slenderness ratio and the volumetric ratio, respectively, indicating a weak positive correlation between those parameters and the strength ratio. The data are widely scattered, however, which explains the small coefficients of determination. The coefficients of determination of the other regression analyses were negligible.

Table 8.3 Coefficients and Standard Errors Obtained from the Linear Regressions

	Estimated Coefficients	Standard Error	t for Test of Significance	Coefficient of Determination r^2
Wall Slenderness Ratio (λ_w)	-0.0095	0.0025	3.83	0.39
Intercept	1.15	0.040	29.9	
Volumetric Ratio of Transverse Reinforcement (ρ_v)	-23.2	6.82	3.40	0.42
Intercept	1.34	0.086	15.5	
Ratio of Transverse Reinforcement (ρ_w)	187	180	1.04	0.06
Intercept	0.858	0.198	4.33	
Effectiveness of Confinement (k_c)	0.802	0.560	1.43	0.12
Intercept	0.931	0.088	10.6	
Thicknesses Ratio (t_c/t_w)	0.0025	0.330	0.008	0.00
Intercept	1.06	0.020	5.38	

8.2 DESIGN PROCEDURES

The provisions of the AASHTO Specifications (1998) for the design of hollow piers with wall slenderness ratios less than 15 are the same as for solid piers. That is, the equivalent rectangular stress block method can be used based on a limiting useful compressive strain of the concrete of 0.003. This was based on the following two observations made by Taylor et al. (1990): (1) the compressive strains at failure of hollow piers with wall slenderness ratios less than 15 and subjected to combined axial load and uniaxial bending were typically larger than 0.003; and (2) the strength ratios of those specimens were essentially equal to or larger than 1.0.

The strength ratios were defined as the measured strength divided by the nominal capacity. To evaluate a given design method the measured strength of the hollow piers should be compared with the nominal capacity of the piers calculated using that same design method. In this case, the nominal capacities of the specimens with wall slenderness ratios less than 15 should be calculated using the equivalent rectangular stress block method. However, Taylor et al. calculated the strength ratios of the specimens subjected to axial load and uniaxial bending assuming a stress-strain curve for concrete that followed the parabolic relationship proposed by Hognestad (1951, 1952), a limiting strain of 0.003, and the maximum strength of the concrete in the test specimen equal to 85% of the compressive strength determined from standard cylinder tests.

The nominal capacities of the specimens tested by Taylor et al. (1990) calculated using equivalent rectangular stress block method and the strength ratios calculated using those nominal capacities are reported in Table 3.1, and are approximately 5% smaller than those reported by Taylor et al. (1990). Figure 8.8 is a plot of the current approximate design line and the strength ratios calculated in Chapter 3 and in Chapter 6 for the specimens tested in previous investigations and in this investigation, respectively. The design curve can be unconservative for piers with wall slenderness ratios less than 20.

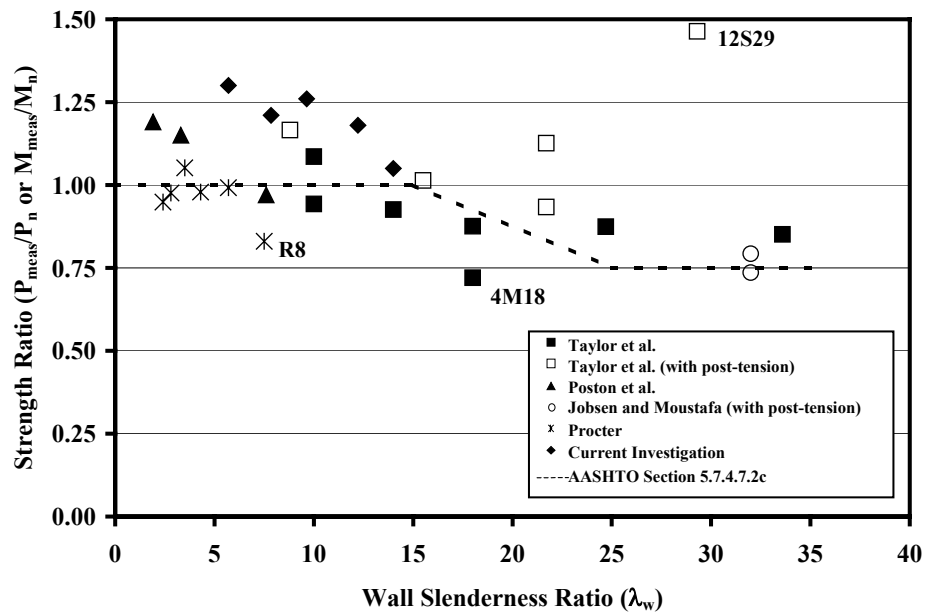


Figure 8.8 Strength Ratios Calculated using the Nominal Capacity of the Cross-Section (P_{meas}/P_n or M_{meas}/M_n)

The specimens whose strength was questioned in Section 3.3.2 are identified in Fig. 8.8 as R8, 4M18, and 12S29. Not including those three specimens, nine points are on the unconservative side of the design curve. Seven of those points are unconservative by 5% or less. The other two specimens, with wall slenderness ratios of 10 and 14 are 6 and 7% unconservative, respectively. Those specimens are 1M10 and 3M14.

It has to be noted that the strength ratios plotted in Fig 8.8 were calculated using the measured concrete strength, while the design nominal capacities are calculated using the specified strength of the concrete, that is smaller than the measured strength. It was shown in Section 3.3.3 that the strength ratios calculated using estimated design compressive strengths were larger than the

reduction factors from AASHTO Specifications (1998). Therefore, it is judged that the current approximate design approach (AASHTO 1998) produces reasonably safe designs of hollow rectangular concrete piers.

In Fig. 8.8 the specimens with wall slenderness ratios between 5 and 20 can be grouped into three sets: (1) specimens with post-tensioned reinforcement; (2) specimens subjected to combined axial load and biaxial bending; and (3) specimens subjected to combined axial load and uniaxial bending. Strength ratios of the first two groups tend to be larger than those of the third group. Also, the strength ratios of the last group of test results are less than 1.0 for wall slenderness ratios equal or larger than 10. However, the general trend is the same in the three sets of results: strength ratios decrease as wall slenderness ratios increase.

As noted in Section 8.1.4 the effect of the loading pattern must be investigated to determine the following hypotheses: (1) if, as Fig. 8.8 suggests, hollow rectangular piers with wall slenderness ratios larger than 10, without post-tensioned reinforcement, and subjected to simultaneous axial load and uniaxial bending have lower strength than their nominal capacity; (2) if, as the trend exhibited in Fig. 8.8 suggests, the strength ratios of hollow concrete piers with wall slenderness ratios larger than 15 and subjected to combined axial load and biaxial bending are less than 1.0; and (3) if the strength ratios of piers subjected to biaxial bending are larger than those of piers subjected to uniaxial bending.

The available experimental data are still a small set of results, but suggest the trends mentioned above. If those trends are investigated the results can be used to adjust the design methods in a way similar to Fig. 8.9, if it is demonstrated

that it is needed, or can be used to introduce the loading pattern as a parameter for the design of hollow piers with very thin walls.

8.3 SUMMARY

The relationships between various parameters and the calculated value of the strength ratio were studied in this chapter. Wall slenderness ratio is the main parameter influencing the strength ratios.

The same trends were found for specimens subjected to axial load and uniaxial bending and for specimens subjected to axial load and biaxial bending. Strength ratios of hollow piers with wall slenderness ratios less than 15 tend to be slightly larger for biaxial than for uniaxial bending.

The maximum compressive strain in the concrete of the test specimens subjected to combined axial load and biaxial bending, with wall slenderness ratios less than 15, was estimated to be larger than 0.003. Therefore, the design method from the Section 5.7.4.7.2.b (AASHTO 1998) is valid for piers subjected to simultaneous axial load and biaxial bending.

Design provisions for hollow rectangular piers from the AASHTO Specifications (1998) are judged to produce safe designs for hollow piers with wall slenderness ratios less than 15 and subjected to combined axial load and uniaxial bending. Still, it is recommended not to change the current design provisions.

To improve the performance of the piers, cross-ties should be provided at every intersection of transverse reinforcement and the most highly stressed longitudinal bars.

More research has to be conducted to find if the following trends are true: (1) hollow rectangular piers with wall slenderness ratios larger than 10, subjected to simultaneous axial load and biaxial bending have a lower strength than their nominal capacity; (2) the strength ratios of hollow concrete piers with wall slenderness ratios larger than 15 and subjected to combined axial load and biaxial bending are less than 1.0; and (3) strength ratios of piers subjected to biaxial bending are larger than those of piers subjected to uniaxial bending. The results from those investigations should be used to evaluate the current design provisions for hollow piers.

Chapter 9 Conclusions

9.1 SUMMARY

Recent years have brought an increasing use of hollow concrete box sections for piers and pylons supporting large or tall bridges. Construction of hollow sections with slender walls is facilitated by the use of high-performance concrete and efficient slip-forming techniques. Defining the wall slenderness ratio as the longest length of the unsupported wall divided by the wall thickness, ratios are approaching 30 in modern construction.

The behavior of thin-walled sections has been assessed in several earlier investigations. Taylor et al (1990) and Taylor and Breen (1994) concluded that no reduction in strength should occur for cross-sections subjected to combined axial load and uniaxial bending with wall slenderness ratios less than 15. Results from Poston et al. (1985), however, indicated that a slight reduction of flexural strength of as much as 3% might occur with biaxial bending for wall slenderness ratios as low as 7.5.

The objectives of this project were to investigate the behavior of thin-walled concrete compression members and determine if a reduction in capacity occurs for hollow concrete sections with wall slenderness ratios between 5 and 15, subjected to simultaneous axial load and biaxial bending.

A summary of the experimental program, the analytical models used in the study, and the limitations of this investigation are presented in the following sections.

9.1.1 Experimental Program

Five rectangular hollow concrete columns were tested in this investigation under simultaneous axial load and biaxial bending. The strong-axis eccentricity was approximately 38% of the depth of the columns, while the weak axis eccentricity was approximately 25% of the width of the columns. The ratio of eccentricity about the strong axis of bending to eccentricity about the weak axis was approximately 3 for all specimens. The wall slenderness ratio ranged from 6 to 14. The test specimens were designed in accordance to the 1998 AASHTO LRFD Bridge Design Specifications.

9.1.2 Confinement Models

The material models developed by Mander et al. (1988b) and Saatcioglu, M. and Razvi, S. R. (1992) for confined concrete were used to estimate the response of the piers. Sectional analysis of each specimen was performed using a fiber model of the cross-section. The capacities and moment-curvature response were calculated and compared with the measured response.

9.1.3 Overall Finite Element Model

A finite element model was used to calculate the behavior of the test specimens. The model consisted of: (1) two 3-dimensional solid elements (bricks) through the thickness of the walls, (2) a plastic model of the concrete in compression and a smeared crack representation of the concrete, and (3) non-linear geometry to take local buckling into account.

The analytical results were compared with the measured data from the five specimens tested in this investigation and sixteen hollow, concrete piers tested previously.

9.1.4 Limitations of the Investigation

The experimental program and the analytical models focused on quasi-static, monotonic loading of rectangular hollow concrete columns. Neither cyclic loading nor transverse loads were considered.

The experimental program was limited to axial loading with simultaneous biaxial bending, with a ratio of strong- to weak-axis eccentricity approximately equal to 3. No shear was introduced in the tests. Wall slenderness ratios varied between 6 and 14. The compressive strength of the concrete in the test specimens varied approximately between 28 and 41 MPa (4000 to 6000 psi).

9.2 CONCLUSIONS

Based on the results of the experimental program, the analytical models used to estimate the behavior of the specimens, and a study of tests results from previous investigations, the following conclusions can be made.

1. The main parameter that controls the variations in the value of the strength ratio of hollow rectangular concrete piers is the wall slenderness ratio. The strength ratio decreases as the wall slenderness ratio increases.
2. An equivalent rectangular compressive stress block gives conservative estimates of the axial capacity of hollow, rectangular concrete piers with wall slenderness ratios less than 14, subjected to simultaneous axial load and biaxial bending.

3. The approximate design method specified in Section 5.7.4.7.2.c of the 1998 AASHTO LRFD Bridge Design Specifications produces safe designs of hollow, rectangular concrete piers loaded under simultaneous compression and biaxial bending with wall slenderness ratios less than 15.
4. The approximate design method specified in Section 5.7.4.7.2.c of the 1998 AASHTO LRFD Bridge Design Specifications produces reasonably safe designs of hollow, rectangular concrete piers with wall slenderness ratios smaller than 35.
5. Effectiveness of confinement plays an important role in the strength of thin-walled piers. If not properly confined, the strength of hollow piers may be limited by buckling of the longitudinal reinforcement.
6. The material models for confined concrete used in this research provided accurate estimates of the axial capacity and moment-curvature response of hollow piers tested in this investigation. However, the ultimate curvature was overestimated using both models.

9.3 DESIGN RECOMMENDATIONS

The AASHTO 1998 design procedures for hollow rectangular concrete piers are valid for piers subjected to axial compression and biaxial bending.

To improve the performance of the piers, cross-ties should be provided at every intersection of transverse reinforcement and the most highly stressed longitudinal bars. In this way the effective unbraced length of the longitudinal bars is reduced to the vertical spacing of the transverse reinforcement.

9.4 RESEARCH RECOMMENDATIONS

The following areas of future research are recommended:

- The effect of loading pattern should be studied in detail. Three loading patterns can be identified with respect to the eccentricity of the applied load: (1) uniform compression, (2) combined axial compression and uniaxial bending, and (3) combined axial compression and biaxial bending. For wide ranges of wall slenderness ratios, specimens have been tested under only one loading pattern (Table 8.2). More research should be conducted, however, to determine if the following trends are also true: hollow rectangular piers with wall slenderness ratios larger than 10, subjected to simultaneous axial load and uniaxial bending do not reach their nominal capacity; (2) strength ratios of hollow concrete piers with wall slenderness ratios larger than 15 and subjected to combined axial load and biaxial bending are less than 1.0; and (3) strength ratios of piers subjected to biaxial bending are larger strength ratios of piers subjected to uniaxial bending.
- The seismic behavior of hollow concrete piers with large wall slenderness ratios has not been studied. The effect of cyclic loads, simultaneous action of shear, axial load and bending, and the arrangement of the confining elements have been studied or are under current study for hollow columns with wall slenderness ratios less than 5. Further study is needed to understand the seismic behavior of hollow concrete piers with large wall slenderness ratios and different

levels of axial load to define the requirements needed to obtain acceptable seismic performance.

Appendix A Measured Material Properties

The results of the materials tests performed in this investigation are documented in this appendix. The results are also compared with expressions that are commonly used to estimate some of the parameters.

A.1 CONCRETE

The compressive strength, stress-strain properties and tensile strength of the concrete were measured using 150 by 300-mm (6 by 12-in.) cylinders. All concrete cylinders were tested between one day before and two days after the day that the corresponding hollow pier specimen was tested.

The compressive strength of the concrete used to construct the hollow piers varied from 27 to 43 MPa (3900 to 6200 psi), with an average of approximately 34 MPa (5000 psi). The compressive strength of the concrete of the solid blocks varied from 30 to 50 MPa (4300 to 7200 psi), with an average of approximately 37 MPa (5300 psi).

The measured concrete properties are summarized in Section A.1.1. Comparisons between the measured modulus of elasticity, stress-strain curves, and tensile strength and expressions commonly used in design are reported in Sections A.1.2, A.1.3, and A.1.4, respectively.

A.1.1 Measured Concrete Material Properties

Cylinder compression tests were conducted in accordance to the ASTM C39 (1999) using a Forney testing machine with a capacity of 2700 kN (600 kips). The rate of loading was 270 to 310 kN per minute (60 to 70 kips per minute) and

the cylinders were capped using neoprene bearing pads confined within steel caps at the ends. Three cylinders were tested for each hollow pier specimen and for each solid block.

Stress-strain curves for the concrete were measured during tests of two or three cylinders for each pier specimen. For Specimen P6 only one stress-strain curve was measured. The stress-strain curve tests were conducted in the same test machine and using the same capping method that was used for the compression cylinder tests, but the loading rate was reduced to 45 to 65 kN per minute (10 to 15 kips per minute). Values of stress and strain were obtained up to and including the maximum load. It was not possible to obtain data on the descending branch of the stress-strain curve. The modulus of elasticity of the concrete was calculated by ASTM C 469 (1994).

Split-cylinder tests were conducted in accordance with the ASTM C496 (1996) using a Tinius Olsen testing machine with a capacity of 900 kN (200 kips). Three cylinders were tested for each hollow pier specimen and each end block, except for the top end block of Specimen P14.

Table A.1 summarizes the average compressive strength data from three cylinders tested for each specimen. Table A.2 lists the key parameters from the stress-strain curves and the calculated modulus of elasticity of the concrete. The strain at peak stress varied between 0.0018 and 0.0022. Table A.3 summarizes the data obtained from the average of three split-cylinder tests for all specimens.

Table A.1 Compression Strength of Concrete

Spec. ID	Bottom Solid Block			Hollow Pier			Top Solid Block		
	f'_c MPa (psi)	COV	Age at test (days)	f'_c MPa (psi)	COV	Age at test (days)	f'_c MPa (psi)	COV	Age at test (days)
P6	49.7 (7210)	0.010	197	26.9 (3900)	0.092	184	31.5 (4570)	0.050	155
P8	50.5 (7320)	0.014	214	27.4 (3970)	0.006	194	30.3 (4400)	0.014	172
P10	29.9 (4340)	0.069	183	35.1 (5090)	0.040	177	34.3 (4980)	0.020	113
P12	30.8 (4460)	0.020	193	42.3 (6130)	0.015	181	34.7 (5040)	0.006	124
P14	34.1 (4950)	0.041	132	42.7 (6200)	0.019	125	37.7 (5470)	0.041	113

Table A.2 Average Concrete Parameters Determined from Stress-Strain Data

Spec ID	Peak Stress			Strain at Peak Stress ϵ_0			Modulus of Elasticity		
	Number of Cylin. Tested	Average MPa (psi)	COV	Average	COV	Number of Cylin. Tested	Average MPa (ksi)	COV	Age of Cylin. (days)
P6	1	31.7 (4600)	-	0.0023	-	1	21700 (3150)	-	184
P8	1	26.6 (3860)	-	0.0018	-	2	23100 (3350)	0.041	194
P10	1	34.4 (4990)	-	0.0020	-	2	27600 (4000)	0.046	177
P12	2	42.0 (6100)	0.016	0.0022	0.180	3	30300 (4400)	0.049	181
P14	2	41.7 (6050)	0.062	0.0021	0.095	3	28300 (4100)	0.023	125

Table A.3 Tensile Strength of Concrete from Split-Cylinder Tests

Spec. ID	Bottom Solid Block			Hollow Pier			Top Solid Block		
	f_t MPa (psi)	COV	Age at test (days)	f_t MPa (psi)	COV	Age at test (days)	f_t MPa (psi)	COV	Age at test (days)
P6	3.8 (550)	0.022	197	2.6 (380)	0.110	184	2.6 (370)	0.110	155
P8	3.7 (530)	0.210	214	2.3 (330)	0.076	194	2.8 (410)	0.037	172
P10	2.4 (340)	0.310	183	3.2 (460)	0.048	177	2.8 (410)	0.093	113
P12	2.8 (410)	0.071	193	3.5 (510)	0.049	181	2.9 (420)	0.029	124
P14	2.8 (400)	0.073	132	3.3 (480)	0.046	125	-	-	-

A.1.2 Calculated Concrete Material Properties

The measured material properties (modulus of elasticity, stress-strain curve and tensile strength) are compared with common expressions used to estimate the properties in this section.

A.1.2.1 Modulus of Elasticity

The modulus of elasticity for concrete, E_c is defined in the ACI-318 (1999) as:

$$E_c = 4730\sqrt{f'_c} \text{ (MPa)} = 57,000\sqrt{f'_c} \text{ (psi)} \quad (\text{A.1})$$

where E_c and f'_c are in MPa (psi). In Table A.4 the moduli approximated using Eq. A.1 are slightly larger than the measured values.

Table A.4 Comparison of Measured and Estimated Modulus of Elasticity of the Concrete used in the Hollow Piers

Specimen ID	Measured Modulus of Elasticity MPa (ksi)	Calculated Modulus of Elasticity MPa (ksi)	Ratio of Measured to Calculated Modulus of Elasticity
P6	20300 (2950)	24500 (3560)	0.83
P8	23100 (3350)	24800 (3590)	0.93
P10	27600 (4000)	28100 (4070)	0.98
P12	30300 (4400)	30800 (4460)	0.99
P14	28300 (4100)	31000 (4490)	0.91
		Average	0.93
		St. Dev.	0.06
		COV	0.07

A.1.2.2 Stress-Strain Curve

Figures A.1 to A.5 show the measured stress-strain curves for the concrete used in the specimens and the idealized stress-strain relationship based in principles originally proposed by Hognestad (1951, 1952), which consists of a parabolic ascending branch and a linear descending branch:

$$f_c = f_c' \left(2 \left(\frac{\varepsilon_c}{\varepsilon_o} \right) - \left(\frac{\varepsilon_c}{\varepsilon_o} \right)^2 \right), \text{ if } \varepsilon_c \text{ is less or equal to } \varepsilon_o, \quad (\text{A.2})$$

$$f_c = f_c' \left[1 - 0.15 \left(\frac{\varepsilon_c - \varepsilon_o}{\varepsilon_u - \varepsilon_o} \right) \right], \text{ if } \varepsilon_c > \varepsilon_o, \text{ but less than } \varepsilon_u, \quad (\text{A.3})$$

where f_c and ε_c are the concrete stress and strain; f'_c and ε_o are the peak concrete stress and the strain at the peak stress; and ε_u is the ultimate strain of the concrete, which was considered equal to 0.0038.

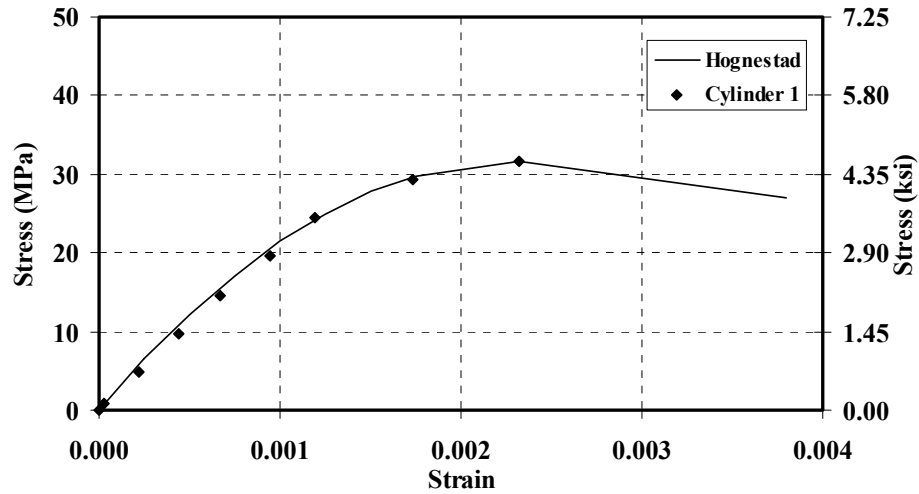


Figure A.1 Stress-Strain Curves for Concrete of Hollow Specimen P6

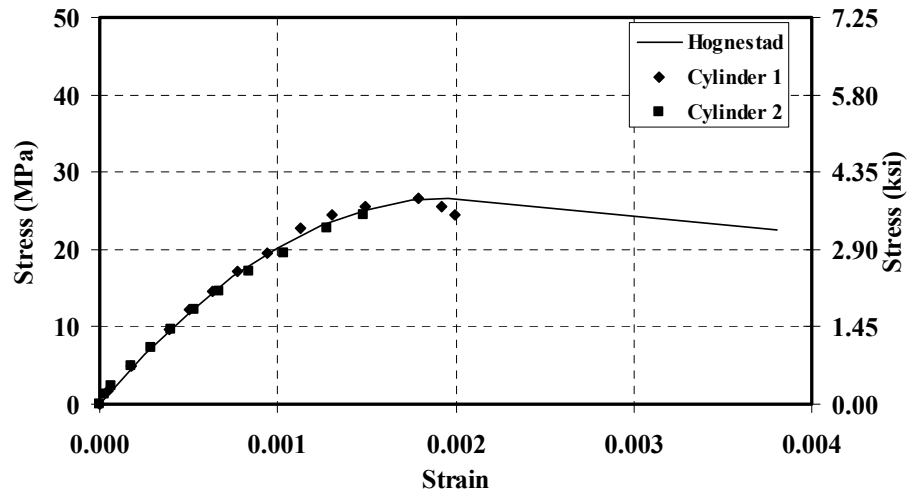


Figure A.2 Stress-Strain Curves for Concrete of Hollow Specimen P8

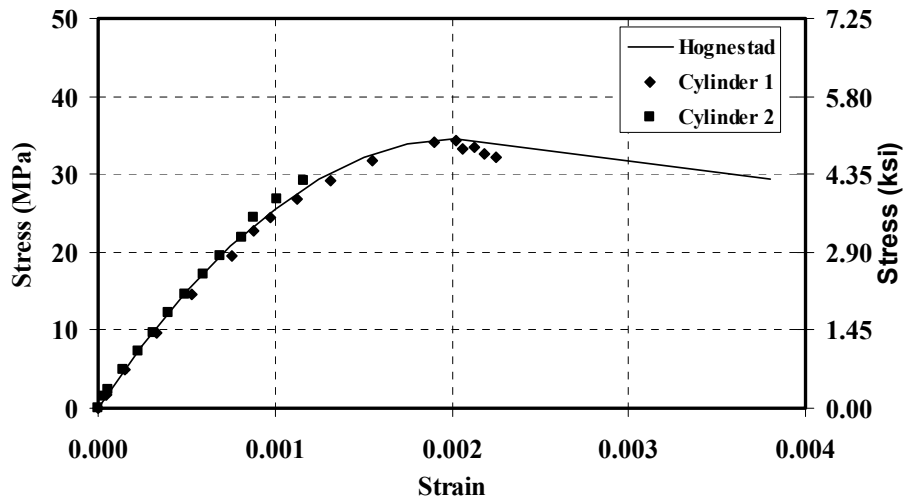


Figure A.3 Stress-Strain Curves for Concrete of Hollow Specimen P10

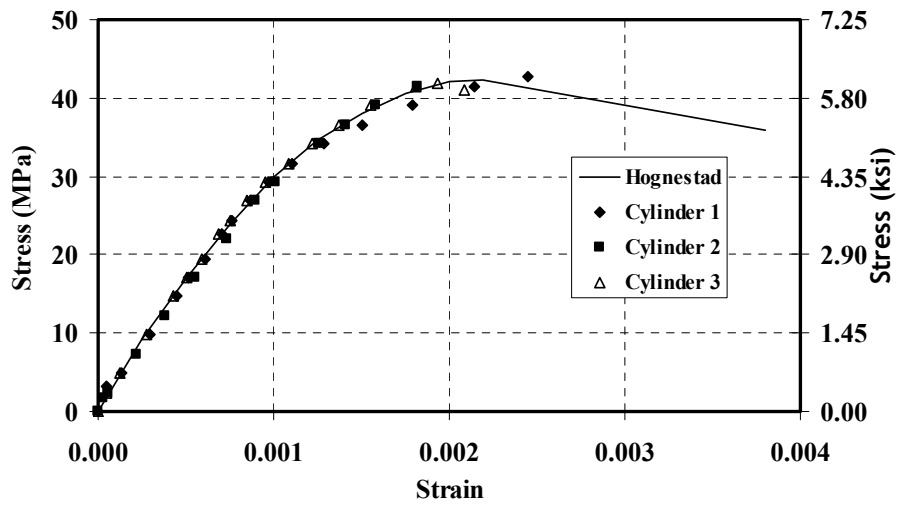


Figure A.4 Stress-Strain Curves for Concrete of Hollow Specimen P12

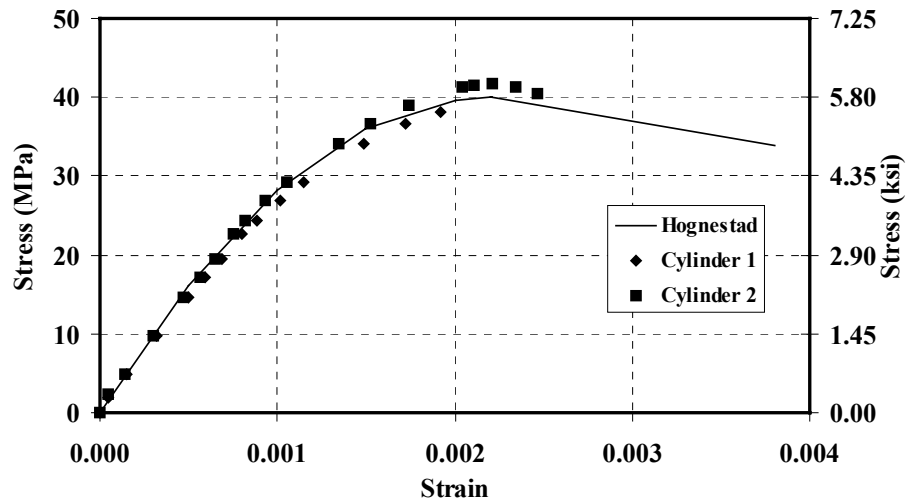


Figure A.5 Stress-Strain Curves for Concrete of Hollow Specimen P14

A.1.2.3 Tensile Strength

The split-cylinder tensile strength of the concrete, f_t , can be calculated using the following expression (Mirza, Hatzinikolas and MacGregor, 1979):

$$f_t = 0.53\sqrt{f'_c} \text{ (MPa)} = 6.4\sqrt{f'_c} \text{ (psi)} \quad (\text{A.4})$$

where f_t and f'_c are in MPa (psi). As can be seen in Table A.5, tensile strengths approximated using Eq. A.4 are very close to those measured in split-cylinder tests.

Table A.5 Comparison of Measured and Estimated Tensile Strength of Concrete

Specimen ID	Measured Tensile Strength MPa (psi)	Estimated Tensile Strength MPa (psi)	Ratio of Measured to Estimated Tensile Strength
P6	2.6 (380)	2.8 (400)	0.95
P8	2.3 (330)	2.8 (403)	0.82
P10	3.2 (460)	3.2 (457)	1.01
P12	3.5 (510)	3.5 (501)	1.02
P14	3.3 (480)	3.5 (504)	0.95
Average			0.95
St. Dev.			0.08
COV			0.08

A.2 REINFORCEMENT

The measured properties of the steel reinforcement are described in the following sections. All tension tests were conducted using a Tinius Olsen test machine with a capacity of 900 kN (200 kips). Table A.6 summarizes the average yield stress, calculated using the 0.2% offset method, and the strength of the three steel bar sizes used in the project. Four bars were tested for each bar size.

The 6-mm diameter (#2) bars were the only reinforcement that exhibited a well-defined yield plateau. The average strain at onset of strain hardening began was 0.0059, with standard deviation of 0.0012. The average strain-hardening modulus of elasticity, defined as the initial slope of the measured hardening curve,

was 2260 MPa (330 ksi), with standard deviation equal 60 MPa (9 ksi) (Table A.7).

Table A.6 Measured Strength of the Steel Reinforcement

Bar Size mm (in.)	Yield Stress MPa (ksi)		Ultimate Stress MPa (ksi)	
	Average	COV	Average	COV
3.2 (0.135)	600 (87)	0.011	640 (93)	0.011
6.0 (0.250)	510 (74)	0.008	600 (87)	0.011
12.0 (0.500)	490 (71)	0.029	765 (111)	0.027

Table A.7 Measured Hardening Properties of the Steel Reinforcement

Bar Size mm (in.)	Hardening Modulus of Elasticity MPa (ksi)		Strain at Onset of Strain Hardening mm/mm (in./in.)	
	Average	COV	Average	COV
3.2 (0.135)	600 (87)	0.011	-	-
6.0 (0.250)	2260 (330)	0.027	0.0059	0.20
12.0 (0.500)	7240 (1050)	0.048	-	-

A.2.1 Longitudinal Reinforcement

The longitudinal reinforcement used in all five specimens was 6-mm diameter (#2) deformed reinforcement imported from Sweden. The average yield stress was 510 MPa (74 ksi). Figure A.6 shows a typical stress-strain curve.

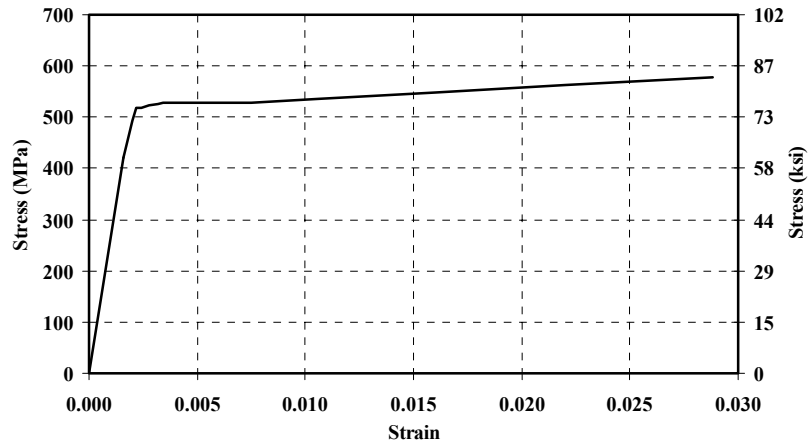


Figure A.6 Stress-Strain Curve for Longitudinal Reinforcement

A.2.2 Transverse Reinforcement

Transverse reinforcement was fabricated using No. 10 gage smooth wire, (3.4-mm (0.135-in.) diameter). The average yield stress was 600 MPa (87 ksi). Figure A.7 shows a typical stress-strain curve.

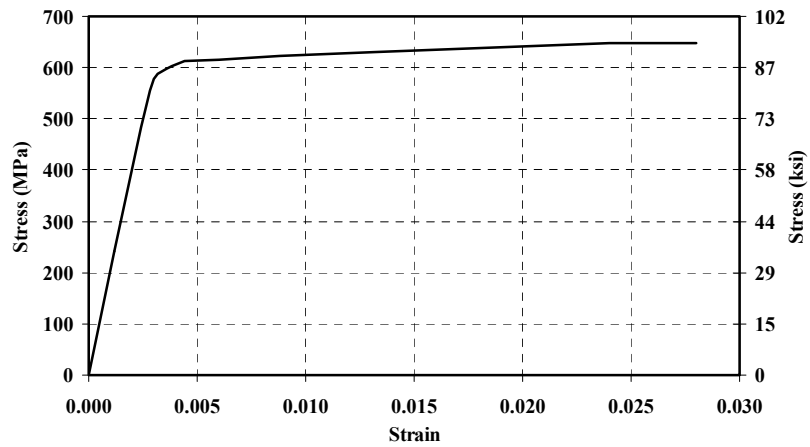


Figure A.7 Stress-Strain Curve for Transverse Reinforcement

A.2.3 Reinforcement in End Blocks

The reinforcement used in all the end blocks was 12-mm diameter (#4) deformed bars. The average yield stress was 490 MPa (71 ksi). Figure A.8 shows the stress-strain curve obtained from a typical tension test.

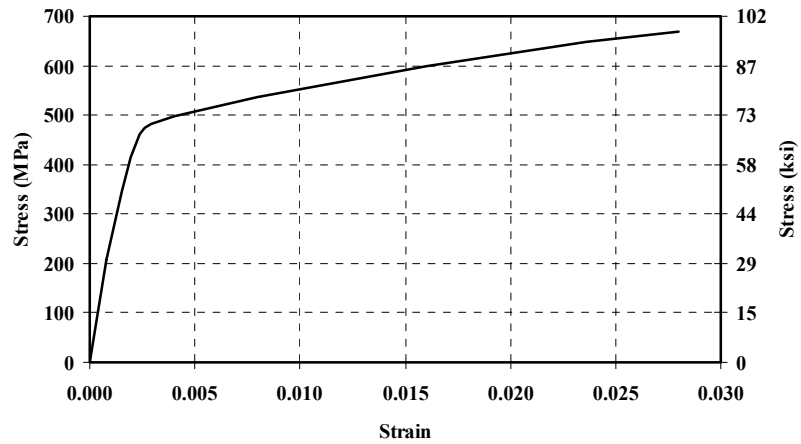


Figure A.8 Stress-Strain Curve for Deformed Reinforcement in End Blocks

Appendix B Measured Response of the Test Specimens

The measured response of the five test specimens is documented in this appendix. The data are presented in five sections: horizontal displacements measured along the compression walls, which were used to monitor the profiles of the walls; vertical displacements measured at the center of the solid blocks; vertical displacements measured at the edges of the solid blocks; vertical displacements measured along the tension walls which were used to calculate curvature; and horizontal displacements measured at the top of the top solid block. The locations of the instruments, and the instrument designations, are described in Chapter 4.

B.1 HORIZONTAL DISPLACEMENTS MEASURED ALONG THE EAST AND NORTH WALLS

The out-of-plane responses of the two walls in compression (north and east walls) were measured using 24 linear potentiometers distributed as shown in Fig. B.1. Figures B.2 through B.11 show the data recorded by the linear potentiometers. Data from all potentiometers at the same level are shown in the same plot. The individual curves are not identified, because they are too close together and it would be confusing. Positive displacements represent displacements of the walls away from the axial axis of the column.

Two instruments, P2 and P6, did not appear to be working properly while Specimen P6 was tested. Measurements from Instrument P6 showed high noise, but the data followed the same trend as the other four instruments located at the same level (Fig. B.2b). Readings from Instrument P2, however, did not even

follow the trend of the other instruments at the same level (Fig. B.2a). Both instruments were repaired and functioned properly for the other four test specimens.

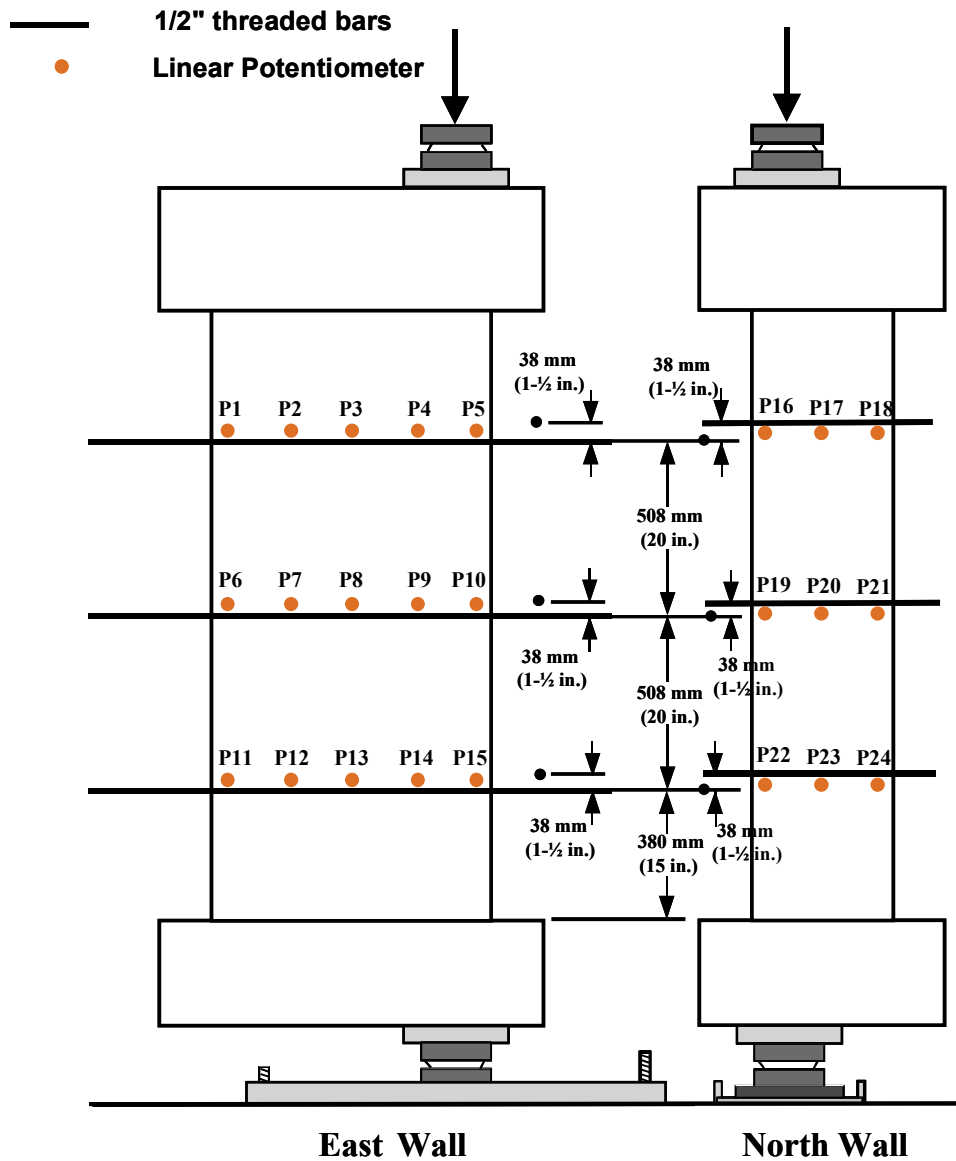
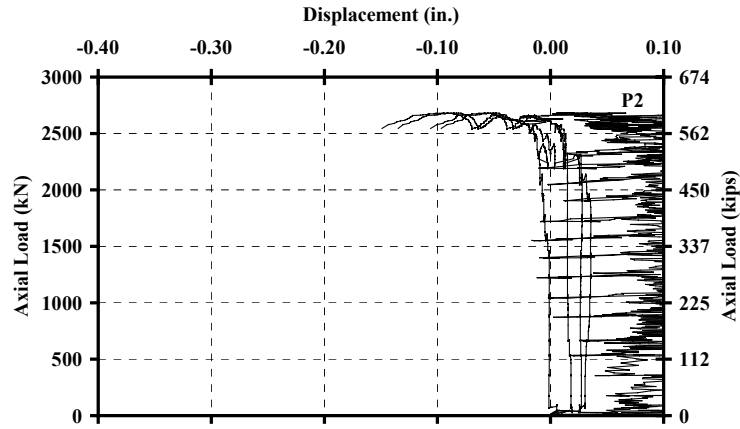
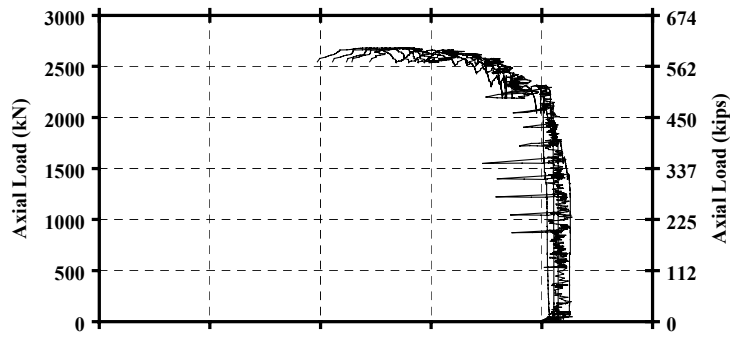


Figure B.1 Distribution of Linear Potentiometers used to Measure Horizontal Displacements of the Walls in Compression

(a) P1, P2, P3, P4, P5



(b) P6, P7, P8, P9, P10



(c) P11, P12, P13, P14, P15

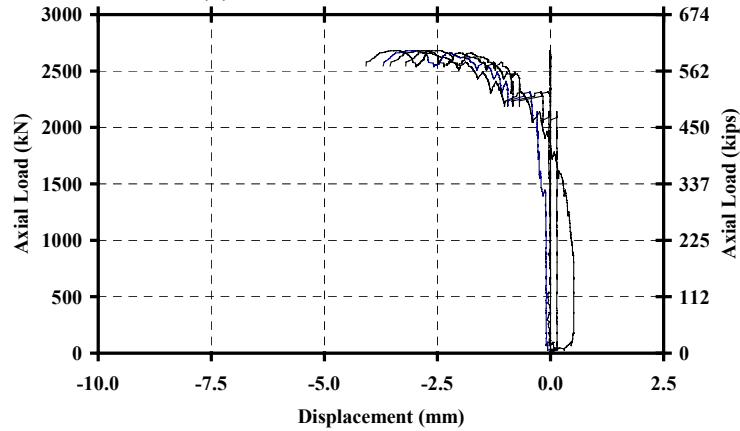
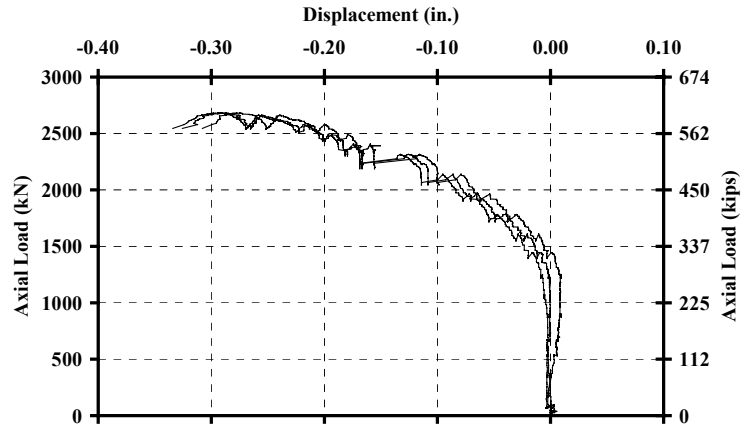
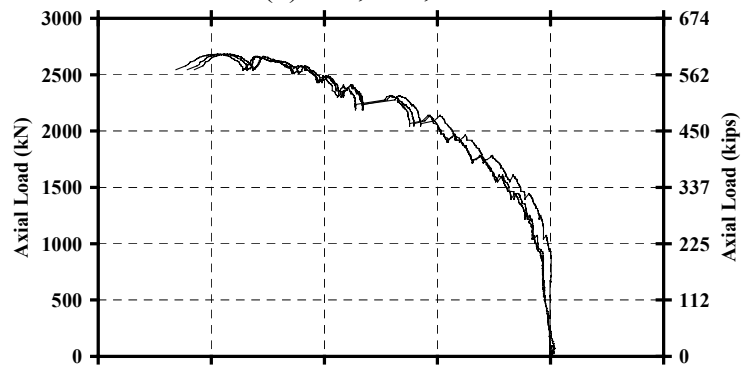


Figure B.2 Horizontal Deflections of East Wall, Specimen P6

(a) P16, P17, P18



(b) P19, P20, P21



(c) P22, P23, P24

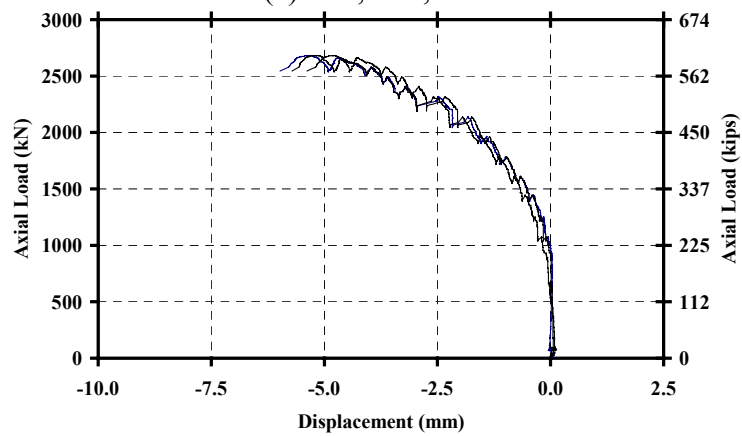
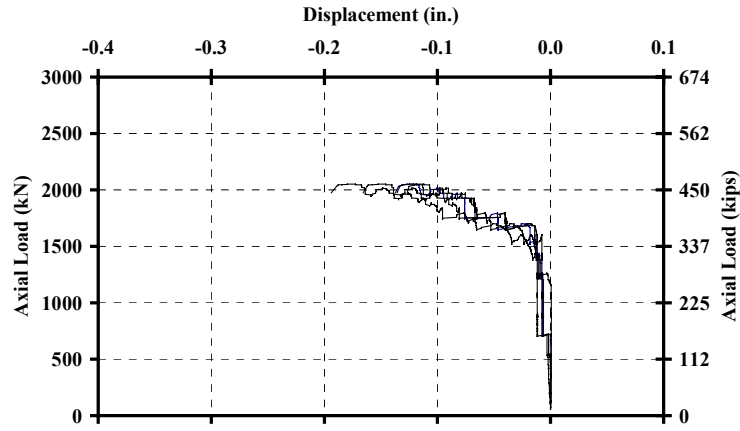
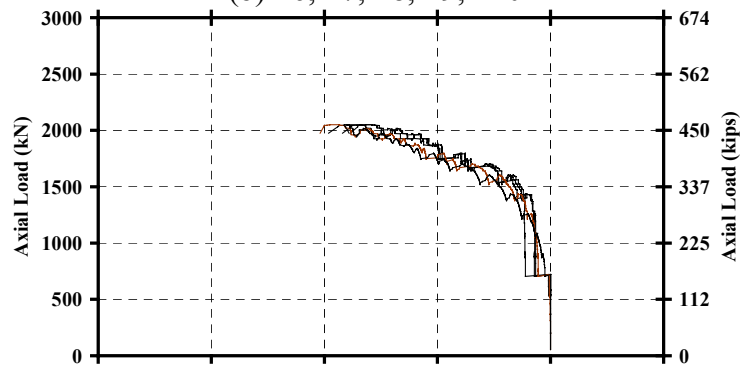


Figure B.3 Horizontal Deflections of North Wall, Specimen P6

(a) P1, P2, P3, P4, P5



(b) P6, P7, P8, P9, P10



(c) P11, P12, P13, P14, P15

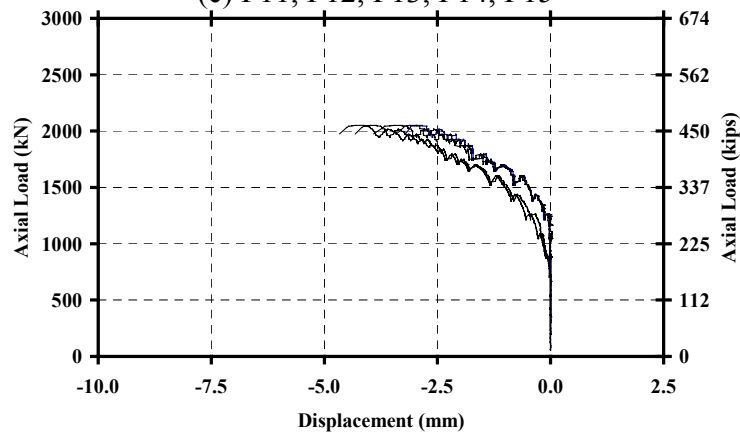
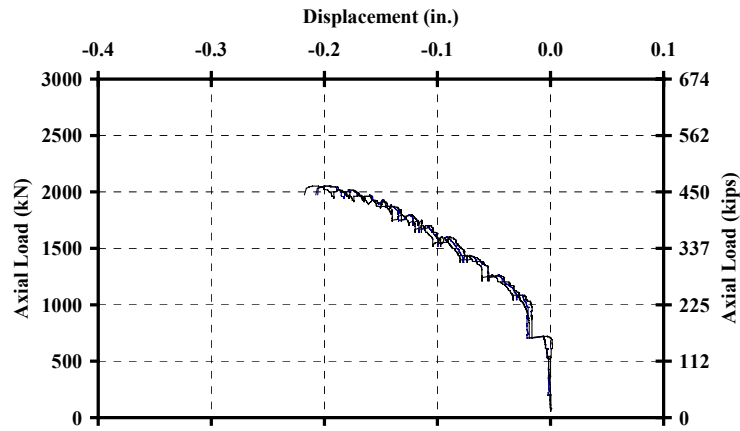
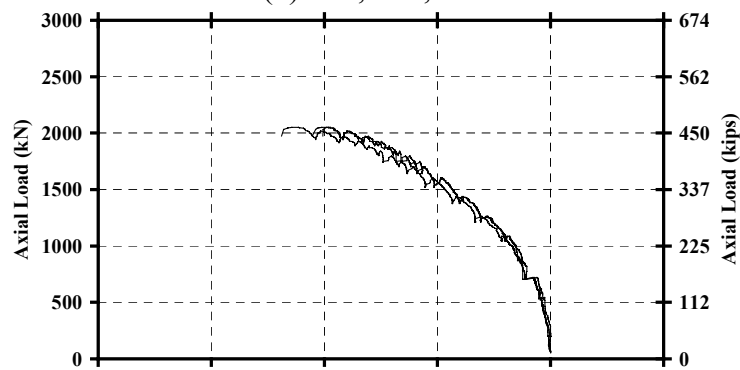


Figure B.4 Horizontal Deflections of East Wall, Specimen P8

(a) P16, P17, P18



(b) P19, P20, P21



(c) P22, P23, P24

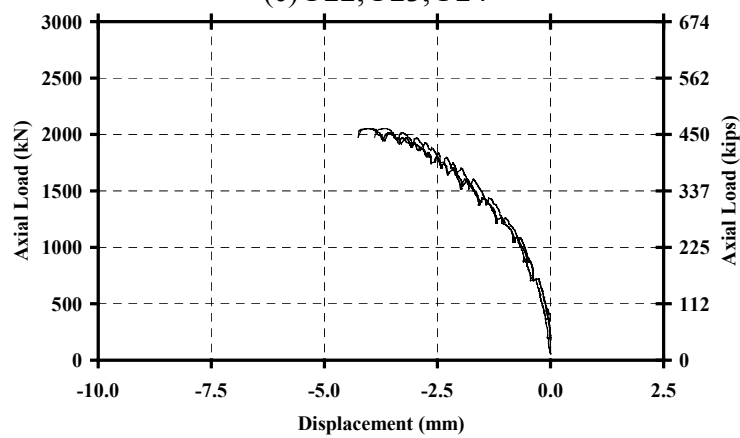
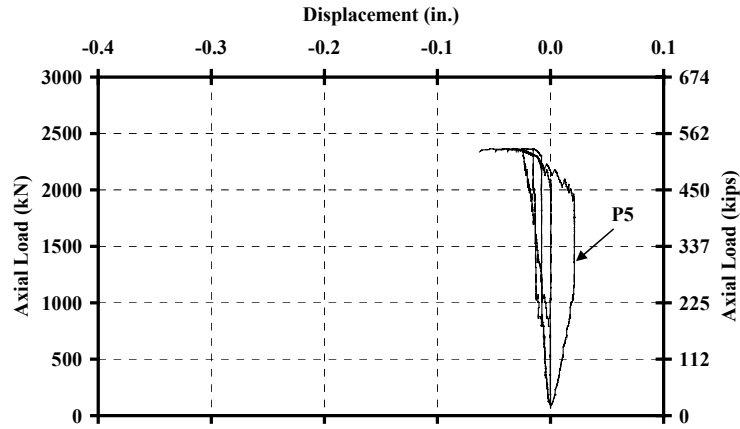
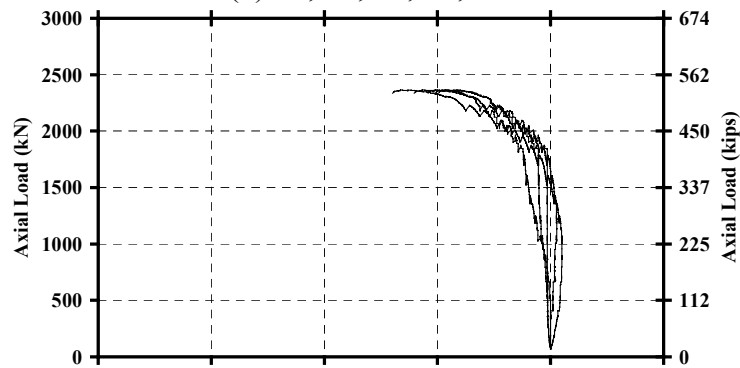


Figure B.5 Horizontal Deflections of North Wall, Specimen P8

(a) P1, P2, P3, P4, P5



(b) P6, P7, P8, P9, P10



(c) P11, P12, P13, P14, P15

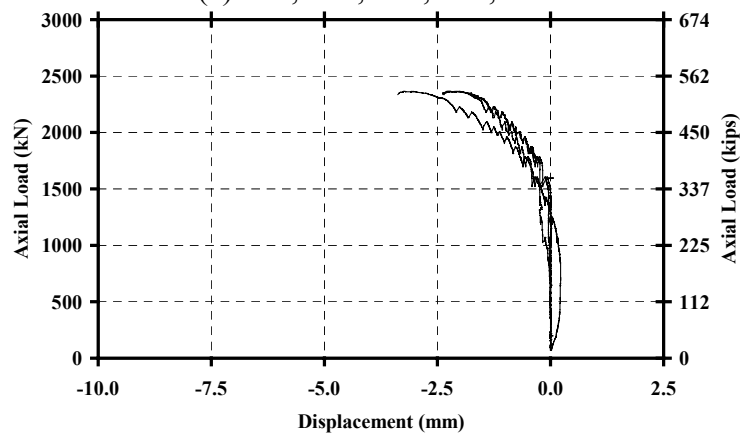


Figure B.6 Horizontal Deflections of East Wall, Specimen P10

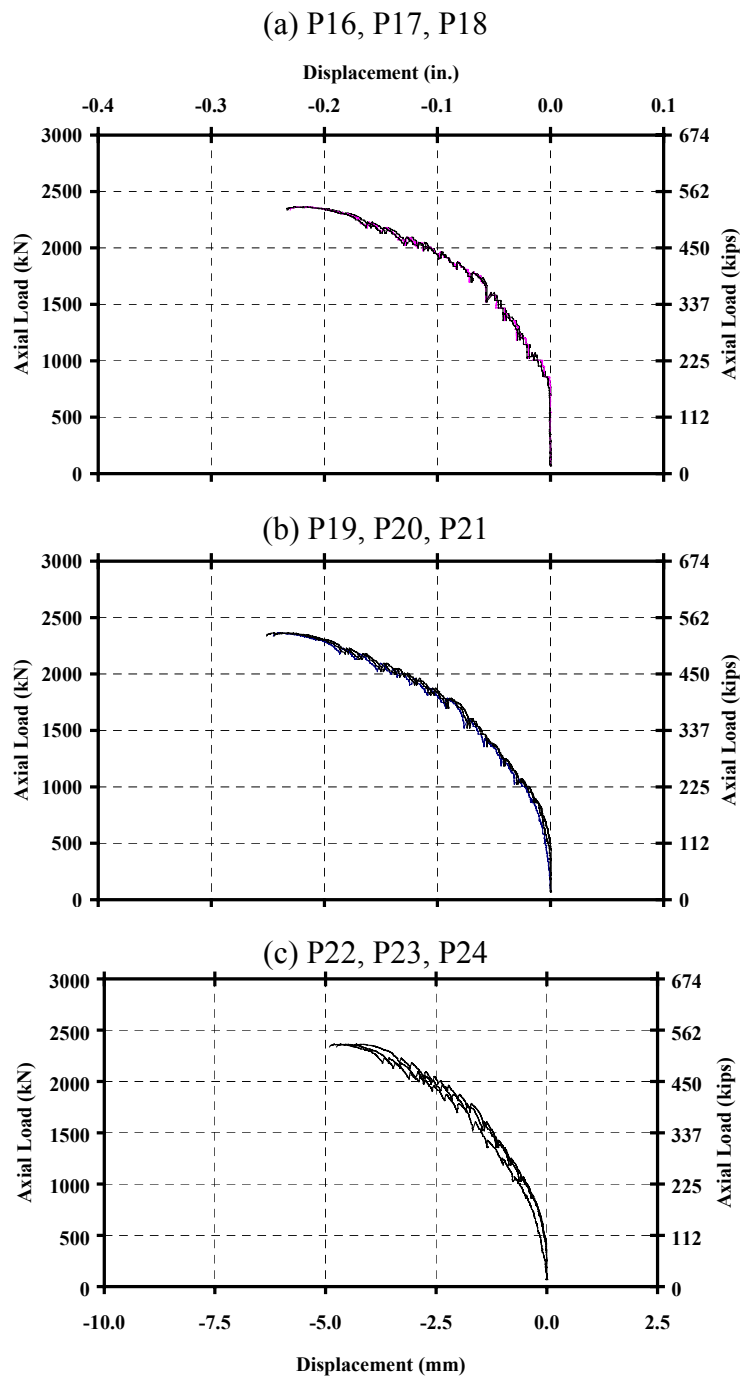
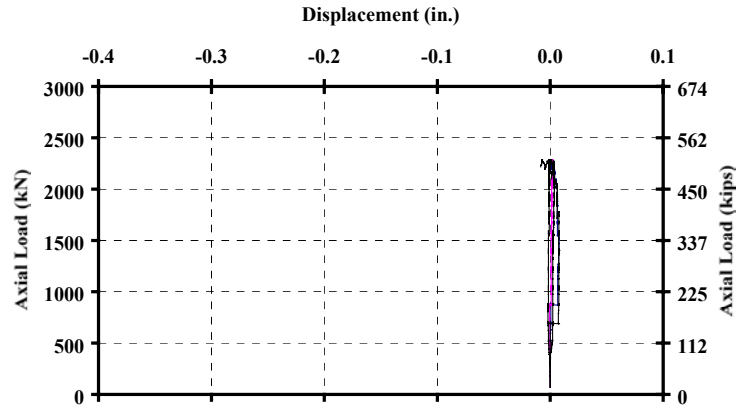
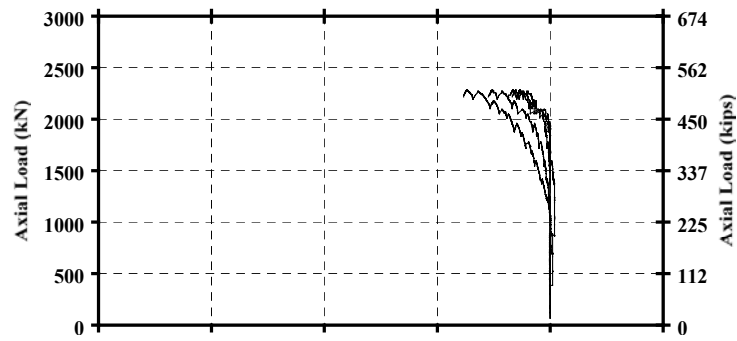


Figure B.7 Horizontal Deflections of North Wall, Specimen P10

(a) P1, P2, P3, P4, P5



(b) P6, P7, P8, P9, P10



(c) P11, P12, P13, P14, P15

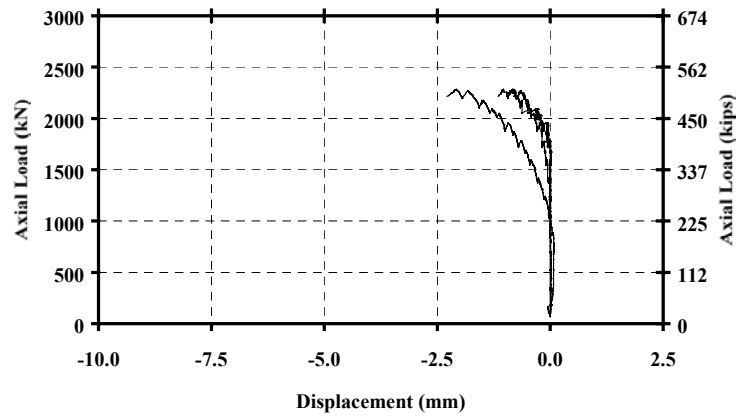
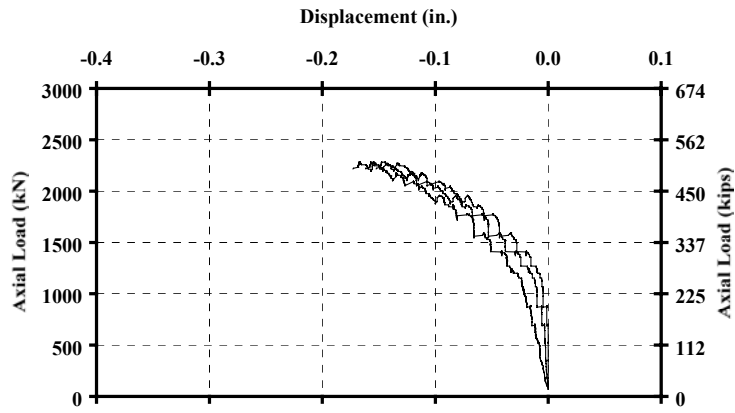
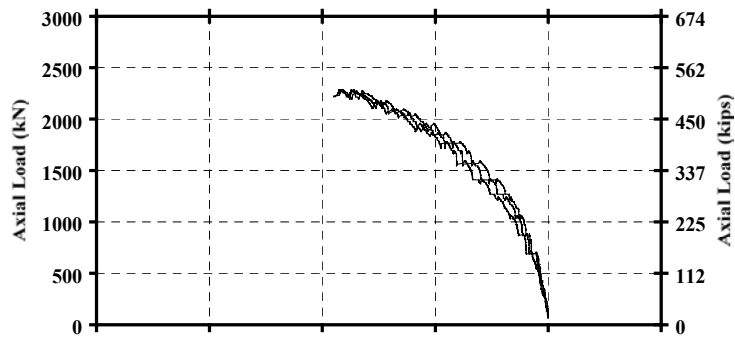


Figure B.8 Horizontal Deflections of East Wall, Specimen P12

(a) P16, P17, P18



(b) P19, P20, P21



(c) P22, P23, P24

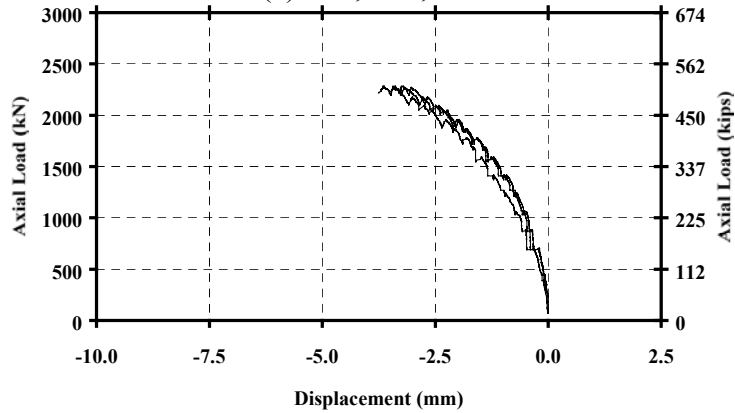
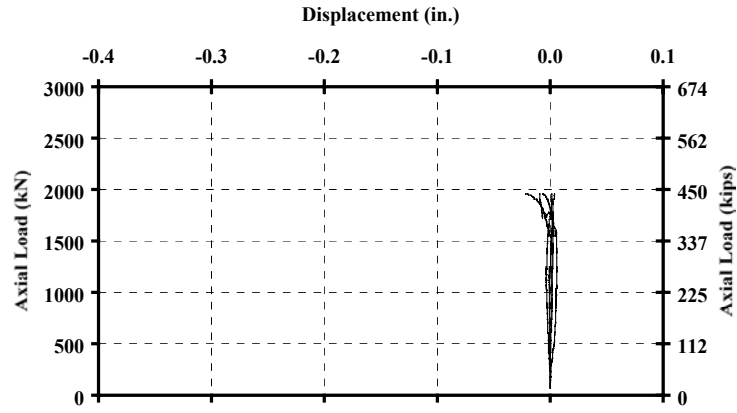
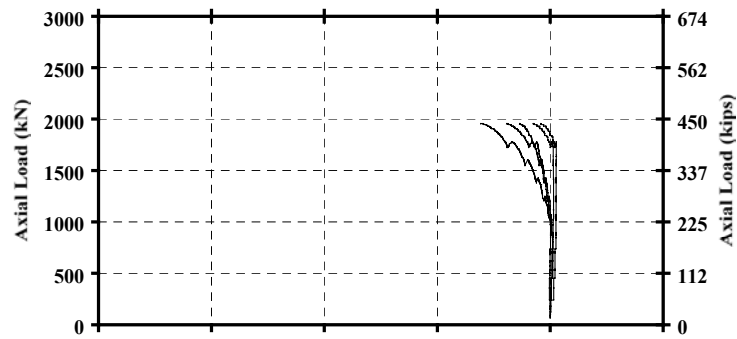


Figure B.9 Horizontal Deflections of North Wall, Specimen P12

(a) P1, P2, P3, P4, P5



(b) P6, P7, P8, P9, P10



(c) P11, P12, P13, P14, P15

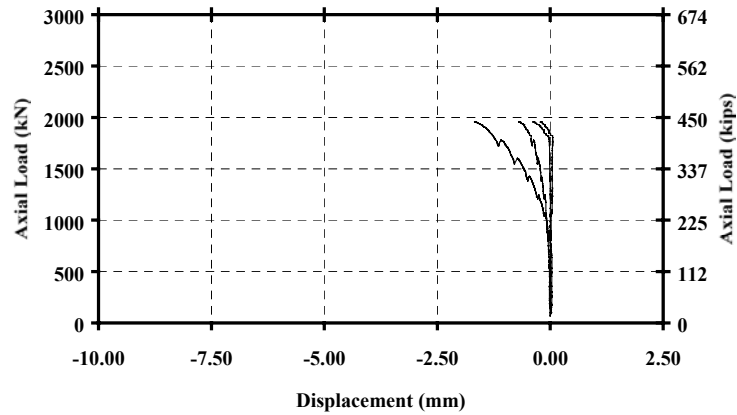
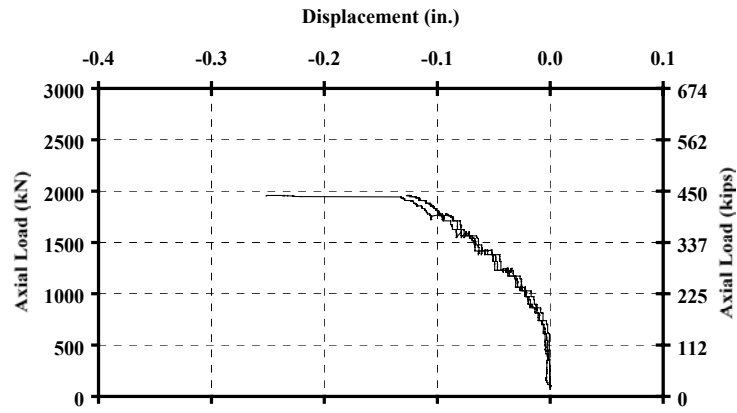
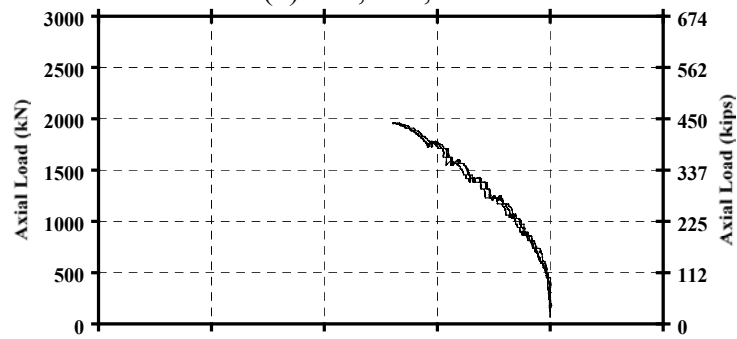


Figure B.10 Horizontal Deflections of East Wall, Specimen P14

(a) P16, P17, P18



(b) P19, P20, P21



(c) P22, P23, P24

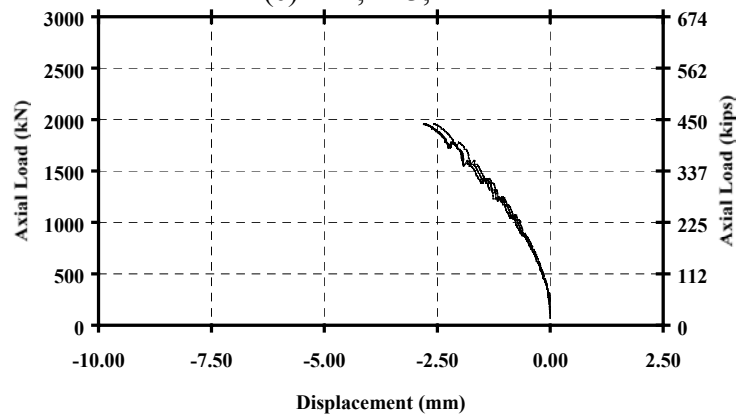


Figure B.11 Horizontal Deflections of North Wall, Specimen P14

B.2 VERTICAL DISPLACEMENTS MEASURED AT THE CENTER OF THE SOLID BLOCKS

The vertical displacements used to calculate the axial shortening of the specimens were measured at the geometric center of the top surface of the top end block, and at the bottom surface of the bottom end block. The vertical displacements for the five specimens are plotted in Fig. B.12. Positive displacements correspond to downward movement of the end blocks.

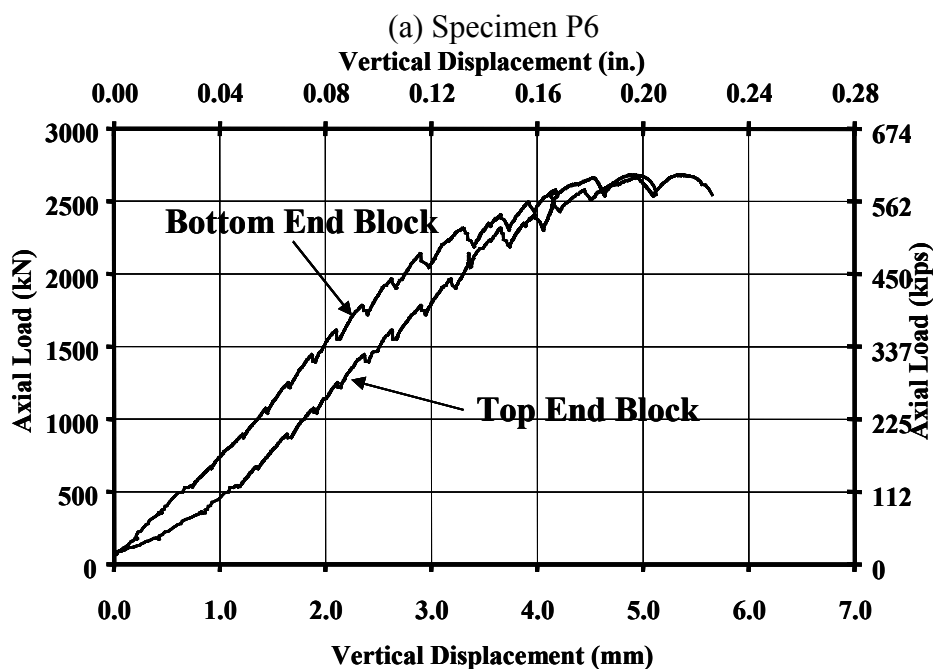


Figure B.12 Vertical Displacements Measured at Center of End Blocks

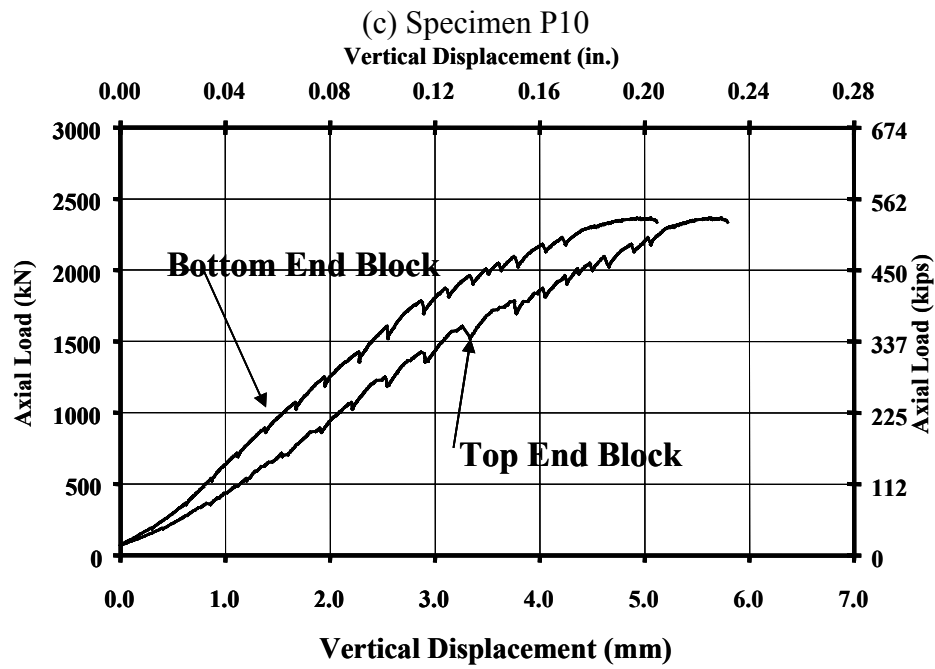
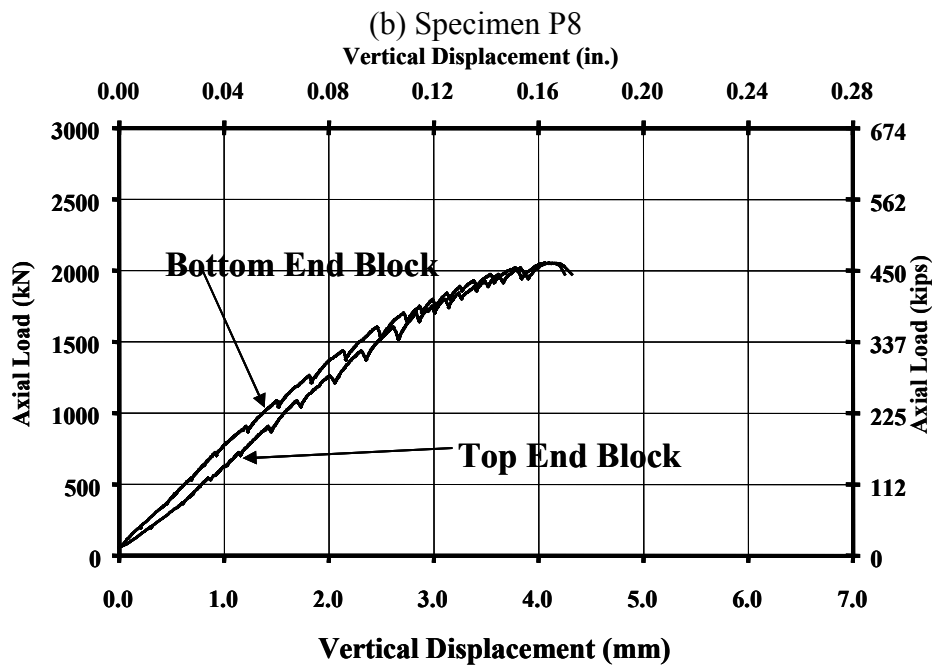


Figure B.12 (cont.) Vertical Displacements Measured at Center of End Blocks

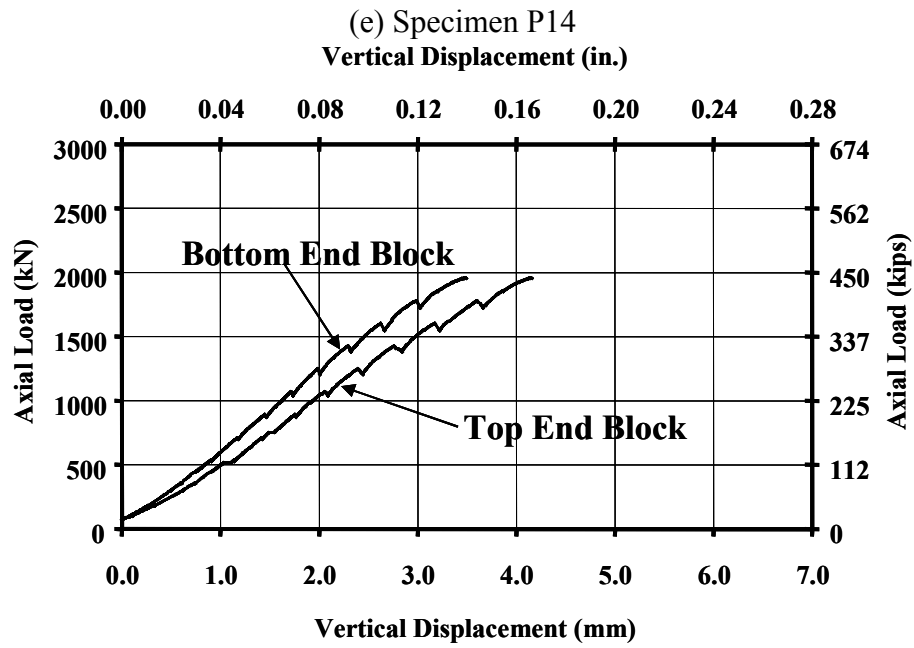
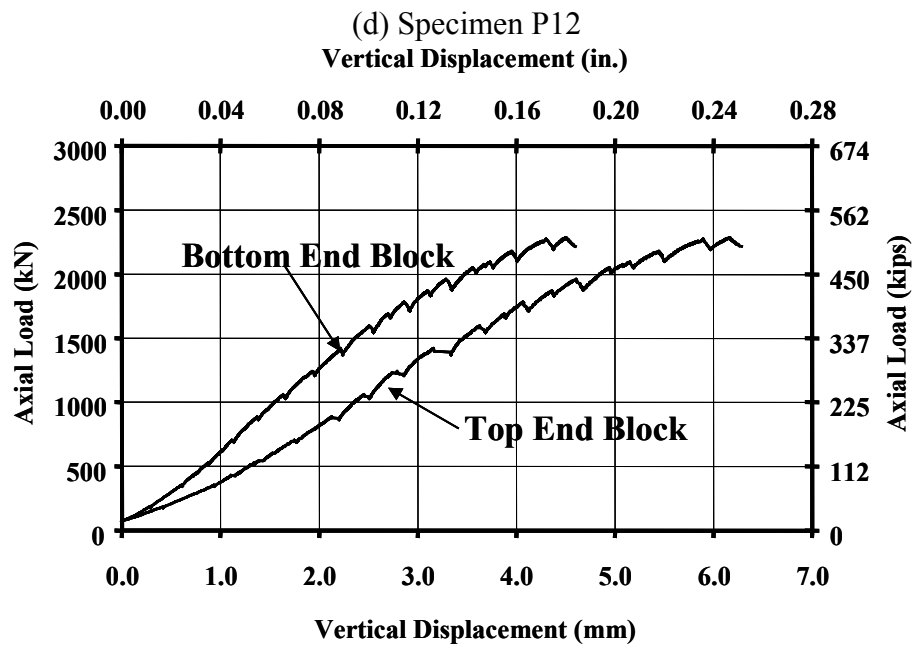


Figure B.12 (cont.) Vertical Displacements Measured at Center of End Blocks

B.3 VERTICAL DISPLACEMENTS MEASURED AT THE EDGES OF THE SOLID BLOCKS

The vertical displacements were also measured along the edges of the top of the top end blocks and the bottom of the bottom end blocks in order to calculate the rotation of the blocks. Negative displacements of the top solid block as well as positive displacements of the lower solid block correspond to downward displacements of the blocks. Figure 4.31 shows the location of the instruments on the top end block.

The vertical displacements of the five specimens are shown in Fig. B.13. The notation defined in Chapter 4 is used to identify the displacement curves for the individual instruments.

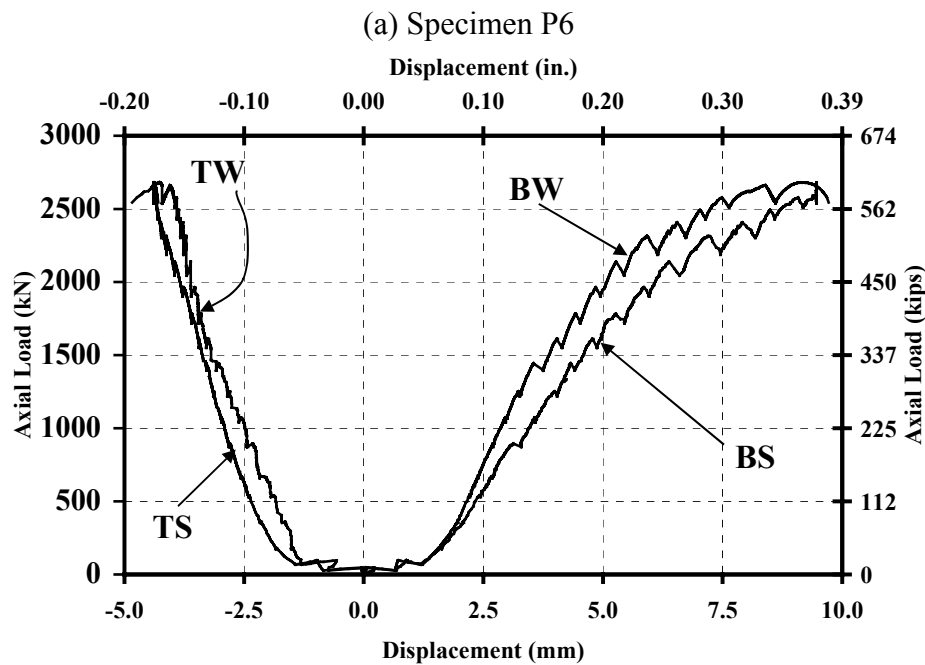


Figure B.13 Vertical Displacements measured at the middle of the West and South Edges of the End Blocks

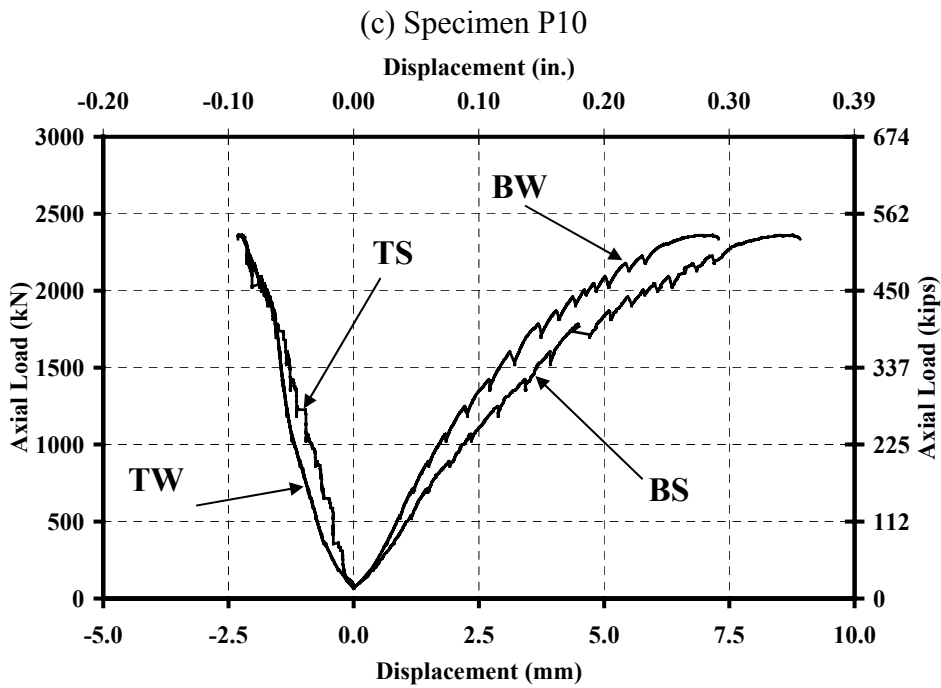
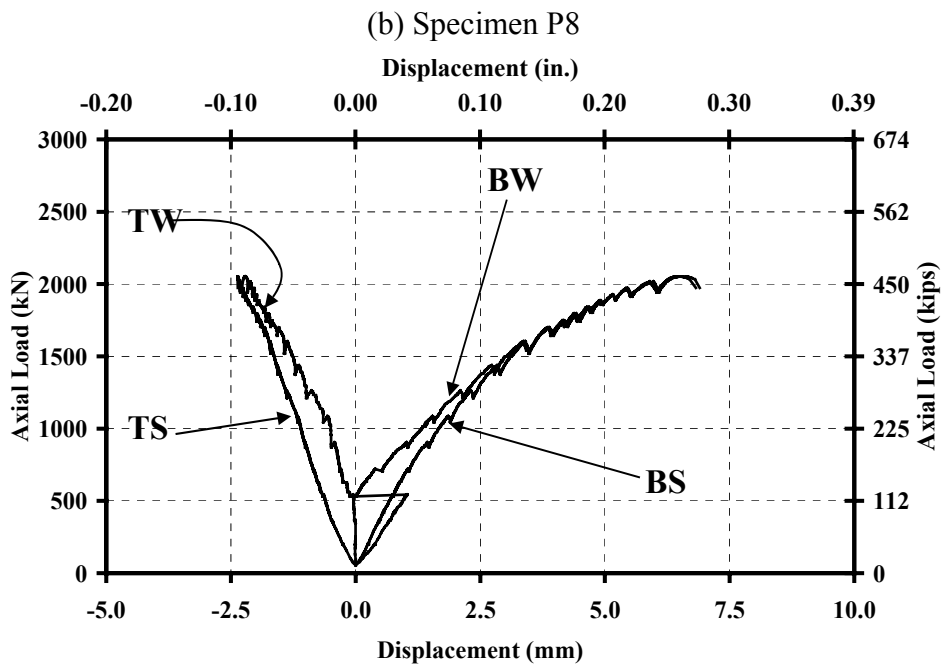


Figure B.13 (cont.) Vertical Displacements measured at the middle of the West and South Edges of the End Blocks

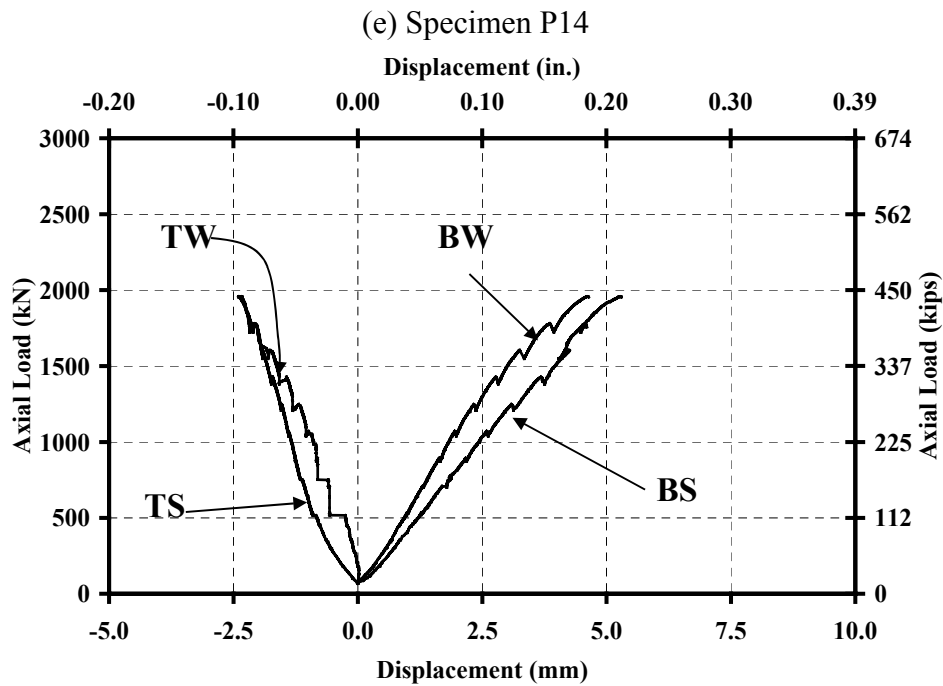
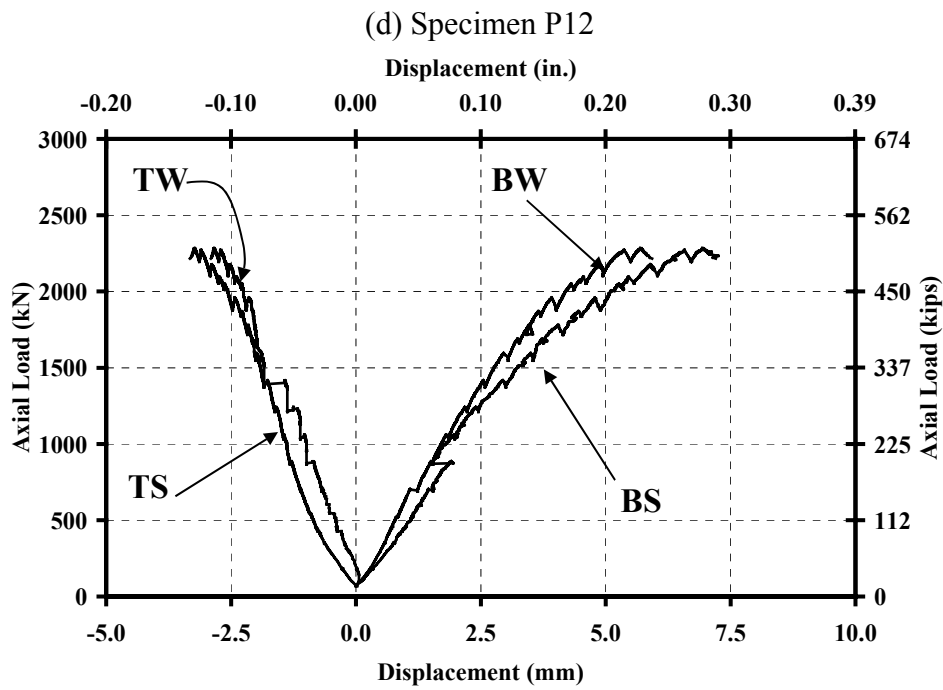


Figure B.13 (cont.) Vertical Displacements measured at the middle of the West and South Edges of the End Blocks

B.4 VERTICAL DISPLACEMENTS USED TO CALCULATE CURVATURE

Figure B.14 shows the readings from the four instruments along the west wall used to measure the curvature of the piers in the north-south direction. Figure B.15 shows the readings from the instruments along the south wall used to measure the curvature in the east-west direction. Data were only obtained at one level of the short wall for Specimens P6 and P8 because two instruments did not function during these tests.

The positive sign corresponds to compression, while the negative sign corresponds to extension (the south-west corner of the specimens experienced the highest tensile stresses in the hollow pier). The same notation defined in Chapter 4 is used to identify individual instruments.

Instruments ET and EB appear not to have functioned properly (Fig. B.15). The instruments did not record readings for Specimens P6, P8, and P14, and recorded displacements for load levels greater than 50% of the failure load for piers P10 and P12.

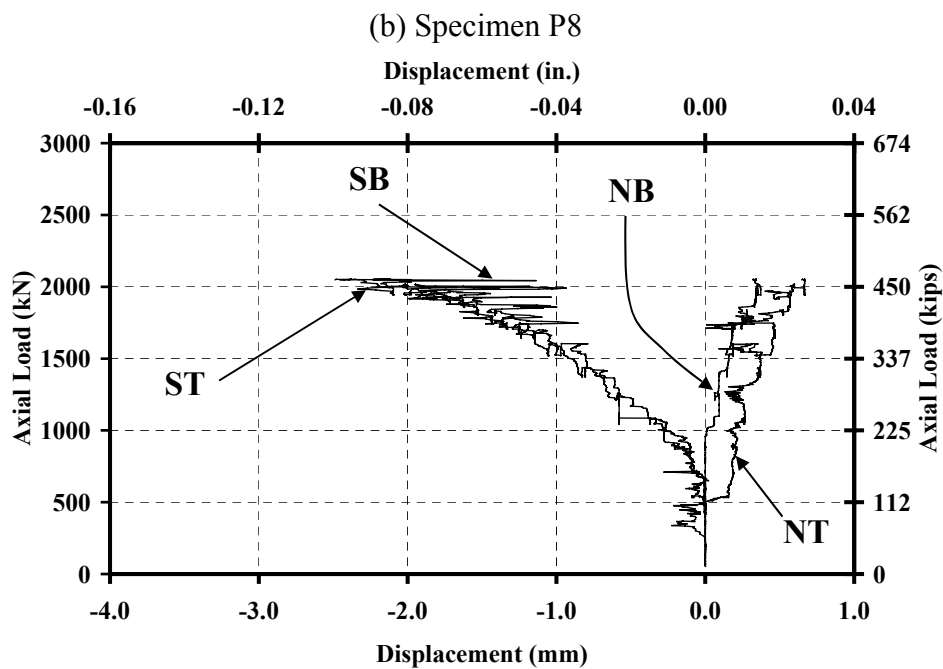
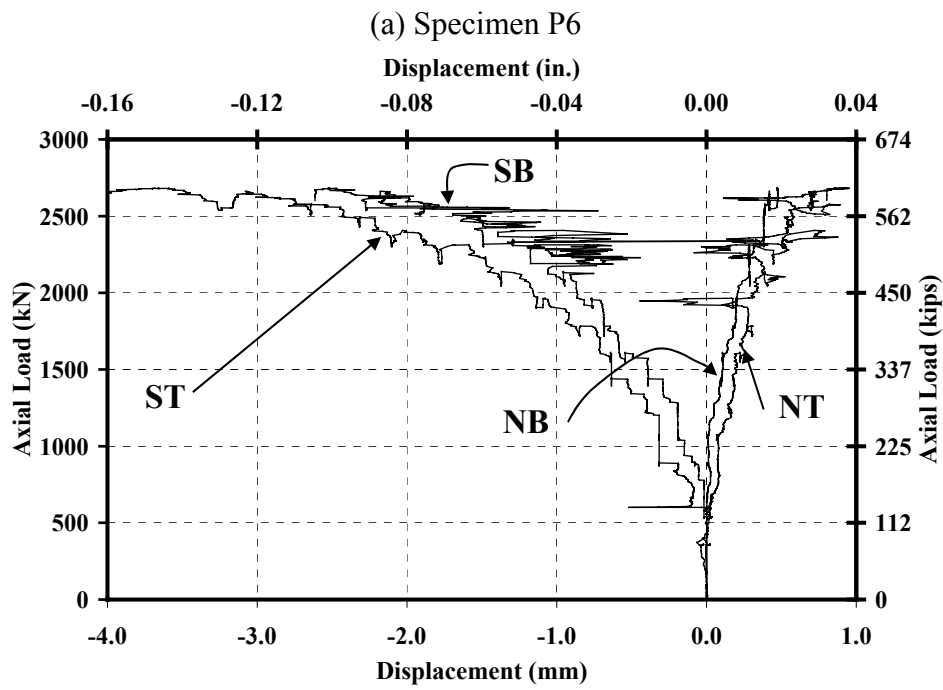
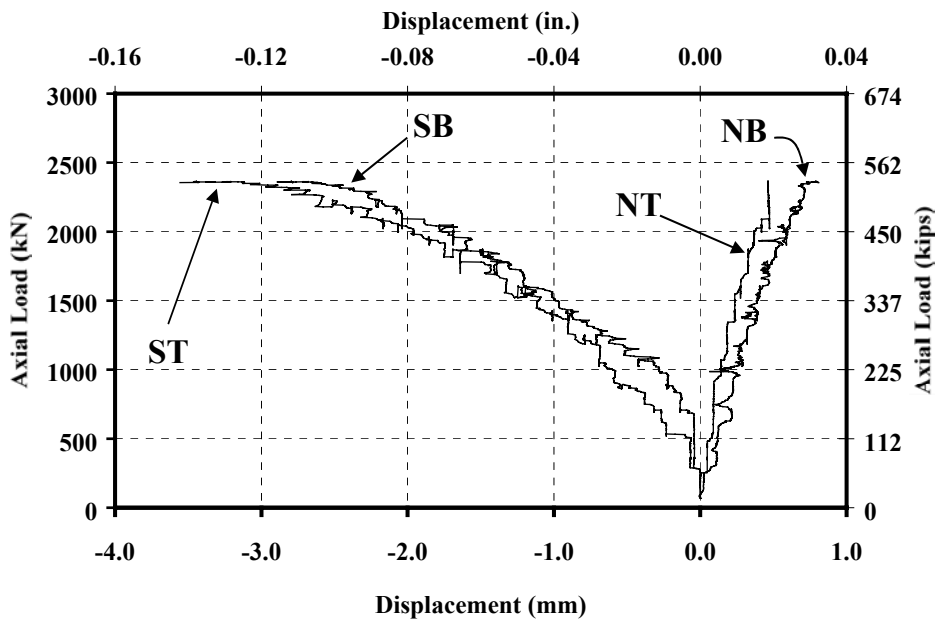


Figure B.14 Vertical Displacements Along the West Wall Used to Calculate Curvature in the North-South Direction

(c) Specimen P10



(d) Specimen P12

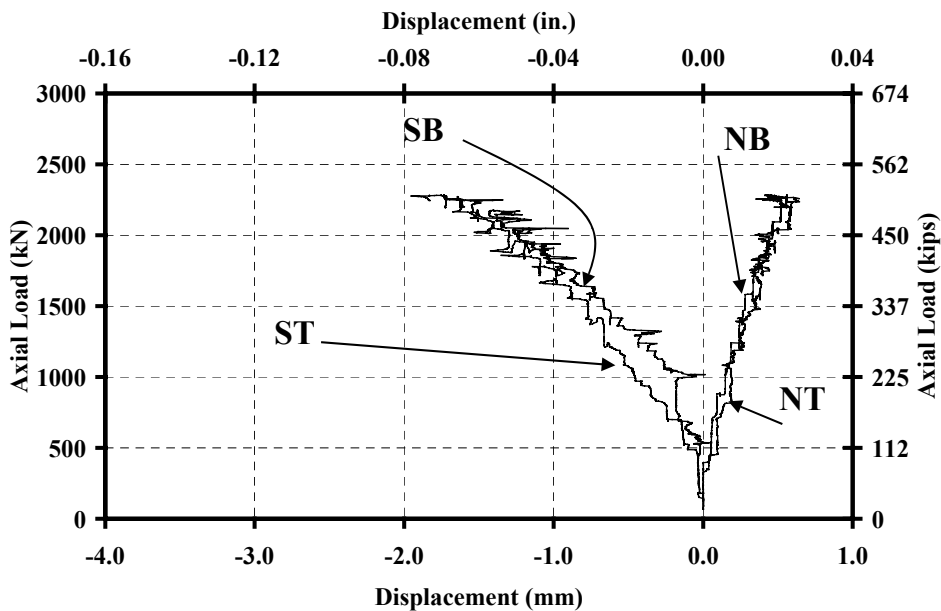


Figure B.14 (cont.) Vertical Displacements Along the West Wall Used to Calculate Curvature in the North-South Direction

(e) Specimen P14

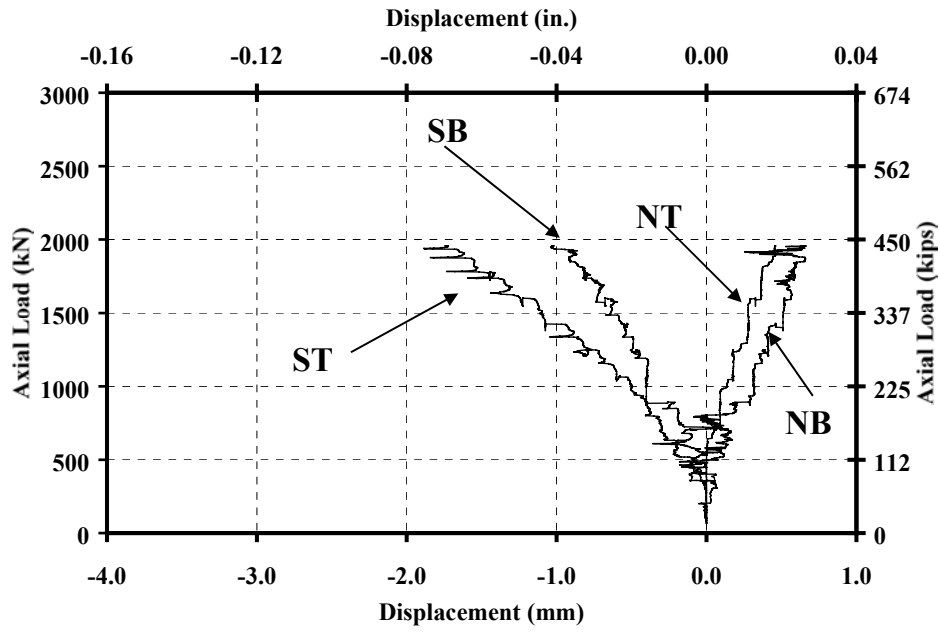


Figure B.14 (cont.) Vertical Displacements Along the West Wall Used to Calculate Curvature in the North-South Direction

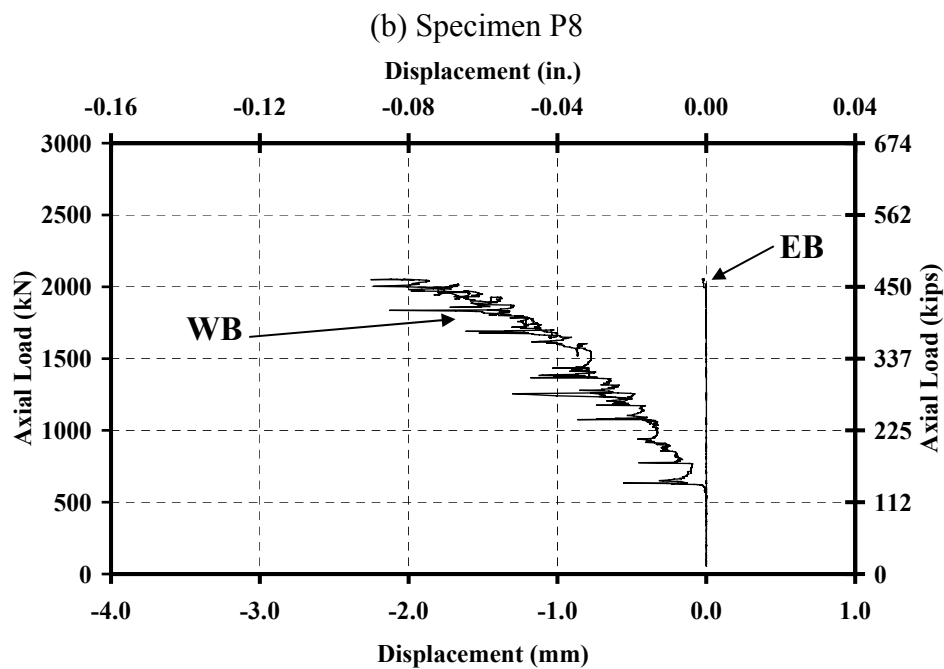
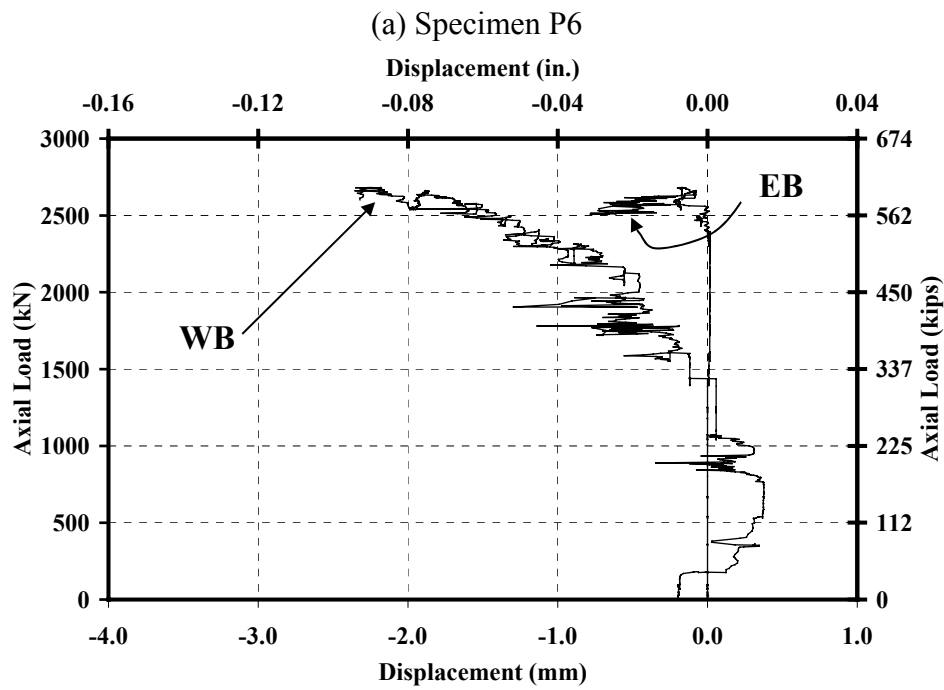


Figure B.15 Vertical Displacements at South Wall Used to Calculate Curvature in the East-West Direction

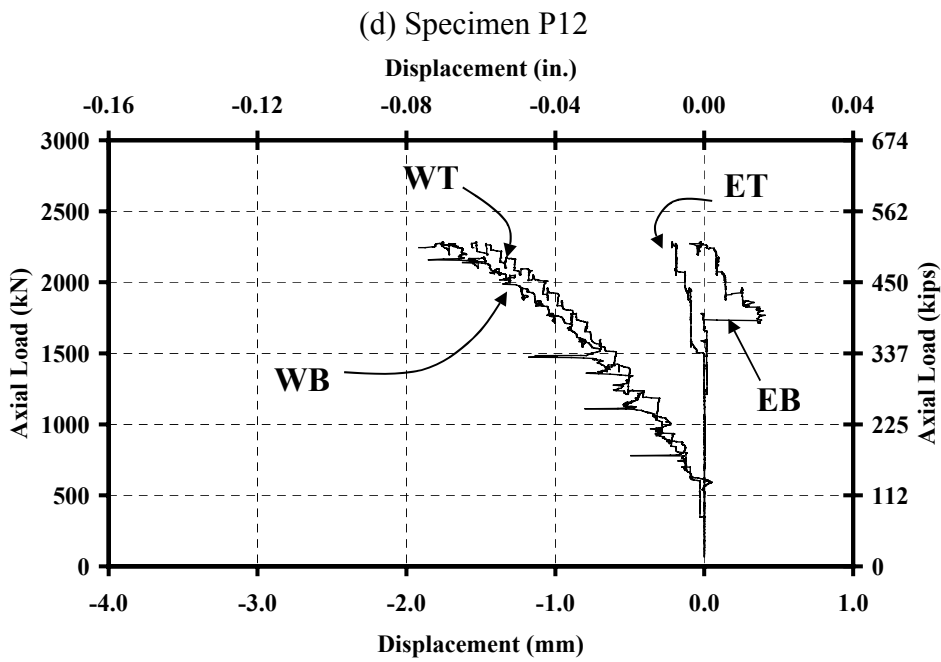
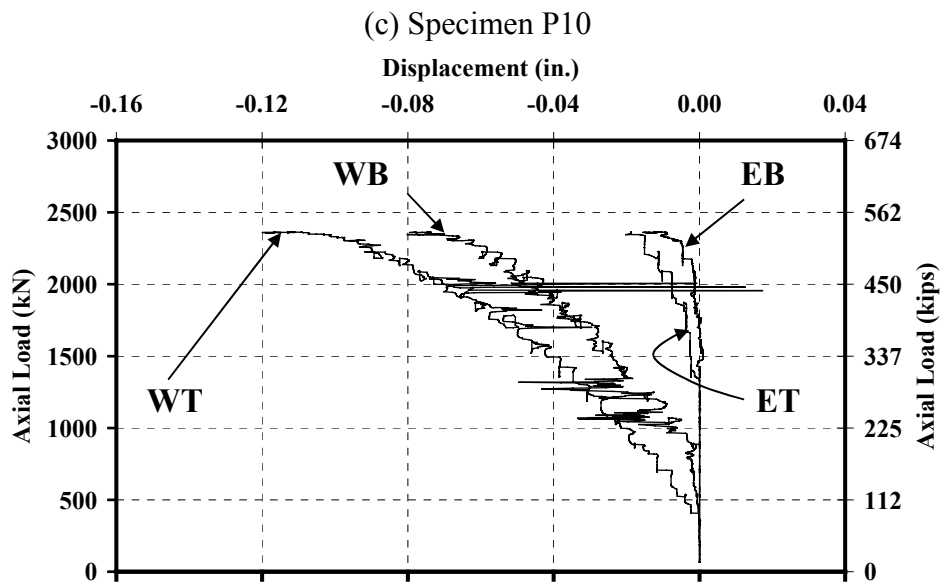


Figure B.15 (cont.) Vertical Displacements at South Wall Used to Calculate Curvature in the East-West Direction

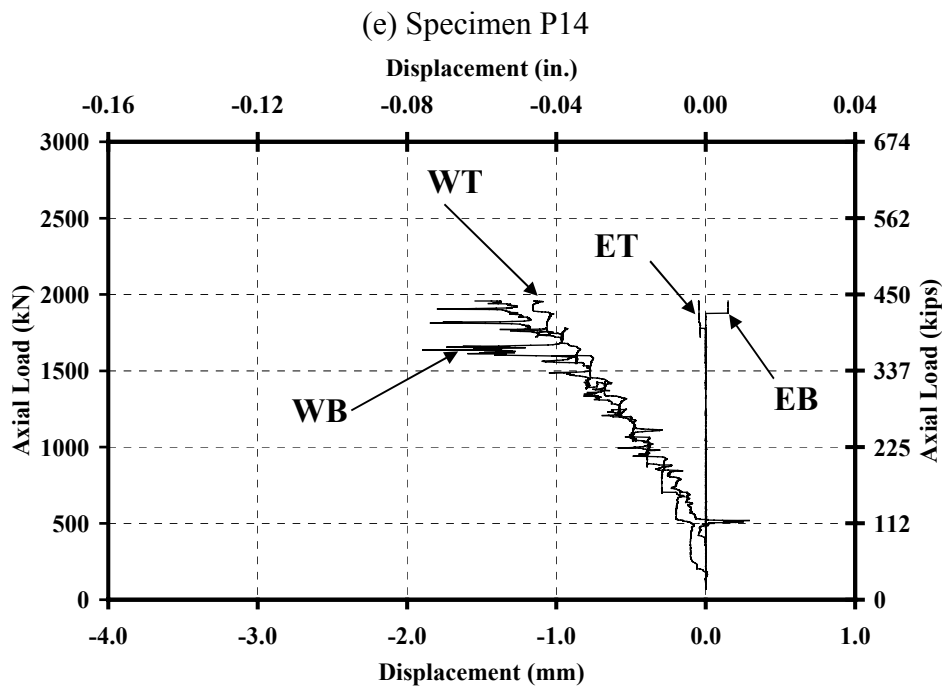


Figure B.15 (cont.) Vertical Displacements at South Wall Used to Calculate Curvature in the East-West Direction

B.5 HORIZONTAL DISPLACEMENTS MEASURED AT THE TOP SOLID BLOCK

The horizontal displacements of the top solid blocks were measured in two orthogonal directions (north-south and east-west) at the locations shown in Fig. 4.32. Data recorded at the top end blocks are shown in Fig. B.16 through B.20.

The positive sign of the displacement corresponds to a displacement to the south or the west. For Specimens P6 and P8, Instrument HEW indicated almost zero displacements (Fig B.16 and B.17), suggesting that it was not working properly during those two tests.

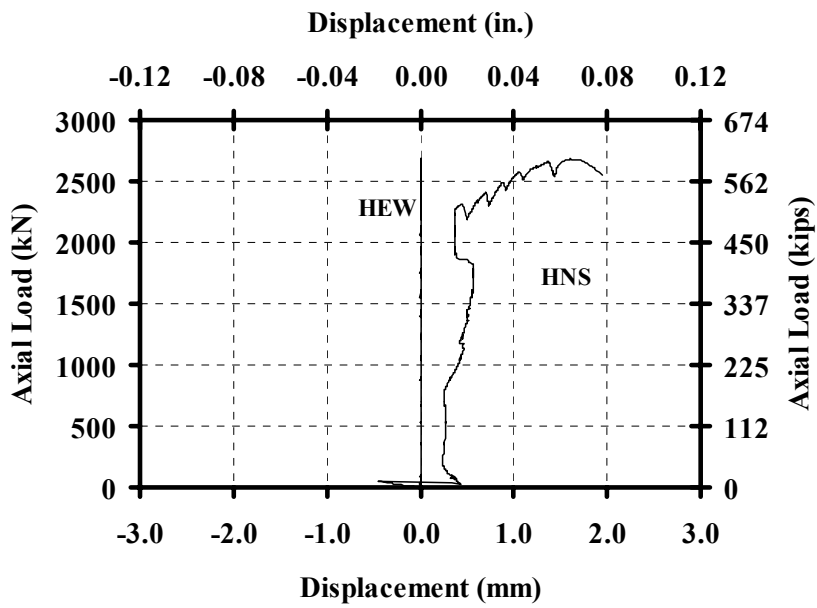


Figure B.16 Horizontal Displacements Measured at the Top End Block of Specimen P6

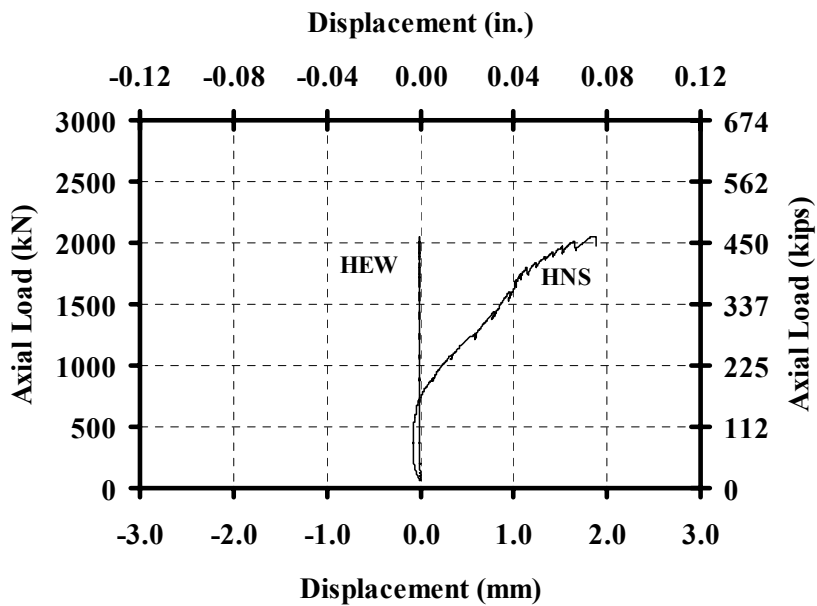


Figure B.17 Horizontal Displacements Measured at the Top End Block of Specimen P8

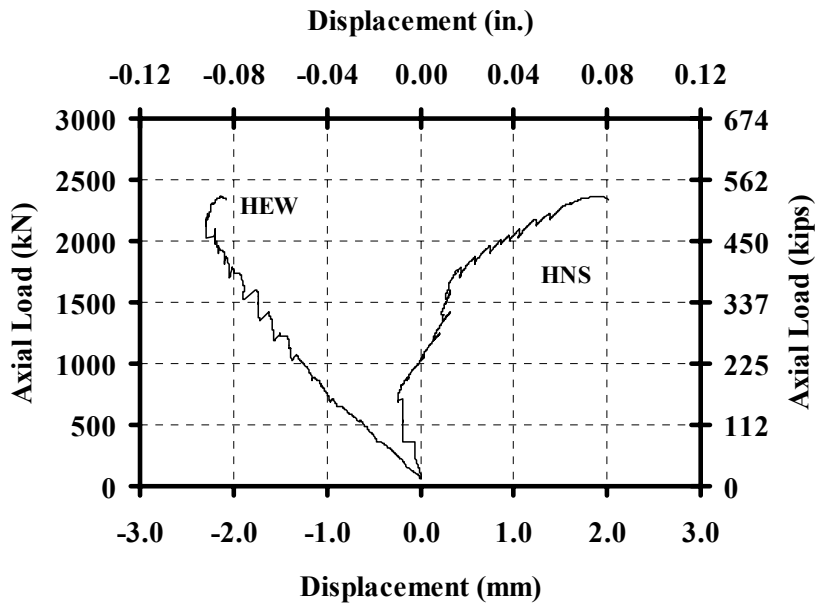


Figure B.18 Horizontal Displacements Measured at the Top End Block of Specimen P10

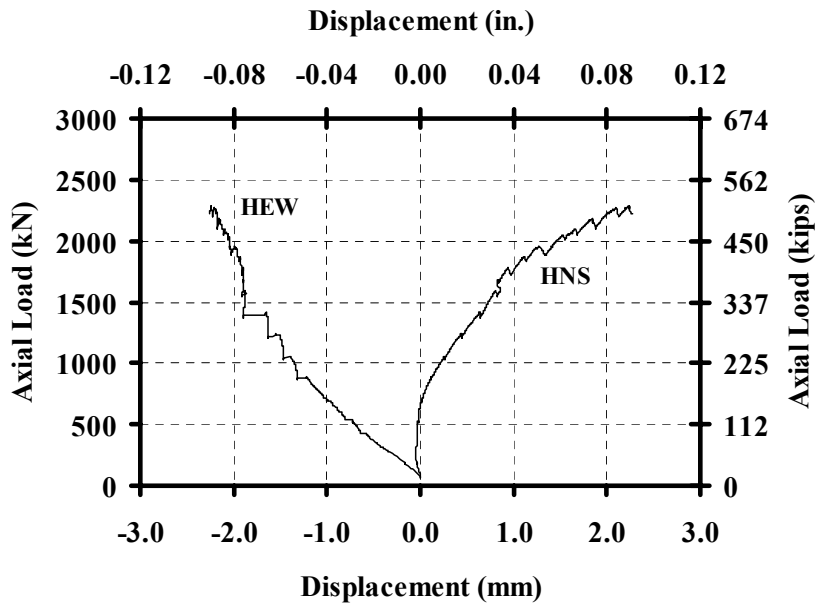


Figure B.19 Horizontal Displacements Measured at the Top End Block of Specimen P12

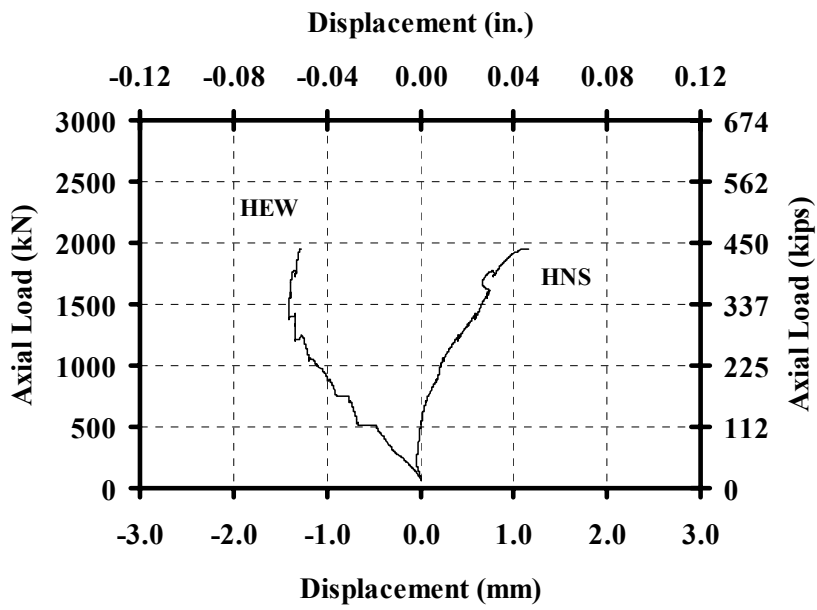


Figure B.20 Horizontal Displacements Measured at the Top End Block of Specimen P14

Appendix C Stress-Strain Models for Confined Concrete

Two analytical approaches for modeling the stress-strain curves for confined concrete were used in this study to evaluate the performance of the test specimens. Background information on each of the analytical models and the calculations needed to apply these models to the test specimens are presented in this appendix.

C.1 USE OF MODELS FOR CONFINED CONCRETE IN HOLLOW PIERS

Most of the experimental and analytical studies of confined concrete have considered the behavior of circular or square columns confined by spirals, circular hoops, or square hoops where the confinement provided by the transverse reinforcement is equal in the directions defined by the principal axes of the columns.

The analytical models proposed by Mander et al.(1988b) and Saatcioglu, M. and Razvi, S.R. (1992) address the possibility that the confinement stresses are unequal in perpendicular directions.

Neither of the research studies mentioned above considered confined concrete in rectangular, hollow concrete columns, or addressed the behavior of columns with such low amounts of transverse reinforcement. However, Mander et al. (1988a) tested columns with rectangular sections that were designed as models of the flange region of hollow columns.

Figure C.1 shows a typical cross-section of a pier tested in this investigation and the approximate location of the neutral axis, determined from

the observed crack patterns as presented in Chapter 5. The behavior of all five test specimens was similar. The south wall of each specimen exhibited cracks along its entire length, while the cracks in the west wall extended approximately two-thirds the length of the wall. The north and east walls were subjected to compressive stresses, but the south end of the east wall did crack near failure. Due to the nature of the applied load, all four walls were subjected to strain gradients along their lengths.

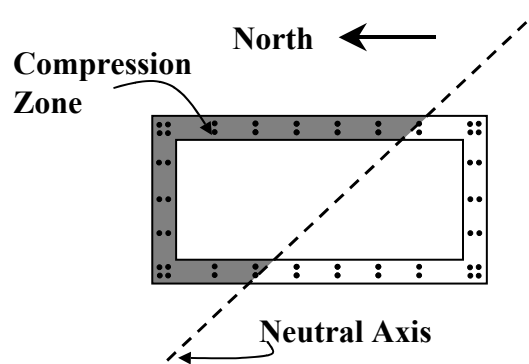


Figure C.1 Typical Location of the Neutral Axis of a Hollow Pier Tested in this Investigation

C.2 MANDER, PRIESTLEY AND PARK

Mander et al. (1988b) developed a unified stress-strain model for confined concrete in circular or rectangular sections under monotonic or cyclic loading. The confining reinforcement can be spirals, circular hoops, or rectangular hoops, with or without cross-ties. The confining stresses need not be equal along the axes of the column.

The analytical model was verified using the measured response of approximately 40 circular, square, and rectangular reinforced concrete columns subjected to uniaxial compression (1988a). These test specimens had volumetric ratios of transverse reinforcement between 0.006 and 0.079. The volumetric transverse reinforcement ratios in the rectangular columns ranged from 0.016 to 0.079, with an average of 0.047.

C.2.1 Analytical Model

The parameters used to define the stress-strain relationship for confined concrete developed by Mander et al. (1988b) are shown in Fig. C.2.

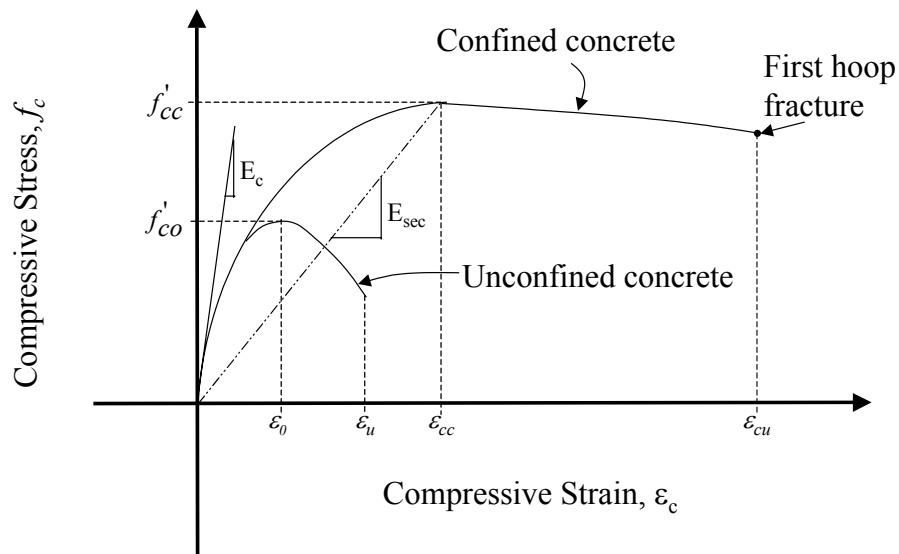


Figure C.2 Stress-Strain Model Proposed for Monotonic Loading of Confined and Unconfined Concrete (1988b)

The stress-strain curve is defined for axial strains from zero to the first hoop fracture using the following relationship:

$$f_c = \frac{f'_{cc} x^r}{r - 1 + x^r} \quad (C.1)$$

where f'_{cc} is the compressive strength of the confined concrete, which is determined using a graphical procedure, as discussed later. The term x is defined as:

$$x = \frac{\varepsilon_c}{\varepsilon_{cc}} \quad (C.2)$$

where ε_c is the compressive strain, and ε_{cc} is the strain corresponding to the maximum compressive strength of the confined concrete:

$$\varepsilon_{cc} = \varepsilon_0 \left[1 + 5 \left(\frac{f'_{cc}}{f'_{co}} - 1 \right) \right] \quad (C.3)$$

where f'_{co} and ε_0 are the maximum compressive strength and the corresponding strain of the unconfined concrete. Measured values of f'_{co} and ε_0 are reported in Appendix A for the specimens tested in this investigation. The remaining term, r , is defined as:

$$r = \frac{E_c}{E_c - E_{\text{sec}}} \quad (C.4)$$

where

$$E_c = 5000 \sqrt{f'_{co}} \text{ (MPa)} \quad (C.5a)$$

$$E_c = 60200 \sqrt{f'_{co}} \text{ (psi)} \quad (C.5b)$$

$$E_{\text{sec}} = \frac{f'_{cc}}{\varepsilon_{cc}} \quad (C.6)$$

The lateral confining stresses provided by the transverse reinforcement are defined as the total force in the transverse reinforcement divided by the vertical area of the confined concrete. These stresses may be expressed as:

$$f_{lx} = \frac{A_{sx}}{sd_c} f_{yh} = \rho_x f_{yh} \quad (C.7)$$

$$f_{ly} = \frac{A_{sy}}{sb_c} f_{yh} = \rho_y f_{yh} \quad (C.8)$$

where f_{yh} is the yield stress of the transverse reinforcement; A_{sx} is the total area of transverse reinforcement that is positioned parallel to the x axis; A_{sy} is the total area of transverse reinforcement that is positioned parallel to the y axis; ρ_x and ρ_y are the transverse reinforcement ratios parallel to the x and y directions, respectively; s is the vertical spacing of the transverse reinforcement; and b_c and d_c are the core dimensions (measured center to center of the hoops) parallel to the x and y directions, respectively (Fig. C.3).

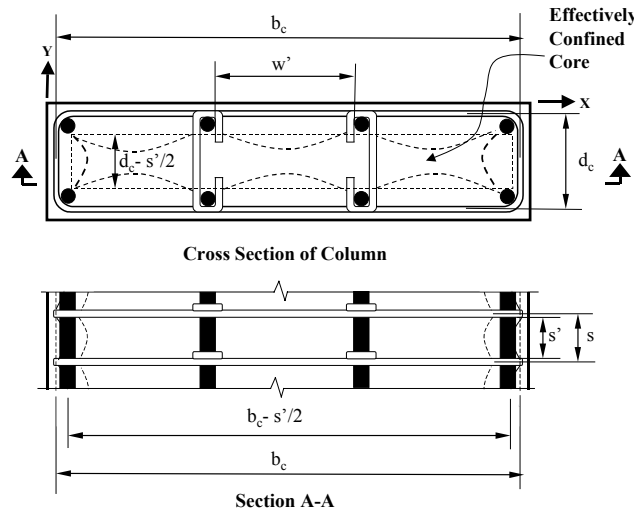


Figure C.3 Effectively Confined Core for Rectangular Hoop Reinforcement (1988b)

The effective transverse confining stress depends on the spacing of the longitudinal and transverse reinforcement in each direction and is defined as:

$$f'_{lx} = k_e f_{lx} \quad (C.9)$$

$$f'_{ly} = k_e f_{ly} \quad (C.10)$$

where k_e is the confinement effectiveness coefficient for rectangular hoops.

$$k_e = \frac{\left(1 - \sum_{i=1}^n \frac{(w'_i)^2}{6b_c d_c}\right) \left(1 - \frac{s'}{2b_c}\right) \left(1 - \frac{s'}{2d_c}\right)}{(1 - \rho_{cc})} \quad (C.11)$$

The term w'_i is the clear distance between adjacent longitudinal bars; s' is the vertical clear spacing between hoops (Fig. C.3); and ρ_{cc} is the ratio of the area of longitudinal steel to the area of the confined core ($b_c * d_c$).

The ratio of confined compressive strength to unconfined compressive strength can be determined from a chart for rectangular cross-sections provided by Mander et al.⁽³⁵⁾ The chart represents the solution of a five-parameter, multiaxial failure surface developed by Willam and Warnke (1975).

The ultimate concrete compression strain, ε_{cu} , is defined as the longitudinal strain at which the first hoop fractures, and is determined using an energy approach. The additional strain energy of confined concrete is assumed to be provided by the energy stored in the transverse reinforcement. This hypothesis leads to the following expression for energy balance within the cross-section:

$$U_{sh} = U_{cc} + U_{sc} - U_{co} \quad (C.12)$$

where U_{sh} is the strain energy capacity of the transverse reinforcement per unit volume of concrete core; U_{cc} and U_{co} are the strain energy capacities per unit volume of the confined and unconfined concrete, respectively; and U_{sc} is the energy stored in the longitudinal steel in compression. Equation C.12 can be rewritten as

$$\rho_s A_{cc} \int_0^{\varepsilon_{sf}} f_s d\varepsilon_s = A_{cc} \int_0^{\varepsilon_{cu}} f_c d\varepsilon_c + \rho_{cc} A_{cc} \int_0^{\varepsilon_{cu}} f_{sl} d\varepsilon_c - A_{cc} \int_0^{\varepsilon_u} f_c d\varepsilon_c \quad (C.13)$$

where ρ_s is the volumetric ratio of transverse reinforcement to concrete core; A_{cc} is the area of the concrete core; f_s and ε_s are the stress and strain in the transverse reinforcement, ε_{sf} is the fracture strain of the transverse reinforcement; f_c and ε_c are the compressive stress and strain of the concrete; ε_{cu} is the ultimate concrete compressive strain of the confined concrete; f_{sl} is the stress in the longitudinal reinforcement; and ε_u is the ultimate strain of the unconfined concrete.

Results from tests by Mander et al. (1984) on reinforcing bars of various diameters and grades indicated that the integral used to define U_{sh} may be assumed to be

$$\int_0^{\varepsilon_{sf}} f_s d\varepsilon_s = 110\rho_s (\text{MJ/m}^3) \quad (\text{C.14a})$$

$$\int_0^{\varepsilon_{sf}} f_s d\varepsilon_s = 29\rho_s (\text{in-kip/in}^3) \quad (\text{C.14b})$$

Using for the unconfined concrete a parabolic relationship based in principles originally proposed by Hognestad, and assuming that the strain capacity of unconfined concrete, ε_u , is equal to 0.0038, and the peak stress is equal to the measured cylinder strength, the integral of U_{co} becomes approximately

$$\int_0^{\varepsilon_u} f_c d\varepsilon_c = 0.003 f_c' (\text{MJ/m}^3) \quad (\text{C.15a})$$

$$\int_0^{\varepsilon_u} f_c d\varepsilon_c = 0.003 f_c' (\text{in-kip/in}^3) \quad (\text{C.15b})$$

with f_c' in MPa (ksi). Equation C.15 was calculated assuming a strain at the peak stress equal to 0.002. If the strain energy of unconfined concrete with the strain at peak stress between 0.0018 and 0.0022 is calculated using Eq. C.15, the error in the estimate of U_{co} is less than 2%.

Knowing the stress in the confined concrete from Eq. C.1 and f_{sl} from the stress-strain relationship for the longitudinal reinforcement (Appendix A) the limiting compressive strain, ϵ_{cu} , of the concrete can be determined.

C.2.2 Application of Model to Hollow Piers

In order to apply the analytical model developed by Mander et al. (1988b) to the hollow piers, the cross-section was divided into two areas, based on the amount of transverse reinforcement: the corners and the clear span of the walls. Distinct confinement was provided in each area. The corners were square and were heavily confined by hairpins in both directions (Fig 4.8). The vertical spacing of the hairpins was the same as that of the transverse reinforcement.

The confining reinforcement in the walls consisted of the legs of the U-shaped bars along the length and cross-ties through the thickness of the walls (Fig. 4.2). Because the cross-ties were distributed in a checkerboard pattern, the vertical spacing s' in Eq. C.11 (Fig. C.3) had to be adjusted.

Arching action is shown as second-degree parabolas with an initial slope of 45° in Fig C.4. It was assumed that arching action occurred between layers of cross-ties, over a length of two times the spacing of the transverse reinforcement. Therefore, the minimum effective area occurred midway between the levels of transverse reinforcement, and the thickness of the effectively confined core was reduced to $d_c - 1.5 s'/2$.

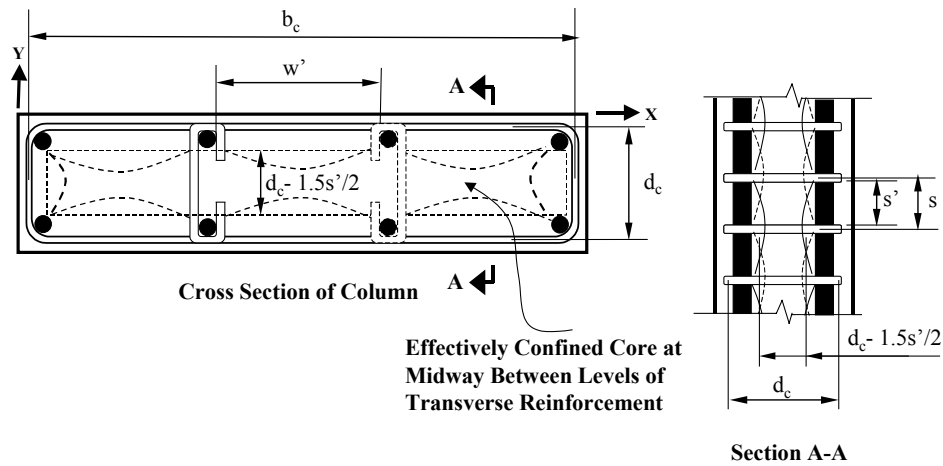


Figure C.4 Effectively Confined Core for Rectangular Reinforcement and Checkerboard Distribution of Cross-Ties

Table C.1 summarizes the cross-sectional dimensions used to calculate the effective confining stresses and the strength of the confined concrete in the east walls. The value of w'_i shown corresponds to the average value in each wall, but the actual spacing of the longitudinal bars, taken from Fig. 4.3 through 4.7, were used in Eq. C.11. The direction x and y and the core dimensions are shown in Fig. C.5. The confinement effectiveness coefficients, k_e , listed in Table C.1, had very low values. The coefficients calculated for Specimens P10, P12, and P14 were negative, meaning that the reductions in effective core area due to the arching action were larger than the area of the confined core. In those cases the coefficients were reported as 0.00.

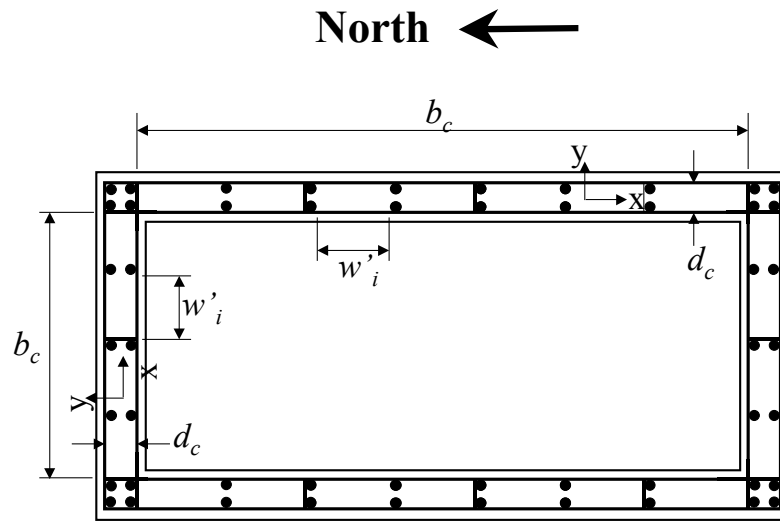


Figure C.5 Definition of Core Dimensions and X and Y Directions for East and North Walls

Table C.1 Dimensions Used to Calculate the Strength of the Confined Concrete in the East Walls

Spec. ID	Vertical Spacing of Confining Reinf.		Average Clear Spacing of Long. Bars	Concrete Core Dimensions		Transverse Reinforcement Ratios		Confinement Effectiveness Coefficient k_e
	s mm (in.)	s' mm (in.)	w'_i mm (in.)	b_c mm (in.)	d_c mm (in.)	ρ_x	ρ_y	
P6	64 (2.50)	60 (2.37)	51 (2.00)	638 (25.12)	73 (2.89)	0.0040	0.0014	0.31
P8	64 (2.50)	60 (2.37)	70 (2.75)	676 (26.62)	54 (2.14)	0.0054	0.0011	0.10
P10	64 (2.50)	60 (2.37)	83 (3.25)	702 (27.62)	42 (1.64)	0.0070	0.0008	0.00
P12	64 (2.50)	60 (2.37)	76 (3.00)	727 (28.62)	29 (1.14)	0.0101	0.0010	0.00
P14	51 (2.00)	47 (1.87)	70 (2.75)	733 (28.87)	29 (1.14)	0.0126	0.0012	0.00

Table C.2 summarizes the cross-sectional dimensions for the north walls, as defined in Fig. C.5. The confinement effectiveness coefficients obtained were almost equal to the ones calculated for the east walls.

Table C.2 Dimensions Used to Calculate the Strength of the Confined Concrete in the North Walls

Spec. ID	Vertical Spacing of Confining Reinf.		Average Clear Spacing of Long. Bars	Concrete Core Dimensions		Transverse Reinforcement Ratios		Confinement Effectiveness Coefficient k_e
	s mm (in.)	s' mm (in.)	w' mm (in.)	b_c mm (in.)	d_c mm (in.)	ρ_x	ρ_y	
P6	64 (2.50)	60 (2.37)	51 (2.00)	232 (9.12)	73 (2.89)	0.0040	0.0013	0.31
P8	64 (2.50)	60 (2.37)	70 (2.75)	270 (10.62)	54 (2.14)	0.0054	0.0011	0.11
P10	64 (2.50)	60 (2.37)	83 (3.25)	295 (11.62)	42 (1.64)	0.0070	0.0010	0.00
P12	64 (2.50)	60 (2.37)	76 (3.00)	321 (12.62)	29 (1.14)	0.0101	0.0009	0.00
P14	51 (2.00)	47 (1.87)	70 (2.75)	327 (12.87)	29 (1.14)	0.0126	0.0017	0.00

Table C.3 summarizes the cross-sectional dimensions used to calculate the effective confining stresses and the strength of the confined concrete in the northeast corner of the piers. The corners were square because all the walls of the piers had the same thickness. Therefore, the reinforcement ratios and the core dimensions were the same in both directions. Also, the concrete on the sides of the corners continuous with the walls was considered to be effectively confined along the length between adjacent transverse reinforcing bars.

Comparing the values of the confinement effectiveness coefficient from Tables C.1, C.2, and C.3, the confining reinforcement was more effective at the corners of the piers than along the walls.

Table C.4 summarizes the calculated effective lateral confining stresses in each direction and the ratios of the confined to the unconfined concrete strength. Because the vertical spacing of the confining reinforcement was the same in Specimens P6, P8, P10, and P12, the ratios of confined to unconfined compressive strength decreased as the core dimensions decreased. In the case of Specimen P14, the ratio of confined to unconfined compressive strength was larger than for Specimen P12 because the vertical spacing of the confinement reinforcement was less. As expected, the ratios of confined to unconfined compressive strength of the concrete are larger at the corners than at the walls.

Table C.3 Dimensions Used to Calculate the Strength of the Confined Concrete in the Northeast Corners of the Piers

Spec. ID	Vertical Spacing of Confining Reinf.		Clear Spacing of Long. Bars	Concrete Core Dimensions		Transverse Reinforcement Ratios		Confinement Effectiveness Coefficient k_e
	s mm (in.)	s' mm (in.)	w' mm (in.)	b_c mm (in.)	d_c mm (in.)	ρ_x	ρ_y	
P6	64 (2.50)	60 (2.37)	57 (2.25)	73 (2.89)	73 (2.89)	0.0050	0.0050	0.53
P8	64 (2.50)	60 (2.37)	38 (1.50)	54 (2.14)	54 (2.14)	0.0067	0.0067	0.48
P10	64 (2.50)	60 (2.37)	25 (1.00)	42 (1.64)	42 (1.64)	0.0088	0.0088	0.41
P12	64 (2.50)	60 (2.37)	13 (0.50)	29 (1.14)	29 (1.14)	0.0126	0.0126	0.35
P14	51 (2.00)	47 (1.87)	13 (0.50)	29 (1.14)	29 (1.14)	0.0158	0.0158	0.45

Table C.4 Confining Stresses and Ratios of Unconfined to Confined Compressive Strength of Concrete Calculated Using Models Developed by Mander et al. (1988b)

Spec. ID	North and East Walls			Northeast Corner		
	Effective Lateral Confining Stresses		Ratios of Confined to Unconfined Compressive Strength of Concrete	Effective Lateral Confining Stresses		Ratios of Confined to Unconfined Compressive Strength of Concrete
	f_{xl} MPa (psi)	f_{yl} MPa (psi)		f_{xl} MPa (psi)	f_{yl} MPa (psi)	
P6	0.73 (106)	0.25 (36)	1.10	1.58 (229)	1.58 (229)	1.35
P8	0.33 (48)	0.07 (10)	1.05	1.92 (278)	1.92 (278)	1.42
P10	0.00 (0)	0.00 (0)	1.00	2.16 (313)	2.16 (313)	1.38
P12	0.00 (0)	0.00 (0)	1.00	2.96 (429)	2.96 (429)	1.44
P14	0.00 (0)	0.00 (0)	1.00	4.22 (612)	4.22 (612)	1.55

Using this model, only Specimens P6 and P8 experienced an increase in the concrete compressive strength due to confinement along the north and east walls. The reduction in the effective area was larger than the core thickness in the other piers, demonstrating the importance of the ratio of the longitudinal spacing of the transverse reinforcement, s , to the core thickness.

The calculated strains at the peak stress in the confined concrete and the coefficient r are summarized in Table C.5. As expected, the strains calculated at the northeast corners were larger than the strains along the walls.

The slope of the descending branch of the stress-strain curve is given by

$$\frac{\partial f_c}{\partial \varepsilon_c} = E_{\text{sec}} \frac{r(r-1)(1-x^r)}{(r-1+x^r)^2} \quad (\text{C.16})$$

Table C.5 Strains and Coefficients Used to Define the Stress-Strain Relationship of Confined Concrete Using the Model Developed by Mander et al. (1988b)

Spec. ID	North and East Walls		Northeast Corner	
	Ratio r	Strain at Peak Stress ϵ_{cc}	Ratio r	Strain at Peak Stress ϵ_{cc}
P6	1.53	0.0033	1.30	0.0061
P8	1.79	0.0025	1.32	0.0062
P10	2.47	0.0020	1.40	0.0058
P12	2.42	0.0022	1.36	0.0070
P14	2.48	0.0022	1.33	0.0083

The descending branch defines the stress-strain relationship for values of strain larger than ϵ_{cc} . Therefore, larger values of r lead to a steeper descending branch of the stress-strain curves. In all cases, the calculated values of r were smaller in the corners than along the walls; therefore, the stress-strain curves that were computed for the confined concrete at the corners had more strain capacity than the confined concrete along the walls.

The limiting compressive strains in the confined concrete in the northeast corners are listed in Table C.6. The limiting strains are large, on the order of ten times the limiting strain of the unconfined concrete.

Table C.6 Limiting Compressive Strain in the Confined Concrete in the Corners of the Test Specimens Calculated Using the Material Model Developed by Mander et al. (1988b)

Specimen ID	Ultimate Compressive Strain
P6	0.027
P8	0.028
P10	0.026
P12	0.028
P14	0.027

C.3 SAATCIOGLU, M. AND RAZVI, S.R.

Saatcioglu, M. and Razvi, S.R. (1992) also developed an analytical model to represent the stress-strain relationship for confined concrete. The model represents the response of concrete subjected to axial stress with a strain gradient, loaded monotonically to failure. The confining stresses provided by the transverse reinforcement need not be equal along the principal axes of the column.

The analytical model was verified using the results from tests of approximately 85 circular (Mander et al. 1988a), square (Sheikh and Uzumeri 1980, Scott et al. 1982, Razvi an Saatcioglu 1989, and Abdulkadir and Saatcioglu 1991), and rectangular (Mander et al. 1988a) reinforced concrete columns. The columns had different configurations of transverse reinforcement, including circular hoops, spirals, square hoops and rectangular hoops. Welded wire fabric was used as the transverse reinforcement in some of the tests.

The test specimens used to verify the analytical model had volumetric transverse reinforcement ratios between 0.006 and 0.079. The volumetric transverse reinforcement ratios in the rectangular columns ranged from 0.016 to 0.079, with average of 0.047.

C.3.1 Analytical Model

The parameters used to define the stress-strain relationship for confined concrete are shown in Fig. C.6. The compressive strength of the confined concrete, f'_{cc} , is given by

$$f'_{cc} = f'_{co} + k_1 f_{le} \quad (C.17)$$

where f'_{co} is the unconfined compressive strength and f_{le} is the equivalent uniform confining pressure. The coefficient k_1 is given by

$$k_1 = 6.7(f_{le})^{-0.17} \quad (f_{le} \text{ in MPa}) \quad (C.18a)$$

$$k_1 = 15.6(f_{le})^{-0.17} \quad (f_{le} \text{ in psi}) \quad (C.18b)$$

The ascending branch of the stress-strain relationship of the confined concrete is given by

$$f_c = f'_{cc} \left[2 \left(\frac{\varepsilon_c}{\varepsilon_{cc}} \right) - \left(\frac{\varepsilon_c}{\varepsilon_{cc}} \right)^2 \right]^{1/(1+2K)} \leq f'_{cc} \quad (C.19)$$

where ε_c is the compressive strain in the concrete, f'_{cc} is the compressive strength of the confined concrete, and ε_{cc} is the corresponding strain in the confined concrete. The parameter K is defined as:

$$K = \frac{k_1 f_{le}}{f'_{co}} \quad (C.20)$$

The equivalent uniform confining pressure is calculated as a weighted average of the equivalent uniform confining pressures in the two directions

$$f_{le} = \frac{f_{ley}b_c + f_{lex}d_c}{b_c + d_c} \quad (C.21)$$

where f_{lex} and f_{ley} are the equivalent uniform confining pressures acting in the x and y directions, respectively. The terms b_c and d_c are the dimensions of the confined core, as defined in Fig. C.7. The equivalent uniform confining pressures, f_{lex} and f_{ley} , are calculated from the average lateral pressures, f_{lx} and f_{ly} :

$$f_{lex} = k_{2x}f_{lx} \quad (C.22)$$

$$f_{ley} = k_{2y}f_{ly} \quad (C.23)$$

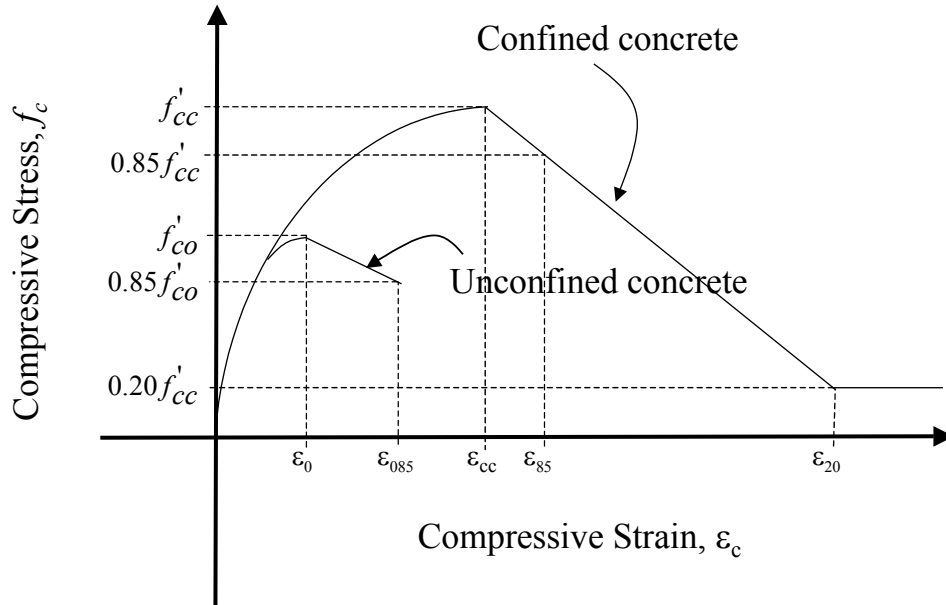


Figure C.6 Stress-Strain Model Proposed for Monotonic Loading of Confined and Unconfined Concrete (Saatcioglu, M. and Razvi, S. R. 1992)

The average lateral pressures are related to the amount of transverse reinforcement:

$$f_{lx} = \frac{\sum A_{sx}f_{yh}}{sd_c} = \rho_x f_{yh} \quad (C.24)$$

$$f_{ly} = \frac{\sum A_{sy} f_{yh}}{sb_c} = \rho_y f_{yh} \quad (\text{C.25})$$

The efficiency factors, k_{2x} and k_{2y} , are given by:

$$k_{2x} = 0.26 \sqrt{\left(\frac{d_c}{s}\right) \left(\frac{d_c}{s_{ly}}\right) \left(\frac{1}{f_{lx}}\right)} \leq 1.0 \quad (f_{lx} \text{ in MPa}) \quad (\text{C.26a})$$

$$k_{2x} = 3.13 \sqrt{\left(\frac{d_c}{s}\right) \left(\frac{d_c}{s_{ly}}\right) \left(\frac{1}{f_{lx}}\right)} \leq 1.0 \quad (f_{lx} \text{ in psi}) \quad (\text{C.26b})$$

$$k_{2y} = 0.26 \sqrt{\left(\frac{b_c}{s}\right) \left(\frac{b_c}{s_{lx}}\right) \left(\frac{1}{f_{ly}}\right)} \leq 1.0 \quad (f_{ly} \text{ in MPa}) \quad (\text{C.27a})$$

$$k_{2y} = 3.13 \sqrt{\left(\frac{b_c}{s}\right) \left(\frac{b_c}{s_{lx}}\right) \left(\frac{1}{f_{ly}}\right)} \leq 1.0 \quad (f_{ly} \text{ in psi}) \quad (\text{C.27b})$$

where s is the vertical spacing of the transverse reinforcement and s_{lx} and s_{ly} are the horizontal spacing of laterally supported longitudinal reinforcement measured parallel to the x and y directions, respectively (Fig. C.7).

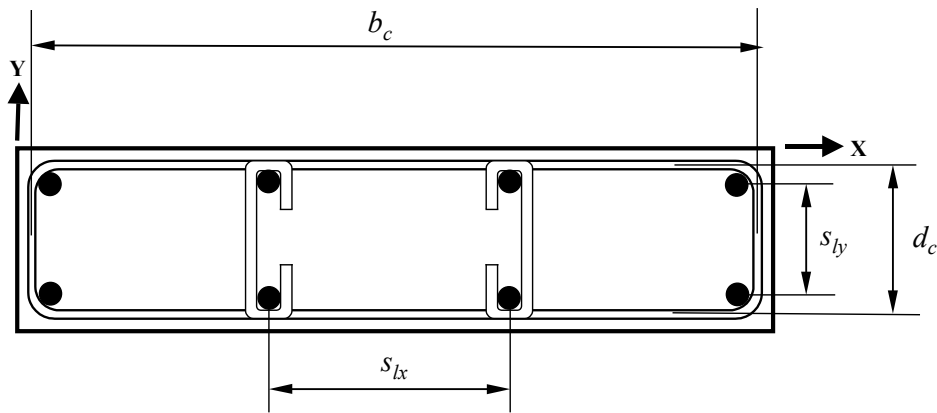


Figure C.7 Effectively Confined Core for Rectangular Hoop Reinforcement (Saatcioglu, M. and Razvi, S. R. 1992)

Three strain levels, ε_{cc} , ε_{85} , and ε_{20} , are used to define the descending branch of the stress-strain relationship for confined concrete (Fig. C.6). The strain at the maximum confined stress, ε_{cc} , is defined as:

$$\varepsilon_{cc} = \varepsilon_0(1 + 5K) \quad (C.28)$$

where ε_0 is the strain at the maximum stress in the unconfined concrete and K was defined in Eq. C.20. The strain corresponding at 85% of the maximum confined stress, ε_{85} , is defined as:

$$\varepsilon_{85} = 260\rho\varepsilon_{cc} + \varepsilon_{085} \quad (C.29)$$

where ε_{085} is the corresponding strain in unconfined concrete and ρ is a weighted average of the transverse reinforcement ratios:

$$\rho = \frac{\rho_y b_c + \rho_x d_c}{b_c + d_c} \quad (C.30)$$

The strain at 20% of the maximum confined stress, ε_{20} , is calculated by assuming that the descending branch of the stress-strain relationship is linear.

The model does not address the ultimate compressive strain of the confined concrete.

C.3.2 Application of Model to Hollow Piers

As in applying of the model of Mander et al. (1988b), the piers were divided into two parts: the corners and the unsupported lengths of the walls. Figure C.8 shows the core dimensions and the direction of the axes used in the east and north walls. The dimensions of the corners are not shown because they were square, and therefore, the dimensions were the same in both directions.

Tables C.7, C.8, and C.9 summarize the cross-sectional dimensions used to calculate the effective confining pressure and the strength of the confined

concrete in the east and north walls and in the northeast corners, respectively. The checkerboard distribution of the cross-ties was introduced in the model by taking the horizontal spacing of laterally supported longitudinal bars, s_{lx} and s_{ly} , as the separation between laterally supported bars that occurred most often in each wall, and using as s the vertical separation between transverse reinforcement (see Fig. 4.3 through 4.7 for the values of the transverse spacing of the longitudinal bars).

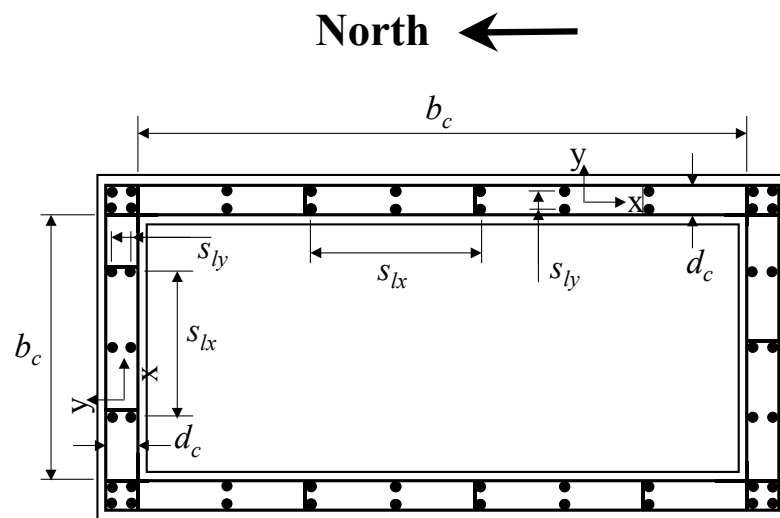


Figure C.8 Definition of Core Dimensions and X and Y Directions for East and North Walls

Except for Specimen P14, the confinement pressures along the north and east walls were similar. Specimen P14 had a confinement pressure in the direction of the thickness of the walls (f_{ly}) that was larger in the north wall than in the east wall by approximately 35%. This condition occurred because Specimen P14 had one more cross-tie at each level of transverse reinforcement along the north wall than the other specimens.

Table C.7 Dimensions Used to Calculate the Strength of the Confined Concrete in the East Walls

Spec. ID	Vertical Spacing of Confining Reinf.	Spacing of Supported Longitudinal Bars		Concrete Core Dimensions		Transverse Reinforcement Ratios		Confinement Pressure	
	<i>s</i> mm (in.)	<i>s_{lx}</i> mm (in.)	<i>s_{ly}</i> mm (in.)	<i>b_c</i> mm (in.)	<i>d_c</i> mm (in.)	ρ_x	ρ_y	<i>f_{lx}</i> MPa (psi)	<i>f_{ly}</i> MPa (psi)
P6	64 (2.50)	114 (4.50)	64 (2.50)	638 (25.12)	73 (2.89)	0.0040	0.0014	2.38 (345)	0.82 (119)
P8	64 (2.50)	152 (6.00)	57 (2.25)	676 (26.62)	54 (2.14)	0.0054	0.0011	3.22 (467)	0.65 (94)
P10	64 (2.50)	178 (7.00)	32 (1.25)	702 (27.62)	42 (1.64)	0.0070	0.0008	4.20 (609)	0.50 (72)
P12	64 (2.50)	165 (6.50)	19 (0.75)	727 (28.62)	29 (1.14)	0.0101	0.0010	6.05 (878)	0.60 (87)
P14	51 (2.00)	152 (6.00)	19 (0.75)	733 (28.87)	29 (1.14)	0.0126	0.0012	7.56 (1097)	0.74 (108)

Table C.8 Dimensions Used to Calculate the Strength of the Confined Concrete in the North Walls

Spec. ID	Vertical Spacing of Confining Reinf.	Spacing of Supported Longitudinal Bars		Concrete Core Dimensions		Transverse Reinforcement Ratios		Confinement Pressure	
	<i>s</i> mm (in.)	<i>s_{lx}</i> mm (in.)	<i>s_{ly}</i> mm (in.)	<i>b_c</i> mm (in.)	<i>d_c</i> mm (in.)	ρ_x	ρ_y	<i>f_{lx}</i> MPa (psi)	<i>f_{ly}</i> MPa (psi)
P6	64 (2.50)	232 (9.12)	64 (2.50)	232 (9.12)	73 (2.89)	0.0040	0.0013	2.38 (345)	0.75 (109)
P8	64 (2.50)	270 (10.62)	57 (2.25)	270 (10.62)	54 (2.14)	0.0054	0.0011	3.22 (467)	0.65 (94)
P10	64 (2.50)	295 (11.62)	32 (1.25)	295 (11.62)	42 (1.64)	0.0070	0.0010	4.20 (609)	0.59 (86)
P12	64 (2.50)	321 (12.62)	19 (0.75)	321 (12.62)	29 (1.14)	0.0101	0.0009	6.05 (878)	0.54 (79)
P14	51 (2.00)	327 (12.87)	19 (0.75)	327 (12.87)	29 (1.14)	0.0126	0.0017	7.56 (1097)	1.00 (145)

Table C.9 Dimensions Used to Calculate the Strength of the Confined Concrete in the Northeast Corners of the Piers

Spec. ID	Vertical Spacing of Confining Reinf.	Spacing of Supported Longitudinal Bars		Concrete Core Dimensions		Transverse Reinforcement Ratios		Confinement Pressure	
	<i>s</i> mm (in.)	<i>s_{lx}</i> mm (in.)	<i>s_{ly}</i> mm (in.)	<i>b_c</i> mm (in.)	<i>d_c</i> mm (in.)	ρ_x	ρ_y	<i>f_{lx}</i> MPa (psi)	<i>f_{ly}</i> MPa (psi)
P6	64 (2.50)	64 (2.50)	64 (2.50)	73 (2.89)	73 (2.89)	0.0050	0.0050	2.98 (432)	2.98 (432)
P8	64 (2.50)	57 (2.25)	57 (2.25)	54 (2.14)	54 (2.14)	0.0067	0.0067	4.02 (583)	4.02 (583)
P10	64 (2.50)	32 (1.25)	32 (1.25)	42 (1.64)	42 (1.64)	0.0088	0.0088	5.25 (762)	5.25 (762)
P12	64 (2.50)	19 (0.75)	19 (0.75)	29 (1.14)	29 (1.14)	0.0126	0.0126	8.41 (1219)	8.41 (1219)
P14	51 (2.00)	19 (0.75)	19 (0.75)	29 (1.14)	29 (1.14)	0.0158	0.0158	9.46 (1371)	9.46 (1371)

The confinement pressures calculated in the northeast corners were larger than the confinement pressures calculated along the walls, due to the larger reinforcement ratio in the corners. The reinforcement in the corners consisted of one “U” shaped transverse bar and one hairpin in each direction (Fig. 4.2 and 4.8). Also, the core dimensions were small, which produced a large confining reinforcement ratio.

Table C.10 summarizes the calculated equivalent lateral pressures and the ratios of confined to unconfined concrete compressive strength. In general, the ratios of confined to unconfined concrete compressive strength decreased as the wall thickness decreased. The ratios were slightly higher for Specimen P14 than

Specimen P12 because the vertical spacing of the confining reinforcement was smaller than for the former.

Table C.10 Confining Stresses and Ratios of Unconfined to Confined Compressive Strength of Concrete Calculated Using Models Developed by Saatcioglu, M. and Razvi, S.R. (1992)

Spec. ID	East Walls		North Walls		Northeast Corner	
	Equivalent Lateral Pressure	Ratios of Confined to Unconfined	Equivalent Lateral Pressure	Ratios of Confined to Unconfined	Equivalent Lateral Pressure	Ratios of Confined to Unconfined
	f_{le} MPa (psi)	Compressive Strength of Concrete	f_{le} MPa (psi)	Compressive Strength of Concrete	f_{le} MPa (psi)	Compressive Strength of Concrete
P6	0.78 (114)	1.20	0.57 (82)	1.15	0.52 (75)	1.14
P8	0.63 (92)	1.17	0.58 (84)	1.15	0.53 (77)	1.14
P10	0.50 (72)	1.11	0.57 (82)	1.12	0.55 (80)	1.12
P12	0.60 (87)	1.11	0.54 (79)	1.10	0.66 (95)	1.11
P14	0.74 (107)	1.12	0.97 (141)	1.15	0.74 (107)	1.12

Unlike the model proposed by Mander et al. (1988b), the ratios of confined to unconfined compressive strength were nearly the same for all sections of each pier. Specimen P6 was the only exception. The calculated maximum confined compressive strength was larger in the east wall than the north wall. While both walls had approximately the same confinement pressures, the core dimension b_c was larger in the east wall, and the reduction coefficients, k_{2x} and k_{2y} , used to calculate the equivalent lateral pressure, are proportional to the core dimensions.

The strains at peak stress and the strains in the descending branch of the stress-strain curves of the confined concrete stress-strain relationships are presented in Tables C.11 and C.12.

Table C.11 Strains used to Define the stress-Strain Relationship of the Confined Concrete along the East and North Walls Using the Model Developed by Saatcioglu, M. and Razvi, S.R. (1992)

Spec. ID	East Walls			North Walls		
	Strain at Peak Stress ϵ_{cc}	Strain at 85% of Peak Stress in Descending Branch ϵ_{85}	Strain at 20% of Peak Stress in Descending Branch ϵ_{20}	Strain at Peak Stress ϵ_{cc}	Strain at 85% of Peak Stress in Descending Branch ϵ_{85}	Strain at 20% of Peak Stress in Descending Branch ϵ_{20}
P6	0.0044	0.0057	0.0111	0.0039	0.0057	0.0137
P8	0.0037	0.0051	0.0115	0.0035	0.0055	0.0137
P10	0.0031	0.0047	0.0120	0.0032	0.0052	0.0141
P12	0.0034	0.0050	0.0120	0.0033	0.0052	0.0136
P14	0.0035	0.0053	0.0131	0.0039	0.0064	0.0172

The strains at peak stress are almost the same for the walls and the northeast corners. The differences occurred in the descending branches of the curves. The strains at 85% and 20% of the peak stress are between 85 and 700% larger in the concrete in the corners than along the walls. The resulting stress-strain relationships in the corners had a more gradual descending branch than the stress-strain relationships along the walls. The larger strains in the northeast corners were calculated using Eq. C.29, which makes the strain at 85% of the peak stress proportional to the ratio of confining reinforcement.

Table C.12 Strains used to Define the Stress-Strain Relationship of the Confined Concrete in the Northeast Corners Using the Model Developed by Saatcioglu, M. and Razvi, S.R. (1992)

Spec. ID	Northeast Corner		
	Strain at Peak Stress ϵ_{cc}	Strain at 85% of Peak Stress in Descending Branch ϵ_{85}	Strain at 20% of Peak Stress in Descending Branch ϵ_{20}
	P6	0.0038	0.0087
P8	0.0034	0.0098	0.0373
P10	0.0032	0.0110	0.0449
P12	0.0035	0.0164	0.0725
P14	0.0035	0.0183	0.0824

The following expression, suggested by Kaar et al. (1978) was used to calculate the limiting compressive strain of the confined concrete:

$$\epsilon_{cu} = 0.003 + \left(\frac{\rho_s f_{yh}}{K}\right)^2 \quad (C.31)$$

where ρ_s is the volumetric ratio of the confinement reinforcement, f_{yh} is the yield stress of the transverse reinforcement in MPa, and K is 100 ($K=15$ for f_{yh} in ksi). Expression C.31 is a lower bound for limiting compressive strains measured on tests of C-shaped reinforced concrete specimens loaded under simultaneous axial load and uniaxial bending.

The calculated values of limiting compressive strains are shown in Table C.13. The values of maximum strain varied widely from 0.004 to 0.036,

increasing as the confinement ratios increased. As expected, the limiting compressive strains in the corners were larger than the strains in the walls.

Table C.13 Limiting Compressive Strain of Confined Concrete of Specimens Calculated Using the Model Developed by Kaar et al. (1978)

Specimen ID	Limiting Compressive Strain	
	East and North Walls	Northeast Corner
P6	0.0039	0.0063
P8	0.0044	0.0090
P10	0.0051	0.0133
P12	0.0071	0.0294
P14	0.0099	0.0364

C.4 COMPARISON OF MODELS FOR STRESS-STRAIN RELATIONSHIPS OF CONFINED CONCRETE

In the following discussion, the material model developed by Mander et al. (1988b) will be called Model M, and the material model developed by Saatcioglu, M. and Razvi, S.R. (1992) will be called Model S.

The same general trend of the ratios of confined to unconfined concrete compressive strength was observed for both models: the ratios of confined to unconfined strength decreased as the wall slenderness ratios increased.

The increase in the compressive strengths of the confined concrete along the length of the north and east walls were larger using Model S than Model M. The calculated confined concrete strengths in the northeast corners were smaller using Model S than Model M.

The biggest difference between the two material models was the relative strength of the confined concrete along the walls and in the corners. Using Model M, the maximum confined compressive strengths were larger in the corners than along the walls. This was because the confinement-effectiveness coefficients (Eq. C.9, C.10, and C.11) were very sensitive to the transverse spacing of the longitudinal bars, w' , especially for thin cross-sections. Because the thickness of the walls was similar or smaller than the distance between the longitudinal bars, the confinement effectiveness coefficients rapidly tended to zero. In the corners the core dimensions were larger than the spacing of the longitudinal bars, resulting in larger coefficients.

Using Model S, the maximum confined concrete compressive strengths occurred along the walls for Specimens P6 and P8, and were essentially the same along the walls and in the corners for the other three piers. The coefficients k_{2x} and k_{2y} , used to calculate the effective lateral pressures, were proportional to the core dimensions (which were larger in the walls than in the corners (see Tables C.7, C.8, and C.9)) and inversely proportional to the average lateral pressures f_l (Eq. C.26 and C.27), resulting in larger coefficients k_2 in the walls than in the corners.

Figures C.9 through C.13 show the calculated stress-strain relationships for the concrete used for unconfined concrete, and material Models M and S (Eq. C.1 and C.15) for confined concrete. The unconfined strengths are reported in Appendix A. The stress-strain curves were plotted up to a strain equal to 0.014 to show their shape.

Both material models produced similar stress-strain relationships for the test specimens. The descending branches of the stress-strain relationships tended to be steeper along the walls than in the corners, because the walls had smaller confining ratios.

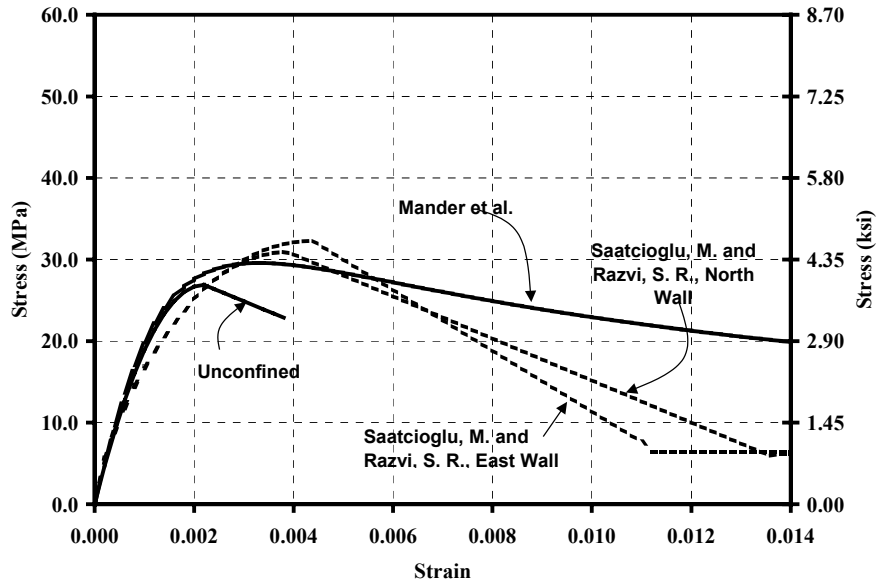
Table C.14 lists the volumetric transverse reinforcement ratios, ρ_s , for the north wall, east wall, and northeast corner. The volumetric ratios along the walls were smaller than the volumetric ratios in the rectangular columns tested by Mander et al. (1988a), and were close to the smallest volumetric ratios in the columns used to verify both material models. On the other hand, the volumetric transverse reinforcement ratios in the corners of Specimens P10, P12, and P14 were within the range of volumetric ratios of the rectangular columns tested, but at the lower end of the range. The volumetric ratios of Specimens P6 and P8 were slightly smaller, but within the range of all the volumetric ratios studied by Mander et al. (1988b) and Saatcioglu, M. and Razvi, S.R. (1992).

In summary, the piers tested had small amount of confinement, but within the range of data used to validate the material models.

Table C.14 Volumetric Ratio of the Transverse Confinement Reinforcement

Specimen ID	Volumetric Ratios of Transverse Reinforcement, ρ_s		
	North Walls	East Walls	Northeast Corners
P6	0.0052	0.0053	0.0099
P8	0.0064	0.0064	0.0134
P10	0.0080	0.0078	0.0175
P12	0.0110	0.0111	0.0280
P14	0.0143	0.0139	0.0315

(a) East and North Walls



(b) Northeast Corner

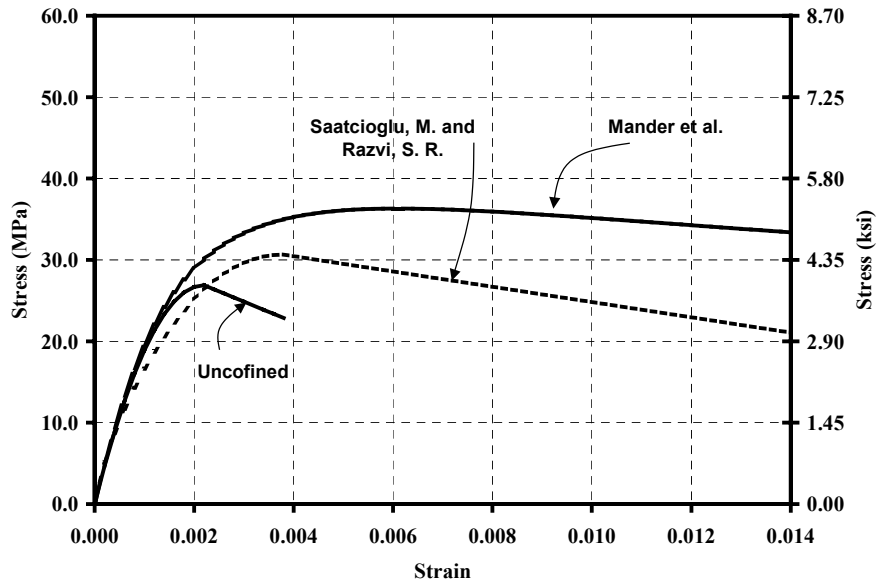
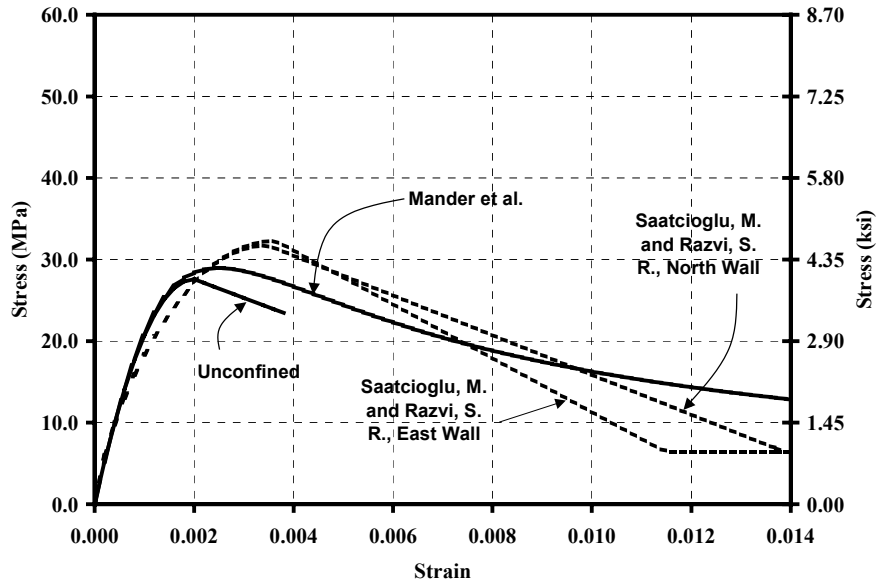


Figure C.9 Specimen P6: Stress-Strain Relationships for Unconfined and Confined Concrete at (a) East and North Walls and (b) Northeast Corner

(a) East and North Walls



(b) Northeast Corner

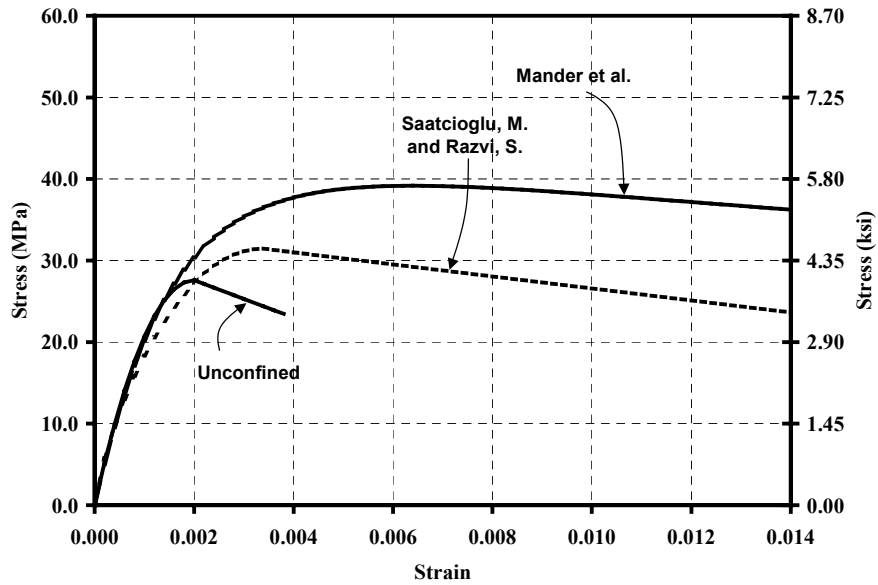
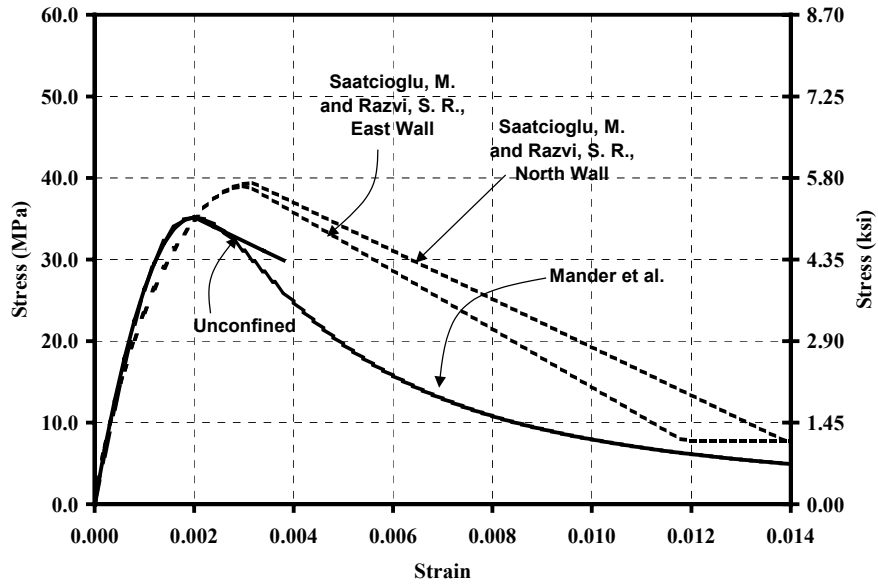


Figure C.10 Specimen P8: Stress-Strain Relationships for Unconfined and Confined Concrete at (a) East and North Walls and (b) Northeast Corner

(a) East and North Walls



(b) Northeast Corner

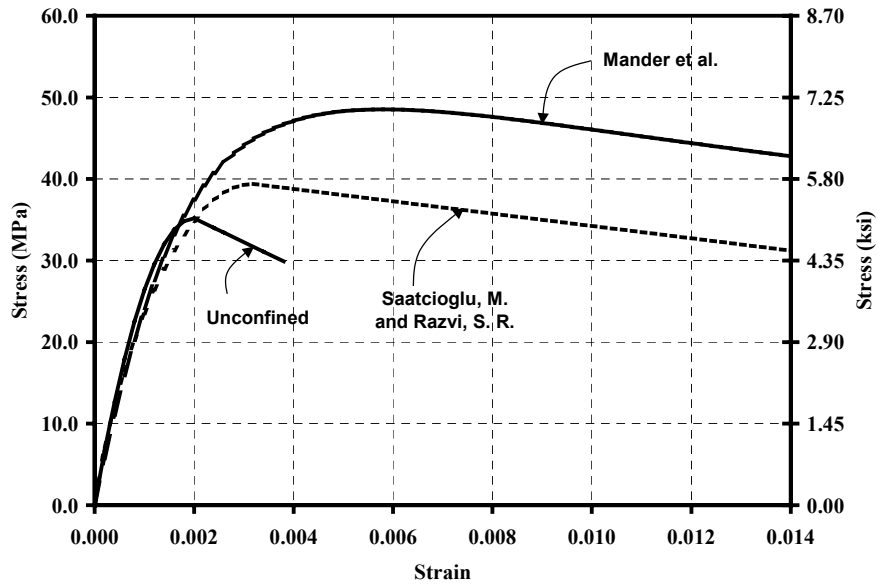
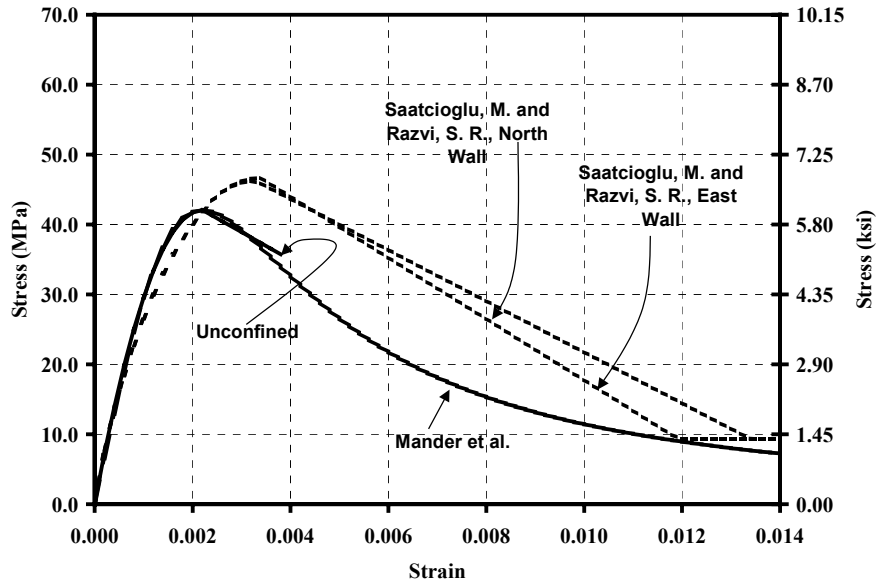


Figure C.11 Specimen P10: Stress-Strain Relationships for Unconfined and Confined Concrete at (a) East and North Walls and (b) Northeast Corner

(a) East and North Walls



(b) Northeast Corner

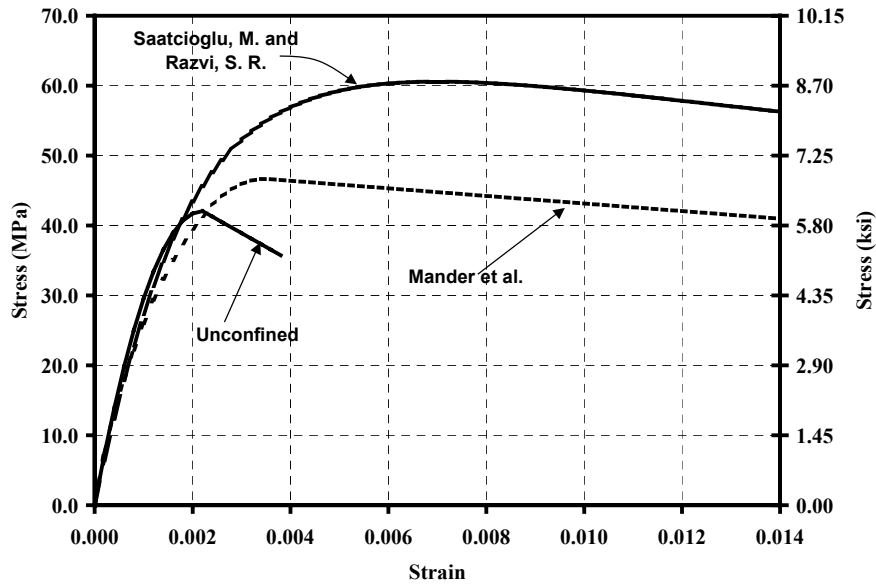
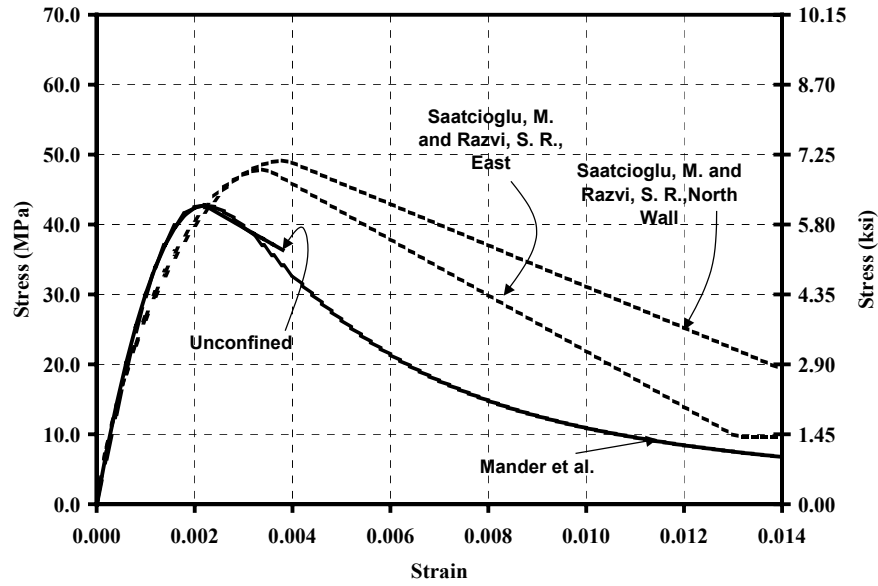


Figure C.12 Specimen P12: Stress-Strain Relationships for Unconfined and Confined Concrete at (a) East and North Walls and (b) Northeast Corner

(a) East and North Walls



(b) Northeast Corner

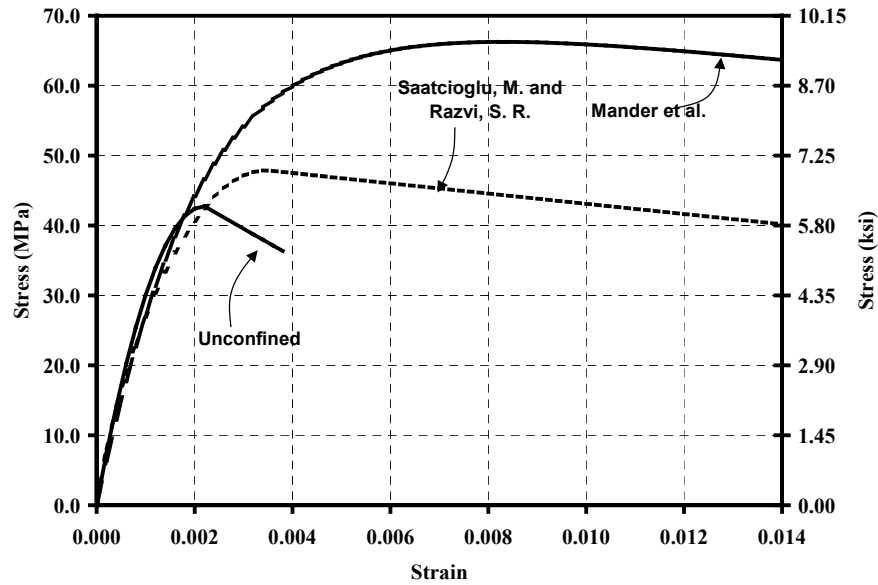


Figure C.13 Specimen P14: Stress-Strain Relationships for Unconfined and Confined Concrete at (a) East and North Walls and (b) Northeast Corner

References

- Abdulkadir, R., and Saatcioglu, M. (1991). "Tests of Concrete Columns Reinforced with Welded Wire Fabric," *Research Report No. 9104*, Dept. Of Civ. Engr., University of Ottawa, Ottawa, Canada.
- American Association of State Highway and Transportation Officials (AASHTO) (1996). *Standard Specifications for Highway Bridges, 16th Edition*, Washington, D.C.
- American Association of State Highway and Transportation Officials (AASHTO) (1998). *LRFD Bridge Design Specifications, 16th Edition*, Washington, D.C.
- American Concrete Institute, (1999). *Building Code Requirements for Structural Concrete (ACI 318-99) and Commentary (ACI 318R-99)*, Farmington Hills.
- American Concrete Institute, (1990). *Standard Tolerances for Concrete Construction and Materials (ACI 117-90)*, Farmington Hills.
- American Society for Testing and Materials (1994). "Standard Test Method for Flexural Strength of Concrete (Using Simple Beam With Center-Point Loading)," *ASTM C293-94*, West Conshohocken, Pennsylvania.
- American Society for Testing and Materials (1994). "Standard Test Method for Flexural Strength of Concrete (Using Simple Beam With Third Point Loading)," *ASTM C78-94*, West Conshohocken, Pennsylvania.
- American Society for Testing and Materials (1994). "Standard Test Method for Static Modulus of Elasticity and Poisson's Ratio of Concrete in Compression," *ASTM C469-94*, West Conshohocken, Pennsylvania.
- American Society for Testing and Materials (1996). "Standard Test Method for Splitting Tensile Strength of Cylindrical Concrete Specimens," *ASTM C496-96*, West Conshohocken, Pennsylvania.

- American Society for Testing and Materials (1999). "Standard Test Method for Compressive Strength of Cylindrical Concrete Specimens," *ASTM C39/C39M-99*, West Conshohocken, Pennsylvania.
- Bayrak, O. and Sheikh, S. A. (2001). "Plastic Hinge Analysis," *Journal of Structural Engineering*, ASCE, Vol 127(9), 1092-1100.
- Bresler, B. (1960) "Design Criteria for Reinforced Concrete Columns Under Axial Load and Biaxial Bending," *Journal of the American Concrete Institute*, Vol. 57, 481-490.
- Bresler, B. and Gilbert, P. H. (1961). "Tie Requirements for Reinforced Concrete Columns," *ACI Journal*, ASCE, Vol 58(5), pp. 555-570.
- Chang, T. Y., Taniguchi, H. and Chen, W. F. (1987). "Nonlinear Finite Element Analysis of Reinforced Concrete Panels," *Journal of Structural Engineering*, ASCE, Vol 113(1), 122-140.
- Ernst, G. C. (1952). "Stability of Thin-Shelled Structures," *Journal of the American Concrete Institute*, 277-291.
- Fialho, J. F. L. (1970) "Static Model Studies for Designing Reinforced Concrete Structures," Paper SP 2409, *Models for Concrete Structures*, ACI Special Publication SP-24, American Concrete Institute, Detroit, 215-220.
- Furlong, R. W. (1979). "Concrete Columns Under Biaxially Eccentric Thrust," *American Concrete Institute Journal*, Vol. 76(10), 1093-1118.
- Gujarati, D. (1995). *Basic Econometrics*, 3rd Ed., McGraw-Hill.
- Harris, H. G., White, R. N. and Sabnis, G. M. (1999) "Structural Modeling and Experimental," CRC. Press, Boca Raton, Florida.
- Hibbitt, Karlson and Sorensen, Inc. (1994a). *ABAQUS Theory Manual*.
- Hibbitt, Karlson and Sorensen, Inc. (1994b). *ABAQUS User's Manual*.
- Hognestad, E. (1951). "A Study of Combined Bending and Axial Load in Reinforced Concrete Members," *University of Illinois Engineering Experiment Station Bulletin*, Series No. 399.

- Hognestad, E. (1952). "Fundamental Concepts in Ultimate Load Design of Reinforced Concrete Members," *Journal of the American Concrete Institute*, 117-139.
- Jobse, H. J. and Moustafa, S. E. (1984). "Applications of High Strength Concrete for Highway Bridges," *PCI Journal*, 44-73.
- Kaar, P. H., Fiorato, A. E., Carpenter, J. E. and Corley, W. G. (1978). "Limiting Strains of Concrete Confined by Rectangular Hoops," *PCA Research and Development Bulletin*, PCA, 1-12.
- Kent, D. C. and Park, R. (1971). "Flexural Members With Confined Concrete," *Journal of the Structural Division*, ASCE, Vol 97(7), 1969-1990.
- Kupfer, H., Hilsdorf, H. K. and Rusch, H., (1969). "Behavior of Concrete Under Biaxial Compression," *ACI Journal*, Vol 66, 656-665.
- MacGregor, J. (1988). *Reinforced Concrete – Mechanics and Design*, Prentice Hall, N.J.
- Mander, J. B., Priestley, M. J. N. and Park, R. (1983). "Behavior of Ductile Hollow Reinforced Concrete Columns," *Bulletin of the New Zealand National Society for Earthquake Engineering*, Vol. 16, No. 4, 273-290.
- Mander, J. B., Priestley, M. J. N. and Park, R. (1984). "Seismic Design of Bridge Piers," *Research Report No. 84-2*, University of Canterbury, New Zealand.
- Mander, J. B., Priestley, M. J. N. and Park, R. (1988a). "Observed Stress-Strain Behavior of Confined Concrete," *Journal of Structural Engineering*, ASCE, Vol 114(8), 1827-1849.
- Mander, J. B., Priestley, M. J. N. and Park, R. (1998b). "Theoretical Stress-Strain Model for Confined Concrete," *Journal of Structural Engineering*, ASCE, Vol 114(8), 1804-1826.
- Mau, S. T. (1990). "Effect of Tie Spacing on Inelastic Buckling of Reinforcing Bars," *ACI Structural Journal*, Vol 87(6), 671-677.
- Mau, S. T. and El-Moabsout, M. (1989). "Inelastic Buckling of Reinforcing Bars," *Journal of Engineering Mechanics*, ASCE, Vol 115(1), 1-17.

- Mikhail, M. L., and Guralnick, S. A. (1971). "Buckling of Simply Supported Folded Plates," *Journal of the Engineering Mechanics Division*, ASCE, EM5, 1363-1380.
- Mirza, S. A., Hatzinikolas, M. and MacGregor, J. G. (1979). "Statistical Descriptions of Strength of Concrete," *Journal Str. Division*, ASCE, ST6,1021-1037.
- Pagnoni, T., Slater, J., Ameer-Moussa, R. and Buyukozturk, O. (1992). "A Nonlinear Three-Dimensional Analysis of Reinforced Concrete Based on a Bounding Surface Model," *Computers and Structures*, Vol. 43(1), 1-12.
- Pantazopoulou, S. J. (1998) "Detailing for Reinforcing Stability in RC Members," *Journal of Structural Engineering*, ASCE, Vol 124(6), 623-632.
- Park, R., Priestley, M. J. N. and Gill, W. D. (1982). "Ductility of Square-Confined Concrete Columns," *Journal of the Structural Division*, ASCE, Vol 108(4), 929-950.
- Popov, E. P. (1999). *Engineering Mechanics of Solids*, 2nd Ed., Prentice Hall, Upper Saddle River.
- Poston, R. W., Gilliam, T. E., Yamamoto, Y. and Breen, J. E. (1983). "Verification of Analysis Programs for Solid and Hollow Concrete Bridge," *Research Report 254-1*, Center for Transportation Research, The University of Texas at Austin, Austin, Texas.
- Poston, R. W., Gilliam, T. E., Yamamoto, Y. and Breen, J. E. (1985). "Hollow Concrete Bridge Pier Behavior," *Journal of the American Concrete Institute*, 779-787.
- Procter, A. N. (1977). "Hollow Rectangular Reinforced Concrete Columns," *Civil Engineering*, (London), 45-49.
- Razvi, S. R. and Saatcioglu, M. (1989). "Confinement of Reinforced Concrete Columns with Welded Wire Fabric," *ACI Structural Journal*, Vol. 85 (5), 615-623.
- Saatcioglu, M. and Razvi, S. R. (1992). "Strength and Ductility of Confined Concrete," *Journal of Structural Engineering*, ASCE, Vol 118(6), 1590-1607.

- Saheb, S. M. and Desayi, P. (1990). "Ultimate Strength of R.C. Wall Panels in Two-Way In-Plane Action," *Journal of Structural Engineering*, ASCE, Vol 116(5), 1384-1402.
- Scott, B. D., Park, R. and Priestly, M. J. N. (1982). "Stress-Strain Behavior of Concrete Confined by Overlapping Hoops at High and Low Strain Rates," *ACI Journal*, Vol. 79 (1), 13-27.
- Shanley, F. R. (1947). "Inelastic Column Theory," *Journal of the Aeronautical Sciences*, ASCE, Vol. 14, 261-268.
- Sheikh, S. A. and Uzumeri, S. M. (1980). "Strength and Ductility of Tied Concrete Columns," *Journal of the Structural Division*, ASCE, Vol 106(5), 1079-1102.
- Shebourne, A. N., Liaw, C. Y. and March, C. (1971) "Stiffened Plates in Uniaxial Compression," *Publications*, International Association for Bridge and Structural Engineering, Vol. 31, No. 1.
- Swartz, S. E. and Rosebraugh, V. H., (1974) "Buckling of Reinforced Concrete Plates," *Journal of the Structural Division*, ASCE, Vol. 100(1), 195-208.
- Swartz, S. E., Rosebraugh, V. H. and Berman, M. Y. (1974). "Buckling Tests on Rectangular Concrete Panels," *Journal of the American Concrete Institute*, 33-39.
- Taylor, A. W. and Breen, J. E. (1994). "Design Recommendations for Thin-Walled Box Piers and Pylons," *Concrete International*, Vol. 16 (12), 36-41.
- Taylor, A. W., Rowell, R. B. and Breen, J. E. (1990). "Design and Behavior of Thin Walls in Hollow Concrete Bridge Piers and Pylons," *Research Report 1180-1F*, Center for Transportation Research, The University of Texas at Austin, Austin, Texas, November.
- Taylor, A. W., Rowell, R. B. and Breen, J. E. (1995). "Behavior of Thin-Walled Concrete Box Piers," *ACI Structural Journal*, Vol. 92 (3), 319-333.
- Timoshenko, S. (1936). *Theory of Elastic Stability*, 1st Ed, McGraw-Hill, New York.

- Whitney, C. (1937). "Design of Reinforced Concrete Members Under Flexure or Combined Flexure and Direct Compression," *Journal of the American Concrete Institute*, 483-513.
- Willam, K. J. and Warnke, E. P. (1975). "Constitutive Model for the Triaxial Behavior of Concrete," *Proc. International Association for Bridge and Structural Engineering*, Vol 19, 1-30.

Vita

Raúl Hernán Santa María was born in Santiago, Chile, on May 27th, 1966. His parents are Mireya Oyanedel and Hernán G. Santa María, and he has four brothers and one sister. He completed high school at the Saint George's School, in Santiago, where he was given the 1983 Mathematics award to the best student in mathematics. From 1984 to 1989 he studied Civil Engineering at the School of Engineering of the Pontificia Universidad Católica de Chile, Santiago, Chile. He graduated in 1990 and received the Department of Structures award. He worked for five years in a structural design office, and lectured at the School of Engineering of the Pontificia Universidad Católica. In 1997 he received an M.S. in Civil Engineering from the University of Texas at Austin, Texas. He currently is Assistant Professor at the School of Engineering of the Pontificia Universidad Católica de Chile.

Permanent address: Departamento de Ingeniería Estructural y Geotécnica,
Vicuna Mackena 4860, Macul, Santiago, Chile

This dissertation was typed by the author.